Automated diagnosis of

Diabetic Maculopathy from Retinal Images

A THESIS

submitted for the award of the degree of

DOCTOR OF PHILOSOPHY

By

Jyoti Prakash Medhi

DEPARTMENT OF ELECTRONICS AND ELECTRICAL ENGINEERING

INDIAN INSTITUTE OF TECHNOLOGY GUWAHATI

GUWAHATI - 781 039, INDIA

13 Feb 2021

DEDICATION

This thesis is dedicated to

My Loved ones

for their endless support and encouragement

DECLARATION

This is to certify that the thesis entitled "**Automated diagnosis of Diabetic Maculopathy from Retinal Images**", submitted by me to the *Indian Institute of Technology Guwahati*, for the award of the degree of Doctor of Philosophy, is a bonafide work carried out by me under the supervision of Prof. Samarendra Dandapat. The content of this thesis, in full or in parts, have not been submitted to any other University or Institute for the award of any degree or diploma.

Dated:

Guwahati

Jyoti Prakash Medhi
Dept. of Electronics and Electrical Engineering,
Indian Institute of Technology Guwahati,
Guwahati-781039, Assam, India.

CERTIFICATE

This is to certify that the thesis entitled "**Automated diagnosis of Diabetic Maculopathy from Retinal Images**", submitted by **Jyoti Prakash Medhi**, a research scholar in the *Department of Electronics and Electrical Engineering, Indian Institute of Technology Guwahati*, for the award of the degree of **Doctor of Philosophy**, is a record of an original research work carried out by him under my supervision and guidance. The thesis has fulfilled all requirements as per the regulations of the institute and in my opinion has reached the standard needed for submission. The results embodied in this thesis have not been submitted to any other University or Institute for the award of any degree or diploma.

Dated:

Guwahati.

Dated:

Guwahati

Dr. Samarendra Dandapat

Professor

Department of Electronics and Electrical Engineering

Indian Institute of Technology Guwahati

Guwahati - 781 039, Assam, India.

ACKNOWLEDGMENTS

The work would not have been completed without the contribution and support of many people. Here, I would take the opportunity to thank them all.

The most important acknowledgment of gratitude I wish to express is to my mentor and guide Prof. Samarendra Dandapat of the Department of Electronics and Electrical Engineering, who has put his immense support, encouragement, and valuable suggestions, experience, and wisdom at my disposal. He provided critical advice in my calculations and my research work and did suggest many significant additions and improvements. It has been a great enriching experience for me to work under his authoritative guidance. It was only because of his keen interest and continuous supervision that I gave my work this extent form. I am indebted to him for his time and the patience he has shown in training me to become a successful researcher with principles.

My heartfelt thanks to my doctoral committee members, Prof. Shaik Rafi Ahamed, Prof. S. R. Mahadeva Prasanna, Prof. Sanasam Ranbir Singh, and Prof. Salil Kashyap for their moral support, thorough evaluations and suggestions that improved my research work. I would like to express my deepest sense of gratitude for the most wonderful human-being and technically sound person, respected Prof. Prabin Kumar Bora, who inspired and encouraged me with his massive words and blessings.

I am also thankful to the Head of the Department and the other faculty members for their kind help in carrying out this work. I express my gratitude to all the members of the research and technical staff of the Department for their timely help.

My sincere thanks to Prof. S. R. Nirmala, former colleague, friend, and mentor who helped me in every possible way during my research and technical writings.

It was wonderful to meet many unknown faces and to make many friends. I am thankful to my friends of IIT Guwahati especially Sandeep and Tousif, for their love, care, support, and assistance during my doctoral studies. I am grateful to the members of the EMST Laboratory and friends,

Malaynath, Argha, Anurag, Sibsankar, Sonu, Dorothy, Jiss, Vineeta, Tilendra, Salman, Sibasis, Prabhakara, Samarjit and many more, for their immeasurable and tremendous support, who helped me whenever I need them.

I would like to thank all my colleagues at workspace Gauhati University especially, Prof. Eeshankur Saikia, Prof. Debabrat Baishya, Prof. Debasish Bhattacharjee, and Prof. Upasana Bhattacharjya for their expert suggestions in biological and mathematical analysis. Everyone here has encouraged and supported me well in the journey of my Ph.D.

I am very much grateful to Dr. Nilotpal Borah, Dr. Santanu Barthakur and their team of Guwahati Eye Institute for their help and expert advice. The addition of new database from their institute, with annotations added a significant support to my research.

I am obliged to GOD for showering his blessings, grace, and divine guidance all throughout this journey of mine. I was true to myself and solely dedicated my thesis to Him. My deepest gratitude goes to my caring parents, brother, sister, wife, my dearest son Evyavan, and family for their constant support, love, and sacrifice without whom I could not have completed this work. I attribute this achievement to them for their silent prayers for my success and making me stand in this position.

I want to thank all those people who have helped and contributed directly or indirectly to complete my work.

Jyoti Prakash Medhi

ABSTRACT

Ophthalmology is the study of structure, function, and diseases of the eye. This complex sense organ eye facilitates the vision and perception of the surrounding. But unfortunately, due to aging and several eye associated disorders, the experience of reduced visual acuity has become common among the patients, and if left untreated, it leads to vision impairment and even vision loss. Accordingly, the main focus of the ophthalmologists is to diagnose and manage such types of vision impairments. The recent technological advancements in imaging technologies have upgraded the ophthalmological diagnosis and eventually made it possible to detect minute structural features and anomalies. But high patient to doctor ratio increases the challenges for proper management of the patients. Therefore, to meet up the requirement, the involuntary methods for retinal image analysis are much more convenient and aid the ophthalmologists to screen at a faster rate. Hence, in this thesis, we have taken an engineering perspective and developed automated image analytics methods for the diagnosis of one such vision-threatening retinal disease called Diabetic Maculopathy (DM).

Extended diabetes for a longer period starts effecting the vision due to leakage of blood and its components (lesions) over the retina. These depositions become vision threatening if they precipitate over the macula. Such retinal deformity is termed as DM and may lead to vision impairment if not diagnosed in time. The analysis of DM is possible through the evaluation of fundus and optical coherence tomography (OCT) images. This thesis first develops an automated analytics method for the diagnosis of DM using the fundus image. It detects the changes in the retina for the classification of DM. Later, for the investigation of changes in retinal layers with respect to DM progression, the thesis proposes an automated algorithm using the OCT image.

The fundus image analysis for DM diagnosis seeks identification of fovea and lesions over the retina. The deposition of these lesions in the fovea neighborhood signifies the presence of DM, and its severity is measured with their position closer to the fovea. Hence, the accurate position of both fovea and lesions is an essential factor. In this thesis, we have identified the exact fovea location with the help of avascular property of fovea, and the novelty of the approach is that it is independent of

the optic disc (OD) and fovea geometrical relation. The method is further improvised to detect the fovea in severe DM cases by generating and matching the ellipse template. Under this condition, most of the existing algorithms fail to locate fovea. The detection of OD is necessary to mark the fovea neighborhood, and it is detected by the property of OD, possessing maximum blood vessels. The lesions are identified with the help of their color information, and the method is upgraded by the addition of shade correction and false-positive elimination. The DM is classified into mild, moderate, and severe stages based on the position of these lesions in the calculated fovea neighborhood. Along with classification, the thesis also evaluates the deposition intensity and classifies it into the average and acute stage.

The fundus images are subjected to monitoring the changes occurring over the retina. But due to DM, the retinal layers also get effected with blood leakage and deposition of blood due to the growth of fragile new blood vessels. Hence, the requirement of OCT image analysis comes into the picture. During DM, the retinal layers are subjected to blood and exudate deposition, which alters the retinal thickness. Therefore, the automated diagnosis system requires estimation of retinal thickness with localization of inter-retinal cysts. The OCT images are highly susceptible to speckle noise, and the novelty of the thesis work is the elimination of it using Guided image filtering along with preserving the edge information. Thereafter the retinal layer thickness is obtained with the help of automated level set algorithms that detects variational boundaries leaving no component undetected. The boundary separation for the detection of cysts is the positive aspect of the algorithm, which detects the cyst area efficiently.

Proposed algorithms are evaluated thoroughly for accuracy and statistical reliability. For the investigations with the fundus image, our methods are experimented on various publicly available databases. Among these, only a few have manually annotated information for comparison. For attaining annotations, we have consulted three ophthalmologists from the Guwahati Eye Institute and evaluated the algorithms. To verify the algorithms on local clinical images, we have also collected fundus images from the hospitals. For OCT images we have analyzed the algorithms on collected color OCT images from local hospitals. Later, for the performance comparison we have conducted tests following state-of-art algorithms on two publicly available database.

We want to add in a general clinical context that the proposed algorithms may be treated as a solution to the specific ophthalmologic problem with its engineering perspective.

Contents

List of Figures

List of Tables

List of Abbreviations

AHE	Adaptive Histogram Equalization
AMD	Age-related Macular Degeneration
ANN	Artificial Neural Network
ANOVA	Analysis Of Variance
AUC	Area Under the Curve
BM3D	Block-Matching and 3D
BV	Blood Vessel
CAD	Computer Aided Diagnosis
CI	Confidence Interval
CLAHE	Contrast Limited adaptive Histogram Equalization
cm	Centimeter
CME	Cystoid Macular Edema
CNN	Convolutional Neural Networks
CSME	Clinically Significant Macular Edema
CWS	Cotton Wool Spot
DC	Dice Coefficient
DIARET DB0	Standard Diabetic Retinopathy Database Calibration level 0
DIARET DB1	Standard Diabetic Retinopathy Database Calibration level 1
DM	Diabetic Maculopathy
DME	Diabetic Macular Edema
DR	Diabetic Retinopathy
DRIVE	Digital Retinal Images for Vessel
DT-CWT	Dual Tree Complex Wavelet Transform
DWT	Discrete Wavelet Transform

EHD	Edge Histogram Descriptor
ELM	External Limiting Membrane
FA	Fluorescein Angiography
FFA	Fundus Fluorescein Angiography
FN	False Negative
FOV	Field Of View
FP	False Positive
FS	Fourier Spectrum
G1	Grader 1
G2	Grader 2
GBPF	Gaussian Band Pass Filter
GCL	Ganglion Cell Layer
GDD	Gaussian Data Description
GEI	Guwahati Eye Institute
GIF	Guided Image Filter
GLCM	Gray Level Co-occurrence Matrix
GMM	Gaussian Mixture Model
GW	Gabor Wavelet
HE	Hard Exudates
HM	Hemorrhage
HOS	Higher-Order Spectra
HPF	High Pass Filter
HRF	High Resolution Fundus
ILM	Inner Limiting Membrane
INL	Inner nuclear layer
IPL	Inner plexiform layer
IRMAs	Intra Retinal Microvascular Abnormalities
IS/OS	Inner Segment / Outer Segment
LBP	Local Binary Pattern
LDA	Linear Discriminant Analysis

LME	Laws Mask Energy
LPF	Low Pass Filter
LSFCM	Level set Spatial Fuzzy Clustering Algorithm
M	Masked
MA	Microaneurysm
ME	Macular Edema
MP	Misclassified Proportion
NB	Naive Bayes
NCSME	Non-Clinically Significant Macular Edema
NFL	Nerve Fiber Layer
NN	Neural Network
NV	Neo-Vascularization
OCSC	OPTIMA Cyst Segmentation Dataset
OCT	Optical Coherence Tomography
OD	Optic Disk
ODD	Optic Disk Diameter
ONL	Outer Nuclear Layer
OPL	Outer Plexiform Layer
PDE	Partial Differentiation Equation
PPV	Positive Predictive Value
RBF	Radial Basis Function
RETOUCH	The Retinal OCT Fluid Detection and Segmentation Benchmark and Challenge
ROI	Region Of Interest
RPE	Retinal Pigment Epithelium
RTA	Retinal Thickness Analyzer
S	Sensitivity
SD-OCT	Spectral Domain OCT
SE	Soft Exudates
SNR	Signal to Noise Ratio
SVM	Support Vector Machine

TD-OCT	Time Domain OCT
TN	True Negative
TP	True Positive
U	Unmasked

1

Introduction

Contents

1. Introduction

The human eye is the most sensitive and complex sense organ responsible to see the objects around us. The navigation through vision enables us to understand and communicate with the world and critically determines the quality of life. But unfortunately, with the modern lifestyle, people suffer from a collective experience of reduced visual acuity, vision impairments, and even vision loss. One of such sight-threatening diseases is the Macular Edema (ME). ME occurs due to prolonged systemic diseases like diabetes, high blood pressure, aging, retinal pigmentosa, and uveitis [1, 2]. During ME, the central vision gets affected, and it causes irreversible changes in the retina with indications such as blurred central vision, washed-out colors, distortion in shape and size, and reading difficulties [3]. For example, as shown in Figure 1.1, the first image shows the typical vision of a healthy person, and the second image represents the vision with blurry and washed out distortions. With a higher degree of effect over central vision distortion, the patient may be able to see the clock but cannot justify the time as shown in Figure 1.1(c).

Figure 1.1: ME effect on vision: [a] Normal (healthy) vision, [b] Blurry and blocked vision due to ME and [c] Blocked central vision with ME.

The most perilous form of ME is called Diabetic Maculopathy (DM) or Diabetic Macular Edema (DME), which results from prolonged diabetes. Therefore, the diagnosis and management of DM is essential. However, due to the increased patient population, the diagnosis of DM poses a significant challenge for the ophthalmologists. In recent years, the advancement of high-resolution imaging modalities has led the healthcare procedure into a revolutionary state and helped the ophthalmologists to diagnose with non-invasive procedures. The plethora of information obtained from these devices can be effectively used for the prognosis and the diagnosis of retinal pathologies. The computer-aided analysis of these information can help ophthalmologists perform fast and reliable diagnosis with efficient management. Therefore, researchers are currently aiming at formulating automated methods for the diagnosis of diseases from retinal images.

In this thesis, we have designed fast and accurate algorithms for automated detection of DM. Providing more insights into the proposed algorithms, it contains two analysis schemes, using fundus (2D image of the retina) and optical coherence tomography (OCT) (cross-sectional image of retinal layers) images. Both the analysis method finds the changes occurring in the central retina due to DM and, thus, determines the classification of DM severity. The proposed work in the thesis is distributed in three broader topics with significant contributions in each . First, the efficient detection of the fovea in fundus image using avascular property of blood vessel (BV)s in macular region and with ellipse fitting for the challenging pathogenic cases, where DM lesions cover the fovea. The second topic is detecting DM lesions eliminating false positive (FP)s caused by retinal reflections during exudate detection and discarding BVs during dark lesion identification using fundus image. Finally, the third section is comprised of OCT image analysis for DM, contributing proper removal of speckle-noise with the help of Guided image filtering (GIF). This step enhances the layer detection and DM identification. The contents discussed in the first chapter of the thesis are mentioned below.

Chapter content: Section 1.1 gives a brief idea of eye physiology and corresponding pathology caused due to DM. The imaging modalities, are introduced in section 1.2, which are essential to visualize and understand retinal changes during such pathological conditions. The automated diagnosis of DM using fundus and OCT image is discussed over section 1.3. Section 1.4 presents the challenges and opportunities faced during the automated detection process. The literature on DM analysis is discussed in section 1.5 and the scope of the present work is covered thereafter in section 1.6. The sections conclude with the organization of the thesis deliberated in section 1.7.

BACKGROUND

To proceed with the thesis findings, we need to understand eye physiology and pathology, along with the function of imaging modalities and image analytics, in connection to ophthalmological evaluations of DM. The process continues with the findings of challenges and opportunities faced during evaluation and signal processing issues to formulate the automated detection algorithms.

1.1 Eye Physiology and Pathology

This section details the eye physiology with a stress into discussion of retina. Later, the changes occurring in the retina due to DM progression is introduced to have a clear picture of the findings

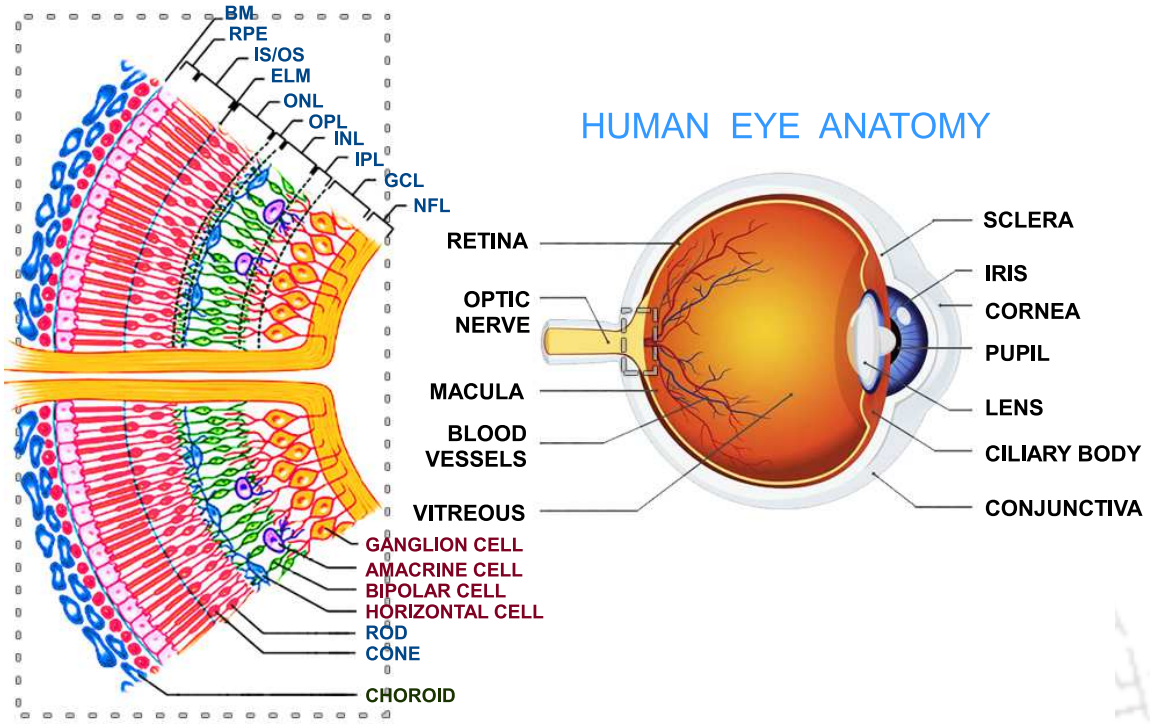

Figure 1.2: Human eye anatomy and illustration of retina layer.

required for proposing automated algorithms for DM detection. For a detailed study of eye anatomy, the reader is suggested for referring textbooks or similar materials such as [2–4]. The right side image of the Figure 1.2 (*image courtesy: http://www.nvisioncenters.com*) shows a cross-section of human eye anatomy. It consists of cornea, iris, pupil, lens, vitreous, optic nerve, retina, macula, and choroid [4].

The cornea is a transparent, clear layer in front of the eye responsible for transmission and focusing of light into the eye. Behind the cornea lies the iris and pupil, which regulates the amount of light falling inside the eye. Light entering from the pupil focuses through the lens at the retina. The lens is adjusted with the help of ciliary muscles. Between lens and retina lies a jelly-like transparent substance called vitreous for filling the middle portion of the eye. The retina is located at the back of the eye and is a complex structure of central neuronal circuitry, comprising 200 million neurons, including 120 million rods and about 1 million cone photoreceptor [5]. The light entered focuses at retina, over macula center called fovea. The fovea contains the maximum number of cone cells than rods. Thus fovea plays a significant role during vision processing and is directly associated with central vision. The cross-section of retinal tissue, as shown in expanded form towards left in the Figure 1.2 (*image*

courtesy: http://www.retinareference.com), is comprised of ten layers. The outermost layer of retina, the Retinal pigment epithelium (RPE), lies adjacent to the choroid and absorbs light for reducing back reflection to the retina. The Inner segment / outer segment (IS/OS) layer contains photosensitive outer segments of rods and cones. External limiting membrane (ELM) is the separator of the photoreceptor and the Outer nuclear layer (ONL). The ONL contains the rods and cones cell bodies. The outer plexiform layer (OPL) followed after ONL contains the synapses between photoreceptor axons and neuron dendrites. Next Inner nuclear layer (INL) comprises the cell bodies of neurons and Muller cells. The synapses of these neurons and ganglion cells form the Inner plexiform layer (IPL). The cell bodies of ganglion cells are accumulated in the Ganglion cell layer (GCL). The axons of ganglion cells are comprised of the Nerve fiber layer (NFL). Over the ganglion cells lie the Muller cell endfeet with associated basement membrane forming the Inner limiting membrane (ILM). The dendrites of ganglion cells together form the optic nerve, which is extended to the brain. The optic nerve head visible over retina is called as the Optic Disc (OD).

The light falling over retina at fovea gets absorbed inside the retinal layer and reaches the photoreceptor rods and cones. The rods are sensitive to the low-level light, whereas cone cells are operative in brighter light for perception of color and sharp vision. There are three types of cone cells, namely red, green, and blue. These photoreceptors absorb the light photons, and the process of photo-transduction converts the light received into electrical pulses and transmit it to the brain via nerve, ganglion cell, OD and finally optic nerve. The electrical signal thus transmitted is decoded at the visual cortex of the brain and results in vision.

Due to various eye disorders, structural changes appear in the posterior segment of the eye. Retinopathy refers to the damage caused to the retina as a result of various microvascular complications. Diseases associated with retinopathy include Diabetic Retinopathy (DR), DM or DME, Age-related Macular Degeneration (AMD), hypertensive retinopathy, and glaucoma. The study and investigation of microvascular complications performed in this thesis include DR and, more specifically, DM. The following sections provide insight into the changes occurring in the retina due to DM.

1.1.1 Diabetic Maculopathy

Anyone having type-I or type-II diabetes for a more extended period, on an average of 10 years, develops hypertension and hyperglycemia, causing the inception of Diabetic Retinopathy [5–9]. Elevation of hyperglycemia increases the sugar level in the blood, causing blockage of small BVs that

nourish the retina. It results in a cut down of blood supply reducing the oxygen demand. DM is closely associated with the extent of DR, along with the duration and type of diabetes. A prolonged 25-year progressive type 1 diabetes is subjected to 29% for DM and 17% for Clinically Significant Macular Edema (CSME) [6, 9]. Various changes occurring in the retina due to DR are pictorially shown in Figure 1.3 (*image courtesy: https://www.jirehdesign.com*). As a result of reduced oxygen supply during

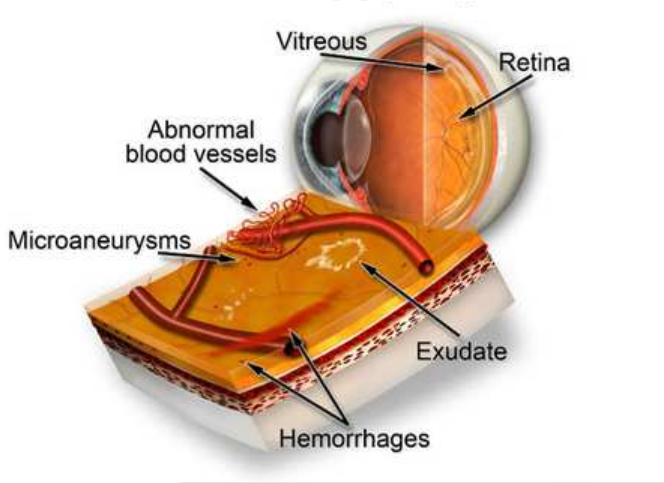

Figure 1.3: Changes over retina due to Diabetic Retinopathy.

hyperglycemia, the BV basement membrane stb arts thickening with selective degeneration. It leads to structural weakness of BVs with dilation of capillary walls causing focal vascular endothelial cell proliferations called Microaneurysm (MA)s. These are red lesions with small beaded like structure out-pouching from retinal BVs, as seen in Figure 1.3. These MAs at a later stage may burst leaking blood, and its constituents or become thrombosed [10]. These leaked dead blood cells over retina gives rise to the second form of red lesions named as Hemorrhage (HM)s. HMs are comparatively larger than MAs, shown as blood leakage in Figure 1.3. Along with blood, plasma leakage (lipid and protein extracts) from abnormal retinal capillaries gives rise to bright lesions. These do not possess any regular shape or size but appear in clumps or circinate rings. Depending on their amount of deposition, in ascending order, they are named as Cotton Wool Spot (CWS), Soft Exudates (SE) and Hard Exudates (HE). In Figure 1.3, only exudates are shown as white patches. These lesions are non-transparent and blocks the light from falling over the retina. On severe stage of DR new vessels are formed through the venous circulation pathway either on the OD or anywhere in the retina, due to retinal ischemia, and called as Neo-Vascularization (NV). Fine tufts of delicate vessels occurs rapidly forming arcades on the surface of the retina. As they begin to multiply, they also extend on

the posterior surface of the vitreous. They are fragile, porous and often prone to rupture, causing a pre retinal sub-hyaloids or a vitreous HMs. Formation of new vessels may be asymptomatic until HM appears, when acute vision loss may also occur [3, 11, 12]. Based on all these complications and their occurrences, DR is categorized in various stages such as Background DR, Pre-proliferative DR, DM, and Proliferative DR. When the lesions get deposited in the macular neighborhood, DR is referred to as DM. During DM, the physiological changes in retina initiates over its surface and gradually affects the retinal layers. The new BV formed from choroidal or retinal vasculature as a result of retinal ischemia started penetrating retinal layers and burst with the fluid accumulation within the intracellular spaces of the OPL and results in retinal thickening. It originates from the leakage of perifoveal retinal capillaries at advanced stages of DR [13]. Pictorial representation of these events is represented in Figure 1.4 [14]. With the deposition of bright and dark lesions in the fovea neighborhood, the central sharp vision experiences reduced visual acuity. DM/DME is of two types, focal and diffuse form. Vascular dysfunction causing localized thickening of retina is focal DM, mainly arising from MAs, and less caused by intra-retinal microvascular abnormalities (IRMAs). Here, fluid leakage occurs to a great extent, which is usually followed by HEs. The HE pattern may be either focal or ring structured. The diffuse DM is caused across posterior pole of retina as a result of diffuse leakage of BVs from MAs and arterioles. It is usually observed in both eyes with a similar or extensively different

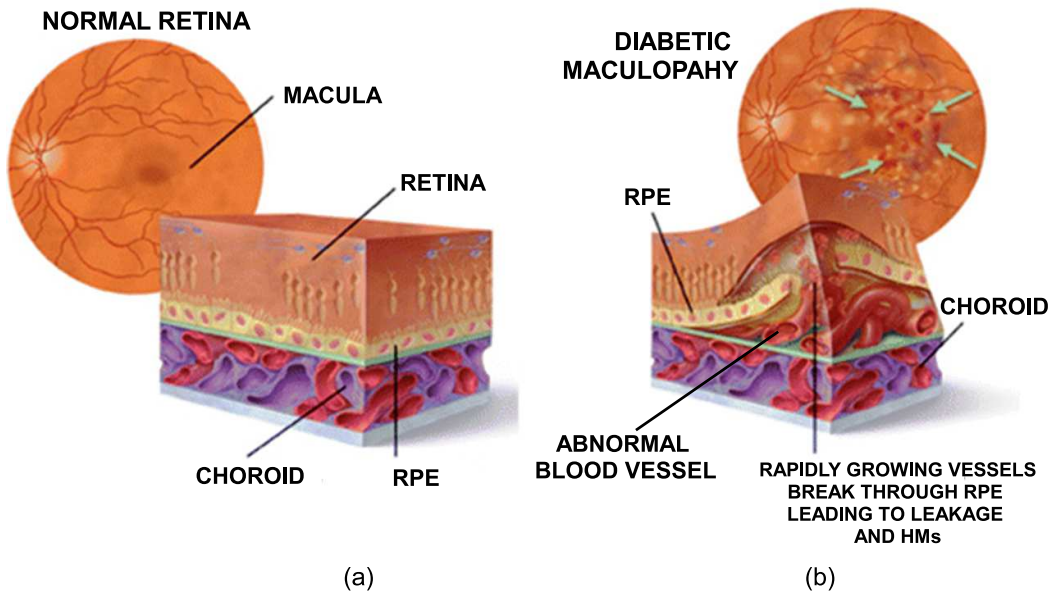

Figure 1.4: Changes occurring in retinal layers with respect to DM: (a) Normal (healthy) retina, (b) Retina affected by DM.

degree of leakage. Another type of class called ischemic, exudative and hybrid are also perceived in DM [11, 12, 15, 16]. If left untreated, these consequences of DM, also known as cystoid macular edema (CME), cause interruption of the central vision, retinal detachment, leading to blindness.

The identification of these changes occurring in the retina is the primary responsibility of the ophthalmologists in-order to locate and diagnose DM. The direct visual examination of the retina results in inadequate clinical information due to the complex anatomy of the eye and, therefore, is insufficient for evaluation. Hence, ophthalmologists rely on advanced imaging techniques to visualize both the surface and subsurface structure of retina for qualitative and quantitative assessment of DM. The next section elaborates on such imaging techniques along with the clinical perspective drawn from them.

1.2 Imaging modalities

Ophthalmologists prefer advanced imaging techniques for visualization and assessment of retinal disorders to perform proper diagnosis. For posterior imaging modalities, popular procedure includes Color Fundus Photographs, Fundus Fluorescein Angiography (FFA). On the other hand, among anterior imaging, we have slit lamp and lenses, Retinal Thickness Analyzer (RTA), and Optical Coherence Tomography [8, 17–19] are presently preferred by ophthalmologists. Among these techniques, the Fundus photograph is commonly used for various mass retinal disorder analyses such as DR, Glaucoma, DME, AMD. For detail analysis of these disorders, FFA and OCT images are screened along with Fundus images. The following subsection elaborates on fundus, FFA and OCT photographs, and their clinical perspectives.

1.2.1 Fundus Photography

The name ‘Fundus’ originates from the meaning ‘hollow.’ The retina is situated at the back of the hollow organ, the eye. Hence its photography is termed as the fundus photograph. The fundus image is a 2D projection of 3D semi-transparent tissues on a 2D image plane. The fundus camera, in general, is a standard camera with a microscope attached to it. The working principle includes transmission of external light into the eye, which reflects across retina generating 2D fundus image over the imaging surface. Conventional fundus cameras provide a 30 and 45-degree Field of View (FOV) of the retina. Color Fundus Photography is taken in the presence of white light, and the image

intensity contains reflected red, green, and blue wavelength components across the camera sensor. Figure 1.5 shows the image of the fundus camera and color fundus photographed from it. The camera

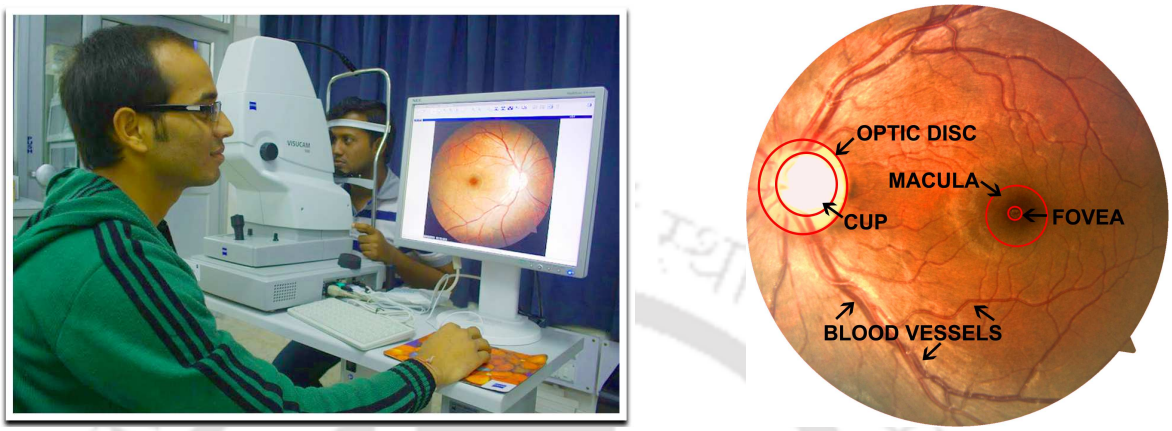

(a) (b)

Figure 1.5: [a] Fundus Camera, [b] Fundus image captured at 45degree FOV.

shown in the figure is situated at EMST Lab, IIT Guwahati, and the photograph taken is the author's left eye fundus at 45-degree FOV. The BVs, OD, Macula, Fovea, Vascular abnormalities, blood, and its constituent deposition can be distinctly observed using a color fundus image.

1.2.1.1 Clinical Perspective:

Fundus photography is referred to as a standard screening tool by ophthalmologists for diagnosis of DR and DM. Various abnormalities such as MAs, HMs, BV deformation, CWS, SE, and HE can be qualitatively assessed using color fundus images. In order to understand the appearance of such abnormalities over fundus image, let us consider Figure 1.6. Figure 1.6(a) here represents a normal fundus image, and the rest images show the presence of various abnormalities due to DR/DM. MAs are approximately less than 125μm in size, covering an area of $1-3$ pixels in various fundus databases [15, 20] with well defined circular edges as seen in Figure 1.6(b). Although the Fundus image is used for MA detection, Fluorescein Angiography (FA) imaging is better suited as it records images with high contrast, making it possible to identify better [21]. MAs and weak capillaries rupture, resulting in deposition of leaked blood cells over retina. Due to the difference in the amount of deposition and rupture, the HMs are irregular in shape with soft boundaries, with a size of more than 125μm. Depending on size and shape, HMs are categorized into three divisions called dot, flame, and blot. The dot HMs are similar to MAs but slightly bigger. Flame HMs are perceivable

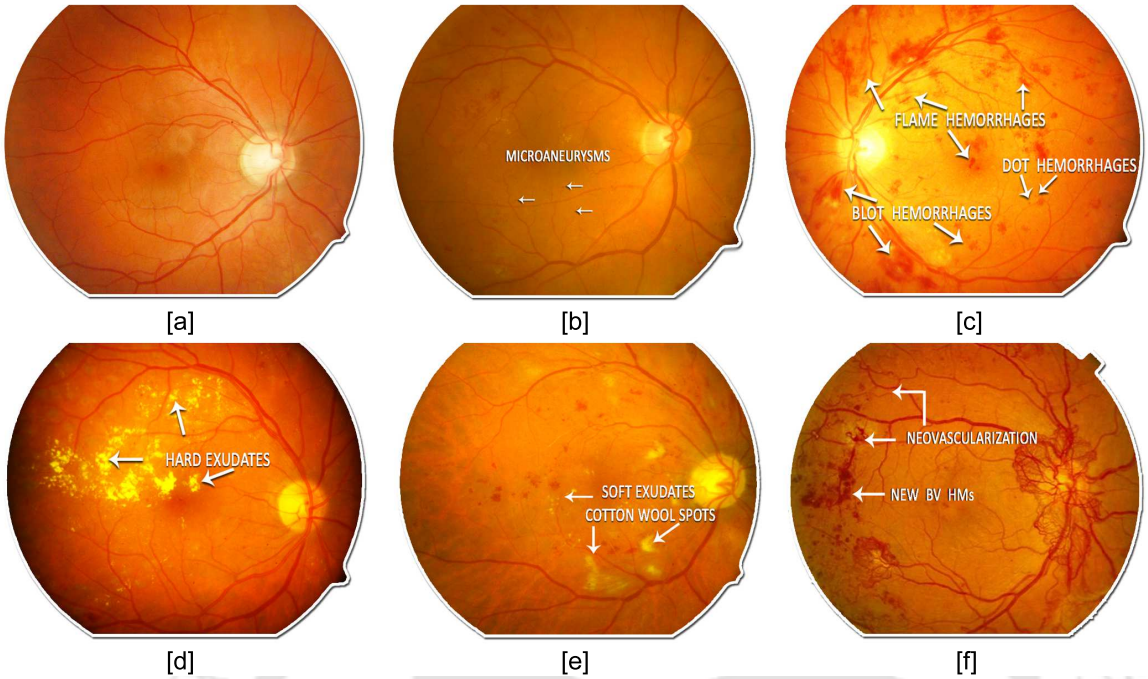

Figure 1.6: Manifestation of DR over Fundus image: (a) Healthy Fundus image, (b) MAs, (c) Various HMs, (d) HEs, (e) SEs and (f) NV.

by their flamed shapes. The blot HMs are the comparatively bigger and irregular in size [15, 20, 21]. Figure 1.6(c) represents a various form of HMs observed in the fundus image. The HEs are yellowish, waxy, shiny deposits over retina. They do not possess any regular shape or size. Sometimes HEs contain HMs at its center [15, 20, 21]. HEs shapes and appearances over fundus image are shown in Figure 1.6(d). SE and CWS are small fluffy yellowish, bright lesions. They do not possess distinct boundaries like HEs. The structures of SE are shown in Figure 1.6(e). As seen in Figure 1.6(f) growth of new BV is the NV stage of DR.

Figure 1.7: DR stages: (a) Healthy fundus, (b) Background DR, (c) Pre-proliferative DR, (d) DM and (e) Proliferative DR.

Depending on the amount of deposition of various lesions over retina, DR is classified into various stages concerning observation in fundus images. As shown in Figure 1.7 the stages are, Background DR, Pre-Proliferative DR, Diabetic Maculopathy and Proliferative DR [15, 20, 21]. For the details of

the DR stages the reader is referred to book [2]. Now we directly move into DM imprints over fundus image.

- Diabetic Maculopathy: DM or DME is thickening of retina originated due to accumulation of intraretinal fluid and/or HEs within 2-2.5 Optic Disk Diameter (ODD)s of the center of the macula, the fovea. Depending on the location and amount of deposition, DM is further classified into three stages.

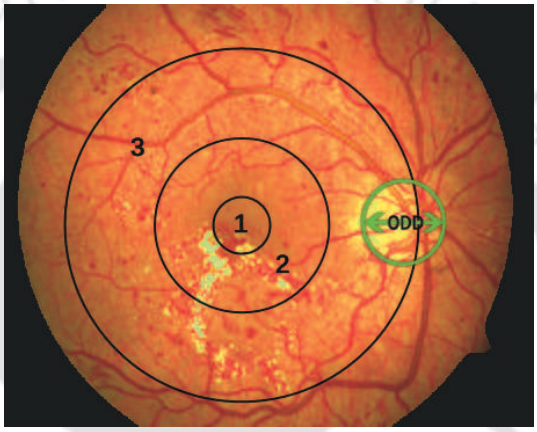

Figure 1.8: Fundus Image showing various stages of DM (region 1=severe, 2=moderate, 3=mild).

Mild: This stage is also known as Non-Clinically Significant Macular Edema (NCSME) and is classified based on the deposition of lesions within a radius of 1 to 2 ODD from fovea center. The region is marked as 3 in Figure 1.8.

Moderate: Moderate stage or CSME is classified with the presence of lesions within a radius of 1ODD from the fovea center. In Figure 1.8 it is marked as 2.

Severe: Severe is a CSME stage when the presence of lesions is identified at a radius of $1/3$ ODD from the fovea center. Marked as 1 in Figure 1.8.

1.2.2 Fundus fluorescein angiography

Fundus fluorescein angiography is Fundus Photography only with imaging in fluorescein environment [13, 18]. During this technique, we inject the fluorescein dye through the antecubital vein. FFA is mainly used for MA, BV, and AMD analysis. Figure 1.9 shows the FFA image used for analyzing MAs and NV examination.

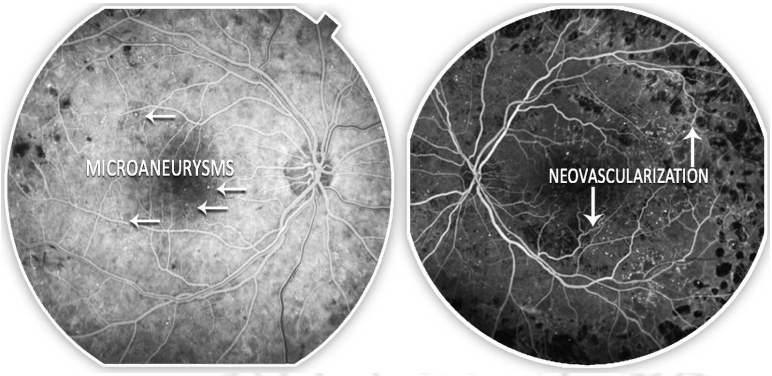

Figure 1.9: FFA image for analysis of MA and NV.

1.2.3 Optical Coherence Tomography

Optical Coherence Tomography camera uses low coherence interferometry, also called white light interferometry, and images the cross-sectional ocular tissue. The low visible coherent light generates high-resolution images. The light penetrates through retina and gets reflected to form a cross-sectional image of the retina. It provides exquisite details of the posterior segment, from the vitreoretinal interface, through a cross-section of all the layers of the retina to the RPE-choroid complex [17, 18]. The OCT generates pseudocolor images with the help of monochromatic lasers. Thus the image formed is also known as pseudo-retinal image. There are two types of OCT scans, one is Time Domain OCT (TD-OCT), and the other is Spectral Domain OCT (SD-OCT). In TD-OCT, A-scans are produced by mechanically moving the OCT instrument. In SD-OCT, a series of A-scans with a cross-sectional reconstruction of a plane through the anterior or posterior segment of the eye, also called B-scans are produced. SD-OCT is found to be faster than the TD-OCT, whose images are complicated to process, compared to SD-OCT images. Recently TD-OCT has been replaced by SD-OCT or Fourier domain OCT having resolution less than 5 micrometers. The OCT camera and captured OCT image is shown in Figure 1.10.

1.2.3.1 Clinical Perspective:

OCT images are used for analyzing the retinal layer distortion concerning intraocular diseases such as myopia, DM, Glaucoma, AMD, Macular holes, Retinal detachment. Ophthalmologists inspect multiple OCT B-scans across the target area to identify the amount of infection. Figure 1.11 (*Image courtesy: https://www.zeiss.com*) represents various retinal layers observed in the macular OCT

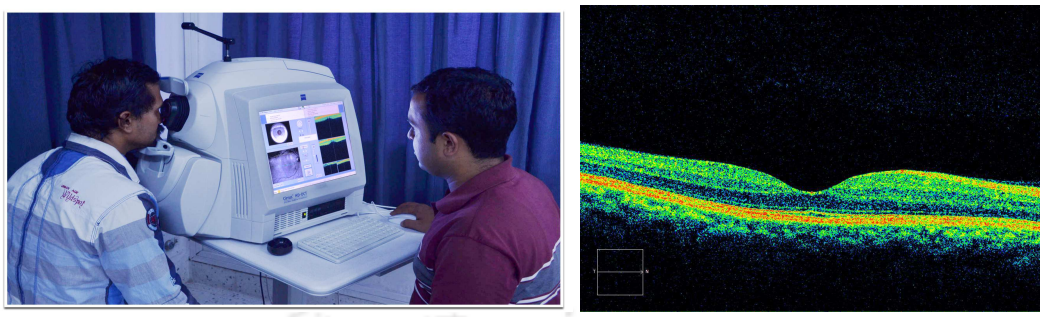

(a) (b)

Figure 1.10: [a] OCT camera, [b] OCT image.

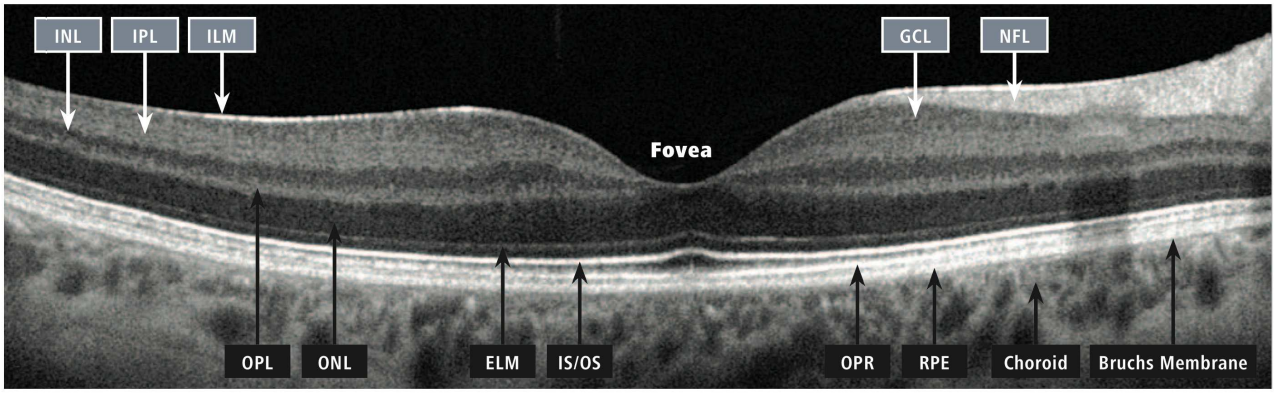

ILM: Inner limiting membrane
IPL: Inner plexiform layer
INL: Inner nuclear layer
OPL: Outer plexiform layer
ONL: Outer nuclear layer
ELM: External limiting membrane
IS/OS: Junction of inner and outer photoreceptor segments
OPR: Outer segment PR/RPE complex
NFL: Nerve fiber layer
GCL: Ganglion cell layer
RPE: Retinal pigment epithelium + Bruch´s Membrane

Figure 1.11: OCT image showing various retinal layers.

scan. To understand the clinical features of DM in the OCT image, let us consider Figure 1.12, which represents various structural changes of retinal layers during different DM stages.

Figure 1.12 (a) represents normal/healthy macular OCT image. The macular thickness is calculated by measuring the perpendicular distance between the ILM and RPE layers of retina. The minimum thickness of macula is obtained at its center, the fovea, and maximum thickness is observed within a region of 3mm diameter. The thickness finally reduces towards the boundary of macula. The foveal thickness in normal retina is $229 \pm 20.46 \mu m$ [22]. During retinal ischemia, deposition of vascular fluid causes an increase in macular thickness leading to the inception of DM. The image Figure 1.12 (b) represents mild DM where the accumulation of vascular fluid has stated. These fluids give rise to intraretinal or subretinal cysts. As a result of deposition, the thickness of the retina starts increasing. In Figure 1.12 (c), we observe a higher amount of deposition and accumulation of exudates. Figure

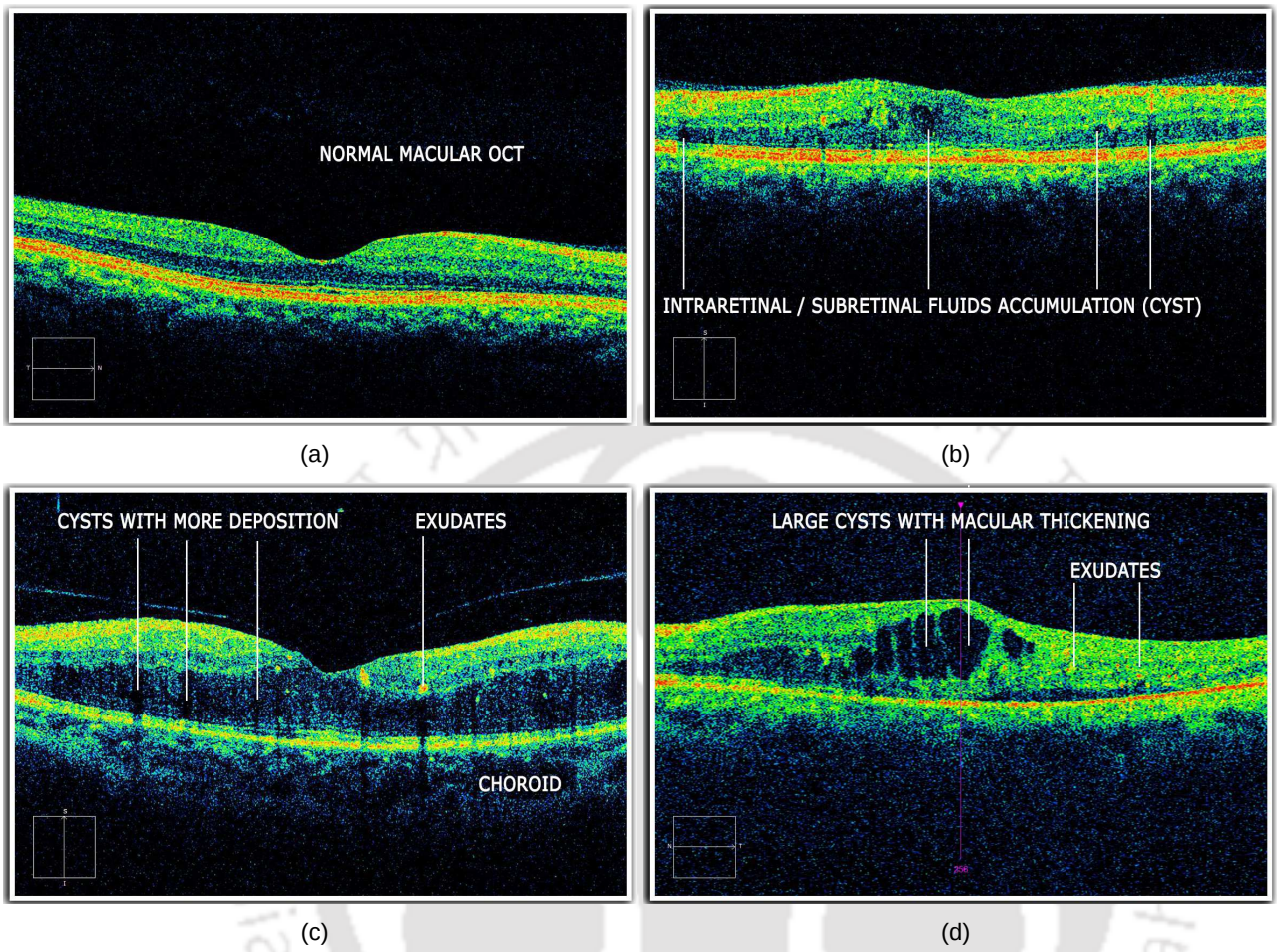

Figure 1.12: Changes of retinal layers observed in OCT image during DM [a] Healthy retina, [b] Formation of cysts, [c] Exudates and higher deposition in cysts, [d] Severe DM case large patches of cysts and exudates.

1.12 (d) shows a severe stage of DM with large cystoid intraretinal fluid pockets in OPL. Thus, during DM analysis using OCT images, ophthalmologists check the thickness variation between ILM and RPE layer with the estimation of vascular depositions and structural changes of retina.

A typical examination of DM requires examination of Fundus and OCT images. Ophthalmologists analyze various features in fundus and OCT images for DM diagnosis. Similar features could be processed using automated analysis methods, also known as computer-aided diagnosis (CAD). The next section enlightens on such a diagnosis process performed by CAD systems and the challenges faced during the process.

1.3 Automated diagnosis of DM

Diabetic Maculopathy is painless, and at the initial stage, it does not have any markable symptoms. Early detection and timely treatment is the only way to control this eyesight threatening disease. Hence, it is essential that the patients with diabetes, must undergo annual eye examination. Such that with a thorough retinal evaluation the presence of DM may be estimated [23]. Hence quality eye care facilities with state-of-the-art equipments are essential for ophthalmologists to diagnose DM. But with inadequate workforce and facilities, it turns out to be non-manageable. Such limitations and challenges are further discussed in the next section. An automatic detection algorithms can provide a helping hand for mass screening process and help the ophthalmologists to concentrate upon the diseased cases. Digital images are unique for this purpose since an efficient computer program can analyze and process these images directly, without or with very little human intervention. Block diagram in Figure 1.13 represents a generalized framework for the detection and analysis of DM. The following subsections enlighten the process of automatic analysis of DM using fundus and OCT

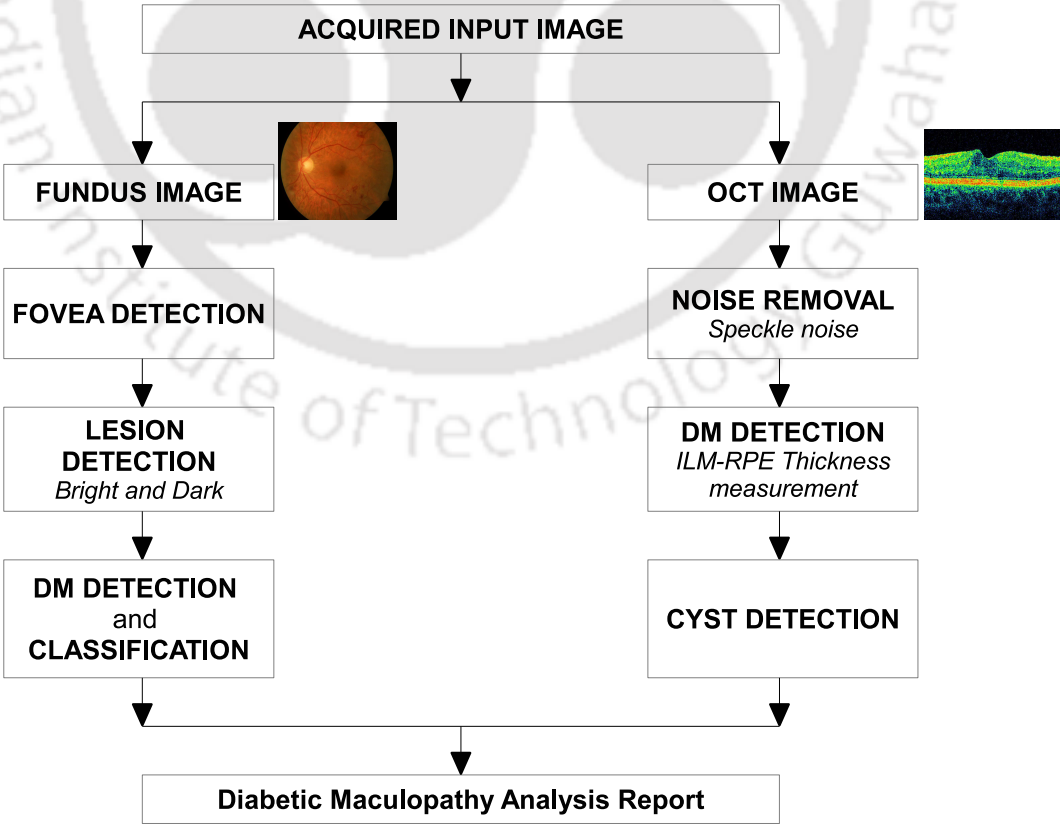

Figure 1.13: General Block Diagram: Diabetic Maculopathy analysis.

image and later continue into various challenges and opportunities encountered during the process. The automated detection scheme of DM using the fundus image is as follows.

1.3.1 Fundus Image analytics

Referring to the block diagram presented in Figure 1.13, the automatic detection, and classification of DM using fundus images mainly consists of three steps. First detection of the fovea, second segmentation of bright and dark lesions, and third detection and classification of DM by localization of lesions in the macular neighborhood. The fundus image of various databases have size, shape, intensity variations. Hence to generalize the automated classification of DM and enhance segmentation, fundus images are required to undergo various preprocessing algorithms. The three steps for detection of DM using fundus image are discussed in the following subsections.

1.3.1.1 Segmentation of Fovea

For proper identification and analysis of DM, detection of exact fovea location and the presence of the lesions in its neighborhood is necessary. Hence detection of fovea is an important step.

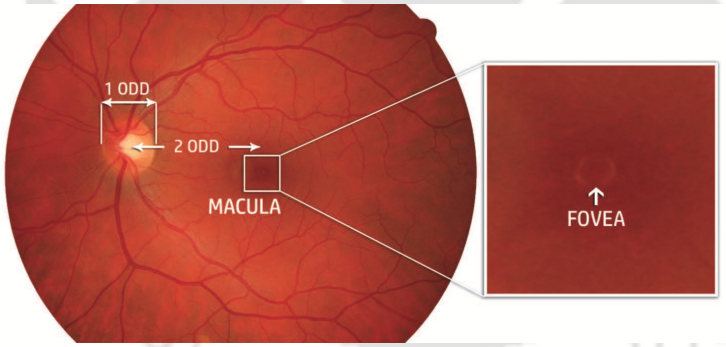

Figure 1.14: Macula and Fovea labelled in healthy fundus image.

The study of fovea's anatomical structure helps in building logic for detection algorithms. The location of the fovea is situated at a distance of 2-2.5 ODD from OD center and temporal to the central axis drawn from the OD center (as shown in Figure 1.14) [24, 25]. It is a very vital piece of information, and many algorithms are based on this property for automatic detection of the fovea. The second important physiological property that may be useful is the BV network around retina. The BV originates at OD and grows radially around retina and moves towards the center in macular direction. Before the BVs reach the macular region, the retinal growth completes, prohibiting further extension of BVs. Therefore, the fovea region is also called as avascular zone [26]. Thus, the BV

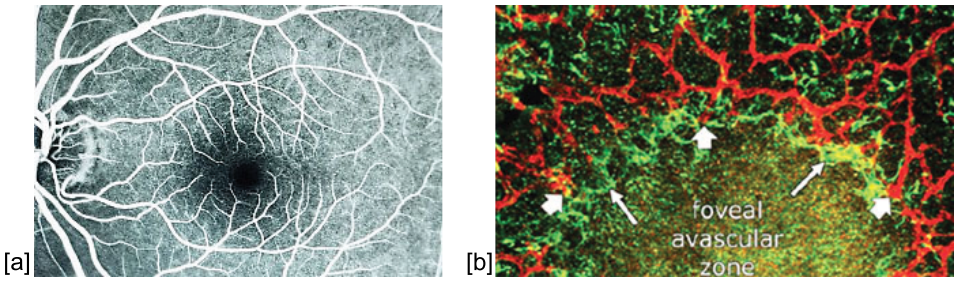

Figure 1.15: [a] BV structure of retina, [b] BV growth along fovea region.

count is maximum in the OD region, whereas zero across the fovea region (refer Figure 1.15 Provis et al. [26]). Hence, detection of OD and/or BV is necessary for the fovea detection. Various approaches have been proposed in the literature for the detection of fovea. Most of the algorithms follow a two-stage approach. In the first step, the Region of Interest (ROI) containing the fovea is determined using the information of various retinal landmarks such as OD, BVs, and its geometric relationship with fovea. In the second step, an algorithm is applied to the ROI for fovea localization. Therefore, detection of OD has become necessary for many algorithms. OD is a homogeneous structure of fundus image appearing bright and yellowish. Various OD properties such as high intensity, circular structure, and BV organization are utilized for its detection. The BV origin is from OD; hence, many algorithms detect BV in-order to detect OD and macula. Once OD is localized, the fovea is obtained at a distance of 2-2.5 ODD from the OD center. The detailed review of fovea detection methods is carried out in chapter 2, along with OD and BV detection, as they hold relevant information in the process.

1.3.1.2 Segmentation of Dark lesions

The dark lesions associated with DM include MAs and HMs (dot and blot). MAs are the earliest detectable signs of DR because their number correlates with the severity of disease found. The other dark lesion associated with the MA responsible for sight-threatening retinopathy with similar intensity is the HMs. HMs are larger in size with irregular shape [8]. Various state of the art algorithms are based on the following five types of methodologies [27], such as Morphological image processing, Supervised Classification, Template matching, Deep Learning, Miscellaneous techniques. The detail discussion of these methods in pros and cons is reviewed in chapter 2.

1.3.1.3 Segmentation of Bright lesions

Estimation of HE deposition in macular neighborhood is associated with DM diagnosis. HEs are originated from lipoprotein and lipid-filled macrophages, which lead to a yellow and waxy appearance. HE's are highly reflective. Therefore, they produce high intensity appearance in digital fundus photographs [28]. These are bright lesions that have no characteristic shape but appear similar to CWS, drusen, and OD. Therefore, the automatic detection of HE is quite challenging. Algorithms based on morphology, active contours, region-based, clustering like k-means, fuzzy c means, classifiers are used in this connection. Chapter 2 details all these methods considering various challenges in the detection process.

1.3.1.4 Detection and Classification of DM

Detection of lesions in the macular region of the fundus image signifies the presence of DM. To identify different stages, one has to determine the presence of both dark and bright lesions in the neighborhood of fovea. Let us reconsider the discussion during the clinical perspective of fundus image, subsection 1.2.1.1, on DM and its classification, represented in Figure 1.8. As per the figure, the presence of lesions anywhere within the outer circle signifies positive DM. The concentric circles shown represent the stages of DM based on the presence of lesions within the circles, which is mild between circle 3 and 2, moderate between 2 and 1 and severe if present inside circle 1. Considering this method of evaluation, every supervised and unsupervised algorithms are formulated. The first requirement is to determine ODD to mark the concentric circles centered at the detected fovea. The methods and their comparison are detailed in Chapter 2. To quantify the severity, the deposition amount may be evaluated based on various features calculated.

1.3.2 OCT Image analytics

As described earlier, the fundus image provides retinal information concerning a 2D image. However, any structural change of retinal layers can not be observed using fundus images. Therefore, to evaluate retinal layer changes during DM, OCT image analysis is required. Referring to Figure 1.13, OCT image inspection requires three major steps, removal of speckle noise, identifying DM cases based on detection of ILM and RPE layer, and measurement of thickness between them and finally determining the cysts present for the positive DM cases.

1.3.2.1 OCT speckle noise removal

The pseudo-retinal image, formed by OCT, is low in contrast, and very much susceptible to multiplicative speckle noise, as seen in Figure 1.16. It is because of various issues, such as non-homogeneous tissue of interest, optical properties of the system, multiple scattering, or motion of subject under evaluation, result in speckle noise that predominate the retinal layers in the images obtained [29, 30]. Therefore, effective removal of these components is very much essential before applying any segmentation algorithm [31–34]. Hence, various algorithms, such as bilateral filter, anisotropic filter, are used in this direction. The detail discussion on these methods, with performance comparison, is carried over in chapter 5.

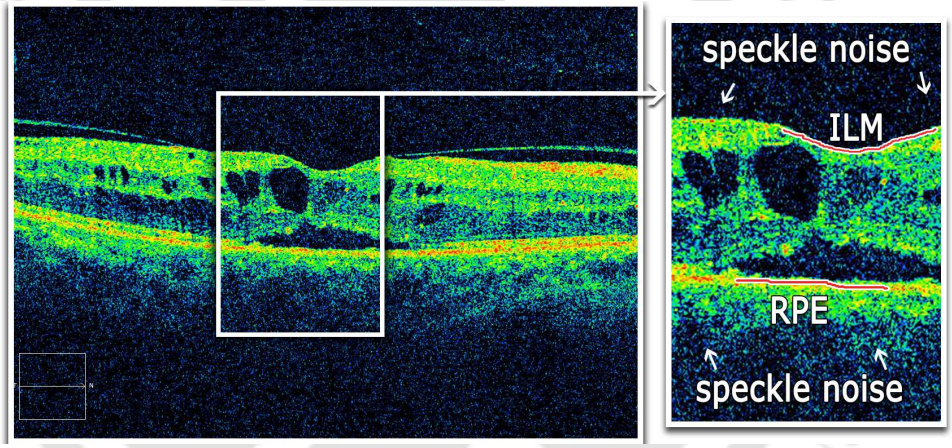

Figure 1.16: Speckle noise observed in OCT image.

1.3.2.2 Identification of DM

In connection to the discussion on the clinical perspective of OCT image section 1.2.3.1, the identification of DM is based on the straight line thickness measurement between ILM and RPE layers. An increase in thickness above standard value signifies DM. Therefore segmentation of ILM and RPE layer becomes obligatory. ILM and RPE are the inner and outermost layers of the OCT image. Using this property algorithms are built for its detection. Once identified, the fovea location is marked at the center, and thickness measurement between the layers is determined. To add more information to the procedure and to increase the efficiency, multiple location thickness are measured. The scale of thickness measurement is considered in the number of pixels instead of microns. Figure 1.17 shows an example of the locations considered for thickness measurement [22, 35–41]. Discussion on the

challenges and layer detection is performed in Chapter 2.

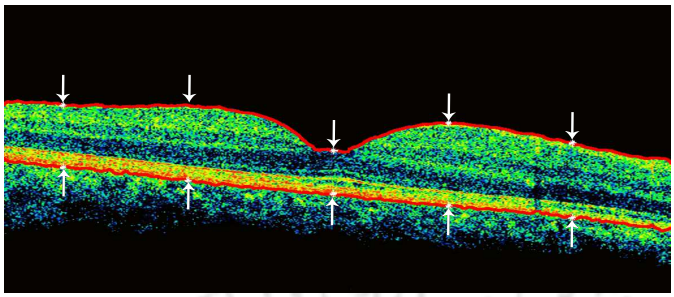

Figure 1.17: Locations for thickness measurement between ILM and RPE layers.

1.3.2.3 Cyst detection

After detecting the presence of DM, the next task is to identify the cysts for positive CME patients. The measurement of cystoid fluid gives more diagnostic information than the central macular thickness [42]. The cystoid fluid appears as dark due to swelling of the macula in DM. Using the dark intensity property, algorithms are built for the detection. Larger the volume of the cyst greater is the edema present.

Automatic detection algorithms for DM identification becomes efficient only when we consider all the pros and cons faced and try to build a robust procedure applicable to every possible image. Therefore, before generating any algorithm, we must assemble the challenges faced and discover the hidden opportunities. The next section highlights every possible challenge and opportunity.

1.4 Challenges and Opportunities

The automated detection algorithm for screening of DM cases is the best possible way for its proper monitoring and management. The early detection of the disease only helps the patient to avoid irreversible vision loss. During the generation of automated algorithms, we need to take care of various perspectives starting from the clinical significance of attending patients to imaging challenges of proper capturing retinal photographs. The analysis criteria progress with considering various signal processing issues being observed and taken care of. Therefore in this section, we discuss various challenges for the automated detection algorithm generation and try finding out the possibilities to build better.

1.4.1 Clinical Challenges

Proceeding with the discussion in the previous section, the asymptomatic nature of vision deterioration in the early stages of DM creates a threat of irreversible vision loss in later stages. Therefore, a typical examination of fundus and/or OCT images by an expert ophthalmologist is mandatory for the prevention of the disease. The exercise of examining patients for the detection of abnormal features is called screening. Screening programs detect DM at early stages, helping the patients to avoid irreversible eye complexities. These screening programs involve manual evaluation and is also a time-consuming process for the ophthalmologists. In developing countries, the state-of-art facility for retina imaging and management are fewer in number than necessary due to the high cost. Also, with limited trained professionals and limited technical assistance, the process of interpreting retinal images consumes considerable time. As a result, ophthalmologists can advise a relatively small set of patients. However, the patient to doctor ratio is deficient, approximately 100,000:1 [43,44], that too for the reported cases and is continuously decreasing due to the high prevalence of diabetes. Again the probability of error increases while screening a large amount of data due to exhaustion. Therefore, various organizations running such screening programs seek new solutions that are cost-effective, efficient, and enable ophthalmologists to screen at a faster rate.

1.4.2 Imaging Challenges: Engineering perspective

Based on the camera setup, imaging conditions, tissue pigmentations, the captured retinal images experience various intensity related issues, due to which any automatic algorithm used for processing of retinal images may not give correct results [8, 17, 18]. The following discussion provides insight into such challenges, and their probable solution is being figured out.

Fundus camera is illuminated externally for imaging as there is no internal illumination possible. The ray of light moving inside the eye reflects across the retina and returns to the camera for imaging. The primary challenge in this process is the small aperture of the pupil. The size of the pupil varies from 2-8mm diameter, and without proper pupil opening, the fundus image is not appropriately illuminated. During imaging operation, the illumination beam and imaging beam must not overlap each other, as this results in decreased image contrast. To avoid this, one must go for mydriasis, which is dilation of the pupil before imaging. It helps more amount of light to fall inside the eye and results in better photography. Trained technicians are required to operate the imaging device and obtain the images

correctly and quickly. Although current fundus cameras are non-mydriatic and user-friendly, still the challenge remains.

The main challenge faced during **FFA Photography** is the application of the Fluorescein dye. Firstly, the procedure requires professional ophthalmologists or nurses to inject the dye. Secondly, few patients (around 2%) get an allergic side effect on the application of this dye requiring medical attention. Finally, as the imaging is done with a fundus camera, an expert is required to get the job done. Therefore, imaging with FFA is a cumbersome process.

As alluded earlier, **OCT Photography** experiences speckle-noise during imaging. With the subject movement, the speckle quantity also increases. The noise predominates the retinal layers in the OCT images captured. Although speckle noise may be minimized, but can not be eliminated while imaging. The only way possible is the utilization of noise removal algorithms.

The next subsection highlights all signal processing challenges faced during automated detection and analysis of DM using fundus and OCT images.

1.4.3 Signal Processing Challenges

Starting from image quality correction to segmentation and later to evaluation, various signal processing challenges are faced during the automated analysis of DM. Considering every aspect helps us in building efficient and robust algorithms.

As discussed in the earlier subsection 1.4.2, due to imperfect imaging, the generated fundus or OCT image quality gets deteriorated and are difficult to process. Variation in luminosity and contrast creates poor illumination of fundus image, and it affects the processing for automated analysis and evaluation of retinal diseases. Illumination variation occurs due to many factors such as acquisition process, inaccurate camera flash reflection, cell pigmentation. The OD and its neighborhood intensity increases in comparison to remaining regions due to uneven illumination. It severely affects the illumination of retinal landmarks. Similarly, for OCT images, the main and foremost challenge is the presence of speckle noise. These unwanted and/or distorted structures pose a challenge for retinal image processing algorithms. Here we discuss various issues that interfere in automated analysis and need to be taken care as pre or post-processing during analysis,

issue 1: With the presence of dust particles over the camera lens, the fundus image captured may

exhibit noisy structures. The noise formed due to such situations represent characteristics of salt and pepper noise. This error can be corrected by proper maintenance of the setup.

issue 2: Due to uneven camera flash, the fundus boundary gets illuminated more, as shown in Figure 1.18 (a). The bright boundary with high intensity interfere with bright lesion or OD detection algorithms due to similar intensity characteristics.

issue 3: Low exposer to light during imaging lead to foreground suppressed by background. One such example is shown in Figure 1.18 (b), where most of the fundus image is covered by a dark background, including the macula. Therefore, such images are generally challenging to process. Similarly, due to improper focusing of the retina, the image captured becomes blur, as shown in Figure 1.18 (c).

issue 4: Another condition emerges when the subject moves his/her eye during the imaging period. In Figure 1.18 (d) represents one such example, where the fundus image is not captured correctly. These dislocated images cause FPs for the algorithms used for position based detections.

issue 5: Next set of challenges for the algorithms are similar intensity of retinal landmarks with the lesions. For example, bright lesions color and intensity range is similar to OD, whereas dark lesions are similar to BV and macula. Moreover, the imaging camera does not contain any filter for color normalization or intensity equalization resulting in similar intensities of background and foreground.

issue 6: The speckle noise present in OCT images makes the retinal layer segmentation process inaccurate. The noise is multiplicative, and traditional filtering operation creates blurring, hampering the layer edge information.

The automated analysis of DM is primarily performed using fundus images, and for detailed analysis, OCT images are operated. During this process, various signal processing challenges faced are clubbed together in the following subsections.

1.4.3.1 Fovea detection challenges

As per the discussion on the segmentation of fovea in subsection 1.3.1.1, automated fovea detection may face various challenges. Such challenges includes,

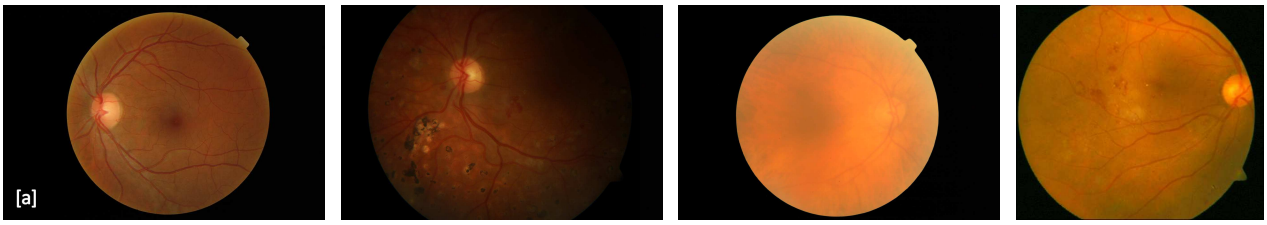

(a) (b) (c) (d)

Figure 1.18: Various cases of improper illumination observed in fundus image: (a) Image from MESSIDOR database with high intensity at the boundary, (b) Image from DIARETDB1 database suffered from background suppression, (c) Image from MESSIDOR, affected by improper focusing, (d) Image from Guwahati Eye Institute, showing error due to subject movement during imaging.

- **Images suppressed by background:** The root cause of this issue is poor illumination. Due to irregular lightening during image capture, the foreground may not be properly illuminated, causing dark appearance. This issue has already been addressed in previous section with an example shown in Figure 1.18 (b).

- **Error in optic disc localization:** For detection of fovea using the OD relationship, it is necessary to segment the OD location accurately. OD is the brightest yellowish region in fundus images. But exudates also appear yellow, and in-case if it contains brightest pixels in it, leads to incorrect detection of OD thus fovea. Figure 1.19 (a) shows one such example.

- **Similar intensity regions:** Fovea is dark. Pathology, like HMs, also has the same color. Because of the similar intensity property, sometimes HMs may get detected as fovea. High probability is when it is situated near the fovea. BVs offer another form of similar intensity hindrance. Although, as discussed earlier fovea region does not contain any BVs, therefore such obstruc-

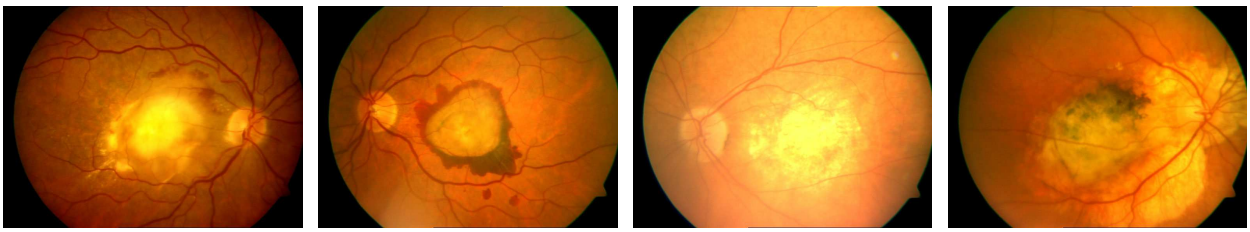

(a) (b) (c) (d)

Figure 1.19: Various challenging cases for fovea detection: (a) Image with exudate intensity more than OD lead to false detection of OD, (b) Similar dark intensity of blood leak will get detected as fovea, (c) Macula region fully covered by lesions lead to non localization of fovea, (d) Image showing severe case where OD and fovea both can not be localized due to enormous leakage.

tions due to BV intensity may not arise. But in cases with abnormal BV growth towards fovea due to prolonged diabetes, may subject to false detection of fovea. Figure 1.19 (d) shows one such condition having neovascularisation and HMs near fovea.

- **High-risk macular edema cases:** During severe stage of DM, abnormality fully covers the fovea region. With fovea being fully covered, its localization becomes very challenging. All examples shown in Figure 1.19 represents high risk DM.

Various algorithms on fovea detection and their considerations on these challenges are discussed in Chapter 2.

1.4.3.2 Lesion detection challenges

Lesion detection includes HEs for bright lesions and MA and HMs for dark lesion identifications. The associated physiological and imaging factors leading to over or under segmentation are listed below.

Bright lesions:

- Similar intensity and color pixels of OD and other bright lesions lead to FPs. As discussed earlier during fovea detection, the process of OD localization is effected due to exudates' alike intensity. Similarly, the reverse case is also applicable during bright lesion detection. Therefore the OD must get masked as a pre or post-processing step during detection process.
- As alluded earlier, variation in tissue pigmentation effects the image quality. Color disparity in images effect segmentation. Hence proper pre-processing is necessary to handle such situations.
- BV and macular reflections in healthy images possesses bright intensity. Therefore during exudate segmentation, they may get identified as bright lesions, although the subject under evaluation is healthy.
- During segmentation along with HEs, SEs, and CWSs are also identified. But the essential information required for DM is HEs. Therefore segregation of HEs from all bright regions becomes a challenging task.

Dark lesions:

- Similar to bright lesions, the intensity and color pixels of BV and macula lead to FPs in dark lesion identifications. Being connected, the BVs may be eliminated using image processing tools. But the difficulty arises with non-connected BV segments. Wrong detection caused by macula may be eliminated using the edge property, as the macular edges are very smooth.
- Tissue pigmentation and Color disparity affect the segmentation process and seeks proper pre-processing.

Among methodological procedures, there are various limitations and opportunities. These topics are reviewed in Chapter 2.

1.4.3.3 Retinal layer detection challenges

As deliberated before, the presence of speckle noise affects the detection of required retinal layers ILM and RPE. With improper filtering technique, the edge information of layers get weaken. However, the edges of the retinal layers vary in intensity even for a single layer. Therefore it becomes challenging to identify edges with traditional edge detection methods. The detection of cystoid fluid posses a challenge due to the rough surface of OCT images. It results in false detection during cyst localization algorithms. Although various challenges are to prevail during OCT analysis, the main challenge lies in the efficient elimination of speckle noises as it hinders all processes carried out for analysis.
The theoretical background of various methodologies for DM analysis are reviewed and detailed in Chapter 2, which helped in lining the objective for DM detection. The literature on automated DM analysis is surveyed in the next section.

1.5 Literature on DM/DME analysis

In the literature, various approaches have been proposed for automatic identification and grading of the DM/DME. Few of them using fundus images are cited below.

Tariq et al. [45] have designed a CAD system for DME grading. Using the geometrical relation of OD and macula, the macula is detected. Later, the Gabor filter bank and Otsu threshold were being used to segment exudates. With exudate features as input to Support Vector Machine (SVM), the algorithm classifies CSME and NCSME cases with an accuracy of 97.53% (STARE) and 97.20% (MESSIDOR) respectively. Tariq et al. [46] have updated their work with the incorporation of the

Gaussian Mixture Model (GMM) classifier. BVs were removed with the help of adaptive contrast enhancement and mathematical morphology. Similar to previous work, exudates were identified using a Gabor filter bank. Exudates were then segmented out using morphological and texture features with GMM. Classification of NCSME and CSME cases were computed with an accuracy of 97.3% (MESSIDOR) and 97.89% (STARE), respectively. Punnolil [47] used morphology and multi-class SVM with texture features of exudates for DM grading. The investigation of retinal vasculature, triangulation approach with positional constraints lead to the detection of macula and fovea. HEs are isolated from other bright regions with the help of texture and mathematical morphology. Multi-class SVM is finally used for grading with sensitivity and specificity of 96.89% and 97.15%, respectively. Akram et al. [48] have designed an automated system for DM classification, where exudates were segmented with the help of Gabor filter bank with segmentation using the Otsu threshold and Hough transform. The HEs were localized using features such as mathematical morphology, energy, the response of filter banks, and classified using SVM. The system recorded an accuracy, sensitivity, and specificity of 97.30%, 92.60%, and 97.80%, respectively. Using curvelet transform, Alipour et al. [49] have generated an automated grading system for DM. The geometric distance from OD foveal region is located, and thereafter, with a curvelet transform, DM is graded. The results were obtained with sensitivity and specificity of 93% and 86%, respectively. Siddalingaswamy and Prabhu [50] have designed a DME classification algorithm. Here using position relations with histogram thresholding OD and macula were obtained. The clustering of HE was done later. The method recorded a sensitivity of 95.60% and specificity of 96.15%. With the help of Neural Network (NN), Ang et al. [51] have generated an automated DME grading algorithm. Here, OD and HEs were detected using mathematical morphology, and fovea is localized using the geometric relationship of OD and macula. The method contributes with 90% sensitivity, 100% specificity, and 96.67% accuracy. Nayak et al. [52] have proposed a NN based DME grading system. With the variation of intensity, OD is localized, and fovea is obtained using the geometric relationship of OD. Mathematical morphology is being used for the identification of exudates. The method recorded a sensitivity and specificity of 95.40% and 100%, respectively. Fleming et al. [53] projected a DME classification algorithm where morphological filters have been used to detect lesion candidates. The system has obtained an accuracy of 99.2% and 97.3% to classify NCSME and CSME cases. Using exudate probability map and wavelet decomposition, Giancardo et al. [54] have graded DM. The fovea and HEs were detected

utilizing Kirsch edge operator and region growing. Later, the color and wavelet analysis are performed to obtain HE features for applying to SVM, to grade the DM. The system generated an area under the curve (AUC) of 0.94. Lim et al. [55] designed a DME grading system. In their work, first OD is removed with the help of extended minima transformation and appropriate threshold. HE is segmented by Watershed transformation and with filtering by Sobel linear. Finally, the position of exudates was found in the fovea neighborhood to grade DME. The method yield a sensitivity, specificity, and accuracy of 80.9%, 90.20%, 85.20%, respectively. Particle Swarm Optimization was used with the median filter for segmentation of exudates along with noise filtration. Later Sreejini and Govindan [56] used morphology and position to determine OD location and performed DME grading. The algorithm recorded an accuracy of 93%. Zaidi et al. [57] operated morphology, Otsu threshold, and Gabor filter for DME identification. Later, the Bayesian classifier identified HE and position constrain to segregate healthy and DME classes. The method generated 94.1% accuracy. Hunter et al. [58] have used NN for automated DM diagnosis. Initially, with the help of a matched correlation, the fovea is localized. After that, maximum intensity and contrast over each candidate were used to identify bright lesions. Finally, on the utilization of morphological, color, and texture features, HE and drusen could be discriminated. The algorithm reported with a sensitivity of 97% and specificity of 80%. Motion pattern analysis was performed by Deepak and Sivaswamy [59] for automated DME detection. Using standard geometrical relation with OD, the macula is identified. Motion pattern generated here from fundus image under evaluation forms a bright smear pattern enhancing the HE characteristics. Later, the radon transform generates motion pattern features. These features were finally applied to Gaussian Data Description (GDD) and Principal Component Analysis Data Description (PCADD) to grade DME cases. The algorithm reached an AUC of 0.98, 0.96, 0.99, 0.96 and 0.92 respectively for five different datasets. Baby and Chandy [60] used Dual-Tree Complex Wavelet Transform (DT-CWT) and GDD for automated identification of DME. Initially, image enhancement is done, and DT-CWT is applied to find wavelet sub-bands. Later, using GDD features were obtained from wavelet coefficients. The algorithm results in a 78.23% precision rate. Content-based image retrieval system is generated by Naguib et al. [61] for DME identification. Morphology and feature projection helped to eliminate BV and OD. Edge Histogram Descriptor (EHD) is operated for generating features, and the system generated 79.2% of the precision rate. Mookiah et al. [6] have designed a Higher-Order Spectra (HOS) bis-spectrum and generates features for DME grading. The system first converts the

fundus image into a one-dimensional signal using Radon transform. Later, features were obtained using bispectrum and cumulant features. The algorithm reported accuracy of 95.93% and 95.56% for two different databases. Discrete Wavelet Transform (DWT), entropy, and neuro-fuzzy inference system formulated the DME classification system. Here, Ibrahim et al. [62] normalized the feature and finalized it with the help of Analysis of variance (ANOVA). The algorithm generated 98.55% accuracy for classifying normal, NCSME, and CSME cases.

The detailed literature with the review of various methods and results obtained are discussed in the subsequent Chapter 2. Although fundus image processing is self-sufficient to detect, analyze, and grade DM. Yet, there are cases where the actual condition of the patient is properly visible on the layer analysis using OCT images. Therefore, as a secondary measure, the OCT analysis is of utmost importance. Such open issues, along with literature and method review, are further deliberated in Chapter 2.

1.6 Scope of the present work

Automated digital fundus and OCT image-based analysis has become a blessing for the fast managing of patients and provides flexibility to the ophthalmologists to concentrate on severe cases more. The CAD provides a pre-screening segregating healthy and retinopathy cases. This approach reduces the workload of medical experts and allows more coverage of patients in a short duration.

As we can understand from the literature mentioned above, the position of lesions with respect to the fovea center is the key to the DM/DME classification. Hence, the exact location of fovea and lesions is essential for automated DM grading. Detection of lesions and macula is a combination of mathematical morphology, thresholding, and the geometrical relationship of OD and fovea [49, 51, 52, 56, 63]. Various algorithms used in these directions include Curvelet transform, Watershed segmentation, Gabor filtering, Kirsch operator, Hough transform, Image inpainting. The extraction of the lesions with exact locations is the primary need of the segmentation methods. The classification or grading then computed with the help of supervised or unsupervised algorithms makes the system complete.

From the challenges being addressed in previous sections, it is clear that various scope is available in the direction of automatic analysis of DM. Therefore, a systematic study carried with considering various issues faced individually helps in building robust methods for the analysis of DM.

1.7 Organization of the thesis

The rest of the thesis contains the proposed steps in accomplishing the aim of the project. **Chapter 2** discusses the methodologies for automated DM analysis and reviews the methods for identifying the open issues for investigation. **Chapter 3**, represents automated algorithm for identification of the fovea. The proposed method is based on the avascular property of fovea, and later it is further improved using ellipse fitting approach. **Chapter 4**, explains the proposed steps for the detection of both dark and bright lesions using color property. It is later followed by the improvisation of the method considering challenges faced during detection. The detected lesions are applied for grading of DM using unsupervised and supervised techniques. In **Chapter 5** automated OCT image analysis is presented using state-of-the-art algorithms. The filtering technique used here preserves the edge information, which in turn is advantageous for retinal layer detection. In **Chapter 6**, conclusions are drawn by summarizing the contributions of the work and mentioning directions for future possibilities.

2

Automated DM analysis: A Review

Contents

This chapter advances the previous discussion on the automated diagnosis of DM. Various processes necessary during DM analysis and their pros and cons are discussed here in detail. Although efficient algorithms exist for detection and analysis of visual acuity, there is always room for improvement in order to increase performance with more convenience for the patient under treatment. Therefore, the main objective of this chapter is to identify the possibilities to improve the automated investigations. From the discussion, we have generated the motivation and formulated the problem statement of this thesis work. The materials/database selected for the investigation of the proposed algorithms are presented towards the end of the chapter.

Chapter content: The discussion on automated DM analysis review is broadly classified into fundus and OCT image analysis. Section 2.2 and section 2.3 carry forward the review. Analysis using a fundus image contains a review of BV, OD, Macula, and Fovea and finally lesions (both bright and dark) detection procedures. During OCT image analysis, we review the speckle noise removal, layer segmentation, and cyst detection algorithms. The sections 2.4 present the motivation and section 2.5 the contribution. The last section 2.6 describes the database details.

2.1 Automated diagnosis of Diabetic Maculopathy

Automated analysis of DM is challenging, and it comprises of various significant steps. As discussed in Chapter 1, Figure 1.13, the fundus image analysis require fovea detection, lesion identification, and estimation of these lesions presence in the macular neighborhood for DM severity measurement. Fovea detection, therefore is a necessary component of the analysis, which demands an investigation of the exact fovea location. During the process, few image correction, localization of other retinal landmarks like BV, OD are essential. The position and area of OD identification is the most crucial requirement for the fovea localization and DM classification. Most of the fovea detection algorithm uses the geometrical distance property of ‘OD and fovea’ for localizing ROI containing fovea. On the other hand, the ODD calculation is necessary to determine the concentric circles around fovea for the DM classification. During the detection of OD, BV network identification add a significant role. The BV originates from OD and this property helps finding OD better. Also the BV network anatomy helps estimating macula position. For algorithms seeking removal of BV from fundus such as ‘inpainting’ also require BV detection. Thus, BV localization becomes an important component for the automated algorithms. Most of the algorithm available in the literature detects these three landmarks efficiently in

healthy retinal fundus images. But the challenge lies to detect their proper location with the presence of lesions manifested during DR or DM. The deposited lesions possess a similar intensity profile like the landmarks, which tend the algorithms to miscalculate the position of fovea or OD.

Similarly, as presented on right half of Figure 1.13, the OCT image analysis requires speckle noise removal, followed by ILM-RPE layer thickness measurement and cyst localization. During the process, primary and unavoidable requirement is the removal of speckle-noise without losing boundary information of edges. Along with this the edges of layers have different intensity throughout, which affects the detection algorithms. The cyst identification stage needs proper isolation of background and foreground.

Therefore, proper analysis of the retinal anatomy along with its changes incurred with disease progression and the limitation of image processing tools for DM identification is necessary. The following sections presents the literature on algorithms and reviews the challenges faced during it's implementation for automated analysis of DM using fundus and OCT images. It helps to enlighten the available tools and identify the area for improvement. The review is classified into two categories constituting fundus and OCT image analysis.

2.2 DM analysis using Fundus image

Cognition of retinal anatomy and the pixel properties possessed over the fundus image of the object under segmentation is the key to apply proper image processing tools for proposing automated analysis algorithms. This section reviews all the pros and cons of various algorithms for the automated DM analysis using fundus images. The review discusses the detection of BV, OD, fovea, HE, MA, and HMs, respectively.

2.2.1 Blood Vessel Detection

Depending on the anatomical location and intensity profile observed in fundus image, BVs posses various information. Such as the BVs network originates from the OD, and it grows vertically, in the OD neighborhood. The growth of primary arteries or the major BVs follow a parabolic path. These three pieces of information are useful during the automated detection of OD. Other properties like BVs have horizontal alignment near the macular neighborhood. The absence of BVs in macula, more specifically in the fovea region and the geometrical relation between BV origin and fovea, is of

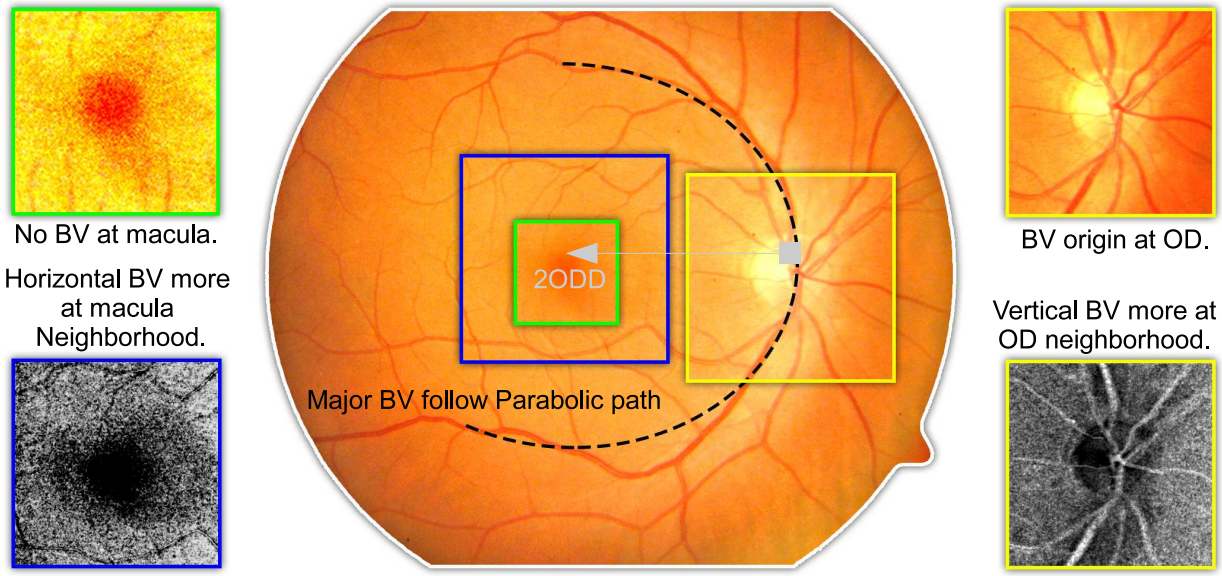

Figure 2.1: Properties of BV in fundus image.

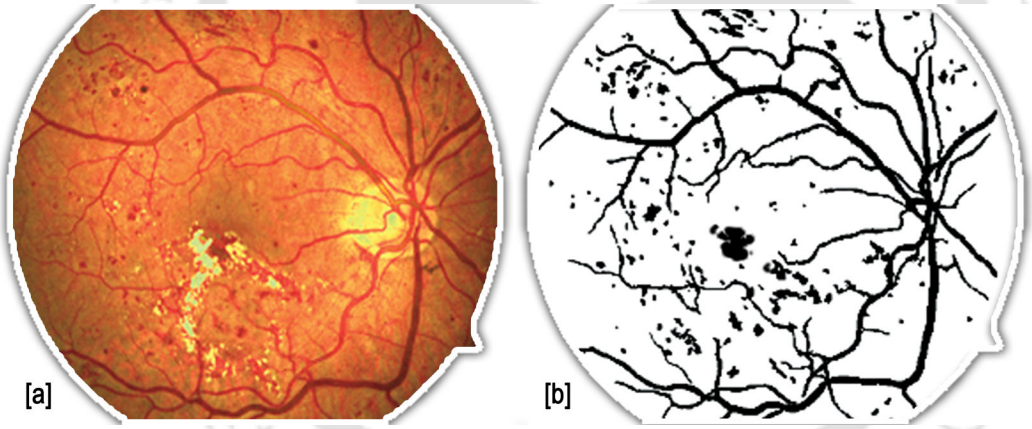

Figure 2.2: Segmentation of all low intensity values during dark region identification: [a] Enhanced fundus image, [b] Segmented all dark regions.

2ODD. These sets of properties are helpful for automated fovea detection. The Figure 2.1 represents all above mentioned BV properties. The segments of the fundus image are taken from the Figure 2.1 to show these properties individually. The segments on the right show the BV origin from the OD center and its vertical alignment near the OD neighborhood. The left segments show absence of BVs in macula and the macula neighborhood having horizontal alignment of BVs.

Apart from these, the intensity-based algorithms generally seek elimination or masking of the BV network to avoid misclassification due to similarity of intensity, as presented in Figure 2.2. Here all the low-intensity values get segmented. These algorithms, which are meant for the detection of the

macula and dark lesions, seek BV removal as a pre or post-processing step. Plenty methods are available in the literature towards the direction of automated BV detection. These methods can be clubbed together into four broader approaches. Such as Adaptive filtering or segmentation [64–66], vessel tracking [67, 68], mathematical morphology [69, 70], and classification [71, 72]. Table 2.1 (akbar et al. [73]) describes an overview of these methods with the results obtained on processing over various publicly available databases.

Table 2.1: Comparison of Blood Vessel Detection methods

Author	Year	Methodologies	Database	Sensitivity	Specificity	Accuracy
Salem et al. [64]	2007	Clustering algorithm	STARE	0.8215	0.9750	NR
Kande et al. [65]	2010	Fuzzy C-means with spatially weighted clustering	DRIVE STARE	NR	NR	0.8911 0.8976
Ng et al. [66]	2010	Scale-space parameters having maximum likelihood estimation	STARE	0.7000	0.9530	NR
Saffarzadeh et al. [67]	2014	K-means clustering and multi-scale line operator	DRIVE STARE	NR	NR	0.9387 0.9483
Panda et al. [68]	2014	Hausdorff symmetry operator, K-means clustering	DRIVE STARE	0.7380 0.8045	0.9739 0.9606	NR
Emary et al. [74]	2014	Local search, artificial bee colony optimization and fuzzy c-means clustering	DRIVE STARE	0.7210 0.6490	0.9710 0.9820	0.9390 0.9470
Qian Zhao et al. [69]	2014	Region growing method, region-based active contour model with level set.	DRIVE STARE	0.7354 0.7187	0.9789 0.9767	0.9477 0.9509
Hassanien et al. [75]	2015	Artificial bee colony optimization along with fuzzy c-means	DRIVE STARE	0.7210 0.6490	0.9710 0.9820	0.9388 0.9468
W. Wang et al. [76]	2018	Multi-scale morphology and seed point tracking	DRIVE STARE	0.7236 0.7486	0.9810 0.9680	0.9449 0.9460
Condurache & Mertins [77]	2012	Hysteresis binary classification paradigm	DRIVE STARE	0.9094 0.8902	0.9591 0.9673	0.9516 0.9595
Xiao et al. [78]	2013	Bayesian model with spatial constraint	DRIVE STARE	0.7513 0.7147	0.9792 0.9735	0.9529 0.9476
Roychowdhury et al. [70]	2014	Gaussian mixture model classifier	DRIVE STARE	0.7250 0.7720	0.9830 0.9730	0.9520 0.9510
Vega et al. [79]	2014	Lattice neural network with dendritic processing	DRIVE STARE	0.7444 0.7019	0.9600 0.9671	0.9412 0.9483
Franklin & Rajan [80]	2014	Neural network, back propagation algorithm	DRIVE	0.6970	0.9830	0.9500
Azzopardi et al. [81]	2015	B-COSFIRE (combination of shifted filter responses) based on existing COSFIRE	DRIVE STARE CHASE_DB1	0.7655 0.7716 0.7585	0.9704 0.9701 0.9587	0.9442 0.9497 0.9387
Li et al. [82]	2016	Cross-modality image transformations and convolutional neural network	DRIVE STARE CHASE_DB1	0.7569 0.7726 0.7507	0.9816 0.9844 0.9793	0.9527 0.9628 0.9581
Zhu et al. [71]	2017	Extreme learning machine	DRIVE LOCAL	0.7140 0.7205	0.9868 0.9766	0.9607 0.9628
Memari et al. [72]	2017	CLAHE, B-COSFIRE along with Frangi matched filters Matched filtering technique along with AdaBoost classifier	DRIVE STARE CHASE DB1	0.8726 0.8085 0.8192	0.9884 0.9798 0.9591	0.9722 0.9514 0.9482

The motivation behind the requirement of automated detection or deletion of BV for the present work is to support the automated detection of OD, Macula, and lesions. Analysis of BVs is not necessary during the process. We may consider any one of the approaches mentioned above. Therefore, with the advantage of less computing time, detection using mathematical morphology is considered

for the proposed algorithms. Although there is a drawback of losing microvessels information, but being redundant it may be ignored. For efficient elimination of the BVs, image inpainting [83, 84] acts as a strong support.

2.2.2 Optic Disc Detection

Optic disc detection is essential during DM analysis. The OD center and its diameter contain information, such as the relative position of both macula region and formation of concentric circles for DM classification. The OD has various explicit properties that are useful for its detection. These include high intensity, circular structure, and BV organization. Several techniques exist in the literature to detect OD [24, 85–87]. Referring to Figure 2.3, we can visualize that the intensity and the color property of OD are similar to the exudates. Thus, the algorithms based on intensity measurement may not be able to differentiate them. The property that distinguishes OD from exudates is its shape. The OD is circular and uniform, whereas exudate is irregular and non-uniform structures. Another important feature of OD is the presence of BV origin.

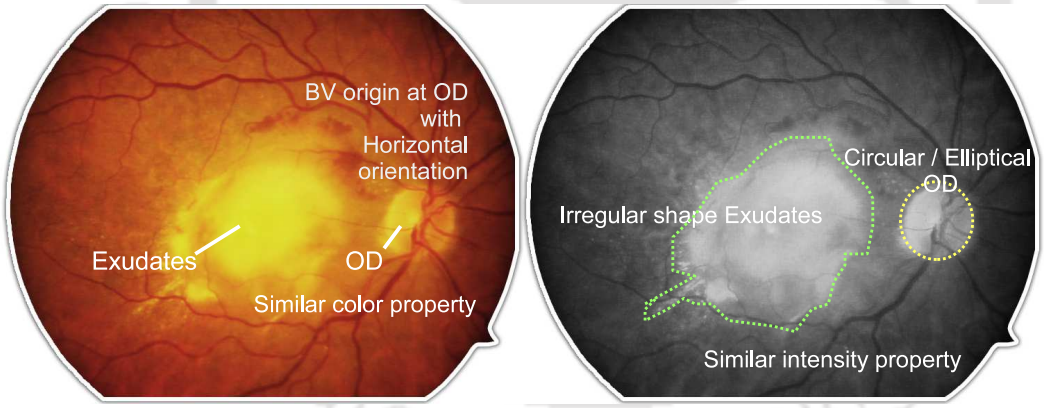

Figure 2.3: OD and HE properties shown in color and corresponding gray scale fundus image.

Considering these factors, the OD detection methodologies may be categorized as property-based, BV convergence, and model-based methods [88].

Property based methods utilize OD assets such as location, intensity, size, color, and shape for its detection. The OD contains the highest intensity value or intensity variation with it's neighboring pixels. Various algorithms detects OD using this property [89–92] with manual or automated threshold. Few algorithms also have included mathematical morphology along with thresholding. Mathematical morphology is applied here to filter out the regions other than OD. Morphological opening and closing operations play the role here. These methods acquire high efficiency in healthy images. But

the detection fails in the presence of exudates with brightest pixels. Figure 2.4 represents few such examples.

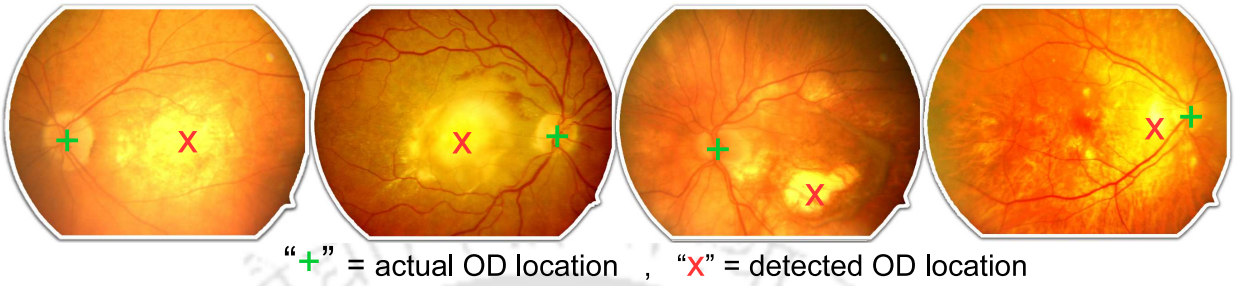

Figure 2.4: Examples of OD detection error, encountered on algorithms based on intensity property.

Therefore, to eliminate this error, the information of circular shape is added along with the high intensity property of OD. Hence, Circular transformations [93], Circular Hough transformation [94–96] are applied. While working on circular object recognition, the ellipse eccentricity in OD shape failed the Hough transform [97]. Hence researchers have updated to elliptical Hough transform [98]. Instead of thresholding to detect OD region, the edge detection (Canny, Sobel etc.) methods are also introduced to locate the high intensity edges [97–100] in addition to elliptical Hough transform. Edge detection methods operate effectively, but they generate under segmentation with low contrast images, as the OD boundary is not detected properly under such circumstances. In order to avoid this limitation, the preprocessing of the image is the solution. Techniques like adaptive histogram equalization (AHE) and Contrast Limited AHE (CLAHE) [93] increase the sharpness of the image improving edge information. All the above-mentioned methods are advantageous and perform better. But most of these algorithm fail in fundus image containing pathology, as large exudates get wrongly classified as OD. Hence, secondary informations are explored for improving the detection scheme.

BV converge from OD and branch out into small vessels through retina. Therefore, when we search for the converging point of BV, OD is obtained. Hence, researchers have used this secondary information to locate the region of interest containing OD, and later, using previously discussed methods, OD is detected in the ROI. In this connection, people have used fuzzy convergence [103] to detect BV origin. Hough Transform is also applied [106] on BVs [120]. To improve the detection, morphological dilation is done on the BV in the OD region. The authors have also applied the same Hough Transform on the brightest 0.35% of the fuzzy convergence, with dilation performed to fill out the gaps due to BVs [103]. ROI containing OD is obtained using the property of the elliptical shape

Table 2.2: Comparison of Optic Disc detection algorithms

Author	Year	Methodology	Dataset	Images	Sensitivity
Sinthanayothin et al. [89]	1999	High intensity variation.	Local	112	0.9911
			STARE	81	0.4200
Lalonde et al. [101]	2001	Hausdorff template matching & pyramidal decomposition.	Local	40	1.0000
			STARE	81	0.7160
Walter & Klein [91]	2001	Largest brightest connected object.	Local	30	0.9000
			STARE	81	0.5800
Osareh et al. [102]	2002	Averaged OD-images template matching.	Local	75	0.9032
			STARE	81	0.5800
Hoover & Goldbaum [103]	2003	Fuzzy convergence of vessels.	STARE	81	0.8900
Foracchia et al. [104]	2004	Geometrical model of vessel structure.	STARE	81	0.9753
Li & Chutatape [24]	2004	Template matching via PCA.	Local	89	0.9900
Lowell et al. [105]	2004	OD Laplacian of Gaussian template & full Pearson-R correlation.	Local	90	0.9900
Ter & Frank [106]	2005	Hough Transform over	STARE	81	0.7160
		Blood Vessels or nearby pixels.	Local	191	0.9634
Park et al. [107]	2006	Brightness and roundness detection.	DRIVE	40	0.9025
Fleming et al. [108]	2007	Elliptical form of blood vessels.	Local	1056	0.9840
Park et al. [109]	2007	Tensor voting and adaptive mean-shift.	STARE	90	0.8400
Ying et al. [110]	2007	Fractal dimension of blood vessels and local histogram analysis.	DRIVE	40	0.9750
Carmona et al. [92]	2008	Approximating elliptical form of optic disc via genetic algorithm.	Local	110	0.9600
Youssif et al. [111]	2008	Vessels' direction matched filter.	DRIVE	40	1.0000
			STARE	81	0.9877
Niemeijer et al. [112]	2009	Vasculature measurements and the k-NN regression.	Local	600	0.9300
Aquino et al. [97]	2010	Morphology, edge detection and circular Hough transform.	MESSIDOR	1200	0.9900
Rangayyan et al. [113]	2010	Gabor filters and	DRIVE	40, 81	1.0000
		BV convergence, phase modelling.	STARE		0.6910
Zhu et al. [95]	2010	Circle detection via Hough transform.	DRIVE	40, 81	0.9000
			STARE		0.4440
Lu & Shijian [93]	2011	Circular transformation and image variation along multiple radial line segments.	ARIA	120,	0.9750
			STARE	81	0.9975
			MESSIDOR	1200	0.9877
Dehghani et al. [98]	2012	Histogram-based template matching	DRIVE	40	1.0000
			Local	273	0.9890
			STARE	81	0.9136
Zubair et al. [114]	2013	Contrast enhancement and morphological transformation	MESSIDOR	1200	1.0000
Yu and Yu [115]	2014	Iterative brightest pixels extraction	STARE	40	0.9500
Anushikha et al. [116]	2016	DWT, PCA	Local	63	0.9475
Maheshwari et al. [117]	2017	Entropy, Fractal dimension	Local	488	0.9519
Joel et al. [118]	2017	PHOG,SURF	Local	1804	0.9500
Abbas [119]	2017	Deep Neural Network	DRION-DB	110	0.8450
			HRF	15	0.8517

of major arteries. Later the position of OD is calculated with the help of generalized Hough Transform in the ROI [108]. A high fractal dimension of the BV converging pattern has also detected the OD region [110]. Therefore we may see from these methods that localizing the OD is improved compared to property based methods.

Model based methods are associated with the generation of templates and matching it with the best possible candidate of OD among various candidates, such as HEs available. OD circular/elliptical geometry is targeted to generate the template. To realize this various image processing tools such as, Hausdorff based template matching with edge map [101], Gray level template with histogram normalization [102], Optic disc model (disc-space) applying PCA [24], Detection filter (Laplacian of Gaussian) template corresponding to major BV in OD region [105], Vascular orientation fitting template [106, 111], Retinal Vasculature around circular template using KNN [112] and so on are used. These methods improve the automated detection to an efficient level.

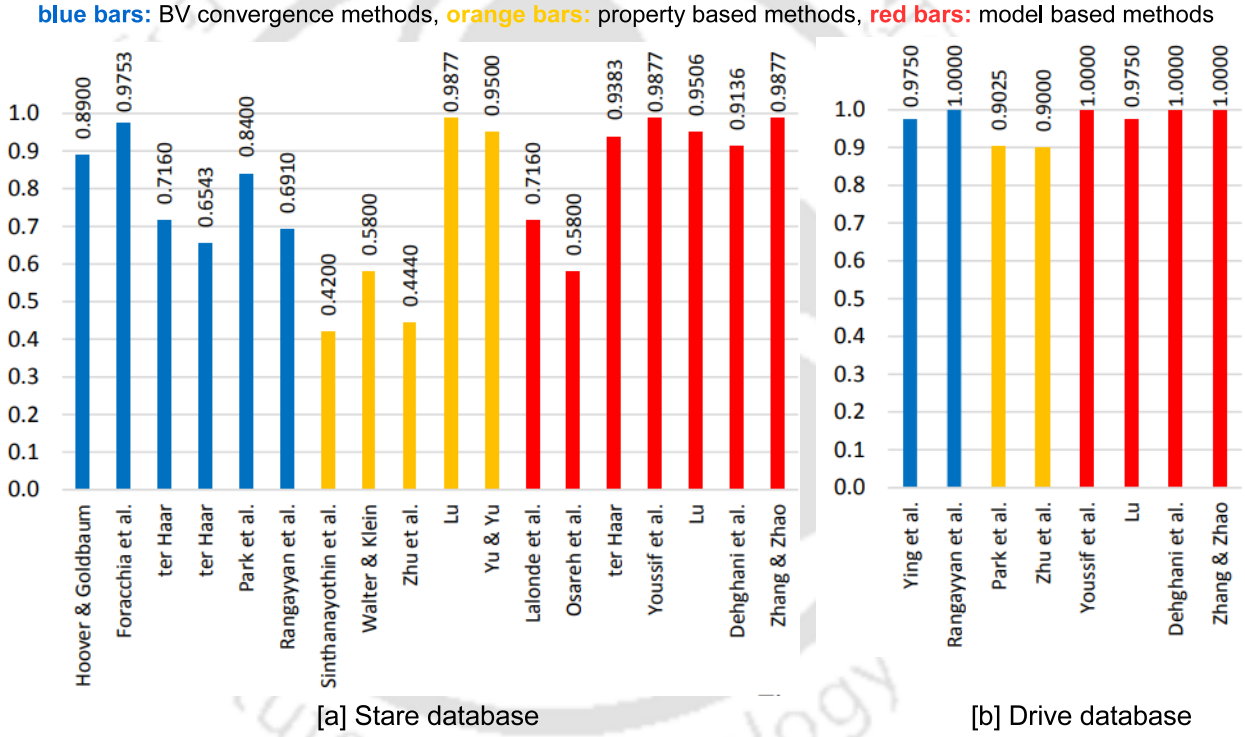

Figure 2.5: Comparison of OD detection sensitivity obtained in various algorithms, [a] STARE database, [b] DRIVE database.

To club and compare the automated detection methods of OD, Table 2.2 (allam et al. [88]) shows the image processing tools applied over various databases and corresponding results obtained. For a better comparison of the methods, sensitivity is presented as column charts, as shown in Figure 2.5. Here column charts are categorized into blue column for BV converge methods, yellow column for property-based methods, and template-based methods are given in red columns. The comparison is presented separately for STARE and DRIVE databases used by the algorithms.

To summarize the review for OD detection, we may point out that property based methods perform

better for healthy images and have a fast computation response. But to detect OD in pathological cases adding secondary information of BVs increases the detection rate. Template-based methods require intensive computations but generate more accurate results. It is also to be added that preprocessing methods improve the functionality of the algorithms. The motivation of OD detection in our proposed work is to help in fovea detection along with DM classification with the help of OD center and ODD, and it's masking to support HE detection. Therefore, two proposed methods based on BV properties and OD with HE relations have been discussed in Chapter 3 and Chapter 4, respectively.

2.2.3 Macula and Fovea Detection

Most of the methods for identifying the fovea are based on a two-step process. The first step comprises of locating the region containing fovea utilizing the geometrical relation of fovea and OD center/BV origin. It is assumed that fovea lies temporal to OD and at a distance of 2-2.5 ODD from OD center or BV origin [24, 25, 85, 96, 121–123]. After obtaining the region containing fovea, the next step is to locate it using various algorithms, such as template matching, thresholding, feature, and appearance-based method. Various authors have performed BV removal before fovea detection to avoid misclassification [85, 121, 122, 124]. Authors have also located fovea using intensity property. Apart from the advantages of these algorithms, the limitation lies in cases involving the presence of dark lesions such as HMs, which share a similar intensity profile as fovea. Also, with the presence of HEs, there is a probability of false localization of HEs as OD. The invalid localization of OD effects the fovea detection and thus the whole process of DM analysis. Figure 2.6 shows few examples of fovea detection error due to the presence of various abnormalities.

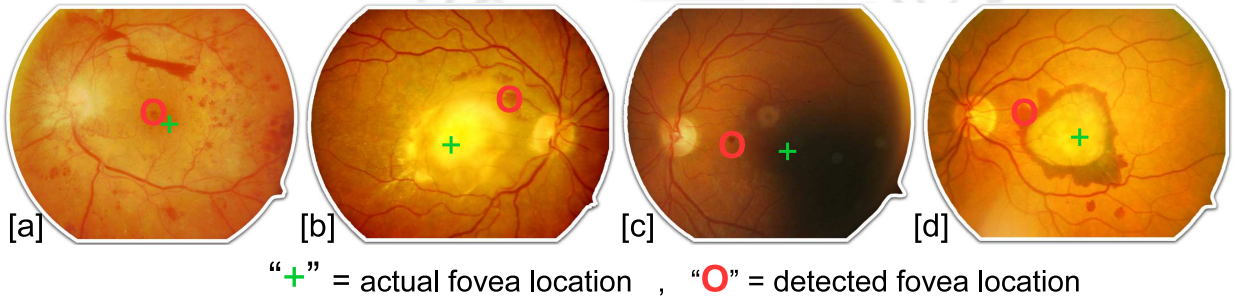

Figure 2.6: Examples of fovea detection error caused by: [a] Presence of HM near macula with similar intensity, [b] Overlapping of macula by HE fails the intensity based algorithms, [c] foreground suppressed by dark background due to camera flash issue, [d] fovea overlapped by blood leakage and leakage intensity getting wrongly detected.

The majority of the state-of-art algorithms initially detects macula and later locates fovea at the

center of macula [85, 96, 121–123]. The macula is the lowest intensity region of the fundus image. This property is used almost in every algorithm for its detection, whether to be globally or locally. The global application of this attribute is applicable only for normal fundus images, as in pathogenic images, dark lesions interfere in the detection process. Using a combination of RGB color plane properties along with mathematical morphology fovea is detected [124, 125]. Most of the remaining automated fovea detection methodologies may be categorized based on OD geometrical spatial relation and vascular arcade temporal relation. The **OD geometrical spatial relation** attribute for automatic detection of fovea is most commonly used by the researchers. The detection of OD, as discussed in the previous section, is performed by various image processing algorithms like PCA, active contour, Hough Transform, Edge detection, template fitting, and KNN classifier [25, 87, 126]. Once the OD center is located after segmenting the OD, the template matching procedure is used around the center of the axis to mark fovea at a distance of 2ODD. Authors have also included the BV arc information along with OD segmentation to create a parabolic template to locate fovea coordinates [24, 108, 112, 127]. Figure 2.7 shows few such examples. Here template [a] is Vascular arc template by Niemeijer et al. [128], [b] is Parabola fitting for fovea detection by Li and Chutatape [24], [c] represents OD and fovea detection using parabolic template with raphe by Tobin et al. [129] and image [d] is parabolic template centred at OD origin by Manuel et al. [130].

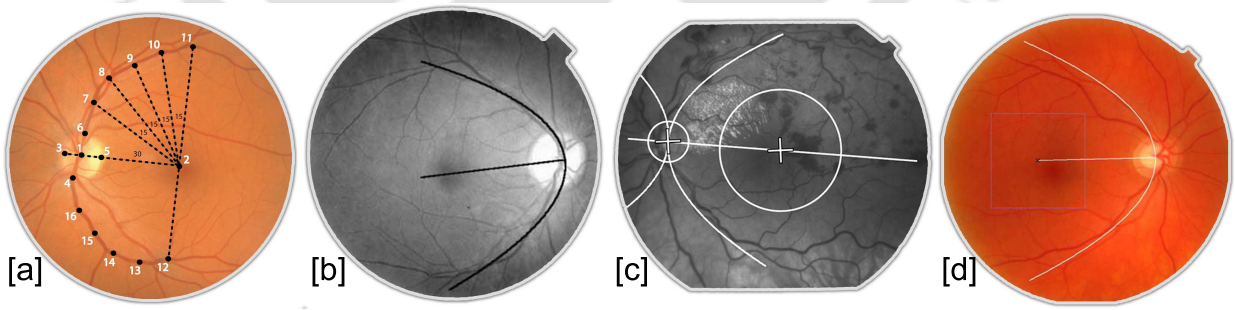

Figure 2.7: Examples of fovea detection using OD centre and parabolic template: [a] Vascular arc template by Niemeijer et al., [b] Parabola fitting for fovea detection by Li and Chutatape, [c] OD and fovea detection using parabolic template with raphe by Tobin et al. [d] Parabolic template centred at OD origin by Manuel et al.

This added information of BV is time-consuming, but it provides more accurate results. Among the methodologies using OD relation, few algorithms have detected the ROI containing fovea using geometrical relation of OD and fovea or BV properties. Later they have used algorithms like thresholding, mathematical morphology, edge detection, Markov chain, Gaussian templates for macula localization to identify fovea [25, 85, 87, 96, 121, 122, 134] utilizing dark intensity attribute. Apart from the limitation

Table 2.3: Comparison of Fovea Detection algorithms

Author	Year	Methodology	Optic Disc detection necessary	Blood Vessel detection necessary	Is affected by pathology	Database Used	Success Rate
Sinthanayothin et al. [89]	1999	Template-based method	Yes	No	Not specified	LOCAL	80.40%
Li and Chutatape [24]	2004	Parabola fitting	Yes	Yes	Not specified	LOCAL	100%
Narasimha-Iyer et al. [25]	2006	Selection of ROI and threshold	Yes	No	Opaque lesions	LOCAL	Not specified
Fleming et al. [108]	2006	Vascular arch detection and template matching	Yes	Yes	Not specified	LOCAL	96.50%
Niemeijer et al. [126]	2007	Cost function and a point distribution model	Yes	Yes	No	LOCAL	94.40%
Sagar et al [96]	2007	Selection of ROI and morphology	Yes	Yes	Not specified	DRIVE, STARE	96%
Tobin et al. [129]	2007	Vascular segmentation	Yes	Yes	Not specified	LOCAL	92.50%
Singh et al. [125]	2008	Appearance-based method	No	No	Not specified	LOCAL, DRIVE, STARE	96.61%
Kose et al. [87]	2008	Selection of ROI, relative locations of optic disk and macula	Yes	No	Not specified	LOCAL	Not specified
Sopharak et al. [121]	2008	Selection of ROI, thresholding and morphology	Yes	No	Not specified	LOCAL	Not specified
Sekhar et al. [85]	2008	Selection of ROI, thresholding and morphology	Yes	No	Yes	DRIVE, STARE	100%
Niemeijer et al. [112]	2009	kNN regressor	Yes	Yes	Not specified	LOCAL	96.8% 89%
Welfer et al. [122]	2011	Selection of ROI and morphology	Yes	No	Large opaque lesions	DRIVE, DIARETDB1	100% 96.62%
Chin et al. [131]	2013	BV density and BV arc fitting	Yes	Yes	Yes	TENOVUS, MESSIDOR	80.8% 72.9%
Manuel et al. [130]	2013	feature extraction	Yes	Yes	Not specified	MESSIDORE	96.92%
Giachetti et al. [132]	2013	Fast radial symmetry transform	No	Yes	No	MESSIDORE	99.10%
Akram et al. [133]	2014	feature set and Gaussian mixture model	No	No	Yes	HEI-MED, MESSIDORE	95.2% 98.4%
Zheng et al. [134]	2014	OD intensity and geometric location, and morphology	Yes	No	Large opaque lesions	DRIVE, HEI-MED, DIARETDB1	100% 98.8% 93.3%
Kao et al. [135]	2014	vessel-free zone and adaptive Gaussian template	Yes	No	dark lesions	DIARETDB0, DIARETDB1, MESSIDORE	93.1% 92.1% 97.8%
Kamble et al. [136]	2017	Signal valley analysis	Yes	No	Not specified	HEI-MED, MESSIDORE	99.4% 99.66%
Cao et al. [137]	2018	Morphological features fitting	No	No	Severe lesions	MESSIDORE	92.92%
Baidaa et al. [138]	2018	Deep neural network	Yes	No	Severe lesions	MESSIDORE KAGGLE	97.78% 95.6%
Chalakkal et al. [127]	2018	connected component analysis	Yes	Yes	Severe lesions	DRIVE, DIARETDB0 DIARETDB1, CHASE, MESSIDOR, STARE, UoA-DR	100%, 97.6%, 97.7%, 100% 98.6% , 95% 100%

of false detection of HEs as OD, the second limitation lies in considering the fovea position to be at the horizontal axis connecting the OD center. If we refer to the anatomy of retina, fovea lies temporal to the horizontal axis passing through the OD center. Therefore, authors have updated these pieces of information later in their algorithms. One more limitation is found in considering fixed Gaussian distribution for fovea template [89], as the fovea region varies among various images and databases. Application of adaptive Gaussian distribution in [135] has recovered this limitation. The second property used for fovea detection is **vascular arcade temporal relation**. Methods using this property

have first obtained BVs, with an emphasis given to the major artery detection. Later, using BV properties with respect to macula like parabolic template using geometrical relationship [24,108,126] and searching region of minimum BV density [96,129,131] are used to locate region containing fovea. Afterward, the dark intensity pixels are marked as the macula, hence obtain the fovea at the center. The discussion done so far is tabulated in Table 2.3 consisting of the method of analysis, the database used, and the accuracy obtained for fovea detection. The efficiency of the methods lies in detecting the fovea automatically very close to its manually located position.

As a summary, we may conclude that the identification of fovea is efficient concerning the two-step process, where the first ROI is obtained then fovea is detected within the region. The process performs better with OD if its detection is robust and not influenced by similar appearance HEs. Otherwise, BV information is necessary. As a primary requirement, we must note that the OD position and diameter is compulsory for DM analysis, which makes it mandatory to localize OD. Various other challenges obtained during fovea localizing include image suppressed by background, resulting from poor lighting conditions during imaging and high-risk DM cases where abnormalities overlap the fovea region. These are the cases where most of the image processing tools fail [Examples mentioned in Figure 2.6]. Therefore during fovea detection, all these limitations must be taken into consideration to attain maximum accuracy. In Chapter 3, we have discussed the proposed fovea detection algorithm considering all facts and challenges.

2.2.4 Exudate detection

The information about exudates, more specifically Hard Exudates size, number, and position, is vital for DM estimation. As discussed in Chapter 1 exudates appear as bright yellowish clusters of various shapes, sizes, and locations. To estimate DM severity, along with the amount of deposition, the thickness of HEs is an essential factor. During automatic detection, various image processing issues are to be dealt with, to detect and locate the exudates accurately. Such challenges involve poor imaging, weak boundaries, misclassification due to other similar intensity objects such as CWS, SE, drusens, and OD [126,139–143]. Various algorithms are proposed in the literature considering these factors. The majority of these automated detection methods are inspired by exudate properties such as bright intensity profile and color information. The algorithms for HE detection are broadly classified into two categories [143–145].

- Unsupervised Methods.
- Supervised Methods.

The **unsupervised methods** are mainly clustering algorithms divided into Direct and Indirect methods. Direct methods deal with the segmentation of exudate components from retina [86, 121, 139, 146]. Whereas, indirect methods identify retinal components and later locate the exudates by inverting the detection [87].

Following are the steps involved in the Direct method of exudate segmentation algorithms.

Step I Pre-processing algorithms for color normalization and illumination correction [contrast stretching, Histogram equalization, CLAHE, Top hat, and Bottom hat] [8, 142].

Step II Background Subtraction [Mathematical morphology, Filtering] [124, 139, 146]

Step III BV removal [Mathematical morphology, Inpainting] [84, 86, 124].

Step IV Bright lesion detection [Mathematical morphology, Edge detection, Thresholding, Active Contour, region-based methods, Gabor filter, clustering methods like k-means, fuzzy c means] [126, 147–150].

Step V Elimination of region other than HE [OD detection and masking (using thresholding, blood vessel relation), other lesion elimination (using thresholding, region-based methods)] [86, 143, 151]

Step VI Post-processing for elimination of over segmentation [Mathematical morphology] [139, 143, 146].

The indirect method of exudate detection uses region growing algorithms to segments out the continuous healthy regions of fundus image. Once detected the inversion of the detection results in exudates localization [87].

The supervised methods are more accurate and useful than the unsupervised classification methods [126, 140, 141, 147–149, 152, 168, 169]. It contains the prior information about the exudate properties before classifier application, making it more efficient to identify. Supervised methods use a part of the database as training images to program the classifier from the features obtained. Later the remaining images called test images of the database are used for determining the feature, and the

Table 2.4: Comparison of Exudate detection algorithm

Authors	Year	Proposed Methodology	Database	Sensitivity	Specificity	Accuracy
Walter et al. [139]	2002	Mathematical morphology	Non-public dataset	92.80%	92.40%	NR
Niemeijer et al. [126]	2007	kNN and linear discriminant	Non-public dataset	95%	86%	NR
Jayakumari and Santhanam [147]	2008	Energy minimization and echo neural network	Private Hospital	90%	NR	NR
Sanchez et al. [152]	2008	Linear discriminant classification	Non-public dataset	88%	NR	NR
Sopharak et al. [121]	2008	Optimally adjusted morphology	Non-public dataset	80%	99.50%	NR
Garcia et al. [140]	2009	1:MLP, RBF, and SVM	Non-public dataset	88.14% 88.49% 87.61%	NR	NR
Sopharak et al. [148]	2009	Fuzzy c-means, morphology	Non-public dataset	87.28%	99.24%	NR
Ravishankar et al. [146]	2009	Mathematical morphology	Non-public, STARE, DIARETDB0, DRIVE	95.70%	94.20%	NR
Welfer et al. [86]	2010	Mathematical morphology	DIARETDB1	70.48%	98.84%	NR
Sopharak et al. [141]	2010	Naive Bayes and SVM classification	Non-public dataset	92.28%	99%	NR
Karegowda et al. [149]	2011	KNNFP and WKNNFP classifiers	DIARETDB1	NR	NR	97.50% 96.67%
Nagy et al. [153]	2011	Majority voting-based ensemble	DIARETDB1	72%	NR	NR
Soares et al. [154]	2011	Morphological operators and adaptive thresholding	DIARETDB1	97.49%	99.95%	99.91%
Amel et al. [150]	2012	Combine K-means and mathematical morphology	Ophthalmologic Images	95.92%	99.78%	99.70%
Rozlan et al. [155]	2013	Morphology & neighborhoods operation	Sungai Buloh hospital	NR	NR	60%
Harangi et al. [142]	2014	Active contour fusion, region-wise classification	DIARETDB1 HEI-MED	92% 87%	68% 86%	NR
Soman and Ravi [156]	2014	Circular Hough transform and bit plane slicing, morphology	Standard DR	93.62%	NR	88%
Kayal and Banerjee [157]	2014	Median filtering, Image threshold	DIARETDB0, DIARETDB1	NR	NR	97.25% 96.85%
Kaur and Mittal [158]	2015	Dynamic region growing	SGHS hospital	NR	NR	98.65%
Haloi et al. [159]	2015	GIMAP and morphology	DIARETDB1 MISP	85.39% 37.14%	NR	NR
Rokade and Manza [160]	2015	Haar wavelets transformation, KNN classifier	DIRETDB0, DIRETDB1, STARE	21.87% 12.50% 25.47%	NR	NR
Jaya et al. [161]	2015	Morphology, Circular Hough transform, Fuzzy SVM	Private Hospital	94.10%	90.00%	NR
Wisaeng et al. [162]	2015	Moving average histogram, Sobel edge detector and Otsu	Local dataset	90.42%	94.60%	93.69%
Raja and Vasuki [163]	2015	Multi directional local histogram equalization, Gabor and SVM	HRF, DIARETDB1	94.76%	99.85%	NR
Annunziata et al. [164]	2015	Multiple-scale Hessian approach	STARE, HRF	NR	NR	95.62% 95.81%
Asha and Karpagavalli [165]	2015	Naive Bayes , Multilayer Perceptron and Extreme Learning Machine	DIARETDB0, DIARETDB1	82% 81% 100%	82% 81% 87%	82% 81% 90%
Lachure et al. [166]	2015	SVM and KNN classifiers	MESSIDOR, DB-rect	90%	NR	NR
Partovi et al. [167]	2016	Dynamic threshold & Morphology	Nikokary eye hospital	76%	98%	97%
Alharthi et al. [151]	2016	Mathematical morphology	Local dataset	86%	80%	NR
Senapati et al. [168]	2016	Texture features, SVM	DIARETDB1, MESSIDOR	100%	94.60%	96.66%
P. Khojasteh et al. [143]	2019	Color space analysis	DIARETDB1, E-OPTHA	99%	96%	98.20%
P. Khojasteh et al. [169]	2019	Deep learning analysis	DIARETDB1 E-OPTHA	99% 98%	96% 95%	98.2% 97.6%

difference between the features performs the classifications. The process of obtaining the features may be done globally from the whole image or the segmented exudate regions. Various features considered for training classifiers include area, compactness, standard deviation, mean intensity, mean

hull, mean saturation, entropy, homogeneity, bounding box, eccentricity. Various methods like the Anova test, Wilcoxon rank test, Ansari Bradley test are performed to identify efficient features among the pool of features. Classifiers like Support Vector Machine (SVM), Fuzzy, Bayesian, Random forest, Gaussian mixture model (GMM) with Bayesian and SVM, forward Artificial Neural Network (ANN) have reported for the detection and classification process. Considering various methodologies, we club them in Table 2.4, where we mention the proposed methodology, database used, and corresponding results obtained.

Based on the literature, it has been observed that the local scheme approach locates maximum exudates, whereas the global scheme determines the brightest pixels. Thresholding or clustering methods are suitable, but edge detection schemes produce efficient results. Limitation in edge detection technique is that they yield noisy results, due to variation in edge intensities requiring post-processing to reduce over segmentation. The property of edges also plays a vital role during the segregation of various similar intensity lesions. Machine learning methods require extensive pre-post processing, whereas supervised methods need proper ground truth data. Considering these factors, we have proposed two algorithms for the detection of exudates. The first algorithm uses the color property of various color plane models for segmentation. The second algorithm considers the elimination of various challenges, as referred in Subsection 1.4.3.2, which are evident during exudate detection. These algorithms are discussed in Chapter 4.

2.2.5 Dark lesions detection

Similar to exudates, the information of dark lesion concerning its size, number, and position is necessary for DM analysis. As alluded in Chapter 1 dark lesions comprises of MAs and HMs, with the difference of size between them. The MAs are of approximately less than 125μm and HMs are higher than 125μm. The thickness of the dark lesions resulting from the amount of blood deposition is also an essential factor for the severity assessment of DM. Analysis of MAs and HMs is suited better in FFA images. Yet, most of the current investigations are done on red-free fundus images. The extraction of red lesion from the retinal image is done after the removal of OD, BVs, and Macula, to avoid wrong identifications. Various standard algorithms are clubbed into following five types of methodologies [27].

- **Morphological image processing:** These are basic image processing techniques where

mathematical morphology is used along with region growing operation for locating the MA and HMs [170–174]. The morphological operations such as opening, closing and top-hat, bottom-hat transformation [175] are operated, in addition to matched filtering [172, 175], thresholding [172], and watershed algorithms [174]. On the detected segments various classifiers like ANN [176], Linear Discriminant Analysis (LDA) [175], kernel density estimation with Gaussian and KNN classifier are simulated [177, 178]. The main limitation of such methods lie in over segmentation during detection.

- **Supervised Classification:** This approach constitutes candidate extraction, feature selection and classification. Various features like back propagation, PCA, 2-D PCA, density analysis, Pixel classification based, double ring filter etc. [172, 173, 178–185] are applied to ANN [176, 181, 185], LDA [176], SVM [70, 182, 184–187], Mahalanobis distance classifier and rule based analysis [188], GMM [70, 186], and Naive Bayes classifier [35]. Supervised classification leads to more accurate dark lesion screening with a backbone of optimal features selection.

- **Template matching:** Templates based on the kernel matching structure of MAs and HMs are formed to segregate the dark lesions. These methods have the advantage of non-requirement of candidate extractions. These templates are created from wavelet transformation [189, 190], multi-scale correlation filtering [191, 192], adaptive weighing and summing [193], and so on. Various dictionaries are created from the extracted samples. This approach extracts, every dark lesions utilizing sparse representation [194], multi-scale Gaussian Filtering [195], Morlet Wavelet [196] etc. for creation of dictionaries. They are later analyzed in classifiers for the detection of MA and HMs.

- **Deep Learning:** This relates to feature extraction methods using approaches such as Convolutional Neural Networks (CNN) [197, 198], Multi-sieving convolutional neural network [199] as classifiers for lesion identifications. Limitations of these methods exist in longer processing time.

- **Miscellaneous techniques:** Various methods like statistical mixture based clustering [200], Amplitude Modulation - Frequency Modulation feature generated clustering [201], H-maxima transform with Naive Bayes classifier decision support system [202], Hessian multiscale analysis followed by binary classifiers [203] are used in the direction of Dark lesion detection.

Table 2.5: Comparison of Microaneurysms Detection algorithms

Authors	Year	Proposed Methodology	Database	Sensitivity	Specificity
Agurto et al. [201]	2010	Amplitude Modulation - Frequency Modulation features	MESSIDOR	92%	54%
Rocha et al. [194]	2012	Visual Word Dictionaries, SURF features, SVM Classifier	DIARETDB MESSIDOR	90%	60%
Akram et al. [187]	2014	Hybrid Classifier (GMM and m-Mediods)	DIARETDB MESSIDOR	97.83%	98.36%
Roychowdhury et al. [70]	2014	GMM, k-NN, SVM, AdaBoost Classifiers	DIARETDB1 MESSIDOR	80% 100%	85% 53.16%
Figueiredo et al. [203]	2015	Anisotropic wavelet bands, Cartoon texture decomposition	DIARETDB0 DIARETDB1 MESSIDOR	72.48% 77.38% 75.11%	80% 80% 91.81%
Ren et al. [204]	2017	Imbalanced data analysis, Extreme learning machine, Ensemble learning	E-Ophtha	96.10%	82.10%
Srivastava et al. [205]	2017	Multiple kernel learning, Support Vector Machines	DIARETDB1 MESSIDOR	Not Specified	Not Specified
Kar et al. [206]	2018	Curvelet, Differential Evolution algorithm	DIARETDB1 MESSIDOR	95.23%	95.12%
Dai et al. [199]	2018	Multi-Sieving-CNN, image-to-text mapping	DIARETDB1	Not Specified	Not Specified

Table 2.6: Comparison of Hemorrhages Detection algorithms

Authors	Year	Proposed Methodology	Database	Performance measure
Gardner et al. [181]	1996	ANN using back propagation	NA	Sensitivity-73.80%
Zhang and Chutatape [182]	2005	2-D PCA, SVM	Private Dataset (30)	True Positive Ratio - 89.10%
Hatanaka et al. [188]	2008	Density Analysis, Mahalanobis distance classifiers	Private Dataset (125)	Sensitivity- 80%, Specificity-80%
Saleh et al. [202]	2012	h-maxima transform, multilevel threholding	Private Dataset (98)	Sensitivity 87.53%, Specificity 95.08%
Tang et al. [207]	2013	Splat based feature classification, k-NN classifier, ROC curve 0.96	MESSIDOR	ROC curve 0.96
Figueiredo et al. [203]	2015	Anisotropic wavelet bands, Cartoontexture decomposition	DIARETDB0 DIARETDB1 MESSIDOR	Sensitivity 74.36%, Specificity 85% Sensitivity 73.58%, Specificity 100% Sensitivity 86%, Specificity 90%
Grinsven et al. [198]	2016	Fast CNN, Selective Data Sampling	KAGGLE MESSIDOR	ROC = 0.894, ROC = 0.972
Srivastava et al. [205]	2017	Multiple kernel learning	DIARETDB1 MESSIDOR	ROC = 0.92
Kar et al. [206]	2018	Curvelet, Differential Evolution algorithm	DIARETDB1 MESSIDOR	Sensitivity 97.67%, Specificity 97.74%

We assemble the discussed algorithm detail with recorded performances in the Table 2.5 and 2.6 (biyani et al. [27]). As a summary of the discussion, we have analyzed that the morphological processing methods are basic algorithms with the limitation of variation in structuring elements, and the detection results large amount of over segmentation. Supervised classification generates efficient outputs, but extensive pre and post-processing is required. Template matching also has added for improvement of dark lesion detection with the help of dictionary formation. Deep learning methods are more suitable as they consider every aspect with one drawback of high computation time. Again Morphological processes, if combined with classifiers, yield better results. Analyzing the scope of

dark lesion detection, we may summarize that although there are efficient methods available, but there is always room for improvement in terms of reducing the number of False Positives (FP)s. Therefore, considering the aspects for improvement, we proposed two algorithms for dark lesion detection reducing over segmentation, and discussed in Chapter 4

2.3 DM analysis using OCT image

This section presents the review of various algorithms used for the automated DM analysis using OCT images. Various steps and the associated methodology are discussed below,

2.3.1 Speckle noise removal

Continuing the discussion in Chapter 1, Subsection 1.3.2.1, the speckle noise present in OCT image causes misclassification in any of the detection algorithms. The noise components possess sharp edges that get identified along with the segmented output. Therefore, suppression or proper elimination of these noise constituents are compulsory. The literature for noise removal techniques include fusion techniques like statistical analysis model, least-squares fitting, Partial Differentiation Equation (PDE) based non-linear diffusion, averaged multiple B-scans. In the statistical analysis model [32], a Normal-Laplace fusion model has been used for improving the input OCT image. The least-square fitting is combined with histogram matching to boost the contrast. Along with these, other noise-reducing filtering methods like low pass filter, median filter, Gaussian filter are also applied [31, 33, 34]. The limitations of these methods lie in the fact that the filtering process weakens the edge information of the OCT layers. On the contrary, bilateral filter, anisotropic diffusion, non-linear complex diffusion filters are used, which preserve the edges along with the smoothing of the OCT image. But these methods also have the disadvantage of bringing gradient reversal artifacts (gradients of the image tends to change direction after manipulating it) to the output or cartooning the output image [33, 208, 209]. Other methods like block-matching and 3D (BM3D) filtering and sparse transform methods on wavelets and curvelets are also popular. But their limitation lies in edge distortion in case of block matching based methods due to disagreement of edges in consecutive blocks. Whereas, the transform-based algorithms produce artifacts near the edges. Recently various deep learning methods are also reported; however, due to the consideration of the additive noise model, these algorithms are not suitable for speckle noise in OCT. Figure 2.8 shows few examples

of speckle noise filtered output. The zoomed version contains the original image and filtered outputs of low pass filter, bilateral filter and BM3D filter. The observation gives filtered image with blurred response resulting weakening edges.

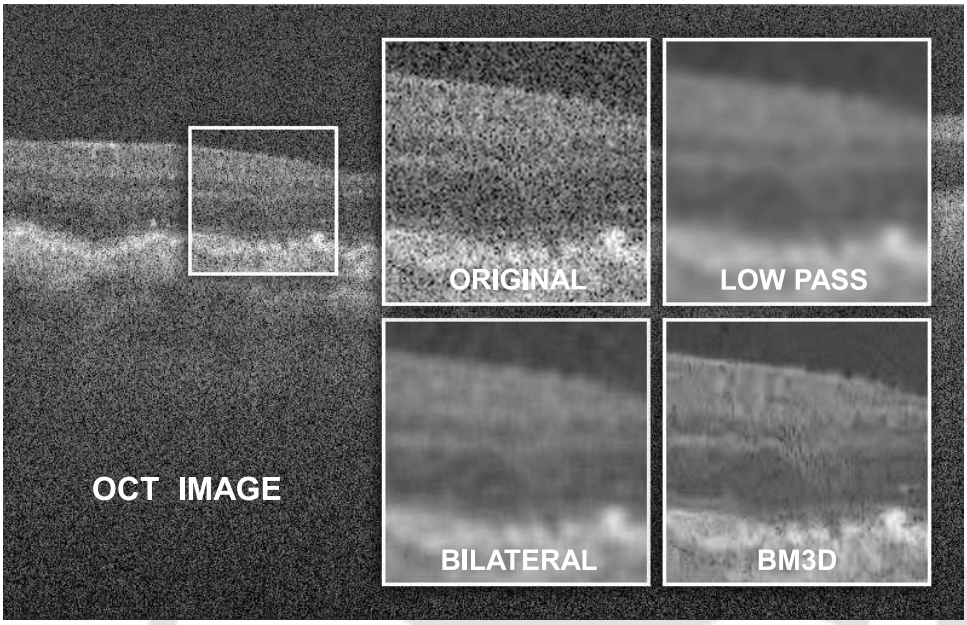

Figure 2.8: Response of various filters on speckle noise elimination, Top row First image is input OCT, predominated by speckle noises, Second image shows the filtering output by Gaussian low pass filter which weakens the edge information to a higher extent, Second row First output represents bilateral filter with hazy and gradient reversal, and finally the last image is the output of BM3D filter with smearing effect.

The main challenge of OCT speckle-noise reduction algorithms is the preservation of edge details. Most of the current methodologies reduce speckle noise but also cause edge smoothing. This issue severely affects the processes like layer detection and cyst detection. The speckle noises being multiplicative do not hold good for additive noise models. Therefore de-noising algorithms must effectively identify the edges to avoid applying filter operation over them. In this connection, we have introduced guided image filtering for OCT images, which preserves the edge information along with the removal of speckle noise. The detailed discussion on the filtering methodology with comparison to other filters is elaborated in Chapter 5.

2.3.2 Layer segmentation

The next challenge of DM analysis is the detection of retinal layers, mainly ILM and RPE, and after that, measure the thickness between them. An increase in thickness between the layers indicate positive DM. The detection of layers is affected by the presence of optical shadows formed due to

retinal BVs and the variational layer boundaries [209]. The methods for layer segmentations from literature can be listed into three categories [34] including, 1D gradient peak detection method [22, 35–37], 2D edge detection [38–41] and 3D graph search methods [210,211]. In the 1D gradient peak detection method, multiple A-Scan OCT is used [212]. Based on the intensity variation in each single A-Scan, the two most effective edges are identified using 1D edge detection or gradient operation. Combining all such A-scan, the distance between layers is estimated. During imaging, each A-Scan is acquired separately, providing an option to apply 1D edge detection individually, which overcomes the speckle noise issue generated in 2D B-scan OCT images. Each A-Scan pierce both retinal boundaries providing positive slopes with leading edges, which makes it easier to identify. The 1D process depends on connecting 1D points of each A-Scan, thus making it more susceptible to noise. Therefore, error correction rules became essential to eliminate the issue. The 2D B-Scan images are the photograph of retinal cross-section, which are predominated by speckle noise. As discussed, once these noises are eliminated with lesser tempering the edge information of the retinal boundaries, various layer detection algorithms are applied. Table 2.7 shows an example of a few methods used for layer detection using B-Scan images.

As observed from the literature, B-Scan images require proper elimination of speckle-noise with high output Signal to Noise ratio (SNR). Various algorithms are being used later to estimate the layers of retina. But the limitation lies in the detection of edges as its intensity information throughout the layer is varying, which results in the detection of broken edges. Thus, in our proposed method, we have used the modified Level Set Spatial Fuzzy Clustering Algorithm (LSFCM), which considers the variational boundary intensity condition with an automated level set. The detail discussion of the process is carried in Chapter 5.

2.3.3 Cyst detection

After detecting the retinal layers, the next task is the detection of cysts volume for positive CME patients classification. The measurement of cystoid fluid volume gives more diagnostic information than the central macular thickness [42]. Various approaches have been reported in the literature for cyst detections. These are GVF Snake [39], thresholding and boundary tracing [42], watershed algorithms [223], Graph cut or Graph search approach [224] for the purpose. But these methods fail during the identification of smaller cysts. To overcome this voxel classification based approaches are evaluated [213, 225, 226], which are on the contrary dependant on proper layer segmentation. The

Table 2.7: Comparison of Retinal Layer detection algorithm

Authors	Year	Proposed Methodology	Results
Fernandez et al. [36]	2005	Non-linear complex diffusion process, Coherence enhanced diffusion process, Automatic peak finding procedure, Linear interpolation.	7 edges are extracted for normal eyes but for eyes with pathology, the method is not satisfactory.
Chiu et al. [213]	2010	Graph theory and dynamic programming.	7 layers of normal eyes detected. Compared the result with 2 expertsfor thickness of layers.
Ghorbel et al. [214]	2011	Active contours, K-means, Markov random fields, Kalman filter.	8 layers detected & thickness result compared with 5 experts.
Vermeer et al. [215]	2011	Feature extraction, Classification (SVM), Regularization.	5 interfaces for normal & glaucomatic eyes & thickness maps are derived.
Lee et al. [216]	2013	Graph theory and dynamic programming.	3 layers detected. Compared DOCTRAP results with Spectralis & Cirrus.
Lang et al. [217]	2013	Random forest classifier, Boundary refinement algorithm.	9 retinal layer boundaries are detected.
Srinivasan et al. [218]	2014	HOG descriptors, SVM.	Detected DME & AMD cases accurately. Emphasized on detection of diseases rather than segmenting retinal layers.
Duan et al. [219]	2015	Variational retinal model, Non-linear diffusion processes, Unsharp masking.	7 layers detected for normal eyes.
Hussain et al. [220]	2016	3 approximate reference layers computed, Graph cut, Shortest path algorithm.	Detected 4 retinal layers with pathology & compared the result with 5 state-of-the-art techniques.
Gao et. al. [221]	2016	Graph optimal approach, canny edge detector	Segmented 10 retinal layers.
Eltanboly et al. [222]	2018	Wavelet decomposition based edge tracking, joint MGRF model and Statistical analysis.	Detects 12 layers with quantitative analysis of each layer's changes with respect to diabetes.

layer segmentation in the presence of abnormalities is quite challenging. Other methods, like 3D curvelet transformations based on dictionary learning [227], are applied. Most of these methods are vendor-specific and seek human intervention for acquisition and visualization [228]. In our proposed work, we have introduced background filtration, and after that identification of cysts regions using modified Nick's algorithm. The area of cysts is then identified using the modified LSFCM. The detail discussion on the algorithm is carried in Chapter 5.

2.4 Motivation

The automated detection of DM/DME is necessary for increasing the diagnosis rate, along with reducing the workload of ophthalmologists. Such low-cost approach helps in spreading awareness of the disease and its treatment. Literature reports methods on retinal anatomical feature and lesion detection. The issues faced by automated fundus image analysis algorithms in the literature for OD detection include cases where there are more bright regions other than OD, makes it challenging to determine its exact location. So using the property that OD is generally the brightest structure in the fundus along with shade correction operation and property of containing BV origins may improve the accuracy of detection. Fovea localization as the darkest pit in the image may be difficult in the presence of other dark lesions like blood clots or HMs. As such, utilizing the geometric location of the OD to determine the fovea is possible, along with the property of fovea being the avascular zone. Literature refers to the issues of HEs detection in the presence of SEs and other bright spots. Therefore, the proper differentiation of HEs from these bright spots and the knowledge of HEs properties are vital. Detection of dark lesions, namely, HMs and MAs, also pose concern due to their structures and lack of variation from the background. The studies available in literature establish image pre-processing as a significant step to accomplish the proper identification of these dark lesions. Again elimination of non-candidate structures, basically the BVs, stagnate lesion detection accuracy. The current work strives to achieve a proper BV elimination scheme. For proper grading of DM, the presence of all detected lesions, including the HEs, HMs, and MAs, need to be checked within the desired region of interest surrounding the fovea. So successful and accurate fovea detection is one of the primary requirements in the current work. This is followed by severity grading based on lesion distance from the marked foveal region.

Similarly, the automated OCT analysis algorithms are challenging. Based on the literature, the speckle noise removal is the backbone of the analysis. With proper elimination of noise without affecting the retinal layer is the primary motivation. During the layer detection process considering variational intensity, property is the proper way of processing the algorithm. In the end, the detection of cyst structures require localization and identification of various cysts irrespective of numbers and sizes.

Therefore, it is crucial to properly design the automated algorithm to reduce the problems mentioned above and extract the required candidate features from the fundus image before DM grading.

Along with fundus image processing, OCT image analysis also has become the necessary condition for DM evaluation to understand the retinal tissue damage. Therefore, to create proper awareness of DM followed by accurate diagnosis with the help of automated analysis is the main motivation of this project.

Considering the challenges from the literature review, the work plan of the thesis has been formulated to analyze first with fundus image for grading DM and after that evaluation of OCT images for retinal layer inspections. The work done therefore can be divided into two modules such as,

Module 1: Evaluation of DM using fundus image,

- Localization and detection of fovea.
- Improved detection of lesions (bright and dark).
- Classification of diabetic maculopathy.

Module 2: Evaluation of DM using OCT image,

- Speckle noise removal from retinal OCT image.
- Retinal layer detection and identification of DM.
- Analyzing cyst detection.

2.5 Contribution

The current work thrives on finding a proper solution to the issues faced by researchers in automated analysis of DM. The major contributions in this direction for the thesis are as follows:

(i) Image correction with bright boundary elimination obtaining fundus field of view.

(ii) Detection of fovea, using avascular property, and improvising using the ellipse fitting approach.

(iii) Removal of macular and BV reflection, improving HE detection.

(iv) Improved dark lesions detection by eliminating BV based on the cross-sectional width of vessels.

(v) Enhanced speckle removal in retinal OCT images with improved layer detection.

2.6 Materials / Database

Retinal image databases containing both fundus and OCT images are processed for the evaluation of proposed DM analysis algorithms. In case of algorithm operated on fundus image, the publicly available databases namely DRIVE, DIARETDB0, DIARETDB1, MESSIDOR and HRF are analysed. On the other hand for OCT image analysis, images collected from Guwahati Eye Institute are evaluated along with publicly available OPTIMA Cyst segmentation and Duke University database. The details of the databases are explained below,

2.6.1 DRIVE: Digital Retinal Images for Vessel

The DRIVE database [229] consists of 40 tiff images with two subdivision as training and testing sets, containing 20 images each. Out of 40 images, 33 are devoid of DR and remaining 7 images represent mild DR. The screening of process is carried out in a diabetic patient with a population of 400 between 25-90 years of age. The fundus camera setup consists of Canon CR5 non-mydriatic 3CCD camera with 45 degree FOV. The images are 8 bits per color plane at 768$\times$584 pixels. The FOV for each image is contained in a circular diameter of 540 pixels. The database contains manual annotation of BVs.

2.6.2 DIARET DB0: Standard Diabetic Retinopathy Database Calibration level 0

DIARET DB0 [230] comprises of 130 color fundus images with 20 normal and 110 DR images. The images are collected from Kuopio University hospital. The patient population data is not available for the images. The fundus camera information is unknown with normal imaging settings generally used in hospitals. The images are stored in png format. The FOV here corresponds to 50 degree contained in a non circular boundary. Manual annotation of exudate candidates are marked for algorithm evaluation. The database is termed as “calibration level 0 fundus images”.

2.6.3 DIARET DB1: Standard Diabetic Retinopathy Database Calibration level 1

This is also DIARET DB dataset referred to as “calibration level 1 fundus images” and named as DIARET DB1 [231]. The database is equipped with 89 colour fundus images. Out of 89 images, 84 contain DR signs and rest 5 are healthy images. Similar to DIARET DB0 the database imaging conditions, patient population and camera informations are alike. These images are also collected

from Kuopio University hospital. The FOV of fundus images is 50 degree and contained in a non circular boundary. This database also contains manual annotation of lesions present.

2.6.4 MESSIDOR

The MESSIDOR database [232] consists of 1200 color fundus images acquired by 3 ophthalmologic departments. The images are captured by using a color video 3CCD camera mounted on a Topcon TRC NW6 non-mydriatic retinograph with a 45-degree FOV. The captured images are stored with 8 bits per color plane at 1440×960, 2240×1488, or 2304×1536 pixels in tiff format. Out of 1200 images, 800 images are acquired with pupil dilation (one drop of Tropicamide at 0.5%), and the remaining 400 are non-dilated. 400 images acquired from 3 departments each are categorized into 4 sets, containing 100 images each. The manual annotation performed is based on DR stages and is reported in an excel file. Out of 1200 images, 546 images are normal, and the remaining 654 images contain DR lesions.

2.6.5 HRF: High Resolution Fundus

Among the databases, HRF [233] is recent and equipped with high-resolution fundus images. Due to which the preprocessing requirements of the detection algorithms is minimized. The database contains 15 normal, 15 DR, and 15 glaucomatous images, in the total count of 45. The patient population is mentioned as 18 pairs of same eye captured from 18 subjects. The fundus camera used is Canon CR-1 with an FOV of 45°and a different acquisiti on setting. Experts provided manual annotation of BVs and FOV masks.

2.6.6 E-ophtha

E-ophtha database is generated from OPHDIAT© Tele-medical network for DR screening [234]. The dataset contains both bright and dark lesion images. The image resolutions ranges from 1440×960 pixels to 2544×1696 pixels. Capturing of images is taken at a 45° field of view. The HE containing dataset is consists of 47 positive cases of HEs [with a total count of 12,278 exudates] out of a total of 82 fundus images. The MA dataset carries MAs and small HMs in 148 images [with a total count of 1306 microaneurysms] among a total of 381 images.

The details of the publicly available fundus databases are summarized in Table 2.8.

Table 2.8: Standard publicly available Fundus Image Databases

Database	Full Name	Field of View (FOV) (deg)	Total image	Normal image	Pathogenic image
DIRET DB 0	Standard Diabetic Retinopathy Database Calibration level 0	50	130	20	110
DIRET DB 1	Standard Diabetic Retinopathy Database Calibration level 1	50	89	5	84
DRIVE	Digital Retinal Images for Vessel Extraction	45	40	33	7
HRF	High-Resolution Fundus	45	45	15	30
MESSIDOR	Methods to Evaluate Segmentation and Indexing Techniques in the field of Retinal Ophthalmology	45	1200	546	654
E-OPHTHA	e-ophtha	45	463	195	268

2.6.7 GEI: Guwahati Eye Institute

A total of 260 OCT images are collected from the local hospital, Guwahati Eye Institute, Guwahati. The OCT images are captured using the Cirrus HD-OCT 500 (Carl Zeiss Meditec, Inc.) with software version 8.0.0.518. The images are obtained using a 512$\times$128 macular cube volume scan, which means there are 512 horizontal A-scan for each vertical B-scans, and 128 B-scans are there in the cube over a 6mm square grid around the macular region. The device has an axial resolution of 5 micrometers and a transverse resolution of 15 micrometers. The data acquisition speed of the device is near about 27000 to 68000 A-scans. The images acquired are stored and analyzed in x-z (B mode) frames of 1180$\times$786 pixels. The x-y-z frames of the obtained volumes are 6mm$\times$6mm$\times$2mm volume data cube of voxel size 5μm$\times$15μm$\times$2.5μm respectively. The obtained database of 260 OCT images contain 187 healthy and 73 positive ME cases. Out of 73 ME cases, 40 are effected by CME. The dataset is annotated by two retinal experts independently and the labels are provided to each B-scan OCT images based on the observed changes in the anatomical features of the retina.

2.6.8 OCSC: MICCAI 2015's OPTIMA Cyst Segmentation Challenge dataset

MICCAI 2015's OPTIMA Cyst Segmentation Challenge (OCSC) dataset contains 15 training and 15 testing SD-OCT volumes with cysts resulting from retinal diseases like the retinal vein occlusion and the age-related macular degeneration. These volumes are acquired from different OCT imaging systems namely Spectralis, Cirrus, Topcon and Nidek. The dataset has manual annotation of cysts by two graders. The resolution and density of the volumes vary from 496$\times$512 to 1024$\times$512 and 5 to 200 B-scans, respectively.

2.6.9 Duke University dataset

The Duke dataset is provided by Duke university [218]. The dataset comprises of 45 SD-OCT volumes with 15 subjects each from healthy, DME and AMD patients. The datas are acquired using Heidelberg Inc. Spectralis camera. The B-scans are of size 512×496 pixels and varies from 31 to 97 per volume.

3

Detection of FOVEA using blood vessel relation and ellipse fitting

Contents

3. Detection of FOVEA using blood vessel relation and ellipse fitting

Diabetic Maculopathy originates from the physiological changes occurring across the fovea. The fovea is the inner macular depression, situated at the center of the retina. The fovea contains numerous delicate cone cells, to provide central photopic and high-resolution vision [2]. Any abnormal changes occurring in the fovea or its neighborhood leads to severe damage in vision leading to blindness. Therefore, fovea inspection is a very crucial requirement. It starts with the localization of fovea and obtaining the region of evaluation for DM detection and classification.

In this connection, this chapter proposes an efficient algorithm for fovea localization, considering all the challenges faced during its automated detection. The OD detection is necessary to locate ROI containing fovea. Apart from this prerequisite, the OD and its diameter information are essential to analyze DM. The physiology of the BV network is the best secondary information to be utilized for the identification of OD. The same property is also helpful for fovea localization, which says, OD contains maximum BV whereas, the fovea is devoid of BVs. Hence, with this motivation, we have proposed an algorithm for fovea detection based on BV property. Later, from the performance obtained and drawbacks accumulated, we have updated the algorithm into template-based investigation. Thus the two proposed methods are,

- Fovea localization using blood vessel relation.
- Fovea localization using Ellipse fitting approach.

Chapter content: The chapter discusses two proposed algorithms, as stated above. Section 3.1 explains the fovea detection using the BV relation method. It consists of bright regions such as OD and exudate detection and elimination, followed by ROI identification for fovea localization. The method based on Ellipse fitting is described in Section 3.2, which begins with BV arc detection, followed by OD center localization, utilized for generation of ellipse template. The fovea localization is carried by fitting the generated ellipse template. From the templates obtained per database, a single ellipse template is formulated, with the help of a mathematical model. The mathematical expression for ellipse uses the ODD as the variable, allowing the generation of templates as per the requirement from various databases.

3.1 Proposed fovea localization using BV relation

The proposed approach for fovea localization is inspired by the avascular property of fovea anatomy. Using this property, the ROI containing fovea, is obtained. The novelty of the present algorithm over other methods is that, the fovea location can be obtained directly instead of evaluating the geometrical relationship of OD or BVs. The proposed method is also independent of BV removal. Generally, the image inpainting method [124] is used for BV removal. The method is computationally intensive and requires repetitive iterations to remove BVs. Being independent of this step, it reduces the computational time. After identifying the region containing fovea, the intensity property is used for its localization. As discussed earlier, the detection of OD gets affected in the presence of extensive exudates in algorithms based on intensity analysis. In the proposed method, this issue is eliminated utilizing the property of BV's structure in the OD region.

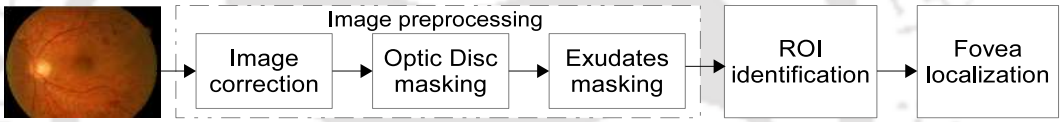

Figure 3.1: Block diagram of Proposed fovea localization using BV relation.

The block diagram of the proposed method is shown in Figure 3.1. The steps include image correction and masking of bright regions (OD and exudates) as preprocessing step. Then the ROI is identified continuing to detection of the fovea inside ROI. The algorithm is a sequential segmentation of various landmarks based on it's color properties. Utilizing RGB, HSI, YCbCr color plane processing, the algorithm is evaluated. Identification of BV and estimating the ROI containing minimum BV is the key to locate the fovea region here. Before applying segmentation, image correction is to be performed for boosting the efficiency of detection.

3.1.0.1 Image correction

To reduce the intra and inter-image variability between images of various databases used, image correction is necessary. The fundus image databases have resolution and illumination variations. Therefore, all the images are resized to 768$\times$576 size, and illumination correction is applied for image quality improvement to enhance segmentation. It has been observed that the presence of a non-uniform background and bright fundus image border interfere in image enhancement and segmentation algorithms. Therefore, the background of a color fundus image should be made uniformly

dark, and the boundary of the fundus is to be masked. Therefore, the input color image is first converted to a grayscale image. The intensity is improved using the contrast enhancement technique. The edges of the fundus image are then obtained using the canny edge detector. Morphological image filling is later performed to fill up the holes. Let L be the image obtained after filling. The image border is obtained by subtracting the dilation from erosion output of image L as given in equation (3.1),

$$x_b = \partial^{(B)}(L) - \varepsilon^{(B)}(L) \tag{3.1}$$

where, x_b is the image border, $\partial^{(B)}$ represents dilation and $\varepsilon^{(B)}$ represents erosion of image L, performed by structuring element B. The selection of B is made depending on prior knowledge of the geometry of the image. A disc structuring element of appropriate radius pixels is used. After the detection of the image border, its coordinates are used to mark the color fundus image. The portion of the fundus image lying outside the border is made pure dark by assigning the gray value 0 to all the pixels. Figure 3.2 shows the steps of Fundus image boundary detection and elimination of the outer boundary region.

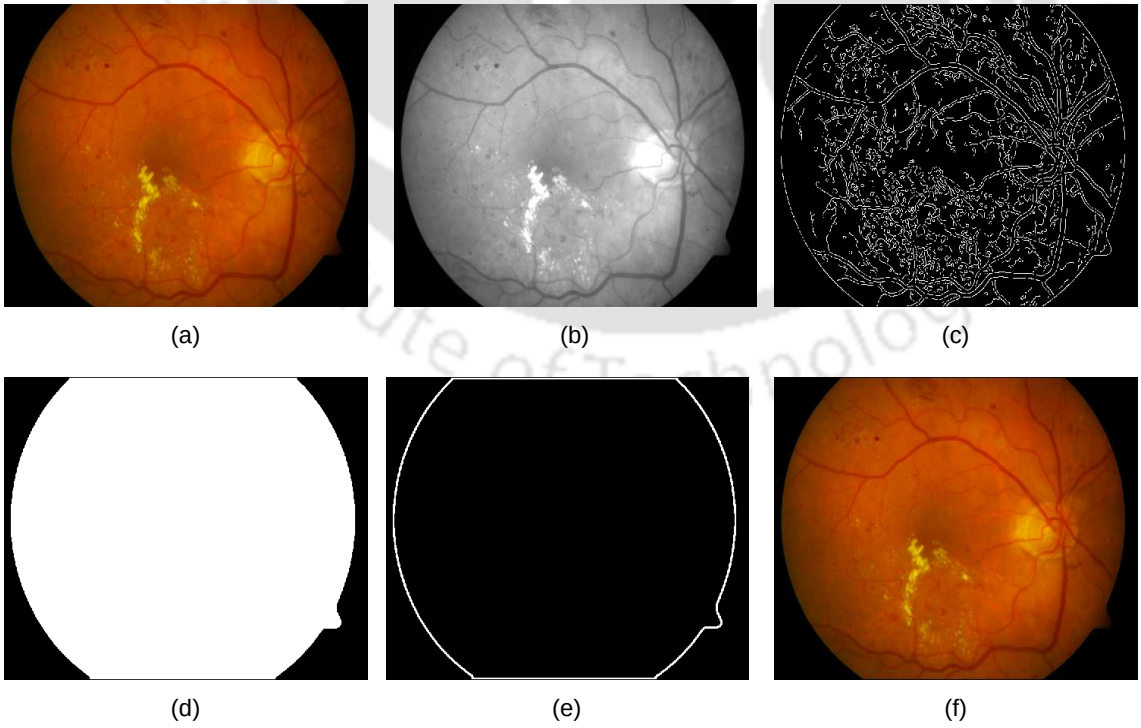

Figure 3.2: Detection of Fundus image boundary and darkening of outer region: (a) Original color image, (b) Enhanced gray scale image, (c) Edge detection using Canny method, (d) Morphological filling, (e) Detected fundus border and (f) Outer region of fundus darkened.

Depending on the illumination variation of images, the color intensity normalization, and the contrast enhancement of the fundus images are required. The basic requirement of image enhancement is to adjust the pixel intensities in such a way that the bright regions become brighter and dark regions get darker. For color intensity normalization, the method proposed by Clara et al. [235] is followed. The algorithm performs color normalization by enhancing the luminance plane of *YIQ* color model instead of enhancing each color plane of *RGB*, as shown in Figure 3.3 (a) and (b). The scheme converts an *RGB* to *YIQ* color plane image. The luminance *(Y)* plane is then considered for transformation according to the following equation,

$$Y_{\text{mod}} = a.Y + b.I + c.Q \tag{3.2}$$

where, Y_{mod} represents modified Y plane. In the above transformation, the parameters a, b and c are dependent on image characteristics. Therefore, they are selected properly to reduce luminance variability and to increase mean contrast levels. This modification is applied only to Y plane, and I plane and Q plane are maintained as it is. The modified color model $Y_{\text{mod}}IQ$ is converted back to

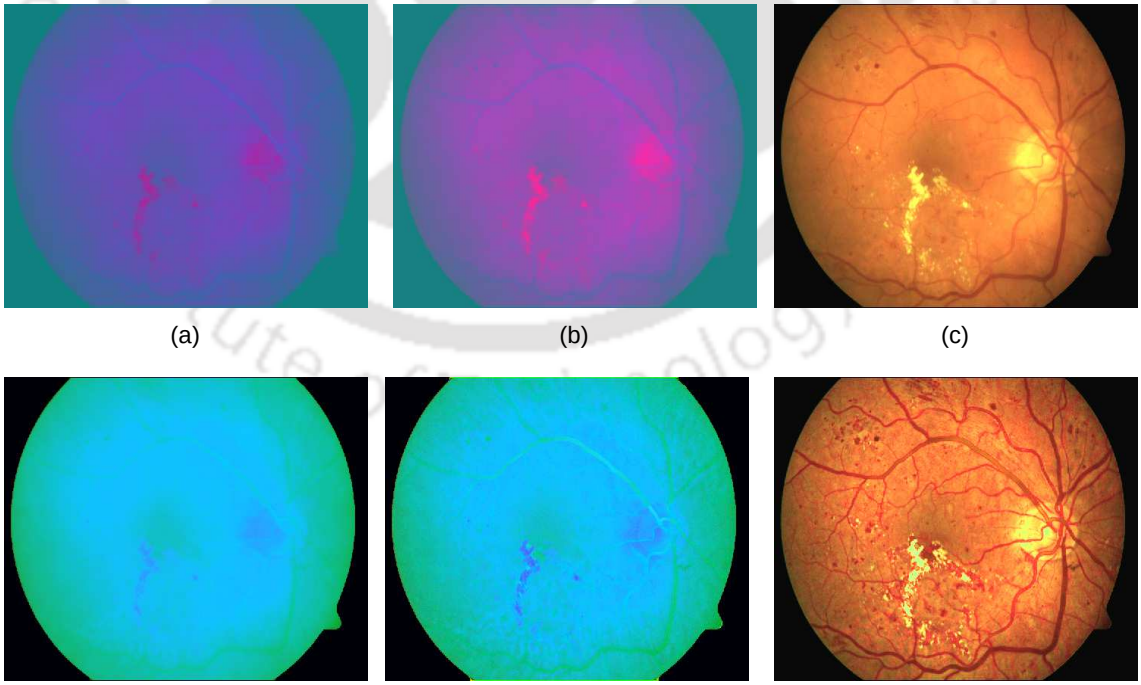

Figure 3.3: Image enhancement: (a) *YIQ* plane image, (b) color normalized *YIQ* plane image, (c) color normalized *RGB* plane image, (d) *HSI* plane image, (e) *HSI* plane image after Top-Hat and (f) Enhanced *RGB* plane image.

RGB color model and the result is shown in Figure 3.3 (c). Let this image be RGB_{mod}

For distinguishing the lesion information from the background, it is important to have high and uniform contrast. A morphological contrast enhancement method is therefore developed based on top-hat transformation. This process is inspired from the algorithm by P.Soille [236] on image contrast enhancement. Top hat opening and closing are implemented as per equation (3.3) on both hue and saturation plane of *HSI* color model of the fundus image.

$$X_2 = x.K + y.\psi(K) - z.\zeta(K) \tag{3.3}$$

where, X_2 is enhanced image and K represents the input image. $\psi(K) = K - \sigma^{(B)}(K)$, is the top-hat opening output and it represents bright regions of the image. $\zeta(K) = \theta^{(B)}(K) - K$, is top-hat closing output and it contains only the dark regions. Here, $\sigma^{(B)}(K) = \delta^{(B)}\left(\varepsilon^{(B)}(\mathrm{K})\right)$ is the morphological opening and $\theta^{(B)}(K) = \varepsilon^{(B)}\left(\delta^{(B)}(\mathrm{K})\right)$ represents morphological closing, performed with a disc structuring element, B. In this work, $[x, y, z] = [1, 1, 1.5]$ is found suitable and used for all the images. The intensity plane information is kept unaltered. After enhancement, the image $H_{\text{mod}}\, S_{\text{mod}}\, I$ as shown in Figure 3.3 (e) is converted back to *RGB* color model. The resultant image contains distinct information of the lesion and various retinal landmarks as shown in Figure 3.3 (f). Figure 3.3 represents the steps for the enhancement procedure. Here, image (a) is the YIQ plane image of output obtained in Figure 3.2(f). The color normalized output and it's corresponding RGB transformed image were shown in image (b) and (c). Image (d) represents the corresponding HSI plane image and image (e) and (f) are the output of Top-Hat transformation in HSI and RGB image formats.

Once image correction is over, we obtain a standard uniform-sized enhanced image. The resultant RGB image [say RGB_{mod}], pictorially represents the required regions of segmentation with better and distinguishable contrast. The output obtained is represented in Figure 3.3. The green and red plane images are thus more suitable for the next segmentation process. The next step in the algorithm is to identify and mask the bright regions, that is OD and HEs. This process enhances the red plane image for better fovea recognition.

3.1.0.2 Optic disc detection and masking

Optic disc and exudates are similar intensity structures observed in the pathological fundus image. OD once detected, followed by OD masking, the remaining bright structures in fundus image are exudates only. From the review discussed in Chapter 2.2.2, to determine the ROI (say ROI-1), which contains OD, the property of presence of maximum BV and circular shape of OD is employed.

The BVs segmentation must be efficient for obtaining the region containing maximum BVs. The green channel provides better contrast between BV and background [24, 123]. Therefore, the green channel image of RGB_{mod} is taken into consideration for the BV detection. To preserve the BV present over OD, the intensity profile of the image is altered. For this purpose, the green channel image is complemented so that the BV's intensity is changed to bright, and OD becomes dark. On the complemented image, morphological opening is performed as given by the following equation, using a ball structuring element.

$$\sigma^{(B)}(I) = \delta^{(B)}\left(\varepsilon^{(B)}(I)\right) \tag{3.4}$$

where, $\delta^{(B)}$ represents dilation and $\varepsilon^{(B)}$ represents erosion applied to image *I*. The morphologically opened image is shown in Figure 3.4(b) for reference. The resultant image is then subtracted from the complemented green channel image, which gives removal of the OD region without affecting the BV structure in it. We may refer Figure 3.4(c). Let the image be named as 'image X'. Image X is then converted to binary image using Otsu's threshold [237]. The output thus obtained consists of BV structure, dark lesions and FP pixels. To isolate BVs from remaining non BV pixels, binary opening is applied to binary image, removing the pixels having less connected neighbors, according to equation 3.5.

$$f_1(x,y) = \begin{cases} 0, & if \quad p_n \leq \lambda_1 \\ 1, & if \quad p_n \geq \lambda_1 \end{cases} \tag{3.5}$$

where p_n represents the neighboring pixels, and λ_1 represents the threshold. The value of λ_1 can vary from 50 to 75 depending on image property. In the proposed algorithm, three sets of values for λ_1 have been used depending on the intensity of BVs. The BV intensity of images in DIARETDB1 is slightly high and thick compared to other databases. Hence the value 65 is used. MESSIDOR and DRIVE database has less intensity BVs. Therefore a value of 55 is used. The images in the HRF

database contain intermediate intensity, and hence a value of 60 is used. The value of λ_1 is fixed as per the observation of algorithm over the databases. The output image obtained is shown in Figure 3.4(d).

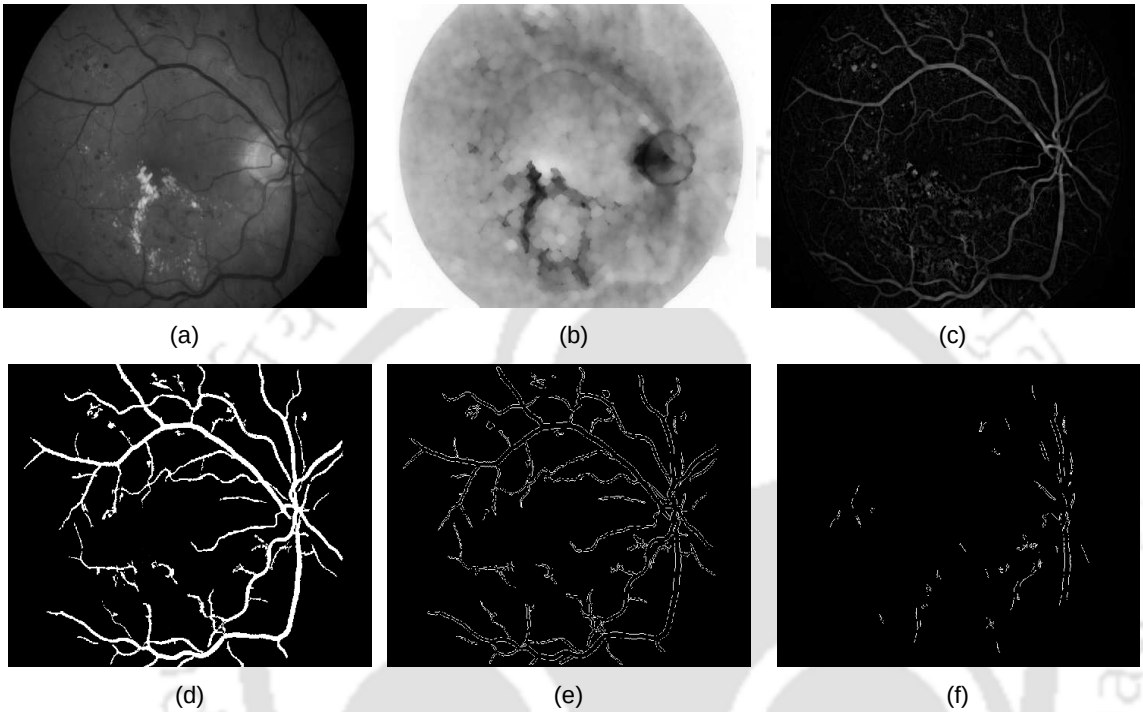

Figure 3.4: Detection of BVs using *GREEN* channel image of RGB color plane: (a) Green plane image of RGB, (b) Morphological opening applied on inverted green plane image, (c) OD removed without effecting BV, (d) Detected BVs, (e) Edges of *(d)* and (f) Vertical edges of *(d)*.

The BVs originated from OD and spread towards the macular direction. Generally, BV are vertically aligned in the vicinity of OD [26]. This property is used for obtaining ROI-1 containing OD. From the detected BV image, the BV edges are obtained using a vertical Sobel mask, shown in Figure 3.4 (f). The images of various databases have OD located either on the left, right, or center. The size of OD is large enough so that even if we divide the fundus image into three vertical stripes, the OD gets accommodated in any one of these strips. Therefore, the image is divided vertically with a window of one-third of the number of rows. Each vertical region is scanned for edge pixels, and the segment with maximum value is considered as ROI-1 for the detection of OD. Corresponding ROI-1 for the processed image is shown in Figure 3.5(a). After detecting ROI-1, the corresponding gray image is considered [Figure 3.5(b)]. The histogram of grayscale ROI-1 is investigated for extracting the high-intensity pixels representing OD. For isolating the bright pixels, Otsu's threshold [237] is used, and the resultant image is shown in Figure 3.5(c). Once the region of bright pixels is detected, a Canny edge operator is applied to find the edges of the region, shown in Figure 3.5(d). To extract the distinct

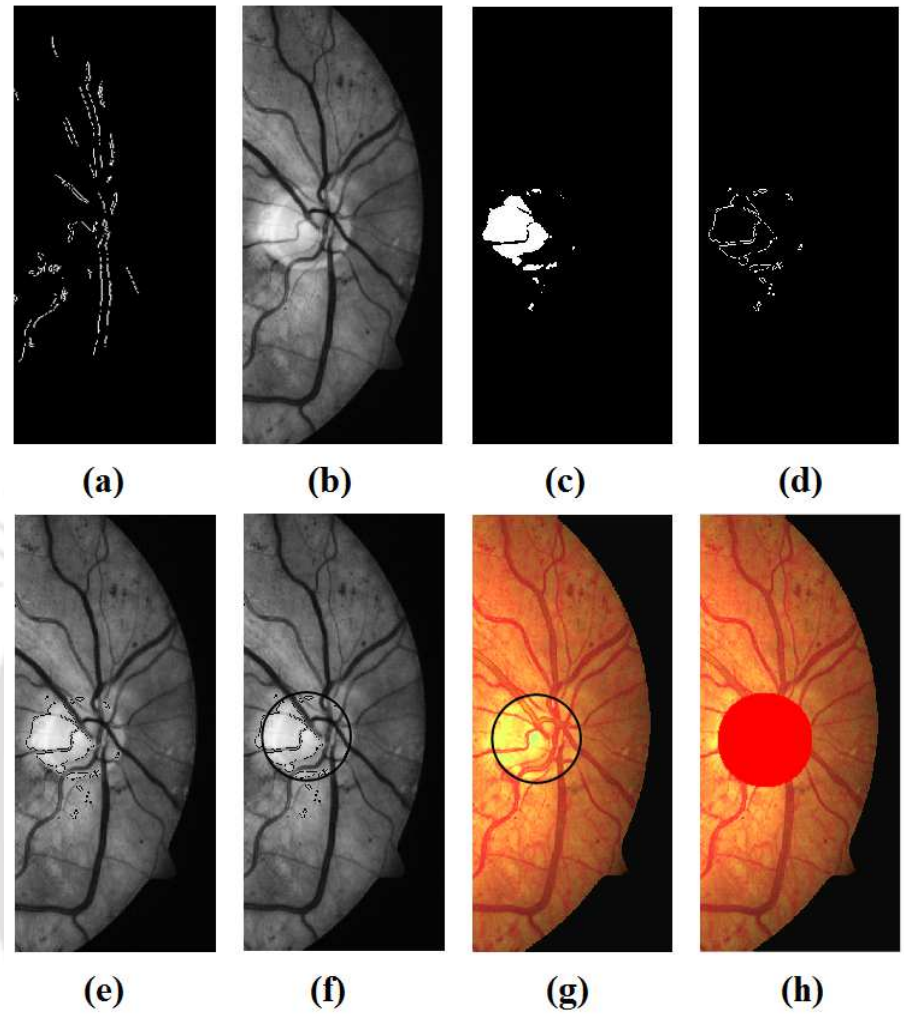

Figure 3.5: OD Segmentation: (a) ROI-1 for OD, obtained from cropped region having maximum vertical BV; (b) Corresponding ROI-1 in gray scale fundus; (c) Binary image after applying threshold; (d) Edges of *(c)*; (e) Overlapped OD edges on gray scale image; (f) Hough Transform applied on the OD edges; (g) Detected OD overlapped on colored fundus image; (h) OD masked.

circular feature of OD, Hough Transform is applied to the edges [85] according to equation (3.6).

$$(x-a)^2 + (y-b)^2 = r^2 \tag{3.6}$$

where, (a, b) is the centre of the circle of radius r that passes through (x, y). The circle is later overlapped with gray scale image as shown in Figure 3.5(f). The centre and diameter of the detected OD is measured and it is stored for future reference. The OD region co-ordinates are used and superimposed on the original color image [Figure 3.5(g)]. Lastly, the detected OD is masked so that it doesn't interfere during exudate detection as shown in Figure 3.5(h).

3.1.0.3 Bright lesion detection

The bright lesion detection is essential for DR or DM analysis. But it is performed here as a preprocessing step, and the image obtained after the process is used for fovea detection. Before detecting the exudates, the processed image is required to undergo further enhancement to ensure efficient detection. Therefore, the OD masked image obtained in the previous subsection is enhanced by adaptive histogram equalization. The Adaptive Histogram is applied on the intensity plane of HSI color model obtained after conversion from RGB to HSI, and the result obtained is converted back to RGB for further processing. Since OD is removed, the high-intensity yellowish color pixels left in the fundus image are the exudates. Thus, for the detection of exudates, color property has been used. The hue plane of *the HSI* color model contains the color attribute, and the saturation plane holds the information about how much the color is diluted with white color. Therefore, the image RGB_{mod} is converted to *HSI* plane. The yellowish color is represented by a range of 30 to 70 in Hue plane. The Hue plane is shown in Figure 3.6(a). The exudates are then segmented out from Hue plane image as shown in Figure 3.6 (a) by selecting the proper threshold given by the equation (3.7)

$$f_2(x,y) = \begin{cases} 1, & if \quad \tau_1 \leq f(x,y) \leq \tau_2 \\ 0, & otherwise \end{cases} \tag{3.7}$$

where, τ_1 and τ_2 represents the threshold range of exudate color (30 and 70). The resultant output image is shown in Figure 3.6(b). The detected exudates in the hue plane is logically ANDed with the saturation plane, whereas the intensity plane information is kept unaltered. The image is converted back to RGB, which appears as shown in Figure 3.6(c). The detected exudate pixels are marked by green color on the original image for labeling, as shown in Figure 3.6(d).

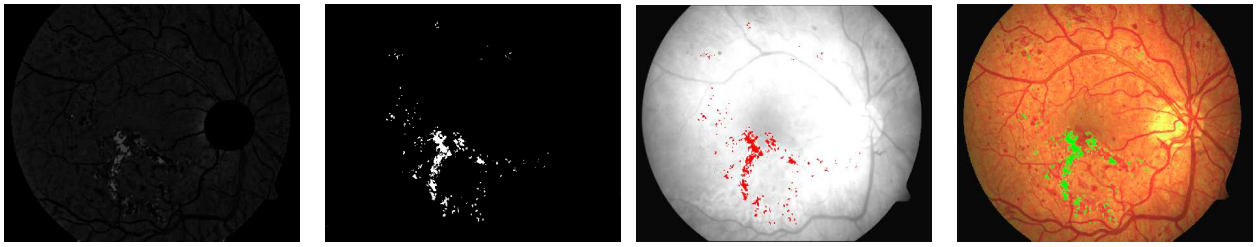

(a) (b) (c) (d)

Figure 3.6: Bright Lesion detection: (a) Hue plane image of OD masked fundus image, (b) Exudates detected applying threshold, (c) RGB image after exudate detection and (d) Exudates overlapped on original RGB image.

3.1.1 ROI identification

Detection of Macula and Fovea is the most critical part of the algorithm. The macula region has a low-intensity profile, and in many cases, it is very much similar to the background, which makes the segmentation difficult. Therefore, two sets of information have been used to detect the macula. The first one is the absence of BVs in the macular region, and the second is the location of the vertical ROI-1 obtained in the OD detection process.

The superior and the inferior arteries of fundus are positioned horizontally to macula. The macula is situated between these two arteries and is devoid of BV. Therefore, the BV detected image obtained in the earlier step [Figure 3.4(d)] is used for further processing. The horizontal canny edge detector is applied to this image for obtaining the horizontal edges of BVs, as shown in Figure 3.7(d). The next step is to identify the ROI containing macula (say ROI-2). For attaining this, horizontal stripes are taken out from the horizontal edge image. Depending on the location of the macula in the image databases, five overlapping horizontal strips are considered with one-third of the total image columns in size. An overlapping of half the window size is also taken into consideration. In order to find the accurate location of the macula, the overlapping is done. Every window is later scanned for minimum horizontal edge pixels present by counting the number of on pixels and is marked as ROI-2, as shown in Figure 3.8(a).

The consideration of minimum horizontal edges does not hold good if ROI-1 for OD detection is obtained in the central region. In such cases, the central horizontal ROI-2 window without overlapping is considered. It is divided into two equal halves vertically and searched for the minimum horizontal edges, and the resultant ROI obtained is updated as ROI-2. Once the ROI-2 has been detected, its co-ordinates are stored for further processing.

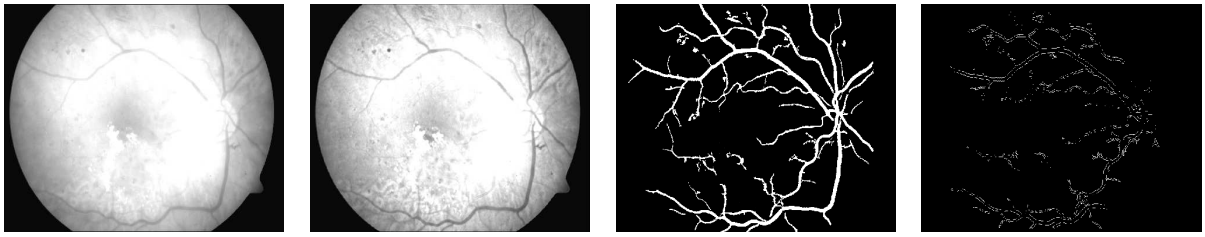

(a) (b) (c) (d)

Figure 3.7: Initial stages of macula detection: (a) *RED* plane image of *Figure 3.6 (c)*, (b) image *(a)* enhanced using top-hat (c) Detected BVs as in *Figure 3.4 (d)* and (d) Horizontal edges of image *(c)*.

3.1.2 Fovea localization from ROI

The searching of the macula and fovea is done on ROI-2 using the intensity property. The RGB image obtained after exudate detection, has more contrasting feature of macula in the red color plane, as can be seen from Figure 3.7(a), than that of the green or blue. Therefore, the red color plane is considered for the analysis. Further enhancement of the macular region is done by applying the black top-hat transformation on the red plane, and the result is shown in Figure 3.7(b). From this image, the region containing macula is selected using the co-ordinates of the ROI-2 window [Figure 3.8(b)]. The next stage includes locating the macula. The intensity of the ROI-2 image is inverted so that the macula becomes bright. The image is then binarized using equation (3.8).

$$f_3(x,y) = \begin{cases} 1, & if \quad f(x,y) \geq \xi_1 \\ 0, & if \quad f(x,y) \leq \xi_1 \end{cases} \tag{3.8}$$

where, ξ_1 represents the Otsu's threshold.

The binary image contains the macular region along with noisy pixels formed by BVs. The image is, therefore, scanned to locate intensity change, which resembles the macula region. The scanning is performed depending on the probable location of the macula. With the help of the ROI-1 location, the scanned region is identified. If the image is macula centered, the binary image is scanned towards right and left starting from the center of ROI-2. For the cases of macula situated on either side of the image, scanning is done starting from the right or left corner of the ROI-2 window. The starting positions, in this case, is determined by the ROI-2 window location. If ROI-2 is situated on the right side of the original image, the scanning will be done from left to right end and alternatively if the window is situated on the left.

After scanning, the largest cluster of white pixels situated close to each other can be considered as the macula region. The remaining regions are made zero [Figure 3.8(c)]. The obtained region is marked as the macula. Edges of the binary image are determined using the Canny method [Figure 3.8(d)]. To detect the circular geometry of the macula Hough Transform is applied to the edges [Figure 3.8(e)]. The detected macula area is overlapped on color ROI-2, as shown in Figure 3.8(f). The same is marked on the original color image [Figure 3.9(a)]. The Fovea is later obtained by calculating the center of the macular circle, as shown in Figure 3.9(b).

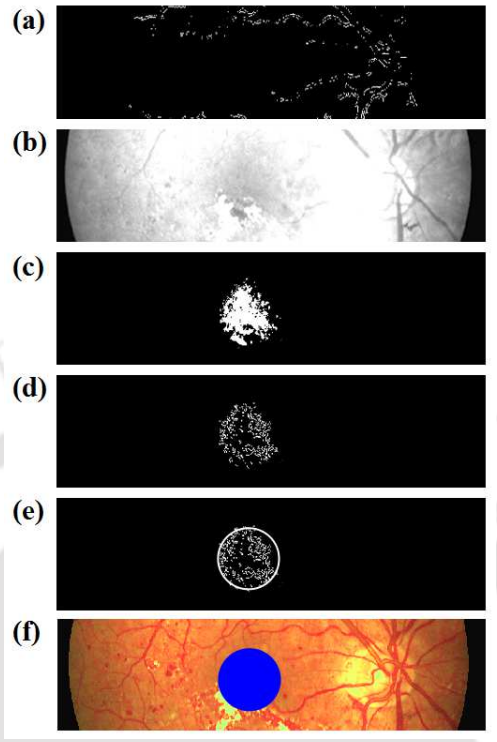

Figure 3.8: Macula detection steps on *RED* channel of RGB color plane: (a) Identified ROI-2 containing macula, (b) Corresponding *RED* plane image, (c) Macula detected using threshold, (d) Edges of detected macula, (e) Circular outline obtained using Hough Transform, (f) Detected macula overlapped in RGB image.

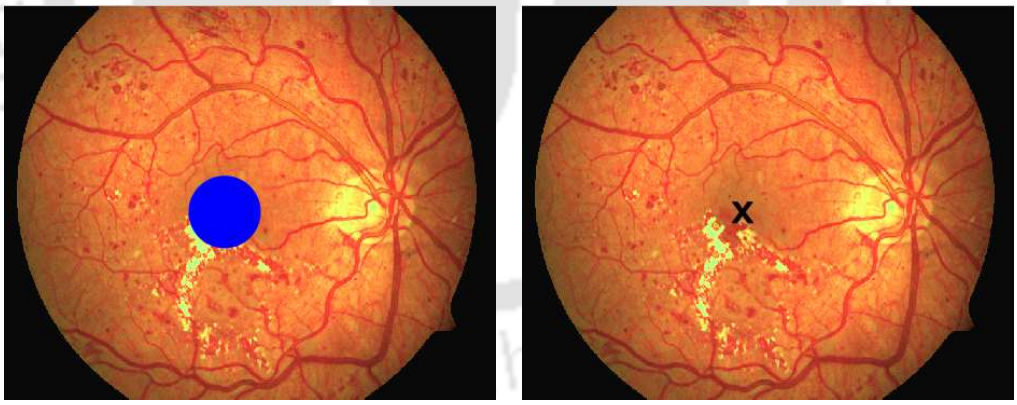

(a) (b)

Figure 3.9: Detection overlapped on original RGB image: (a) Macula detected and (b) Fovea detected.

3.1.3 Results and Discussion

For evaluating the proposed algorithm, we used four publicly available fundus image database. The DRIVE (Digital Retinal Images for Vessel Extraction) [229], DIARETDB1 (Standard Diabetic Retinopathy Database Calibration level 1) [231], MESSIDOR (Methods to evaluate segmentation and

indexing techniques in the field of retinal ophthalmology) [232] and HRF (High-Resolution Fundus Image) [233]. The image set formed consists of a total of 1374 images. As the databases have varying resolutions, all the images were resized to 768×576 for making the evaluation uniform. For verification of the algorithm, manual annotation of the images is done by two experts. These annotations are used as ground truth images.

The fovea detection is efficient when the images are well illuminated. But a few of the images in the databases have illumination problems. In one such case, the macula gets suppressed by dark illumination and submerged with the background. Another case includes improper focusing of the fundus image leading to blurred image. Therefore, the images were first checked so that these cases can be identified. It is achieved by following the method of Tariq et al. [63]. The outputs after processing such cases were shown in Figure 3.10. Thus, the images which do not have visible fovea are excluded from the verification process. It has been found that such cases are present in three databases, image 23 of DRIVE database, image number 27, and 42 from DIARETDB1 and a total of 10 images from the MESSIDOR database.

(a) (b) (c) (d)

Figure 3.10: Identification of images with improper illumination: (a) Image from DIARETDB1, effected by dark illumination, (b) Corresponding output, (c) Image from MESSIDOR, effected by improper focusing, (d) Corresponding output.

The proposed algorithm for fovea detection has been applied to 1361 images. The validation of the detection process is done by estimating the difference between automatic and manual detection. For manual identification, the specialists have marked the location of the fovea in all the images. These locations are used as gold standards. The evaluation of fovea detection is done based on the Euclidean Distance measure of the detected fovea centers from the position of gold centers using equation (3.9),

$$|D| = \sqrt{(x_1 - x_2)^2 + (y_1 - y_2)^2}$$
$$\angle D = \tan^{-1}\left[\frac{y_1 - y_2}{x_1 - x_2}\right] \tag{3.9}$$

where, (x_1, y_1) and (x_2, y_2) represents location of gold standard and automatically detected fovea respectively.

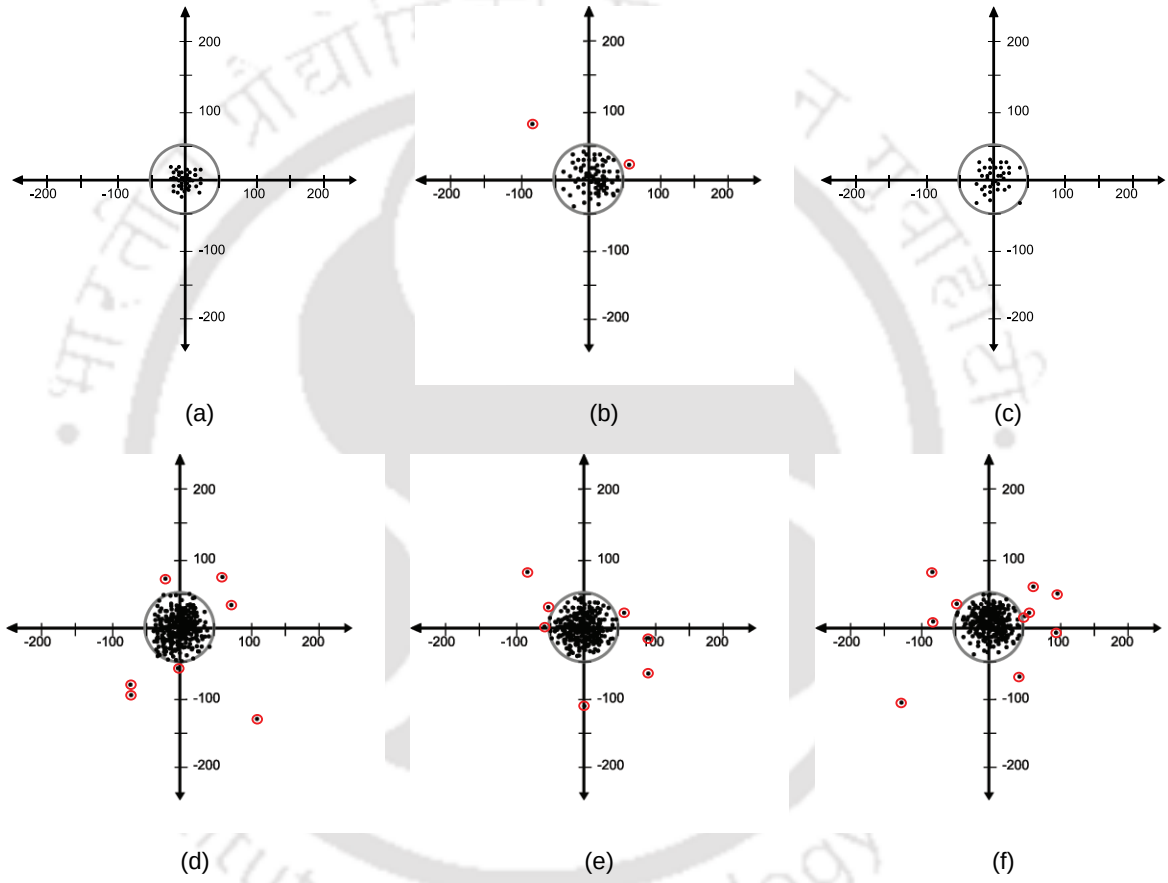

Figure 3.11: Euclidean distance between detected fovea and ground truth for databases, (a) HRF, (b) DIARETDB1, (c) DRIVE, (d) MESSIDOR set1, (e) MESSIDOR set2 and (f) MESSIDOR set3 database.

If the automatically located fovea is lying at a distance of less than 50 pixels from ground truth, then it is considered as correct detection. A similar evaluation method was adopted by Niemeijer et al. [126] and Welfer et al. [122]. For proper validation, the Euclidean distance between the detected fovea and the gold standard along with the angle between them is plotted across X, Y plane, as shown in Figure 3.11. The gold standard is considered to be located at the origin of the plot. Then any point (x,y) represents the Euclidean distance of the detected fovea with proper direction with respect to the gold standard. The bigger circle in the plot represents the evaluation boundary. That is, if the Euclidean distance is within the radius (50 pixels) of the circle, the detection is considered to

be affirmative. The points lying outside the circle were the failed cases (shown within small circles). The distance measure plots are shown for different databases in Figure 3.11(a)-(f). As seen from the results, the algorithm locates fovea with 100% efficiency in HRF (45 out of 45 images) and DRIVE (39 out of 39 images) database, 97.70% (85 out of 87 images) in DIARETDB1 database and 97.98% (1166 out of 1190 images) from MESSIDOR database. The system gives an average detection rate of 98.09%. Few of the failed cases are shown in Figure 3.12. In the images, the '+' symbol represents the actual location of the fovea, and symbol 'X' shows misclassified fovea. In most of the failure cases, the presence of pathogens of similar intensity in the neighborhood of fovea was the cause of misclassification.

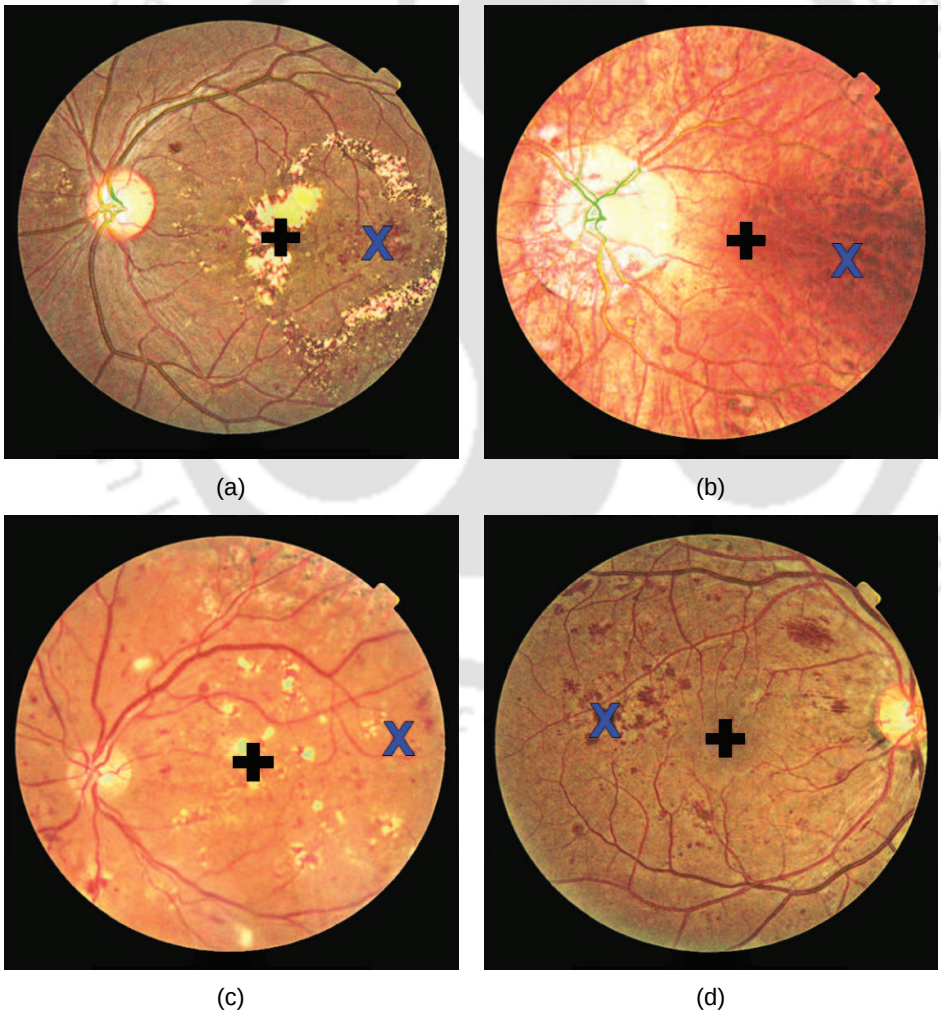

Figure 3.12: Wrong identification of fovea in various databases. The '+' symbol represents actual location of fovea and 'X' is the detected fovea.

The method has been compared with the existing methods of fovea detection in the literature.

Table 3.1: Comparison of fovea detection method applied to 37 images of DRIVE and 89 images of DIARETDB1 database

Methods used	DRIVE database (37 images)				DIARETDB1 database (89 images)			
	Images detected	Percentage detection	Avg. distance from Gold Standard	Average Standard Deviation	Images detected	Percentage detection	Avg. distance from Gold Standard	Average Standard Deviation
Sinthanayothin et al. [238]	29	78.38	62.23	116.45	58	65.17	62.68	84.16
Narasimha-Iyer et al. [25]	31	83.78	29.23	53.88	72	80.90	32.52	56.24
Singh et al. [125]	32	86.49	14.43	14.36	58	65.17	37.93	47.55
Sagar et al. [96]	35	94.59	12.61	14.92	75	84.27	24.79	49.81
Sopharak et al. [121]	19	51.35	122.06	142.87	34	38.20	81.08	90.05
Sekhar et al. [85]	34	91.89	10.45	12.13	60	67.42	30.81	30.22
Welfer et al. [122]	37	100.00	7.39	**5.54**	82	92.13	10.12	14.99
Proposed Method	37	**100.00**	**6.88**	5.85	85	**95.51**	**8.90**	**12.89**

Welfer et al. [122], in their work, have performed a comparison of various fovea detection techniques considering the Euclidean Distance measurement analysis. Their evaluation criteria have been considered for testing the proposed algorithm. The manual annotations done in Welfer et al. [122] are considered to be close enough with our method, and we have resized the images to 640×480 for proper comparison. 37 images of DRIVE and all 89 images of DIARETDB1 databases are considered for the evaluation of the algorithm. The success rate, the average distance from ground truth, and average standard deviation are determined and shown in Table 3.1. The smaller average value of Euclidean Distance signifies better fovea detection. As observed in Table 3.1, the results of the proposed method is better as compared to other algorithms.

The algorithm is advantageous as fovea detection is independent of OD localization. Although efficient with good performance and robust outcome the method fails in a few cases, such as,

- When abnormalities precipitate over the macula, the ROI may not be useful to localize fovea.
- Few cases with non-availability of adequate BV information, the ROI may not be properly detected. Thus will lead to wrong fovea detection.
- The presence of dark abnormalities in macular neighborhood may cause incorrect localization of fovea.

Therefore, to improvise over these limitations, we have proposed an updated fovea detection algorithm based on the generation of an ellipse template from the BV structures. The ellipse template is subjected to template matching for fovea localization. The following section will enlighten the details.

3.2 Proposed Fovea Detection Using Ellipse Fitting

The primary motivation of the proposed method is to take up the challenges related to automatic fovea detection and introduce a robust method to localize fovea. Both OD and BV relations are to be considered for this purpose.

The approach is initiated by obtaining the retinal image field of view (FOV). Then the BV arc is segmented, and the OD center and diameter are obtained. From the segmented BV arc, obtained from various images of the database, an ellipse template is created by taking the average of superimposed, detected BV arc. Later, the fovea is marked in the template at the average of actual fovea positions of the database used. Once finalized, the template is fitted to the OD center for localizing fovea. The steps constituted in the algorithm are discussed in the following subsections, and Figure 3.13 shows the block diagram.

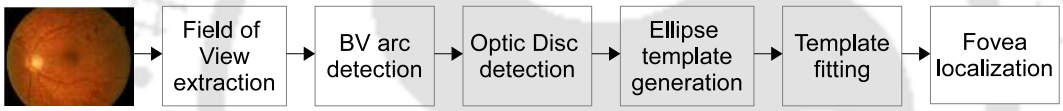

Figure 3.13: Block diagram of Proposed Fovea Detection Using Ellipse Fitting.

3.2.1 Extraction of Field of View

The region beyond FOV of the retinal image may contain intensity imbalance, and it affects the identification process [8]. Therefore the region is formed purely dark to enhance the accuracy of detection. Along with this, another difficulty encountered during segmentation is the presence of bright intensity annular region around the retinal FOV. Therefore, these regions must be nullified, retaining only the required FOV for further processing [8, 139]. It is accomplished by taking the green channel of input color image and performing intensity level slicing to remove regions of low-intensity values, followed by a morphological image filling operation. Say the output is $\boldsymbol{FOV}_{original}$. The original RGB image components corresponding to the $\boldsymbol{FOV}_{original}$ are preserved, and the region outside FOV is made purely dark by assigning zero values to the pixels. From $\boldsymbol{FOV}_{original}$ the diameter of the ***FOV*** is calculated. The next irregularity as mentioned is the bright intensity observed in the edge of the FOV [239]. It is caused due to the improper adjustment of the fundus camera flash. To eliminate these the boarder of FOV containing these bright regions are to be exempted. The algorithm 1 explains the procedure for these FP exemptions. The results obtained are shown in Figure 3.14. It represents stepwise elimination of the bright boundary from FOV.

Algorithm 1: *Bright Boundary elimination*

function BBE;
Input : FOV(L) or Image L
Output: Updated **FOV**(L)
Calculate: Dilation $\partial^{(B)}$ and Erosion $\varepsilon^{(B)}$ of Image L using disc structuring element (SE) (B),
Calculate: $T_1 = \frac{1}{2}\max\left(\textbf{FOV}_{red-plane}\right)$
Detect **FOV** border (X_b) using the expression below;

$$X_b = \partial^{(B)}(L) - \varepsilon^{(B)}(L)$$

Calculate: $T_2 = \frac{1}{10}\text{area}\left(X_b\right)$
if $\begin{bmatrix} \max\left(X_{b_{red-plane}}\right) > T_1 \ \& \\ \text{area}\left(\max\left(X_{b_{red-plane}}\right)\right) > T_2 \end{bmatrix}$ **then**
    update **FOV** : $[\textbf{FOV}(L) = \textbf{FOV}(L) - X_b]$;
    goto **Step 2**
else
    break;
end

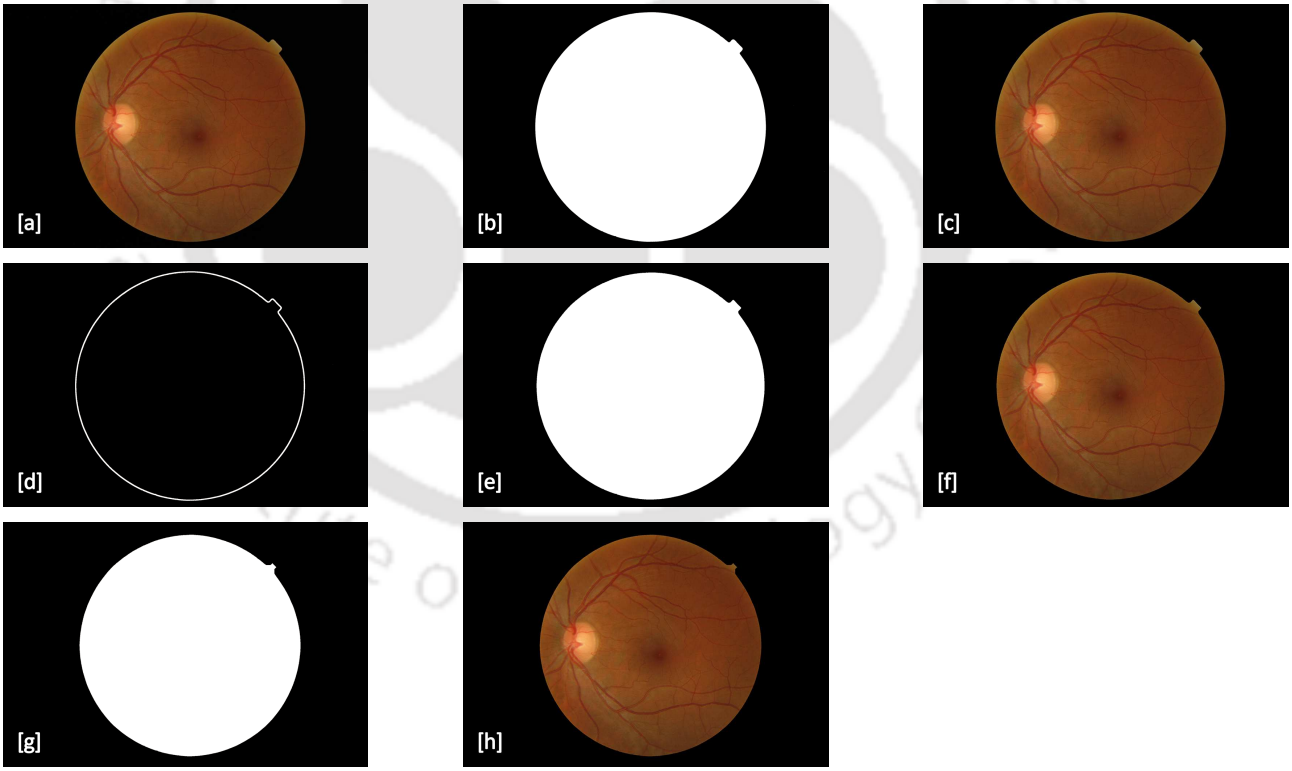

Figure 3.14: Steps showing elimination of bright boundary and obtaining field of view (FOV) image: [a] Original image, [b] image L or $FOV_{original}$, [c] RGB $FOV_{original}$, [d] $FOV_{original}$ boundary for bright noise verification, [e] updated FOV eliminating noisy boundary, [f] corresponding RGB FOV, steps continued.... [g] Final FOV, [h] RGB corresponding to final FOV.

3.2.2 BV Arc detection

To localize BV Arc, the BV network is to be segmented out. For BV detection, we used our previous method, as discussed in Section 3.1.0.2. The result obtained contains the BV network of the corresponding fundus. To isolate the BV arc, morphological area opening is used. It eliminates the small components of BV, which are not part of the BV arc. To visualize the output obtained, we consider four different images of right and left eyes from the DIARETDB1 database. The detected BV arc are shown in Figure 3.15. Here image (a, b) are left eye, and (c, d) are right eye fundus image, and images (e, f, g, h) represents the corresponding BV arc, respectively.

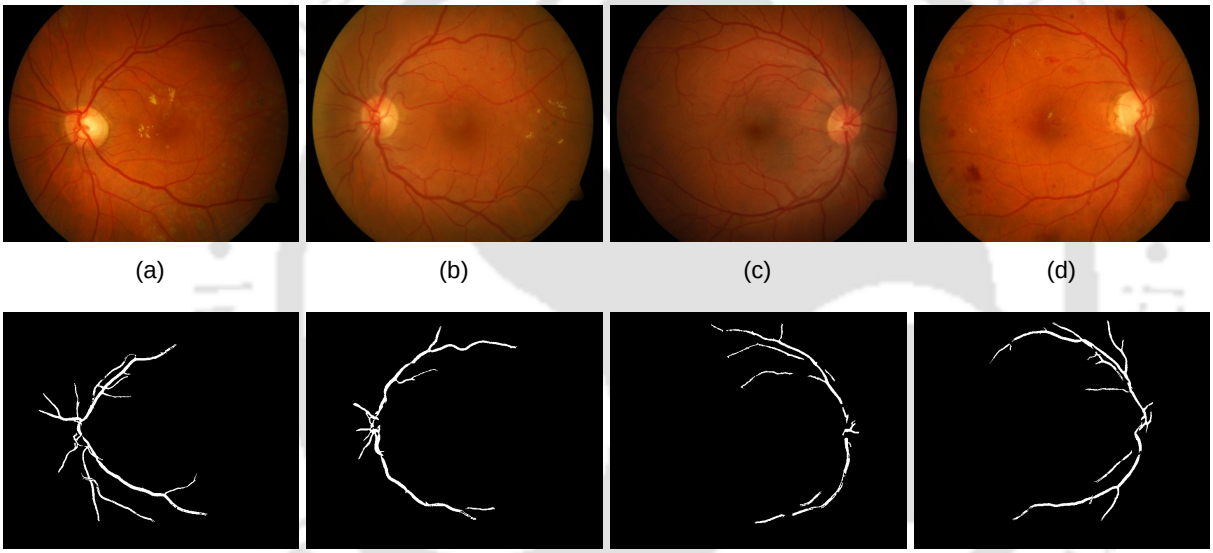

Figure 3.15: BV arc detection: (a)-(d) Original image, (e)-(h) Corresponding detected BV arcs.

3.2.3 OD Centre detection

As discussed in Section 3.1.0.2 the OD is detected and its centre is located. Figure 3.16 shows the fundus image and corresponding detected OD centre position in the second image.

3.2.4 Formation of Ellipse template

In this experiment, we have chosen 20 detected BV arcs from every databases, which includes 10 left and 10 right eye images. Later we positioned these images at the OD center, considering both left and right OD center lying on a straight line and obtain the average ellipse template from the 20 superimposed BV arcs. The image shown in Figure 3.17, represents left eye BV arcs in red color

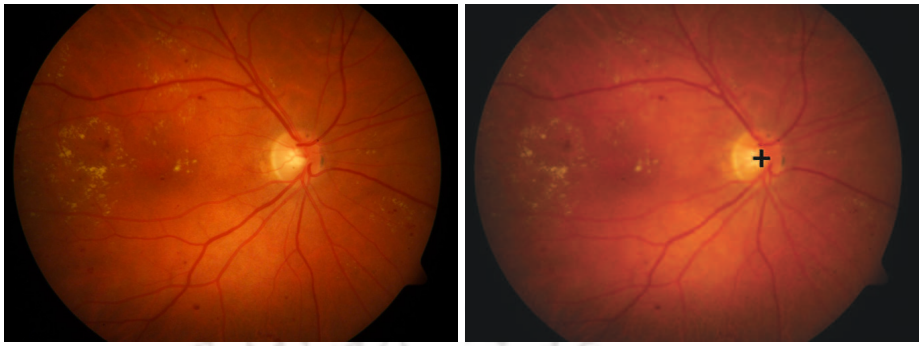

(a) (b)

Figure 3.16: (a) Original image, (b) Marked OD centre in original image.

and right eye BV arcs in blue. The resultant average template is marked in white. The process is repeated for every database evaluated.

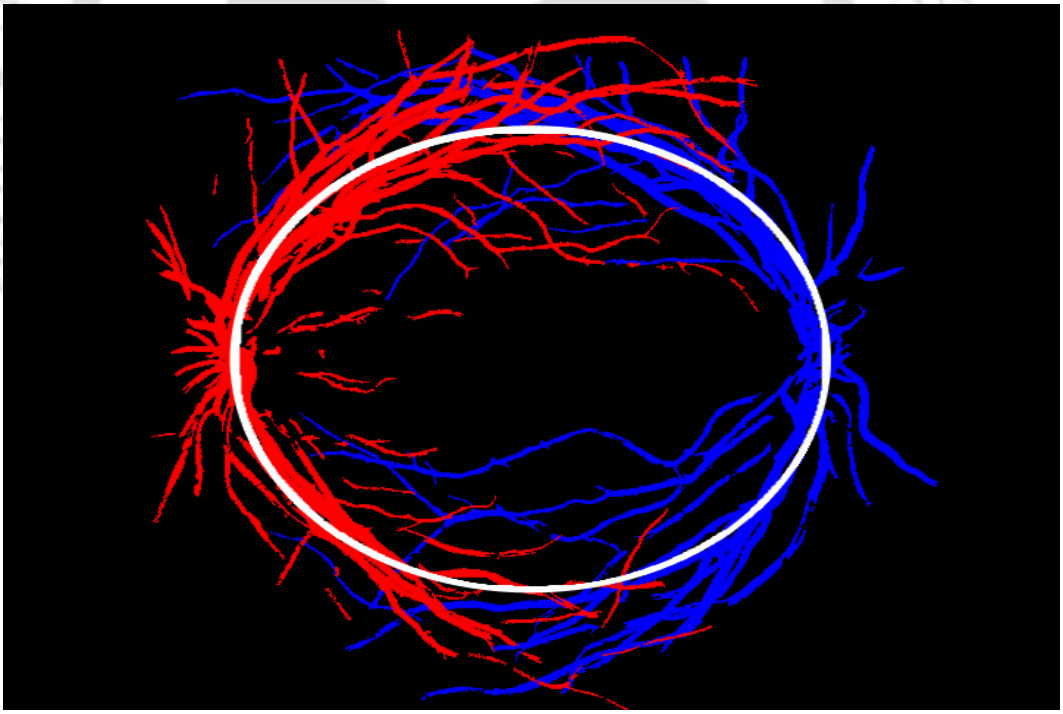

Figure 3.17: Ellipse template, marked in white.

Once the ellipse template is obtained, we manually mark the approximate fovea location. The fovea positions for 70% images of each database are marked manually on the ellipse templates, and the co-ordinates obtained from their average location value is considered as the final fovea position. The remaining 30% image are evaluated as test images. Once the fovea position is marked, we have calculated the angle formed from the detected OD center and fovea according to the equation.

$$\theta = arctan((D_y - V_y)/(D_x - V_x))$$

where (V_x,V_y) and (D_x,D_y) are the coordinates of the manually marked fovea and OD center, respectively. The resultant template is shown in Figure 3.18. Once all the templates of the databases

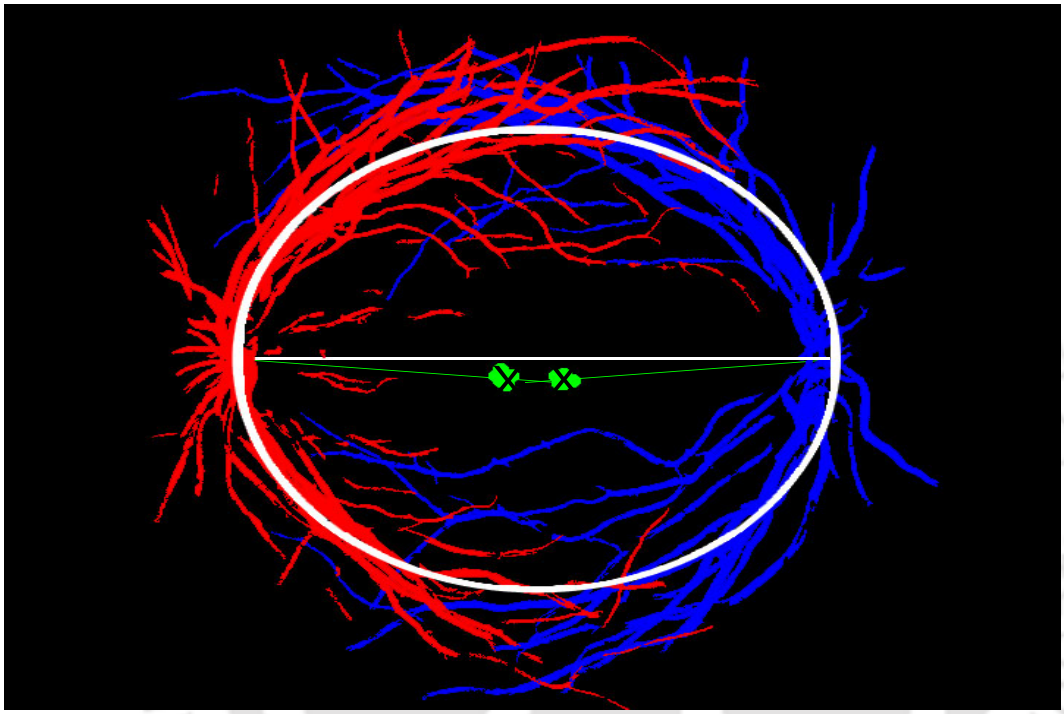

Figure 3.18: Manually marked ellipse fovea template.

are prepared, we need to calculate various parameters associated with the ellipse. Therefore, the template images of various databases are resized to 450 row size, maintaining the column size in constraint proportion to keep the aspect ratio balanced. As shown in the Figure 3.19 an ellipse is a closed type conic section defined using two fixed points F_1 and F_2, each called focus and a distance say $2a$ such that for any point P on the ellipse, $|PF_1| + |PF_2| = 2a$ is always valid [240]. Here, major and minor axis represents the longest and the shortest perpendicular distances. The convergence of these axes is called ellipse center. The endpoints of the major axis are called vertex, and the minor axis is co-vertex. As per these definitions, we need to calculate major axis, minor axis, retinal diameter, ODD, Angle subtended between OD center and fovea and finally fovea distance from OD from every template obtained. To determine the parameter length, we have used a scale software and determined the lengths in centimeter (cm)s. The calculated parameters are tabulated in Table 3.2.

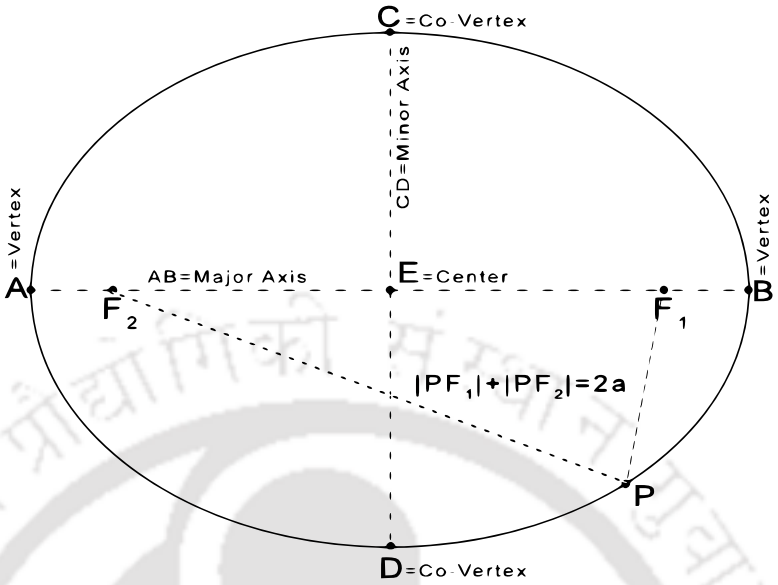

Figure 3.19: Ellipse parameters.

Table 3.2: Parameter calculated from various ellipse template of different databases

Parameter\Database	DRIVE	MESSIDOR	DIARETDB1	HRF	GEI	NETRALAYA
Major Axis (cm)	13.5	10.8	14.4	15.6	14.2	14
Minor Axis (cm)	12.2	10.2	13.2	13.8	13.5	13.2
Retinal Diameter (cm)	18.4	18.8	24	28.3	22.1	26
OD Diameter (cm)	2.4	2.8	2.8	3.2	2.2	2.5
Angle (degree)	5	5.3	5	5.3	5	5.3
Fovea Center Dist (ODD)	2	2.5	2	2.5	2	2.5

The parameters calculated from the ellipse of different database represents that, the value of the parameters vary with respect to the ODD. Therefore in-order to generalize the ellipse template from the set of six templates, we restructure the ellipse equation with respect to ODD as a variable under consideration. To realize this we perform a mathematical model analysis.

Mathematical Model for generalizing Ellipse Template

The standard equation of ellipse is given by,

$$\frac{X^2}{a^2} + \frac{Y^2}{b^2} = 1 \tag{3.10}$$

where, a =major axis and b =minor axis. Let us consider x and y are new variables associated with major and minor axis related to ODD is given by,

$$x = {}^{ODD}/_{\text{Majoraxis}} \tag{3.11}$$

$$y = {}^{ODD}/_{\text{Minoraxis}} \tag{3.12}$$

Referring to the values from Table 3.2 for major and minor axis of various databases, we substitute them in equation 3.11 and 3.12. Thus, the corresponding x and y values are computed. The mean and standard deviation from the various database x and y values are also computed and presented in Table 3.3. From the values thus obtained the next step is to create confidence interval (CI) [241–243].

Table 3.3: Calculated values of x and y in different database

Database	x	y	Mean		Standard Deviation	
			$\bar{x}$	$\bar{y}$	σ_x^2	σ_y^2
DRIVE	0.177	0.197	0.195	0.211	0.036	0.037
MESSIDOR	0.259	0.274				
DIARETDB1	0.194	0.212				
HRF	0.205	0.231				
GEI	0.154	0.162				
NETRALAYA	0.178	0.189				

As the number of samples are less than 30, the confidence interval of 95% confidence level of the mean, is given by,

$$CI_x = \overline{x} \pm t_{\frac{\alpha}{2},n-1}\frac{\sigma_x^2}{\sqrt{n}} \tag{3.13}$$

$$CI_y = \overline{y} \pm t_{\frac{\alpha}{2},n-1}\frac{\sigma_y^2}{\sqrt{n}} \tag{3.14}$$

The significance level and the degree of freedom are to be determined next with the help of the t-distribution table, as shown in Table 3.4 and the z and t distribution as shown in Figure 3.20.

Since, we are finding out 95% confidence level, $CL = 95\% = 0.95$. Therefore, Significance level ($\alpha = 1 - CL = 0.05$) and ($\frac{\alpha}{2} = \frac{0.05}{2} = 0.025$). Hence, Degree of freedom ($df = n - 1 = 6 - 1 = 5$).

Now from the t-distribution table, $t_{0.025,5} = 2.571$.

Therefore, substituting the values in equation 3.13; we get;

$$CI_x = 0.195 \pm 2.571 \times \frac{0.036}{\sqrt{6}} = 0.195 \pm 0.0378 = \begin{bmatrix} 0.156, & 0.232 \end{bmatrix}$$

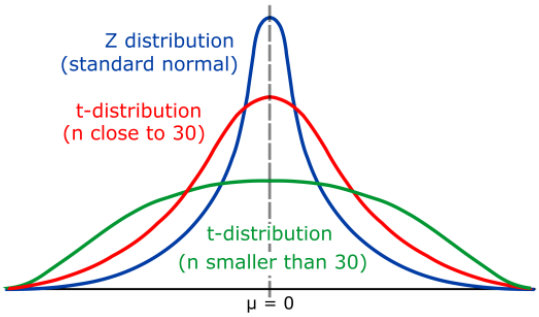

Figure 3.20: *z*-distribution and *t*-distribution.

Table 3.4: t-distribution table

Degrees of Freedom	Significance level 20% (0.20)	10% (0.10)	5% (0.05)	2% (0.02)	1% (0.01)	0.1% (0.001)
1	3.078	6.314	12.706	31.821	63.657	636.619
2	1.886	2.92	4.303	6.965	9.925	31.598
3	1.638	2.353	3.182	4.541	5.841	12.941
4	1.533	2.132	2.776	3.747	4.604	8.61
5	1.476	2.015	2.571	3.365	4.032	6.859
6	1.44	1.943	2.447	3.143	3.707	5.59
7	1.415	1.895	2.365	2.998	3.499	5.405
8	1.397	1.86	2.306	2.896	3.355	5.041

Now, we may say that the value 0.1945 lies 95% in the range $\left[\ 0.156,\quad 0.232\ \right]$

Similarly, substituting the values in equation 3.12 we get;

$$CI_y = 0.211 \pm 2.571 \times \frac{0.037}{\sqrt{6}} = 0.211 \pm 0.0388 = \left[\ 0.173,\quad 0.249\ \right]$$

Thus, the value 0.211 lies 95% in the range $\left[\ 0.173,\quad 0.249\ \right]$

From the above range, let us take the extreme most value, the mid-value, and find out the values of the axes of different databases in both the cases.

case-I: taking the extreme most value of both the ranges.

From equation 3.13 and equation 3.14 we have,

$$0.156 = \frac{ODD}{\text{Majoraxis}} \tag{3.15}$$

$$0.173 = \frac{ODD}{\text{Minoraxis}} \tag{3.16}$$

Now, as per the equation 3.15 and 3.16, we may generate different values major and minor axis with

respect to ODD for various databases. The values calculated are tabulated in Table 3.5

Table 3.5: Calculated values of Case I: major and minor axis in cms for different database

Database	ODD	Major axis	Minor axis
DRIVE	2.4	15.3	13.8
MESSIDOR	2.8	17.9	16.2
DIARETDB1	2.8	17.9	16.2
HRF	3.2	20.5	18.4
GEI	2.2	14.1	12.7
NETRALAYA	2.5	16.0	14.5

case-II: taking the mid-value of both the ranges.

From equation 3.13 and equation 3.14 we have,

$$0.195 = \frac{ODD}{\text{Majoraxis}} \tag{3.17}$$

$$0.211 = \frac{ODD}{\text{Minoraxis}} \tag{3.18}$$

Now, with the help of equation 3.17 and 3.18 we calculate different values major and minor axis with respect to ODD for various databases. The values calculated are tabulated in Table 3.6

Table 3.6: Calculated values of Case II: major and minor axis in cms for different database

Database	ODD	Major axis	Minor axis
DRIVE	2.4	12.3	11.4
MESSIDOR	2.8	14.3	13.2
DIARETDB1	2.8	14.3	13.2
HRF	3.2	16.4	15.2
GEI	2.2	11.3	10.4
NETRALAYA	2.5	12.8	11.8

Thus, from the two cases, we can clearly say that the values obtained by using the mid-value of the CI is more close to the original data. The error obtained in Case-I is more than Case-II. Thus, Case-II accuracy is more. Therefore, we can use the value of the mid-value CI to find the values of the axes. Therefore,

$\text{Majoraxis} = \frac{ODD}{0.194}$ and $\text{Minoraxis} = \frac{ODD}{0.211}$

Table 3.7: Calculated values of z for the databases

Database	ODD	m	$z = m/ODD$	$\overline{z}$	σ_z^2
DRIVE	2.4	2ODD=4.80	2	2.25	0.0625
MESSIDOR	2.8	2.5ODD=7.00	2.5		
DIARETDB1	2.8	2ODD=5.60	2		
HRF	3.2	2.5ODD=8.00	2.5		
GEI	2.2	2ODD=4.40	2		
NETRALAYA	2.5	2.5ODD=6.25	2.5		

Therefore the generalized equation of the ellipse for fovea template can be written as,

$$\frac{X^2}{\left(\frac{ODD}{0.194}\right)^2} + \frac{Y^2}{\left(\frac{ODD}{0.211}\right)^2} = 1 \tag{3.19}$$

The next requirement is to obtain the relation of fovea center and OD. Therefore, let us consider, Fovea distance (m) be given by

$$m = z \times ODD \tag{3.20}$$

therefore,

$$z = m/ODD \tag{3.21}$$

Referring to the values from Table 3.2 and substituting equation 3.21, we compute the value of z and also determine the mean and standard deviation. The values found are tabulated in Table 3.7

Therefore, CI_z at confidence interval of 95% with $t_{0.025,5} = 2.571$ is given by, $CI_z = 2.25 \pm 2.571 \times \frac{0.0625}{\sqrt{6}} = 2.25 \pm 0.068 = \left[\begin{array}{cc} 2.182, & 2.318 \end{array}\right]$ Now, we may say that the value 2.25 lies 95% in the range $\left[\begin{array}{cc} 2.182, & 2.318 \end{array}\right]$

From the above range, let us take the extreme most value, the mid-value, and find out the values of the axes of different databases in all the cases.

case-I: taking the extreme low value using equation 3.21

$$2.182 = \frac{m}{ODD} \tag{3.22}$$

case-II: taking the mid value of both the ranges, using equation 3.21

$$2.25 = \frac{m}{ODD} \tag{3.23}$$

case-III: taking the extreme high value, using equation 3.21

$$2.318 = \frac{m}{ODD} \tag{3.24}$$

Now with the help of equation 3.22, 3.23 and 3.24 we determine the new values m say m_1, m_2 and m_3 and calculate corresponding errors generated for the different database tabulated in Table 3.8.

Table 3.8: Calculated values of m_1, m_2, m_3 and corresponding errors

Database	ODD	m	m_1	m_2	m_3	e_1	e_2	e_3
DRIVE	2.4	4.8	5.2	5.4	5.6	**0.4**	0.6	0.8
MESSIDOR	2.8	7	6.1	6.3	6.5	0.9	0.7	**0.5**
DIARETDB1	2.8	5.6	6.1	6.3	6.5	**0.5**	0.7	0.9
HRF	3.2	8	7.0	7.2	7.4	1.0	0.8	**0.6**
GEI	2.2	4.4	4.8	5.0	5.1	**0.4**	0.6	0.7
NETRALAYA	2.5	6.25	5.5	5.6	5.8	0.8	0.6	**0.5**

Referring the Table 3.8, the minimum error is highlighted for the corresponding value of m. Therefore, to fix a value for m, we may choose the mid-value from **case-II**, which corresponds to an average value of the total error. Therefore, we have the fovea distance at a location of $2.25ODD$ from the OD center, that is, $m = 2.25ODD$.

Similarly, we may determine the angle subtended between the OD center and fovea concerning major axis be, $\theta = 5.15$. The resultant ellipse template formed is shown in Figure 3.21.

Therefore, with the known value of ODD for any fundus image, we may generate the ellipse template using equation 3.19 and obtain the probable fovea location at a distance of $m = 2.25ODD$ with an angle $\theta = 5.15$. Now, the next task of the algorithm is to fit this template to locate fovea.

3.2.5 Template fitting

Once the template is created, the vertex is fitted at the OD center to detect fovea using Direct Least Square method [244]. This method is based on conic fitting, considering solution to be generated for an ellipse instead of general conic. An ellipse is a specific case of a conic. An implicit second-order polynomial can represent the conic representation of ellipse.

$$F(a, b) = pa^2 + qab + rb^2 + sa + tb + u = 0 \tag{3.25}$$

with an ellipse constraint

$$q^2 - 4pr < 0 \tag{3.26}$$

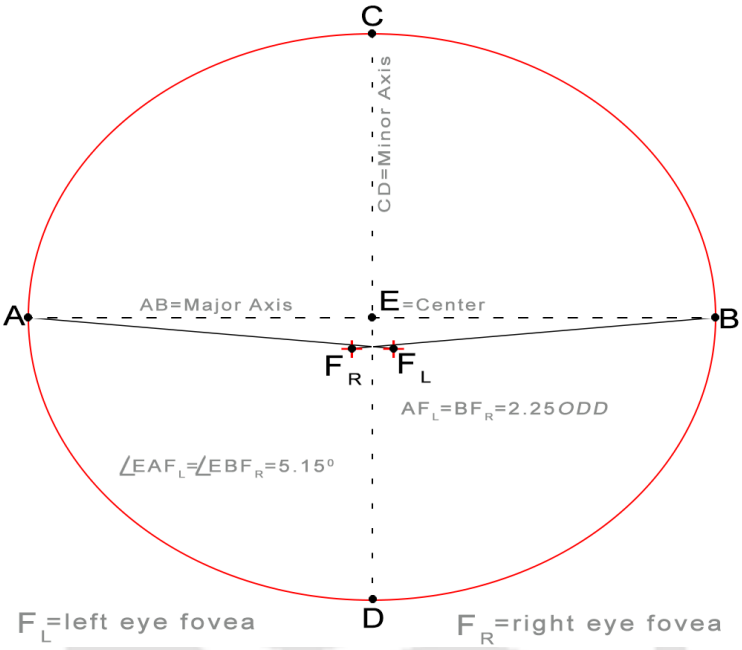

Figure 3.21: Formulated generalized ellipse template.

where p,q,r,s,t,u are ellipse coefficients and (a,b) lying point's coordinates. The F(a,b) is distance of the point (a,b) to the given conic. If we introduced two vectors such that

$$\begin{aligned} j &= [p, q, r, s, t, u]^T \\ k &= [a^2, ab, b^2, a, b, 1] \end{aligned} \tag{3.27}$$

vector representation of these defines as

$$F_j(k) = j.k = 0 \tag{3.28}$$

The fitting of a conic form to points $(a_i, b_i), i = 1....N$ is obtained by minimizing the sum of squared algebraic distances of the points to the conic which is represented by coefficients j

$$\min_j \sum_{i=1}^{N} F(a_i, b_i)^2 = \min_j \sum_{i=1}^{N} (F_j(k_i))^2 = \min_j \sum_{i=1}^{N} (k_i.j)^2 \tag{3.29}$$

For proper ellipse the inequality constraint Eq. 3.26 is updated into an equality constraint,

$$q^2 - 4pr = 0 \tag{3.30}$$

Now ellipse fitting equations modified to

$$\min_{j} \; ||D||^2 \quad subject \quad to \quad j^T C j = 1 \tag{3.31}$$

where D is the design matrix of order $N \times 6$

$$\begin{bmatrix} a_1^2 & a_1 b_1 & b_1^2 & a_1 & b_1 & 1 \\ a_2^2 & a_2 b_2 & b_2^2 & a_2 & b_2 & 1 \\ \vdots & \vdots & \vdots & \vdots & \vdots & \vdots \\ a_N^2 & a_N b_N & b_N^2 & a_N & b_N & 1 \end{bmatrix} \tag{3.32}$$

C is a constraint matrix of size 6×6

$$\begin{bmatrix} 0 & 0 & 2 & 0 & 0 & 0 \\ 0 & -1 & 0 & 0 & 0 & 0 \\ 2 & 0 & 0 & 0 & 0 & 0 \\ 0 & 0 & 0 & 0 & 0 & 0 \\ 0 & 0 & 0 & 0 & 0 & 0 \\ 0 & 0 & 0 & 0 & 0 & 0 \end{bmatrix} \tag{3.33}$$

Now applying the Lagrange multipliers to realize following for the optimum solution j.

$$\begin{aligned} Sj &= \lambda C j \\ j^T C j &= 1 \end{aligned} \tag{3.34}$$

S is the scatter matrix of size 6×6.

$$S = D^T D = \begin{bmatrix} S_{a^4} & S_{a^3 b} & S_{a^2 b^2} & S_{a^3} & S_{a^2 b} & S_{a^2} \\ S_{a^3 b} & S_{a^2 b^2} & S_{a b^3} & S_{a^2 b} & S_{a b^2} & S_{ab} \\ S_{a^2 b^2} & S_{a b^3} & S_{b^4} & S_{a b^2} & S_{b^3} & S_{b^2} \\ S_{a^3} & S_{a^2 b} & S_{a b^2} & S_{a^2} & S_{ab} & S_a \\ S_{a^2 b} & S_{a b^2} & S_{b^3} & S_{ab} & S_{b^2} & S_b \\ S_{a^2} & S_{ab} & S_{b^2} & S_a & S_b & S_1 \end{bmatrix} \tag{3.35}$$

in which the operator S is

$$S_{a^p b^q} = \sum_{i=1}^{N} a_i^p b_i^q \tag{3.36}$$

With the help of generalized eigenvectors Eq. 3.34 is solved. It contains up to six real solutions. Eq. 3.31 depicts the best-fit ellipse. In this method, the first eigenvector (λ) value is calculated. For efficient fitting, the design matrix is decomposed into linear and quadratic part. The same way the scatter part is split into a combined and linear part of the matrix. In our case, we have found the λ as 1.875.

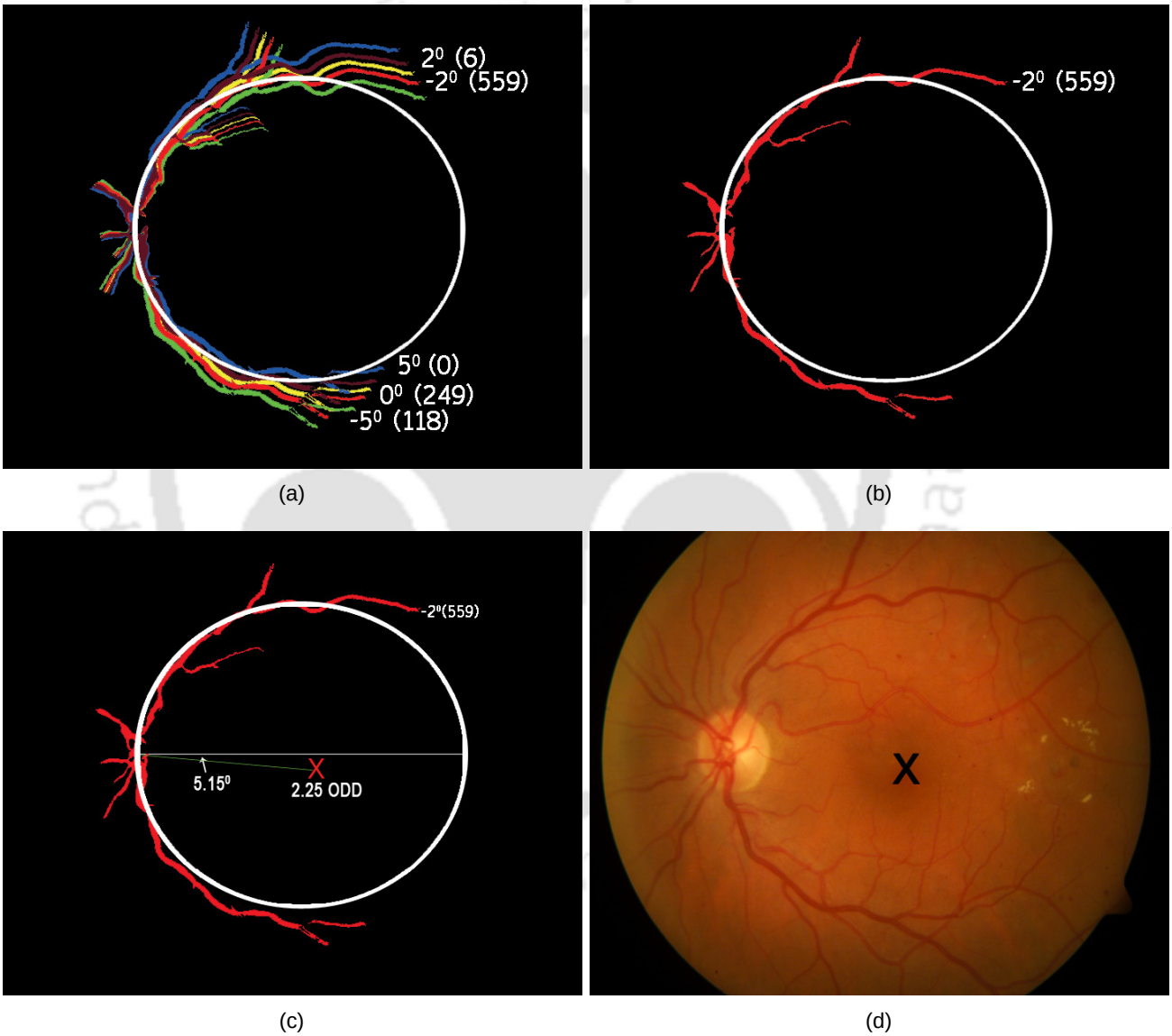

Figure 3.22: (a) Ellipse fitting with rotated BVs, (b) Detected fitting position, (c) Fovea detected , (d) Detected fovea in original image.

To localize the fovea accurately, it is necessary that, the ellipse template must fit over the segmented BV arc. To determine the exact match, we have rotated the segmented BV arc centred at OD centre, in both clockwise and anticlockwise direction by total angle of 10 degrees, in steps of 1

degree rotation. Then for every degree of rotation we count the number of 2's generated from overlapping pixels of template and BV arc. The maximum count obtained is considered as an exact fitting position. Figure 3.22 shows the ellipse fitting with rotating BV arcs. Once the fovea is obtained the performed rotation is reversed to retain the actual position of the image for further processing.

3.2.6 Results and Discussion

The evaluation of the algorithm is carried out to compare with our previous algorithm 3.1, emphasizing the subjects where the algorithm fails to locate fovea along with other methods in the literature. The selection consists of six databases, namely, DRIVE (37images), DIARETDB1 (89images), MESSIDOR (1190images), GEI (50images), NETRALAYA (65images), and HRF (45images).

Total 1476 out of 1489 images are selected for the experiment based on illumination conditions and retinal positions. In this direction, following the method by A. Tariq et al. [63], the images which suffer dark background suppression, improper illumination, and inaccurate focusing of the camera, are eliminated. Along with this, the images which do not have fovea available due to incorrect positioning of the eye during imaging are eliminated. The location of the automatically detected fovea is validated with the standard of 50-pixel Euclidean distance from manually marked gold standard [122, 126]. The detection is considered as positive if the distance lies within the range of 50 pixels. The manual annotation of the fovea centers is done by two experts. The results obtained after applying the algorithm on various databases show 100% efficiency in HRF (45 out of 45 images), GEI (50 out of 50 images), and DRIVE (37 out of 37 images) database whereas 98.88% (88 out of 89 images) in DIARETDB1 database, 98.46% (64 out of 65 images) in NETRALAYA, and 98.74% (1175 out of 1190 images) from MESSIDOR database are recorded. The system gives an average detection rate

Table 3.9: Comparison of fovea detection method applied to 37 images of DRIVE and 89 images of DIARETDB1 database

Methods used	DRIVE database (37 images)				DIARETDB1 database (89 images)			
	Images detected	Percentage detection	Avg. distance from Gold Standard	Average Standard Deviation	Images detected	Percentage detection	Avg. distance from Gold Standard	Average Standard Deviation
Sinthanayothin et al. [238]	29	78.38	62.23	116.45	58	65.17	62.68	84.16
Narasimha-Iyer et al. [25]	31	83.78	29.23	53.88	72	80.90	32.52	56.24
Singh et al. [125]	32	86.49	14.43	14.36	58	65.17	37.93	47.55
Sagar et al. [96]	35	94.59	12.61	14.92	75	84.27	24.79	49.81
Sopharak et al. [121]	19	51.35	122.06	142.87	34	38.20	81.08	90.05
Sekhar et al. [85]	34	91.89	10.45	12.13	60	67.42	30.81	30.22
Welfer et al. [122]	37	100.00	7.39	5.54	82	92.13	10.12	14.99
Proposed Method 1	37	100.00	6.88	5.85	85	95.51	8.90	12.89
Proposed Method 2	37	**100.00**	**4.06**	**3.99**	88	**98.89**	**6.48**	**10.09**

of 98.85% (1459 out of 1476 images).Similar to our previous work [8], the fovea detection algorithm is tested on the DRIVE and DIARETDB1 database so that performance comparison could be evaluated. The result obtained were tabulated in table 3.9. As perceived from the table, results obtained with the ellipse fitting method have improved the fovea detection rate with a decreased average distance from gold standards. In the DIARETDB1 database, fovea detection in image027 fails subjected to improper positioning and poor image quality, resulting in an incomplete BV arc detection. Few fovea detection outputs obtained from the proposed method, where the previous algorithm failed, are shown in Figure 3.23.

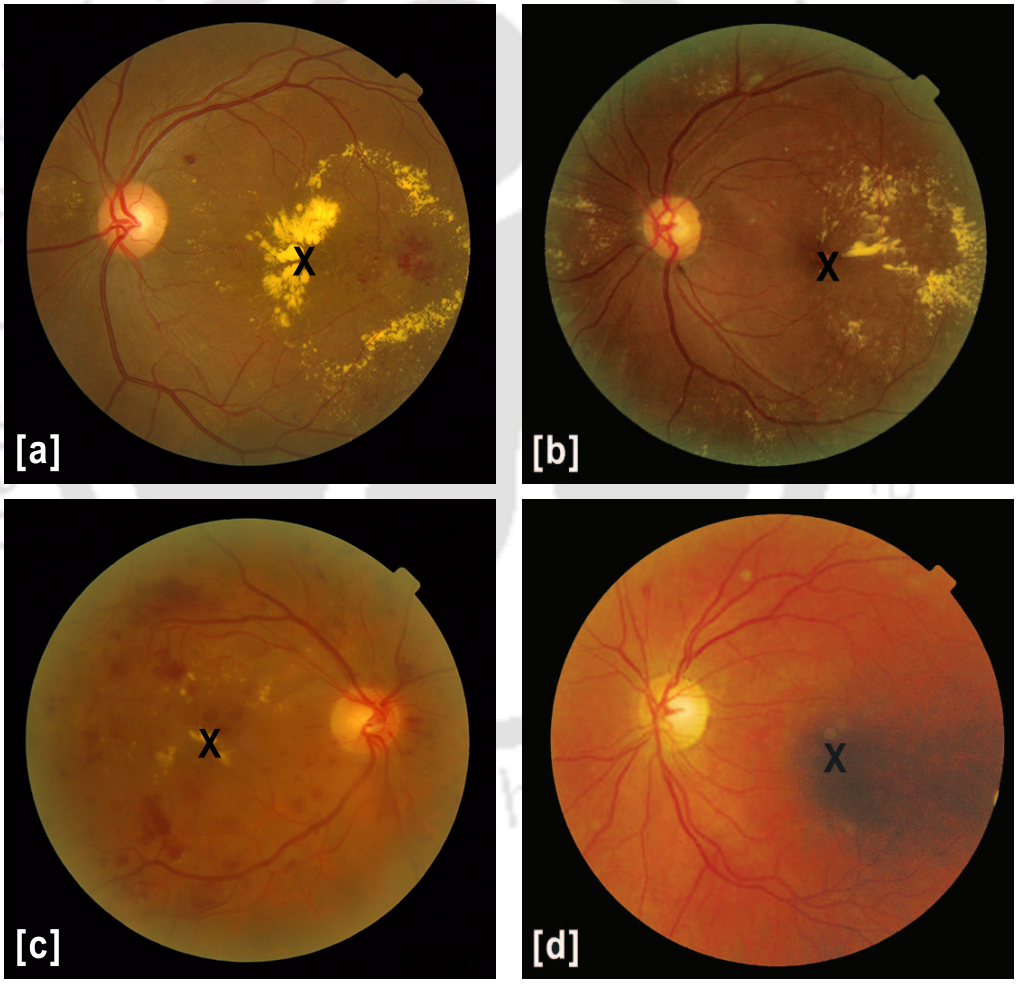

Figure 3.23: Detection of fovea in challenging cases: (a), (b) Abnormalities falling over macula, (c) Similar intensities near fovea, and (d) Fovea suppressed by dark background.

Therefore, from the results obtained, we may conclude that the updated algorithm performs better and detects fovea with negligible position error from actual fovea location.

3.3 Summary

In this study, we proposed a fovea detection method using the BV spread over retina. The availability of BV being more at the OD region serves as the key to the detection of ROI containing OD, where-as the non-availability of BV in the fovea region helps in the identification of ROI of fovea. The algorithm is advantageous over other methods based on geometrical relationships with fovea. Various publicly available databases, viz, DRIVE, DIARETDB1, MESSIDOR, and HRF are used for testing the algorithm. The automated detection of fovea is compared with the manually marked annotation done with the help of ophthalmologists. The decision criterion (gold standard) of correct detection is based on a Euclidean distance within 50 pixels of manual annotation with an image resolution of 600×480. The algorithm detects fovea with an overall efficiency of 98.09% and performs better than the available methods. Although advantageous, the method fails in a few cases where lesions posses similar intensity characteristics or it fully covers the macula. Therefore, to handle such challenges, we have updated the algorithm generating a common ellipse template from detected BV arcs of fundus images. After fitting the template, fovea is detected. The method improves the fovea detection in various cases where the first algorithm fails with an increased detection rate of 98.82%.

Once fovea and ODD gets detected, the next sequence in the automated algorithm is to mark the macular neighborhood and detect the presence of lesions within the mark. Therefore, the positions of lesions (both dark and bright) are to be identified for detection and severity estimation of DM. The algorithm proposed for serving the purpose is discussed in the next chapter. The algorithm considers various challenges of automated detection reducing the amount of FPs.

4

Lesion detection and Analysis of Diabetic Maculopathy

Contents

The early signs of Diabetic Maculopathy includes the presence of retinal lesions, particularly microaneurysms, hemorrhages, and hard exudates in macular neighborhood. These retinal lesion deposition are the outcome of blood vessel rupture caused due to elevated blood sugar levels during severe Diabetes. As per the studies, the fundus image provides a higher amount of sensitivity for the changes during DM in two dimensions. Hence, ophthalmologists examine fundus images for the evaluation of DM. As far as routine screening is concerned, qualitative measure is appropriate, but for DM monitoring and management, the quantitative management measure is necessary. The quantitative test is an onerous task as it includes identification of various sizes and shapes of lesions containing different texture. Hence, manual annotation becomes stressful, tedious, and susceptible to human error. As a solution to this problem, automatic evaluation is the way to bring out efficient management of DM.

The severity of DM is calculated concerning the position and amount of the lesion depositions. The more it is nearer to fovea, severe is the stage of the disease. On the contrary, higher deposition of lesions also create more complication. This chapter primarily focuses on the automatic detection of bright and dark DM lesions, considering the challenges faced during its identification and later classification along with the analysis of DM. As discussed in Chapter 1 dark lesions containing MA and HMs are the first indicators of DM. The bright lesions include CWS, drusen, SE, and HE. Among these, only HE is significant for DM identification. Automatic detection of these lesions is challenging, and various pre and post-processing steps are to be followed along-with.

Chapter content: The chapter discusses the proposed algorithm for automatic detection of lesions and analysis of DM in three divisions of the sections containing HE detection, MA, and HM detection and classification along with analysis of DM. The proposed method for HE localization explained in section 4.1 is based on color property analysis and later is updated by shade correction with removal of the challenges faced during HE detection. After that, the proposed method for MA and HM detection is discussed over section 4.2. Intensity and color based segmentation with the elimination of FPs are addressed here and are improvised with the addition of BVs property analysis. The later section 4.3 is composed of the proposed method for DM classification and analysis. The method includes both unsupervised and supervised models of evaluation. The study performs DM detection and classification, with the addition of determining the intensity of deposition as a part of categorization.

4.1 Localization of Hard Exudates

Among bright lesions, Hard Exudates are the result of multiple depositions of lipid and protein constituents of blood. The presence of these lesions in the macular neighborhood severely affects the central vision by offering blockage to the incidence of light into the macula. Being necessary for quantitative analysis of DM, the proper identification of HE is essential. In this section of the chapter, we have detailed the proposed algorithm for HE detection. HE has a highly reflective, waxy, and yellowish appearance in the digital fundus image. The detection of bright lesion contains various challenges. The main challenge is the color and intensity, which is similar to OD and other bright lesions. Rest of the challenges include reflections generated due to healthy BVs and the macula, which may get identified as HE. Considering these facts and limitations faced during various HE detection algorithms, we propose two HE detection methods. The first algorithm is based on the elimination of similar property pixels and the analysis of color information of exudates for identification. In the second algorithm, we have considered the isolation of HEs from all bright regions and the elimination of various retinal reflections to generate a robust method for identification.

4.1.1 Proposed automated Exudate detection using colour property

The motivation for the proposed method is to automatically locate exudate from fundus image eliminating probable false positives, generally encountered during detection. Hence, the elements responsible for FPs are identified and eliminated beforehand. Once the FPs are removed, the remaining yellowish pixels representing exudates are identified using hue plane property. The hue value of a pixel remains similar, even though the intensities may slightly vary.

As we know, among FPs, OD is the primary component with similar intensity and color information as exudates. Therefore, proper detection and masking of OD is the prerequisite of this algorithm. OD detection method based on intensity property has FPs of bright regions due to camera flash or other bright lesions, namely CWS, HE, and SE. Therefore, to avoid such a situation in OD detection, the BV relation and OD shape information along with color and intensity property is used. The BV network originates from OD and has more concentration in the OD neighborhood. Therefore, using this property ROI for OD is obtained, and after that, OD is detected using the threshold to obtain maximum intensity pixel. Later with the help of circular shape property, the contour of OD is detected. The details discussion of OD localization is carried out in the previous Chapter 3 under subsection

3.1.0.2. Once OD is detected, it is masked so that the exudates detection can be carried forward.

The yellowish pixels left after OD masking belongs to the lesions. Therefore, the color (hue) property of the exudates is considered for the detection. The output image obtained after the OD mask is converted into HSI image and setting a threshold in the hue plane; the yellowish pixels representing exudates are segregated. The detail of the threshold being used here, along with the algorithm description, is already carried out in Chapter 3 under subsection 3.1.0.3. The results obtained after examining the algorithm are discussed in the subsequent sections.

4.1.1.1 Evaluation: HE detection algorithm 1

The algorithm is tested on 1374 images from DRIVE, DIARETDB1, MESSIDOR, and HRF database. Out of total1374 images, 755 contain pathogens such as hemorrhage, microaneurysms, exudates, and the rest are healthy images. Again, out of 755 pathogenic images, 494 are affected by dark lesions, and 330 show the presence of bright lesions. The lesions are quantitatively evaluated by comparing with the manually labeled (ground truth) images. The comparison is based on the number of abnormality pixels detected. The performance of the proposed algorithm is assessed based on *sensitivity*, *specificity* and *misclassified proportion* measurements. This *pixel based measurement technique* helps us evaluate the efficiency of the system, and it is based on four parameters of pixel values, namely, True Positive (TP), False Positive (FP), False Negative (FN) and True Negative (TN). The TP represents correctly identified lesion pixels. FP represents pixels incorrectly identified as lesions. FN are incorrectly rejected lesion pixels, and TN are correctly rejected non-lesion pixels. The sensitivity and specificity measurements are obtained as follows,

$$\text{Sensitivity} = \frac{TP}{TP + FN} \tag{4.1}$$

$$\text{Specificity} = \frac{TN}{TN + FP} \tag{4.2}$$

The sensitivity is the measurement of actual lesion pixels, which are correctly classified as lesions. More the sensitivity, the better is the detection. The specificity represents the correctly rejected proportion of healthy pixels. The lesion pixels are very few compared to the remaining healthy pixels. Thus, in addition to sensitivity and specificity, Misclassified Proportion (MP) is also estimated as given in (4.3).

$$\text{MP} = \frac{FP}{TP + FP + FN + TN} \tag{4.3}$$

The algorithm is applied to all 1374 images, and the result of lesion detection is compared with the corresponding ground truth image. If the image is devoid of lesions, the processed image results in a clear image. Table 4.1 shows the result of bright lesion detection on all databases concerning sensitivity, specificity, and misclassified proportions. The algorithm detects all exudate components of the DIARETDB1 and HRF database. The algorithm records the detection rate of 86% in the DRIVE database and 98.28% in the MESSIDOR database. The average (mean) sensitivity, specificity, and misclassified proportions recorded are 77.73%, 98.72%, and 1.003%, respectively.

Table 4.1: Summary of bright lesion (exudate) detection

Databases	No. of Images tested	Images with Exudate	Exudate detected images	Average Sensitivity (%)	Average Specificity (%)	Misclassified proportion (%)
DRIVE	40	7	6	72.23	98.45	1.19
DIARETDB1	89	28	28	79.81	98.92	0.94
MESSIDOR	1200	291	286	72.61	97.62	1.02
HRF	45	4	4	86.26	99.89	0.86

The performance of proposed algorithm and the comparison with Sopharak et al. [121], Walter et al. [139], Welfer et al. [86], Harengi et al. [245] and Harengi et al. [246] are shown in table 4.2. The results show that the algorithm performs better in detecting the exudates on various images.

Table 4.2: Comparison of exudate detection methods applied on 47 images of DIRETDB1 and MESSIDOR database containing hard exudates

Methods	Average Sensitivity (%)	Average Specificity (%)	Average Misclassified proportion (%)
Sopharak et al. [121]	43.48	99.31	0.68
Walter et al. [139]	66	98.64	1.34
Welfer et al. [86]	70.48	98.84	1.10
Harangi et al. [246]	75.76	91.25	1.59
Harangi et al. [245]	79.82	95.64	1.28
Proposed method	**85.23**	**98.89**	**0.71**

Although results are promising, this algorithm is limited to the detection of all exudate candidates. The classification of HE is not addressed here for analysis. Moreover, the results show some FPs in standard healthy images due to the presence of retinal reflections. Therefore, to improve over the limitations, we propose a robust algorithm based on shade correction property.

4.1.2 Proposed improved automated HE detection

Considering the challenges faced for HE detection, we propose an improved HE detection method. The algorithm segregates out the HE from the rest bright regions eliminating OD, SE, CWS, and reflections of BV and Macula. HE can be distinguished from similar bright lesions such as CWS or drusen by the strength of their boundary edges. In contrast, CWS, SE, and drusen are diffused structures with considerably less sharp edges. This information is utilized in the proposed system to distinguish HEs in the fundus image. However, the presence of other bright regions, including the OD, BV, and macular reflections, makes it difficult to detect HEs accurately. The algorithm, at first, eliminates these obstructive features and then attains all possible candidate regions, resembling exudates, and classifies them into HEs using edge strength property. The overall HE detection scheme is comprised of three main steps, namely:

Step I Image enhancement and illumination correction.

Step II Coarse Detection of Exudate Candidates.

Step III Fine Detection of HE from other bright lesions.

The reflections created from healthy and younger retinal images give rise to bright artifacts in BV and macula boundaries, which result in FPs during HE detection. Following two steps constitute the novelties of improvising HE detection scheme:

- Bright structures observed beside the BVs are removed using a BV template.
- Macular reflections in the fovea neighborhood are removed using RGB color properties.

4.1.2.1 Image correction and component extraction

This subsection details the image correction steps essential for improving the detection of HEs. The first and foremost FP encountered during the segmentation is the presence of bright intensity beyond retinal FOV. Therefore, these regions must be eliminated by retaining the FOV only for further processing [8, 139]. It is accomplished by taking the green channel of the input image and performing intensity level slicing to remove regions of low-intensity values, followed by morphological image filling operation. Say the output obtained is $\boldsymbol{FOV}_{original}$ or '*image L*'. The original RGB image components corresponding to the *image L* are preserved, and the outer FOV region is made purely dark by assigning zero values to the pixels.

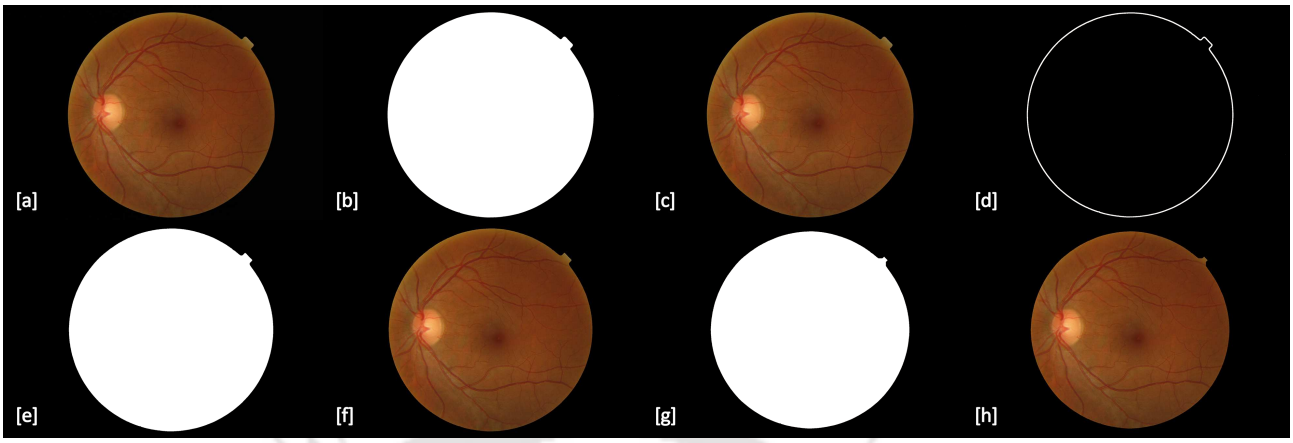

Figure 4.1: Steps showing elimination of bright boundary and obtaining field of view (FOV) image: [a] Original image, [b] image L or $FOV_{original}$, [c] RGB $FOV_{original}$, [d] $FOV_{original}$ boundary for bright noise verification, [e] updated FOV eliminating noisy boundary, [f] corresponding RGB FOV, steps continued.... [g] Final FOV, [h] RGB of final FOV.

The second FP experienced is the bright intensity observed in the outer circle of the FOV [239], caused due to the improper handling of fundus camera flash. Exempting the border of FOV containing the FPs is the way out to eliminate this FP. The algorithm 1 for bright boundary elimination discussed in Chapter 3 explains the procedure of the second FP exemption. The FOV obtained after the process (*updated FOV*) is considered as final FOV, and the corresponding RGB image is stored for further processing. One such example is shown in Figure 4.1.

The third hindrance causing FPs in HE detection is the presence of OD. The OD appears yellowish with bright intensity and is very much similar to HE, and one cannot distinguish between OD and HE using color or intensity property [8, 87, 235] without color normalization. Abramoff et al. [17] suggested that the OD candidate regions can be detected by considering the highest intensity pixels of the image and yellow color value from hue plane. Hence, utilizing the hue property with proper enhancement, the OD is detected and masked in the proposed method. The proposed steps are discussed in algorithm 2: The justification of few parameters mentioned in algorithm 2 are as follows, CLAHE in the algorithm represents Contrast Limited Adaptive Histogram Equalization. It is applied on the YIQ color model to enhance the exudates and on the HSI color model to enhance OD. The selection of ROI_{radius} is based on the fact as explained by D.A. Godse [247] is that the OD is a vertical oval structure, with an average 1.76mm and 1.92mm of horizontal and vertical dimensions. These dimensions are equivalent to $1/8$ and $1/7.33$, width and height of retinal image diameter, respectively. $ROI_{radius} = FOV_{diameter}/7.5$ is considered such that the OD gets well equipped within ROI. The

Algorithm 2: *Optic Disc elimination*

function ODE;
Input : Updated color **FOV** or I_{RGB}
Output: Optic Disc Masked, I_{ODE}

Calculate: I_{enh1} : $I_{RGB} \rightarrow I_{YIQ}$
$I_{YIQ_{\text{modified}}} = \text{CLAHE}\left(I_{Y-plane}\right)$
$I_{YIQ_{\text{modified}}} \rightarrow I_{RGB_{\text{modified}}} = I_{enh1}$

Calculate: I_{enh2} : $I_{RGB} \rightarrow I_{HSI}$
$I_{HSI_{\text{modified}}} = \text{CLAHE}\left(I_{I-plane}\right)$
$I_{HSI_{\text{modified}}} \rightarrow I_{RGB_{\text{modified2}}} = I_{enh2}$

Calculate: I_{m1} : $\text{MEDIAN FILTER}\left(I_{enh1_{G-plane}}\right)$
$\text{window size}\ (40 \times 40)$

Determine shade corrected image (I_{SC}); $I_{SC} = I_{enh1_{G-plane}} - I_{m1}$

Segment bright regions from background (I_{bright});

$$I_{bright} = I_{SC} > T_1 \; ; T_1 = 35$$

Eliminate bright pixels other than OD in I_{enh2} $I_{enh2} = I_{enh2} - I_{bright}$

Calculate Region of Interest (ROI) center and radius;

$$ROI_{center}(a, b) = \max\left(I_{enh2}\right) \; ROI_{radius} = imageL_{diameter}/7.5$$

Locate ROI containing OD using; $(x-a)^2 + (y-b)^2 = (ROI_{radius})^2$

Eliminate BV from green channel ROI using mathematical morphology;

$$ROI = \delta^{(B)}\left(ROI\right); B = \text{disc SE}$$

Segment ROI bright regions from background (ROI_{bright});

$$ROI_{bright} = ROI > T_2 \; ;$$

$$T_2 = \frac{\max(k) - [\max(k)]/8}{255};$$

Locate OD center from detected ROI_{bright}:
Find $ROI_{bright(center)}$
if $ROI_{bright(center)} \in FOV$ (first vertical − half) **then**
  shift$[ROI_{bright(center)}] \rightarrow$ first horizontal pixel of $\left[ROI_{bright(center)}\right]$;
  $OD_{center}(a_1, b_1)$=updated $ROI_{bright(center)}$;
else
  shift$[ROI_{bright(center)}] \rightarrow$ last horizontal pixel of $\left[ROI_{bright(center)}\right]$;
  $OD_{center(a_1,b_1)}$=updated $ROI_{bright(center)}$;
end
Locate OD using;

$$(x-a_1)^2 + (y-b_1)^2 = (ROI_{radius}/2)^2;$$

Compute: $I_{ODE} = I_{enh1} - OD$

value of threshold T_1 is set based on experimental setup, as discussed in Section 4.1.2.4. While measuring T_2, k represents the image portion in intensity plane under the ROI, $\max(k)$ represents maximum pixel value within the OD region.

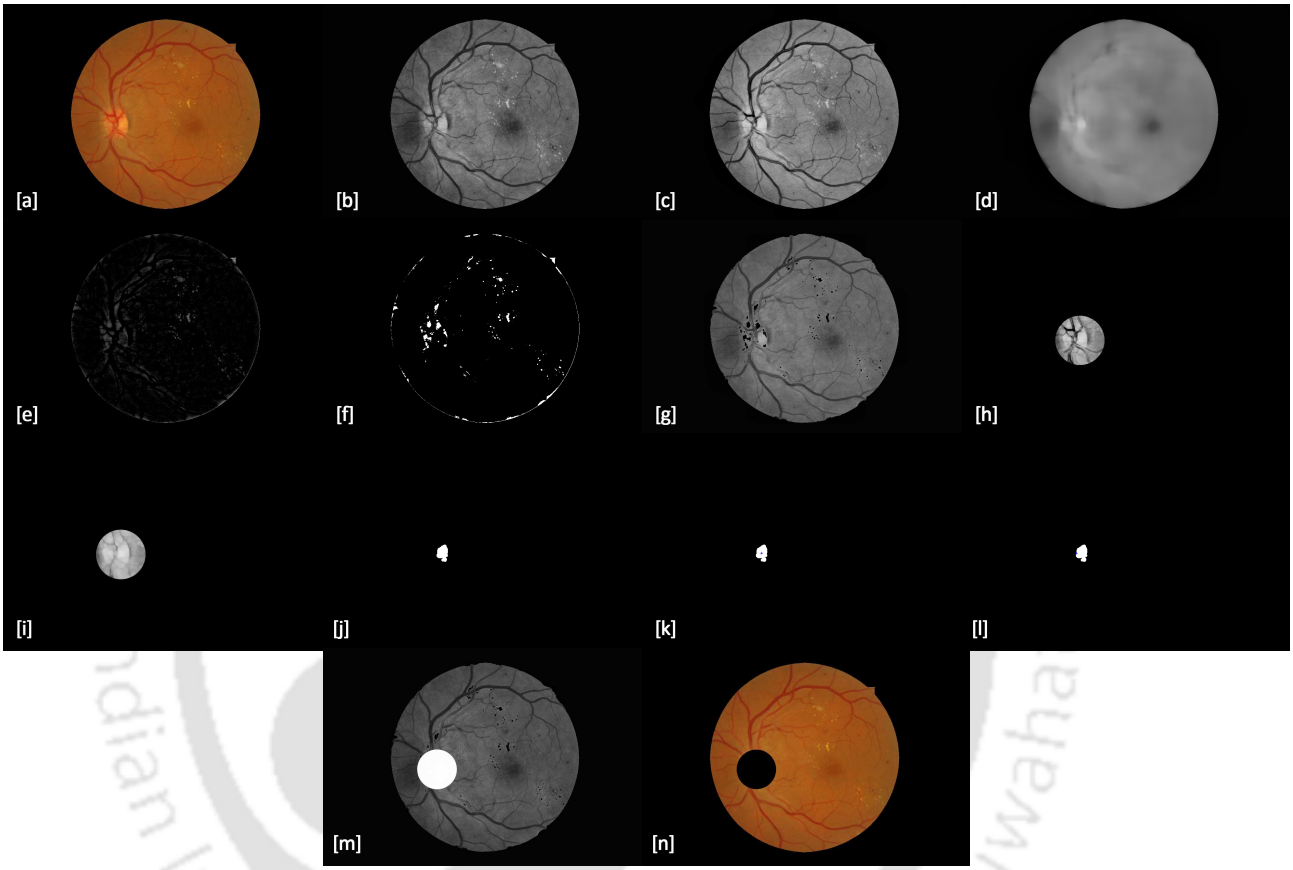

Figure 4.2: Steps showing OD elimination: [a] FOV image, [b] green plane Enhancement 1, [c] green plane Enhancement 2, [d] Median filtered image (window 40×40), [e] Shade corrected image, [f] Bright regions [g] Bright regions masked, [h] ROI containing OD, [i] BV removed morphologically [j] OD segment located, [k] & [l] Segment centroid placing, [m] OD detected and [n] OD eliminated from color FOV.

The fourth FP occurring in HE detection are the bright spots beside the blood vessels. To detect BV, we follow our previous work in Chapter 3 Subsection 3.1.0.2. In the detection process, threshold detecting the BV is considered at higher value so that the major arteries only get detected. The detected BVs are then dilated using disc SE, and resultant output is considered as BV mask I_{BV}. By eliminating these masked regions, the BV reflections are removed. Figure 4.3 (a) represents one example of BV reflections and Figure 4.3 (b) shows the BV mask.

The fifth FP encountered is macular reflections, which is observed in normal and healthy retinal images resulting in FP during exudate segmentation. To handle this issue, we have used the RGB color model properties. The distinguishable characteristics of macular reflection with exudates is the

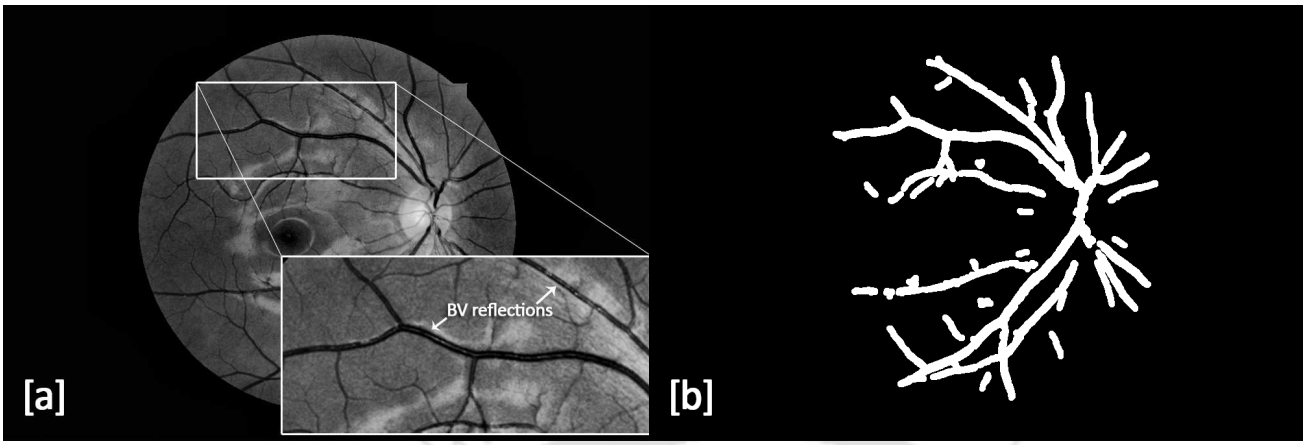

Figure 4.3: Retinal reflections and its removal: [a] BV reflections, and [b] BV mask.

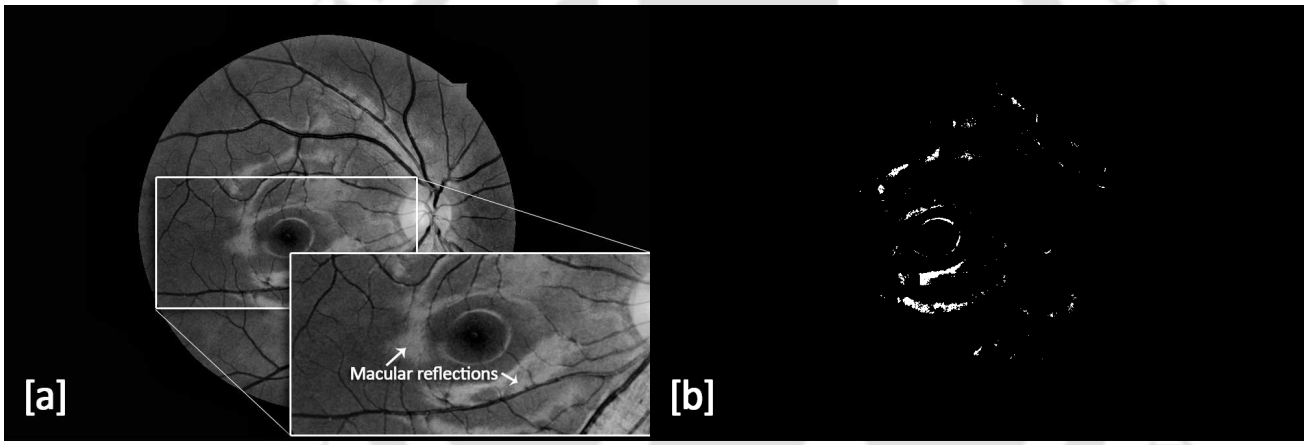

Figure 4.4: Retinal reflections and its removal: [a] Macular reflections, and [b] Macular reflection mask.

color information. Macular reflection is bright in color, whereas exudates are yellowish. As we know, the bright color is formed by the combination of positive values of R, G, B planes, whereas yellow color is formed with only R and G positive values with nil value in blue plane. Therefore, identifying FP having pixel intensities in all the R, G, B plane does the job. This step is done as a post-processing in the exudate detection process. Figure 4.4 (a) represents one such macular reflection example with detected output in Figure 4.4 (b).

4.1.2.2 Coarse Exudate candidate detection

After image correction, the resultant image, I_{ODE}, is ready for exudate detection. The stepwise procedure for exudate localizing is described in Algorithm 3.

The corresponding justification of algorithm 3 is mentioned herewith. As the intensity and color

Algorithm 3: *Locating Exudate candidates*

1 function ED;
Input : Preprocessed input image, I_{ODE}
Output: Exudate detected image, I_{ED}

2 Enhance I_{ODE} processing H and S plane of corresponding HSI model and resuming back to RGB plane. Considering K as the image under process,

Calculate: Morphological opening and closing

$$\sigma^{(B)}(K) = \delta^{(B)}\left(\varepsilon^{(B)}(K)\right),\ \theta^{(B)}(K) = \varepsilon^{(B)}\left(\delta^{(B)}(K)\right)$$

Calculate: Top Hat opening and closing

$$\psi(K) = K - \sigma^{(B)}(K)$$

$$\zeta(K) = \theta^{(B)}(K) - K$$

Compute Top Hat transformation:

$$I_{ODEe}(K) = x.K + y.\psi(K) - z.\zeta(K)$$

3 Calculate: $I_{m2} \quad : \quad \underset{\text{window size } (30 \times 30)}{\text{MEDIAN FILTER}}\left(I_{ODEe_{G-plane}}\right)$

4 Determine shade corrected image (I_{SC});

$$I_{SC1} = I_{ODEe_{G-plane}} - I_{m2}$$

5 Compute Top Hat transformation over I_{SC1}

$$I_{SCe}(K) = x.K + y.\psi(K) - z.\zeta(K)$$

6 Segment exudate components from background (I_{EXC});

$$I_{EXC} = I_{SCe} > T_1\ ;\ T_1 = 35$$

7 Eliminate BV reflection FPs

$$I_{EXC1} = I_{EXC} - I_{BV}$$

8 Eliminate Macular reflection FPs $\rightarrow I_{ED}$

property of exudate pixels are better suited, hence, enhancement is performed in the HSI color model, and the result is converted back to RGB. Top hat transformation helps in enhancing bright pixels more brighter and dark background into more darker transformation. The value of $[x, y, z]$ in the transformation is considered as $[1, 1, 1.5]$ as mentioned in Chapter 3 Subsection 3.1.0.1 for the database under consideration. The output thus obtained contains all the exudate candidates containing CWS, SE, and HE. Figure 4.5 represents the sequential steps performed for the detection of exudate candidates.

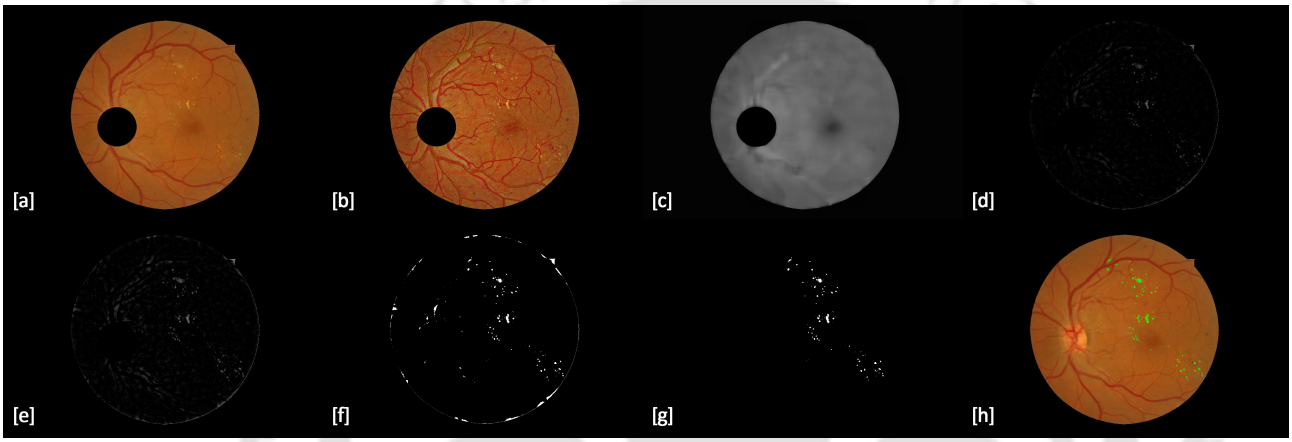

Figure 4.5: Steps showing coarse Exudate detection: [a] OD removed FOV, [b] Enhanced using Top hat transformations, [c] Median filtered image (window 30×30), [d] Shade corrected image, [e] Enhanced using top hat [f] All bright regions, [g] Exudates detected after elimination BV and Macular reflections and [h] Exudates marked over color FOV image.

4.1.2.3 Fine HE candidate detection

SE and CWS differ from HE under their edge strength property. While they generally possess blurry or less distinct edges, HE has sharp and well-defined edges [28]. So, candidate regions with lesser edge strength are eliminated since they are SE. A standard deviation filter is applied to judge the edge strength of these candidates. Standard deviation is a measure of how far the signal varies from the mean value, and the variance represents the power of this variation. The standard deviation filter is applied to the image I_{ED}, followed by canny edge detection to eliminate less distinct edges. Now, a threshold value T_3 is used on the edge image to determine whether a pixel belongs to hard exudate or any other bright artifact without an adequately defined edge strength. The threshold T_3 is set depending on the overall standard deviation value ($std2$) calculated, and is given as,

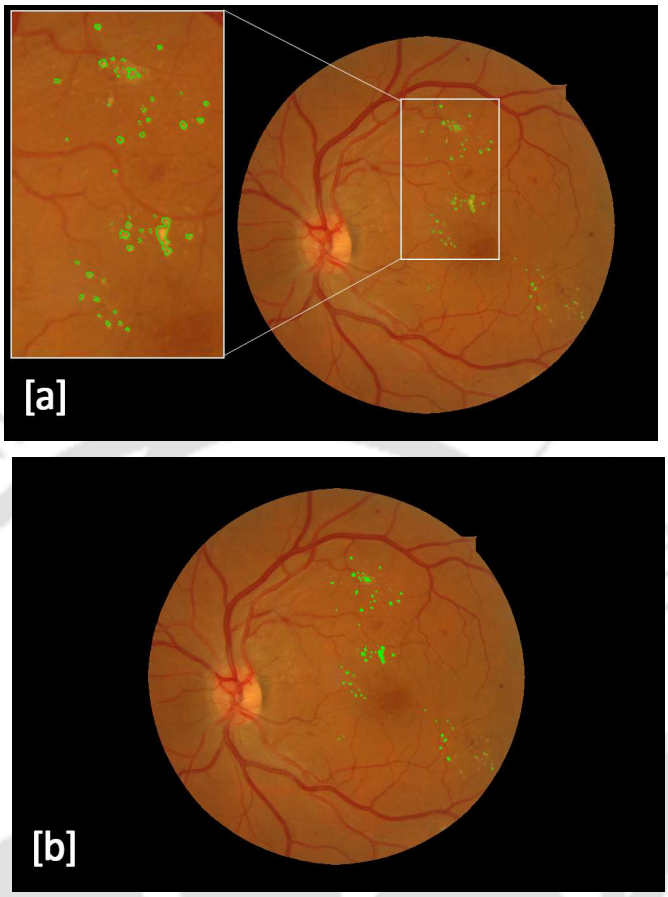

Figure 4.6: Hard Exudate detection: [a] Result of Standard deviation filter obtaining the HE edges, [b] Detected HE marked over color FOV image.

$$\begin{cases} std2 \geq 0.048 & ; \quad T_3 = 0.46 \\ 0.012 \leq std2 \leq 0.020 & ; \quad T_3 = 0.21 \\ otherwise & ; \quad T_3 = 0.05 \end{cases}$$

If the value of edge pixel is less than the threshold, then it is eliminated; otherwise, their values are retained in the output image. Finally, the output image has the edges of the HE region. A region growing algorithm is implemented to create the desired ROI that contains the final HE candidates. Searching for a radius within 10 pixels, if there are HE candidates that fit the region, then these are marked as desired output. The result, thus obtained, are shown in Figure 4.6.

4.1.2.4 Evaluation: HE detection algorithm 2

Evaluation of HE detection based on image-level identification enables us to identify the presence or absence of HEs in the tested image. But the information referring to the amount of HE detection out of

the actual HEs present in the test image is missing in the evaluation process. As shown in Figure 4.7, the manual segmentation, or the ground truth image represents the location and approximate contour of exudate present in the image. Therefore, the evaluation is possible concerning the availability of the detected HEs in these marked locations.

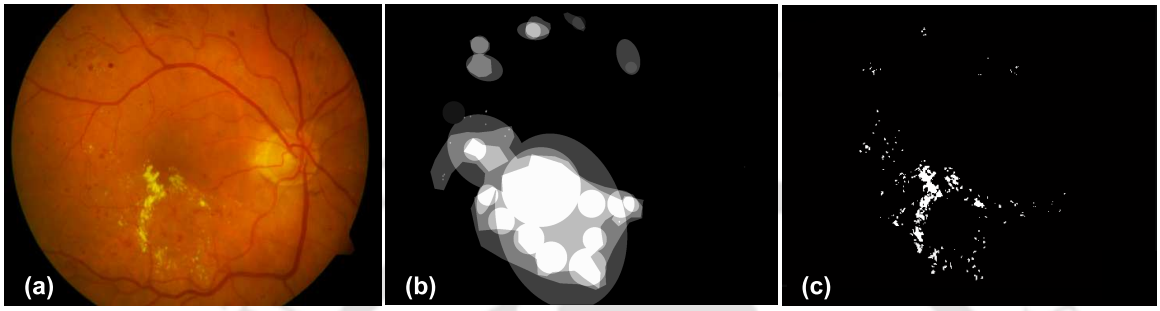

Figure 4.7: Image level evaluation scheme: (a) Original image, (b) Ground truth, (c) Detected exudates.

But if we want to determine the exact amount of HE identified we must go for pixel level evaluation. The pixel level evaluation of individual HEs is possible with the help of publicly available e-ophtha EX database [234]. The database contains precise lesion annotation. Therefore, the evaluation is possible concerning exact HE pixels being correctly identified. Hence, for better evaluation of the proposed HE detection algorithm it is examined through both image and pixel level analysis.

Image level evaluation:

The image-level evaluation of the HE detection algorithm has been tested on 1390 images from the overall 1413 images of the three databases DIARETDB0, DIARETDB1, and MESSIDOR. Images with proper fovea and OD localization, performed by fovea detection algorithms discussed in Chapter 3, are only considered for further segmentation. The automatically detected HEs are compared with the corresponding ground truth image. Figure 4.8 represents the detected HEs and its comparison with the ground truth image. The performance of the proposed system is assessed, employing sensitivity and positive predictive value (PPV) measurements of HE pixels. The PPV is the measurement of the likelihood that retinal image under evaluation with a positive test result has the presence of lesions.

$$\textit{Positive Predictive Value}\,(PPV) = \frac{TP}{TP + FP} \tag{4.4}$$

The results thus obtained are tabulated in Table 4.3. The average (mean) sensitivity and PPV thus obtained are 96.87% and 93.10%, respectively. To evaluate the system performance, it is compared

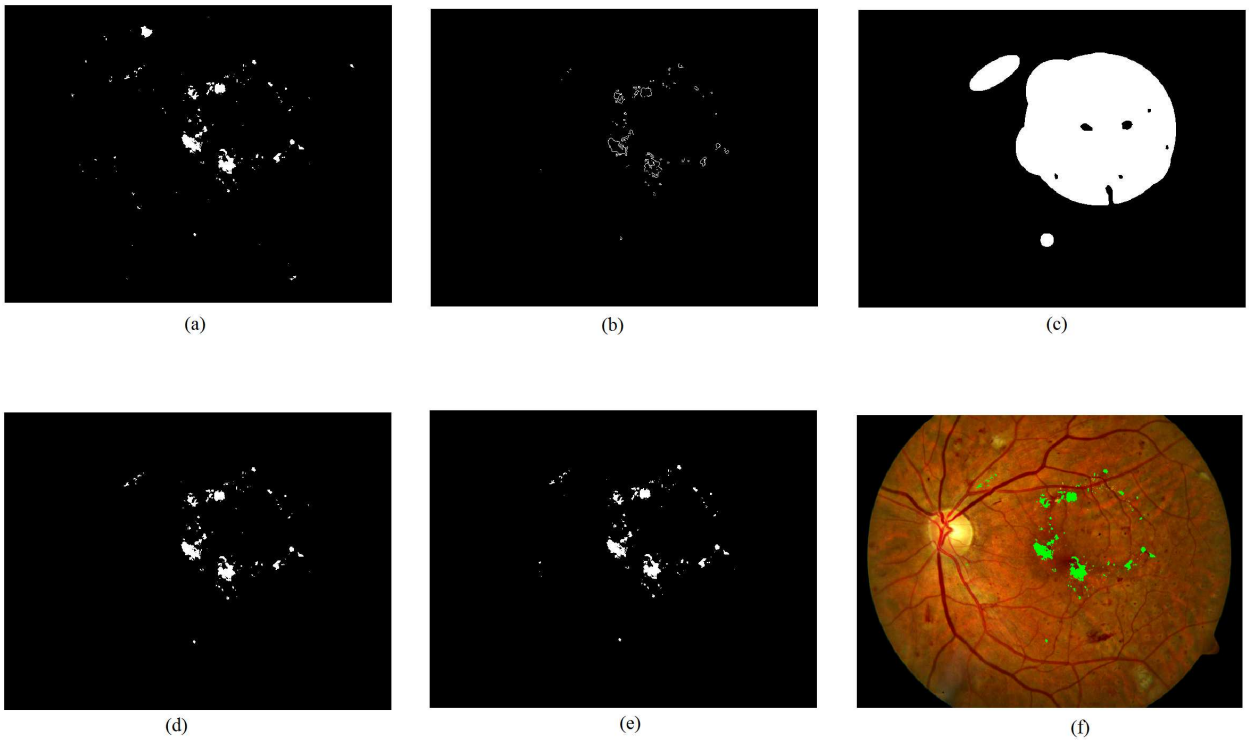

Figure 4.8: (a) All possible hard exudate candidates, (b) Detected HE regions using edge strength, (c) Original Ground Truth Image, (d) True positive HE marked using ground truth, (e) Detected HE regions after region growing (f) Detection overlapped over input color image.

Table 4.3: Result of Hard Exudate detection

Databases	Test Image	Average Sensitivity (%)	Average Positive Predictive Value (%)
DIARETDB1	84	98.36	94.88
DIARETDB0	124	97.17	92.32
MESSIDOR	1182	95.09	92.11

with the methods, as discussed in the previous section for exudate detection. The comparison is represented in Table 4.4, and there it is evident that the proposed algorithm performs better compared to the other and the previously proposed method. The method successfully eliminates the limitations faced during the previous algorithm.

Pixel level evaluation

The pixel-level evaluation determines the number of correctly detected HE pixels. The e-ophtha EX is the only public database which contains precisely labeled ground truth image of lesions based on pixels level annotation. The evaluation, if being done as other standard methods, may not hold good for HE detection.

Table 4.4: Comparison of exudate detection methods applied on 47 images of DIRETDB1 and MESSIDOR database containing hard exudates

Methods	Average Sensitivity (%)	Average Specificity (%)	Average Misclassified proportion (%)
Sopharak et al. [121]	43.48	99.31	0.68
Walter et al. [139]	66	98.64	1.34
Welfer et al. [86]	70.48	98.84	1.10
Harangi et al. [246]	75.76	91.25	1.59
Harangi et al. [245]	79.82	95.64	1.28
Proposed method1	85.23	98.89	0.71
Proposed method2	**98.28**	**99.11**	**0.59**

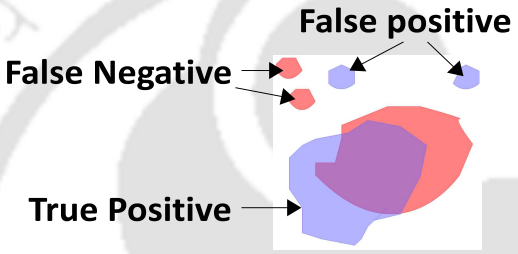

Figure 4.9: True positive and False positive pixel definitions: The red regions represent ground truth and the blue regions denote detected HEs.

For instance, let us consider a case shown in the following Figure 4.9. Here, the regions with blue color represent the detected HE pixels, whereas, the ground truth are marked as red. As per conventional practice, the large HE pixels are considered as TPs, although the contour does not match with the ground truth pixels precisely. If we consider the overlapped regions as TPs, then half of the detected HEs would become FPs, and half of the ground truth region be FNs. Moreover, these evaluations do not hold for small HE segments. Therefore, for pixel-level inspection of HE detection, a hybrid evaluation method has been followed [239] where minimal overlapping of candidate and ground truth have been estimated as per the following.

Considering D_i as connected component of exudate candidates $\{D_1, D_2, ...D_N\}$ and G_j be connected component of ground truth exudate candidates $\{G_1, G_2, ...G_M\}$. Where, the mask of detected exudate and ground truth exudates are given as,

$$D = \bigcup_{1 \leq i \leq N} D_i \quad and \quad G = \bigcup_{1 \leq i \leq M} G_j \tag{4.5}$$

A detected exudate pixel is considered as TP if it belongs to,

$$\{D \cap G\} \cup \left\{ D_i | \frac{|D_i \cap G|}{|D_i|} > \sigma \right\} \cup \left\{ G_j | \frac{|G_j \cap D|}{|G_j|} > \sigma \right\} \tag{4.6}$$

where, $|\cdot|$ is cardinal of a set and σ ranges from 0 to 1. For evaluation, the value of σ is set at 0.2 as considered by Zhang et al. [239]. Because considering $\sigma = 0$ as per Giancardo et al. [248] means if an exudate overlaps ground truth region with even minimum pixels, it is considered as TP, which is not proper for evaluation.

A pixel is called as FP and FN if it belongs to,

$$\{D_i | D_i \cap G = \phi\} \cup \left\{ D_i \cap \overline{G} | \frac{|D_i \cap G|}{|D_i|} \leq \sigma \right\} \tag{4.7}$$

and,

$$\{G_j | G_j \cap D = \phi\} \cup \left\{ G_j \cap \overline{D} | \frac{|G_j \cap D|}{|G_j|} \leq \sigma \right\} \tag{4.8}$$

The remaining pixels are TN. From these information the Sensitivity (S) and Positive predictive value (PPV) are computed. Where, sensitivity provides the information of exact correctly marked exudate pixels and PPV provides the information of detected exudate pixels with respect to annotated exudate pixels by specialists. From the information of sensitivity and PPV the harmonic mean F1-Score is computed by,

$$F1 - score = \frac{2 \times S \times PPV}{S + PPV} \tag{4.9}$$

To validate the proposed detection algorithm, we have manually labeled the images of DIARETDB1, DIARETDB0, and HRF database along with the available e-Ophtha EX database. The individual results thus obtained are summarized in Table 4.5. The evaluation records average (mean) of 87% sensitivity, 90.5% PPV and 88.7% F1-Score. Figure 4.10 shown below represents the pixel level investigation with $\sigma = 0.2$ for three different cases. To concentrate on the exudate regions of the fundus image, the result is shown with the cropped portion containing the exudates only. In the figure green, red, blue, and black pixels are TP, FN, FP, and TN, respectively. The comparison of the proposed algorithm is performed with the available literature, by examining over e-ophtha EX database. The results obtained are shown in Table 4.6. From the comparison, it is evident that the proposed algorithm performs better than the other algorithms.

Table 4.5: Pixel level validation of hard exudate detection on various databases applied

Database used	Sensitivity	PPV	F1-score
DIARETDB0	87.4%	91.5%	89.4%
DIARETDB1	83.5%	88.7%	86.0%
HRF	91.6%	90.3%	90.9%
e-OPHTHA EX	85.6%	91.6%	88.5%

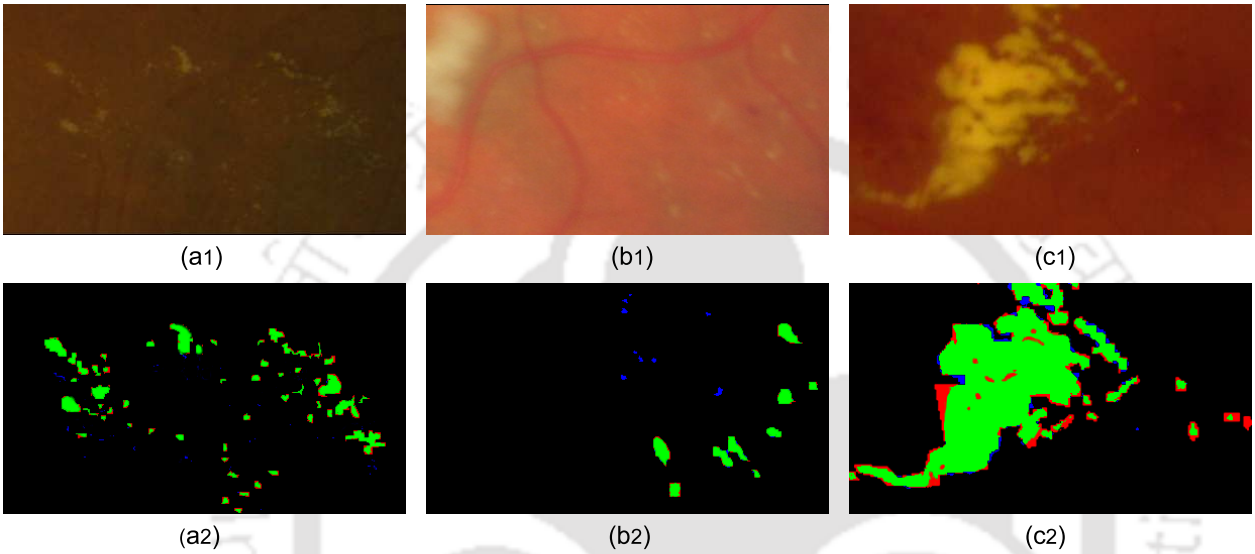

Figure 4.10: Example of pixel level validation on E-Ophtha EX database: (a1,b1,c1) original cropped image, (a2,b2,c2) Results obtained with $\sigma = 0.2$. Here, green, red, blue and black pixels represent TP, FN, FP and TN respectively.

Table 4.6: Comparison of Pixel level validation of hard exudate detection for the proposed method in e-Ophtha EX database.

Year	Sensitivity	PPV	F1-score
Walter et al. [139]	44.0%	65.0%	52.0%
Welfer et al. [86]	79.0%	55.0%	69.0%
Zhang et al. [239]	74.0%	72.0%	73.0%
Imani et al. [249]	80.3%	77.3%	–
Liu et al. [250]	76.0%	75.0%	76.0%
Kusakunniran et al. [251]	56.4%	–	–
Long et al. [252]	76.5%	82.7%	76.7%
Proposed Method	**85.6%**	**91.6%**	**88.0%**

4.1.2.5 Performance of the system with the parameters

The performance of the algorithm depends upon the parameter threshold values, T1 and T2, for determining all bright lesion candidates and desired BV templates, respectively. A fixed value has been set for each of these parameters after experimenting with several images for the given dataset, which

renders the optimum result in the performance of the system. As parameter values are changed from its optimum values, the sensitivity and specificity also change. Figure 4.11 shows the variation of sensitivity and specificity with threshold values T1 and T2. The dip in the curve for values of the threshold shows an increase in the FP rate resulting in low specificity. The threshold values are chosen based on the reduction in false positives. Taking a low value of T1 increases the number of bright pixels chosen and hence, increases the chance of unnecessary bright regions to be eliminated. This also results in some of the excess pixels which do not get eliminated; as a result, leading to low specificity. Similarly, choosing a much larger value of T1 eliminates initial bright lesion pixels to be processed, leading to a decrease in FP rate but also decreases TP rate resulting in low sensitivity. As such, a suitable threshold is chosen according to the curve. The same concept applies to T2, and similarly, T2 is chosen accordingly.

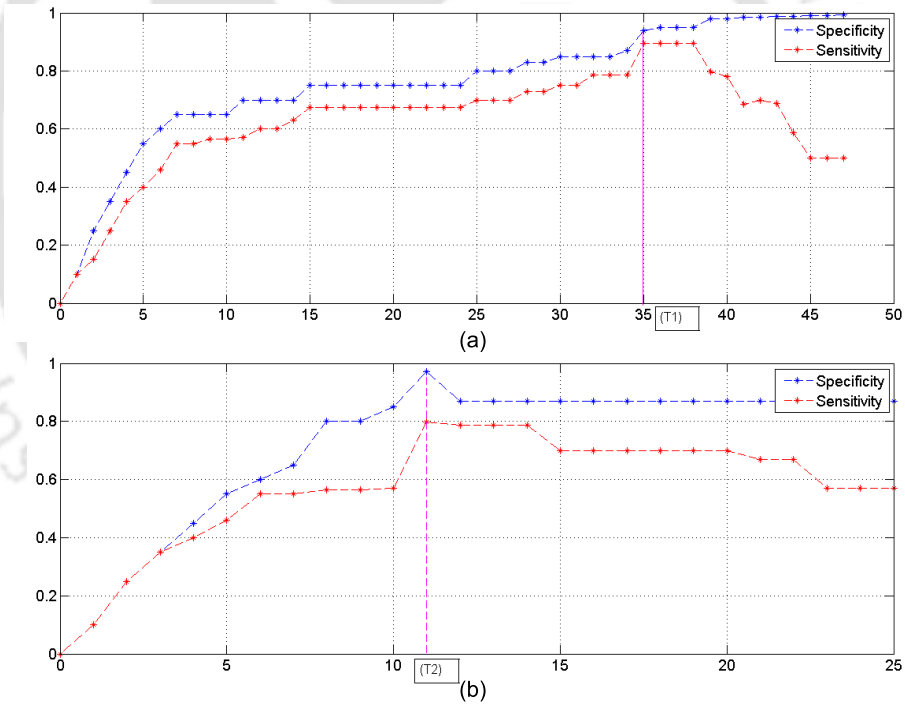

Figure 4.11: Parameter performance variation of sensitivity and specificity (a) with T1, (b) with T2.

Once detection of the HE is complete the next requirement of the automated DM detection is to determine the dark lesions present.

4.2 Localization of Dark Lesion

Dark lesions are formed from the BV outgrowth (called microaneurysms) and the dead blood cells leaked from BV's (called hemorrhages) during diabetes. These are the primary signs of DR and when

the depositions involve the macula, the eyesight becomes threatening. As we may observe from the review of dark lesion detection discussed in Chapter 2 Subsection 2.2.5, various investigations being performed in the direction of dark lesion detection are advantageous in their context. General image processing methods yield FPs, whereas machine learning techniques require more processing time. Considering these factors, we generate two algorithms for dark lesion detection. Where the first algorithm is derived using the color and intensity profile of lesions. The second algorithm is an improved version, constructed based on physiological and imaging issues along with FP elimination encountered during the process.

4.2.1 Proposed Dark lesion detection based on intensity profile

The MAs are bead-like structures formed in the capillary walls of BVs. These lesions are not properly visible in fundus images, and FFA images are required for their efficient detection. As the present algorithm uses fundus images, the distinct and visible MAs are only subjected to segmentation along with HMs. The detection of these structures by direct thresholding is influenced by the presence of the BV network and macula. Since the intensity profile of these features is similar, post-processing is required to eliminate falsely segmented structures, leaving only dark lesions. The combination of morphological processing with region-based segmentation helps in dark lesion detection.

In the proposed algorithm, image X, obtained during BV detection, (Chapter 3 subsection 3.1.0.2) is considered for dark lesion identification. Image X is first filtered using a standard deviation filter to eliminate the effect of macular regions having weak edge boundaries. The output obtained is then binarized using Otsu's threshold. The resultant image [Figure 4.12(b)] contains dark lesions and BV pixels. To eliminate the BVs, morphological dilation is performed by selecting a disc structuring element. The region growing is applied to the BV pixels considering the seed point of the OD mask. It gives only the BV network. The BV image is subtracted from the input image of region growing operation [Figure 4.12(b)], which eliminates all the connected BV regions. To regain the lesion information, morphological erosion is applied to the resultant image with the same structuring element. The output image still contains some isolated BV regions along with dark lesions. Therefore, to suppress these segments, morphological opening is applied to the image, removing the regions having higher connected regions. This process eliminates the effect of BVs, and the resultant image is left with dark lesions, as shown in Figure 4.12(c). The detected dark lesions are marked in blue over the input RGB fundus image shown in Figure 4.12(d).

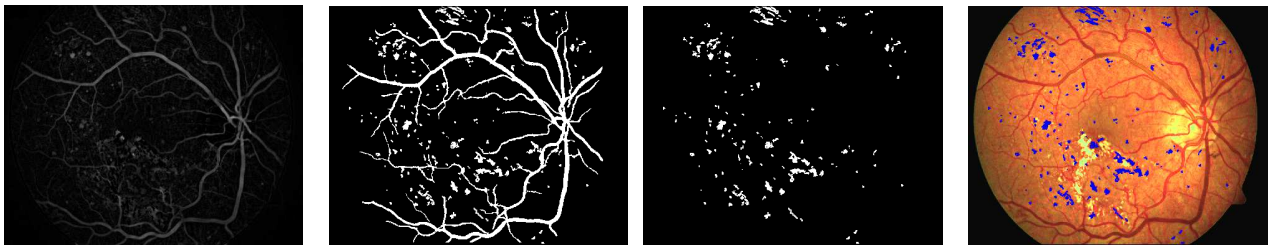

(a) (b) (c) (d)

Figure 4.12: Dark Lesion detection: (a) Image X, (b) Binarized image containing BV and dark lesions, (c) Dark lesion detected after eliminating other components, (d) Dark lesions overlapped on original RGB image.

4.2.1.1 Evaluation: Dark lesion detection algorithm 1

Considering similar image database being discussed in subsection 4.1.1.1, the algorithm is tested on 1374 images. The result of lesion detection is compared with the ground truth images. If the image is devoid of lesions, the processed image results in a clear image. Table 4.7 shows the result of dark lesion detection on all databases. The sensitivity, specificity, and misclassified proportions are calculated for each image containing lesions, and the average value found is mentioned in the table.

Table 4.7: Summary of dark lesion (MAs and HMs) detection

Databases	No. of Images tested	Images with Dark Lesion	Dark Lesion detected images	Average Sensitivity (%)	Average Specificity (%)	Misclassified proportion (%)
DRIVE	40	3	3	94.62	95.89	0.96
DIARETDB1	89	37	36	84.27	91.67	1.13
MESSIDOR	1200	439	423	79.59	96.52	1.62
HRF	45	15	14	91.82	98.54	1.01

Although advantageous, the detection algorithm's limitation lies with generated FPs due to small BV pixels. Therefore, the addition of measurements of BV structure is incorporated for updating the dark lesion detection algorithm. Hence, an efficient algorithm is proposed considering the fact of elimination of FPs.

4.2.2 Proposed improved Dark lesion detection

The novelty in this proposed algorithm includes the use of BV width property to eliminate BVs accurately from the candidate image and hence improve the detection of dark lesions.

The main steps involved in dark lesion segmentation are:

Step I. Image enhancement to correct improper illumination and segmenting out all possible dark regions in the image.

Step II. Removal of vascular structures using vessel width measurement and spatial properties of BVs.

Step III. Fine Detection of dark lesions.

4.2.2.1 Image correction and dark pixel localization

The image rectification steps involved during dark lesion detection are,

- Masking the input image with **FOV**(L) obtained in Section 4.1.2.1 and processing only the FOV region.
- Applying Tophat transformation as discussed in Algorithm 3, on Green plane image of **FOV**(L) twice resulting in converting the dark intensity fundus region to zero value pixel intensity.
- Locating the dark pixels by applying a zero value threshold.

4.2.2.2 Estimation of cross sectional diameter

The dark pixels obtained (say, image y) by applying zero value threshold contains all possible dark regions of fundus image including MAs, HMs, BVs, and Macula. The macula and fovea are located using our proposed algorithm on 'Detection of fovea using blood vessel relation' detailed in Chapter 3 Subsection 3.1. After detection, the macula obtained is masked in the image y. The next motivation is to find the diameter of all the possible dark lesion candidates and subsequently eliminating those that are not satisfying the required condition. The measurement of the vascular diameter is a challenging task, as various changes occur in the retinal BVs during disease. The algorithm finds the diameter of all the possible dark lesions, including the BV, and uses spatial geometry property of the vessels to remove them following Zhang et al. [239]. Initially, the diameter (D) of the ***FOV***$_{original}$ is taken and is used to find the desired parameters to determine vessel width in general. In this case, the parameter is set as $d = D/101$, which is found experimentally. Here, d denotes the average width of the vessels.

The first step in width measurement of the dark lesion candidates involves region extraction of each connected component and subsequent labeling. Now the key is to implement the algorithm on each component. The image skeleton and the edge of each component is determined. The edge

is obtained using the Canny edge detection method. Now, the center pixel in the skeleton image is taken, and a rotational invariant mask is subsequently created, which searches for edge pixels originating from the center [Figure 4.13(b)]. Taking eight possible angles of rotation, $0°$, $45°$, $90°$, $135°$, $180°$, $225°$, $270°$, $315°$, potential edge pixels are determined around the pixel position for each individual angle of rotation. As such, for all 8 angles, 8 edge locations are found, as shown in Figure 4.13(c) generating a rotational invariant mask. Next, the mirror pairs are selected to find the required diameter. Mirror angle is found by shifting to $180°$, and as such, there are 4 pairs present. Then, the Euclidean distance is calculated for each pair using equation, $\sqrt{(x_1 - x_2)^2 + (y_1 - y_2)^2}$. The minimum value obtained is then considered as the width of the cross-section.

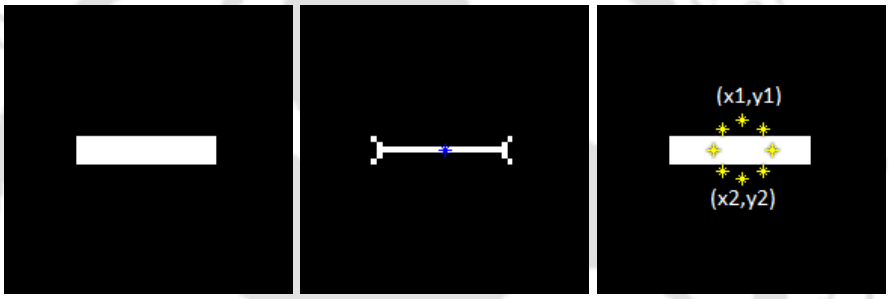

(a) Image Component (b) Image Skeleton (c) Rotational Mask

Figure 4.13: Steps in determining cross-sectional diameter of a segment.

Algorithm 4: *Locating Dark Lesion candidates*

1 function ED;
Input : Dark lesion candidate image, I_{DC}
Output: MAs ($I_{\mu A}$) and HMs (I_{HM}) detected image
2 **Hemorrhage detection:**
(a) Eliminate dark lesion candidates with $diameter \leq d$
(b) Remove residual BV FPs using morphological erosion operation resulting I_{HM}
3 **Microaneurysms detection:**
(a) Eliminate dark lesion candidates with $diameter > d$ [Say, output image be $I_{\mu AC}$]
(b) Mask OD over $I_{\mu AC}$
(c) Perform region growing with seed point across OD, [Say, output image be I_{reg}]
(d) Obtain microaneurysms using $I_{\mu A} = I_{\mu AC} - I_{reg}$
4 Mark input color image with detected MAs and HMs

4.2.2.3 Detection of dark lesions

To retain or eliminate the possible candidates of dark lesions, spatial calibration is performed to determine the required diameter of consideration. Now, the localization of MAs and HMs are done as per the algorithm 4. The sequence of the detection steps are shown in Figure 4.14.

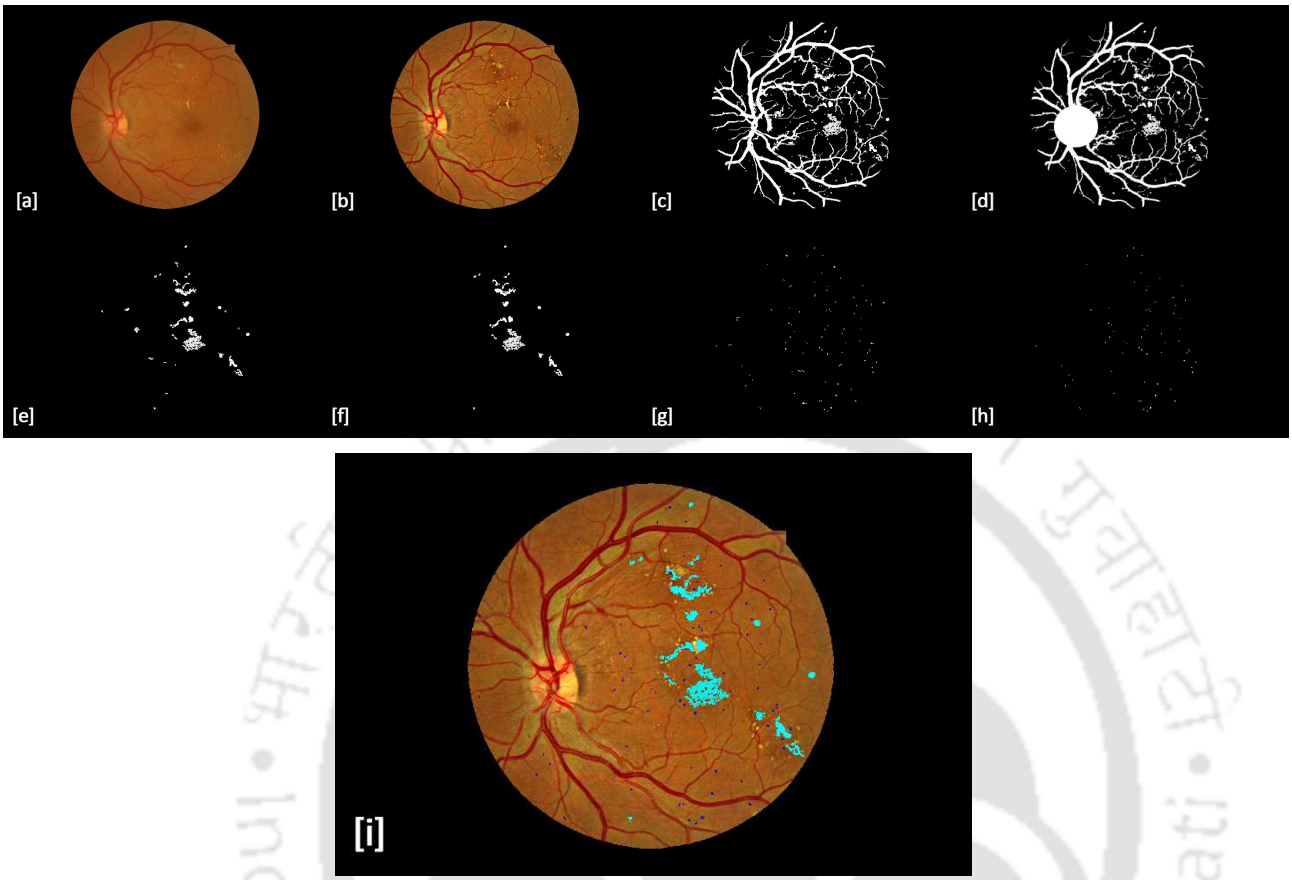

Figure 4.14: Steps showing Dark lesion detection: [a] FOV image, [b] Enhanced using Top hat transformations, [c] All dark regions detected, [d] OD masked over dark regions, [e] HM with FPs [f] Detected HM, [g] MA with FPs, [h] Detected MA and [i] Dark lesions over color FOV (HMs:light blue and MAs:dark blue color marker).

4.2.2.4 Evaluation: Dark lesion detection algorithm 2

To evaluate the algorithm, it is tested on database DIARETDB0, DIARETDB1, and MESSIDOR containing 1390 dark lesion images. The detected MA and HM are compared with ground truth data, and average sensitivity and PPV obtained are tabulated in table 4.8 and 4.9, respectively. The detection

Table 4.8: Result of MA detection

Databases	Tested Images	Average Sensitivity (%)	Average Positive Predictive Value (%)
DIARETDB1	84	76.6	64.8
DIARETDB0	124	84.3	82.9
MESSIDOR	1182	77.2	73.6

of MAs scores an average (mean) sensitivity of 79.37% and PPV of 73.76%. Whereas HMs has an average (mean) sensitivity of 91.56% and PPV of 85.96%.

Table 4.9: Result of HM detection

Databases	Tested Images	Average Sensitivity (%)	Average Positive Predictive Value (%)
DIARETDB1	84	94.3	90.1
DIARETDB0	124	93.6	92.3
MESSIDOR	1182	86.8	75.5

Table 4.10: Comparison of MAs detection methods applied on publicly available databases.

Author	Database	Sensitivity	Specificity
Kuivalainen et al.	DIARETDB0	73.00%	70.00%
Kauppi et al.	DIARETDB1	85.00%	53.66%
Bhalerao et al.	DIARETDB1	82.60%	80.20%
Agurto et al.	MESSIDOR	92.00%	54.00%
K. Ram et al.	DIARETDB1	90.00%	90.00%
Antal et al.	MESSIDOR	76.00%	88.00%
Kauppi et al.	DIARETDB1	80.00%	38.00%
Adal et al.	DIARETDB1	55.00%	80.00%
Roychowdhury et al.	DIARETDB1	80.00%	85.00%
	MESSIDOR	100.00%	53.16%
	MESSIDOR	100.00%	53.16%
Figueiredo et al.	DIARETDB1	77.38%	80.00%
	DIARETDB0	72.48%	80.00%
	DIARETDB1	**76.60%**	**81.60%**
Proposed Method	DIARETDB0	**84.30%**	**93.50%**
	MESSIDOR	**77.20%**	**85.10%**

Table 4.11: Comparison of HMs detection methods applied on publicly available databases.

Author	Database	Sensitivity	Specificity
Kuivalainen et al.	DIARETDB0	92.00%	75.00%
Kauppi et al.	DIARETDB1	16.70%	83.70%
Kauppi et al.	DIARETDB1	80.00%	73.00%
Tang et al.	MESSIDOR	93.00%	66.00%
	MESSIDOR	74.36%	91.81%
Figueiredo et al.	DIARETDB1	73.58%	85.00%
	DIARETDB0	72.48%	80.00%
	DIARETDB1	**94.30%**	**95.36%**
Proposed Method	DIARETDB0	**93.60%**	**97.10%**
	MESSIDOR	**86.80%**	**94.30%**

The comparison of proposed MAs and HMs detection is performed with available standard automated methods and represented in Table 4.10 and Table 4.11. The comparison is based on the experiment being performed on the publicly available database DIARETDB0, DIARETDB1, and MESSIDOR. But the database selection varies in different methods. The proposed algorithm performs better in comparison to others concerning sensitivity and specificity.

The automated algorithm once detects the lesions present; the next step is to classify and grade

DM by obtaining the lesion position in the fovea neighborhood. In this connection, we have proposed both unsupervised and supervised learning to analyze the same.

4.3 Grading Diabetic Maculopathy

Depending on the position of lesions (dark and/or bright) concerning to the fovea, the DM subjects may be divided into four stages. They are, normal stage: absence of lesions, mild stage: lesions located at a region of 2ODD, moderate stage: present at 1ODD and severe stage: when found at $(1/3)$ODD [8, 47, 50, 59, 124]. The stages are marked by concentric circles generated with center at the fovea. Further, the stages are also classified as non-CSME for mild and CSME for moderate and severe stages.

Here, in this section, we have first classified DM based on the position of lesions in the fovea neighborhood and reported the results discussed as unsupervised DM grading in the subsequent subsection. After that, we have analyzed the classification using supervised learning. We apply the lesion's features to SVM classifier for DM classification. Later, the texture features are estimated to determine the lesion deposition.

4.3.1 Unsupervised DM Grading

To mark the DM stages from the fovea center, three regions are created using the following equations.

$$(x - x_1)^2 + (y - y_1)^2 = \left(\frac{z}{3}\right)^2 \tag{4.10}$$

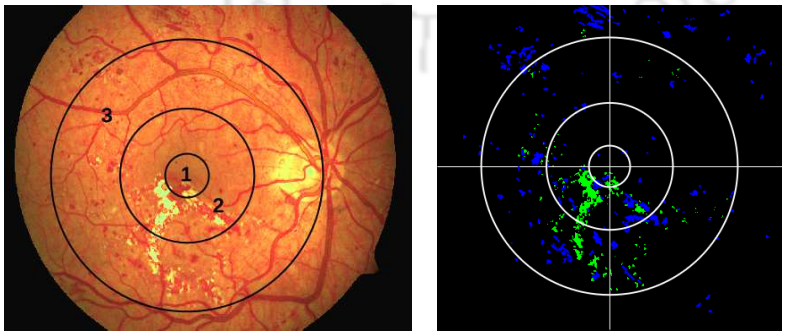

(a) (b)

Figure 4.15: Grading of Maculopathy (a) Fundus Image showing various stages of maculopathy (region 1=severe, 2=moderate, 3=mild) ; (b) Lesions overlapped on different macular regions.

$$(x - x_1)^2 + (y - y_1)^2 = (z)^2 \tag{4.11}$$

$$(x - x_1)^2 + (y - y_1)^2 = (2z)^2 \tag{4.12}$$

where, (x_1, y_1) is the fovea and z represents the diameter of OD. The equations (4.10), (4.11), (4.12) represent the concentric circles marked as circle 1, 2 and 3 respectively in Figure 4.15(a). If lesions are located in these circles, then, the DM is considered as severe, moderate and mild stages respectively. After identifying the DM stage, the severity level may be estimated by calculating the percentage coverage of lesions in these regions. In this connection, the area of the concentric circles are determined using the following equations (4.13) , (4.14), (4.15) respectively.

$$A_{severe} = \frac{\pi z^2}{4} \tag{4.13}$$

$$A_{moderate} = \frac{2\pi z^2}{4} \tag{4.14}$$

$$A_{mild} = \frac{13\pi z^2}{4} \tag{4.15}$$

For severity assessment, the number of lesion pixels lying over the different regions is calculated. Comparing this number with the total area of the annular ring of the concentric circle, one can estimate the percentage coverage of lesions. The comparison is made for calculating lesion coverage during moderate and severe cases of maculopathy. This process has a dual advantage. First, it helps in estimating how much a patient's sight gets affected by DM in a severe case. The more is the percentage coverage of fovea; the more likely the patient to loose vision [23,47,50,54,59,124,253,254]. Second, on repeated examination of a patient under treatment with positive/moderate DM, this helps in estimating the retina condition for preventive measures.

4.3.1.1 Evaluation: Unsupervised DM classification

The unsupervised DM assessment is performed over the first algorithm based on color and intensity profile for Dark and Bright lesion detection. Out of the total of 1374 images being analyzed from DRIVE, DIARETDB1, MESSIDOR, and HRF, the DM assessment is performed on images containing

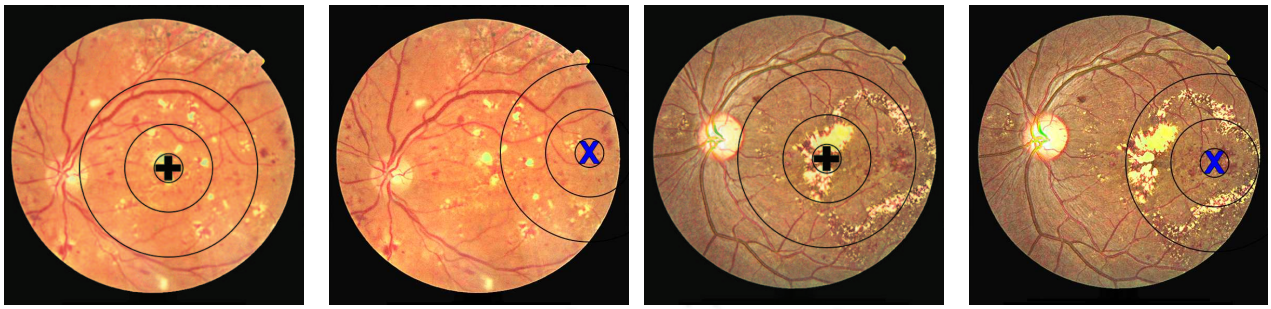

(a) (b) (c) (d)

Figure 4.16: Diabetic maculopathy assessment errors: (a)(c) Actual case and (b)(d) Misclassified case.

lesion. The manual identification done earlier has been used as a gold standard for comparing the result.

Table 4.12: Summary of Maculopathy detection

Databases	No. of image tested with lesions	Detection of Maculopathy cases					Analysing parameter	
		Positive DM case	Correctly Detected (TP)	Correctly Rejected (TN)	Wrongly Detected (FP)	Wrongly Rejected (FN)	Sensitivity (%)	Specificity (%)
DRIVE	8	7	7	1	0	0	100	100
DIARETDB1	38	35	34	3	0	1	97.14	100
MESSIDOR	694	589	560	105	5	29	95.07	95.45
HRF	15	14	14	1	0	0	100	100

The sensitivity and specificity of the proposed method based on DM detection are calculated and are shown in Table 4.12. The proposed DM detection method has been compared with other existing methods. The comparison statement is given in Table 4.13. The result shows that the algorithm performs better for DM identification in different types of images. After the identification of DM, its stage is determined by detecting the presence of lesions over the masks. The results obtained are tabulated in Table 4.14. From the table, we can notice that 3 images with moderate DM are not classified. This is because they are wrongly classified as mild and severe due to improper illumination. The severity of the disease may be evaluated by calculating the percentage coverage of lesions over the masks. In this direction, the overall severity obtained for mild stages ranges between 10% to 37%, moderate cases from 2% to 64%, and severe stages from 7% to 92%.

Improper localization of fovea leads to wrong assessment of DM severity. As shown in Figure 4.16, the images (b) and (d) show the wrong assessment on severity level whereas, the actual one is given in images (a) and (c), respectively. The correct evaluation for both the images is the severe stage of DM, but due to the misidentification of the fovea, the stages are classified as mild. Hence such images do not undergo the evaluation process as discussed in subsection 3.1.3. Figures 4.17

Table 4.13: Comparison of diabetic maculopathy detection

Methods	Average Sensitivity (%)	Average Specificity (%)
Deepak et al. [59]	95	90
Siddalingaswamy et al. [50]	95.6	96.15
Tariq et al. [45]	96.7	98.29
Tariq et al. [46]	97.2	98.32
Zaidi et al. [57]	93.5	95.81
Proposed method	98.05	98.86

Table 4.14: Severity assessment of maculopathy based on DM detected cases

Databases	Mild		Moderate		Severe	
	Input Image	Detected Image	Input Image	Detected Image	Input Image	Detected Image
DRIVE	1	1	3	3	3	3
DIARETDB1	4	4	17	16	13	13
MESSIDOR	126	126	272	270	162	162
HRF	3	3	6	6	5	5
TOTAL	134	134	298	295	183	183

and 4.18 show the steps for determination of DM on images from each database. Figure 4.17 shows the application of the proposed method on normal images from DRIVE and MESSIDOR, respectively. Since no lesions are found in healthy images, they are not processed further for DM classification. Figure 4.18 shows application on pathological images from DIARETDB1 and HRF databases.

4.3.2 Supervised DM grading

In this algorithm, we have determined the features of detected lesions from the original green plane image and utilize them as an input to the SVM classifier. The algorithm first determines the positive DM cases and classifiy them as per the stage of severity. The moderate and severe stage, together called as CSME stage is analysed further based on the features of the individual lesion. To determine the DM stages, the concentric circles are drawn from the fovea center, as discussed in our previous unsupervised learning method given in equations 4.10, 4.11, and 4.12, [Figure 4.15] representing severe, moderate and mild stages respectively. The identification and grading of DM starts from detected lesions localization. The absence of such candidates mark normal and healthy retina. Whereas, with the presence of lesions, we initially obtain their location to determine the DM stage and later estimate the lesion features of CSME stage for classification and grading into average and intense class using the SVM classifier. To train the system, we have used 80% images of every

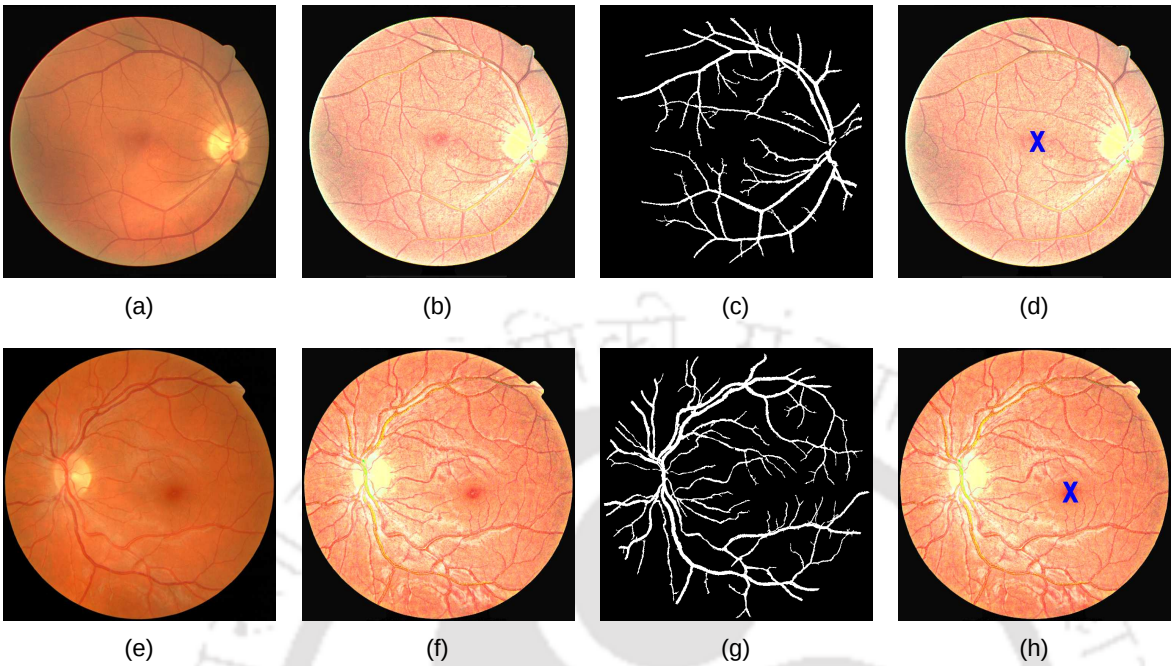

Figure 4.17: Identification of maculopathy stages (a-d) DRIVE and (e-h) MESSIDOR database.

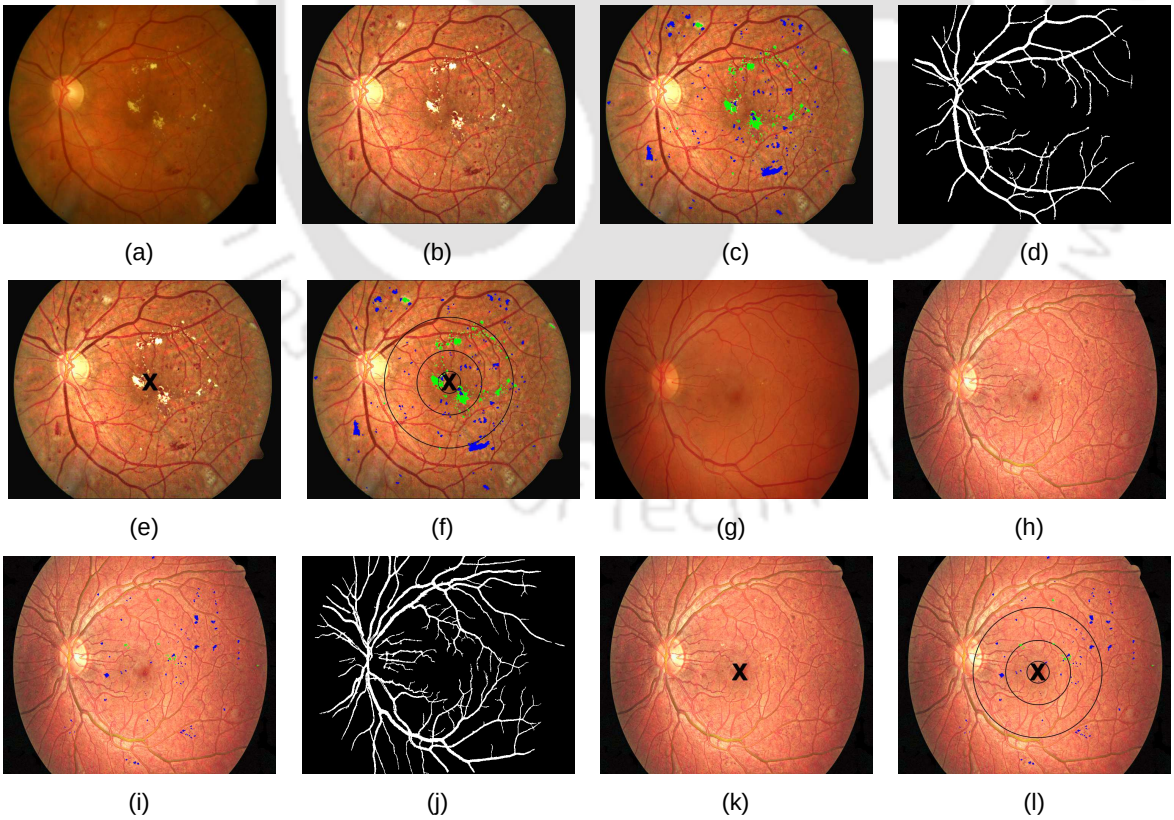

Figure 4.18: Identification of maculopathy stages (a-f) DIARETDB1 and (g-l) HRF database.

database and tested it over the remaining 20%.

4.3.2.1 Feature Extraction

For efficient grading of DM, various features are extracted from the lesions present. The green channel of RGB image containing only lesion areas is considered for the feature extraction. The identification is carried out in two categories, (a) Grading DM classes and (b) Inter lesion classification for CSME cases.

Category A: Grading of DM classes is measured concerning the position of the lesion and the amount of area covered. As lesions occupying a large area and the position nearer to the fovea, both are signs of increased DM severity. To mark the area coverage by lesions, shape-based features like area, perimeter, and circularity is calculated from the detected lesions. The amount of area and perimeter represents the percentage coverage, whereas higher circularity value denotes distinct deposition. Which means more the value higher is the grade. The shape-based features are measured from the connected lesion regions in the image. The boundary pixels do the necessary action to calculate the area and perimeter. The circularity feature is obtained from the area and perimeter to find the compactness of lesions. Considering the boundaries of lesions pixel $b\,(i,j)$ be $B_d\,(i,j)$; the features are,

- Perimeter (f_1): Measures the perimeter of the lesion segments.

$$P = \sum_{i,j=0}^{M,N} B_d\,(i,j) \tag{4.16}$$

- Area (f_2): Calculates the area of the lesion segments.

$$A = \sum_{i,j=0}^{M,N} b\,(i,j) \tag{4.17}$$

- Circularity (f_3): Determines compactness of lesions.

$$C = \frac{4\pi A}{P^2} \tag{4.18}$$

For obtaining position feature, Euclidean distance of the lesion centre and fovea is calculated. Say, (x_1, y_1) is the fovea centre and (x_2, y_2) is lesion centre, therefore the Euclidean distance is given by,

- Euclidean distance: Enumerates lesion closeness from fovea.

$$D = \sqrt{(x_1 - x_2)^2 + (y_1 - y_2)^2} \tag{4.19}$$

The severity of DM is higher for the smaller value of the Euclidean distance. Obtaining these features helps us to grade the classification of DM. One such example is shown in Figure 4.19 for reference. The features obtained for moderate and severe cases, which constitute CSME, are recomputed concerning individual lesions and fed to SVM classifiers along with other features discussed in the next subsection for inter lesion classification.

Category B: Inter lesion classification is performed for CSME cases. The connected lesions present in the CSME region are marked using a label matrix. The inter lesion variability signifies how severe the patient is and what are the properties of lesions present. It classifies whether the deposition is intense or average for both dark and bright lesions. To identify such properties, the texture features are explored. For the classifier, each connected lesion is considered as an object with *m*-features, and the classification is done based on all lesions present in different patient images. To reduce FPs,

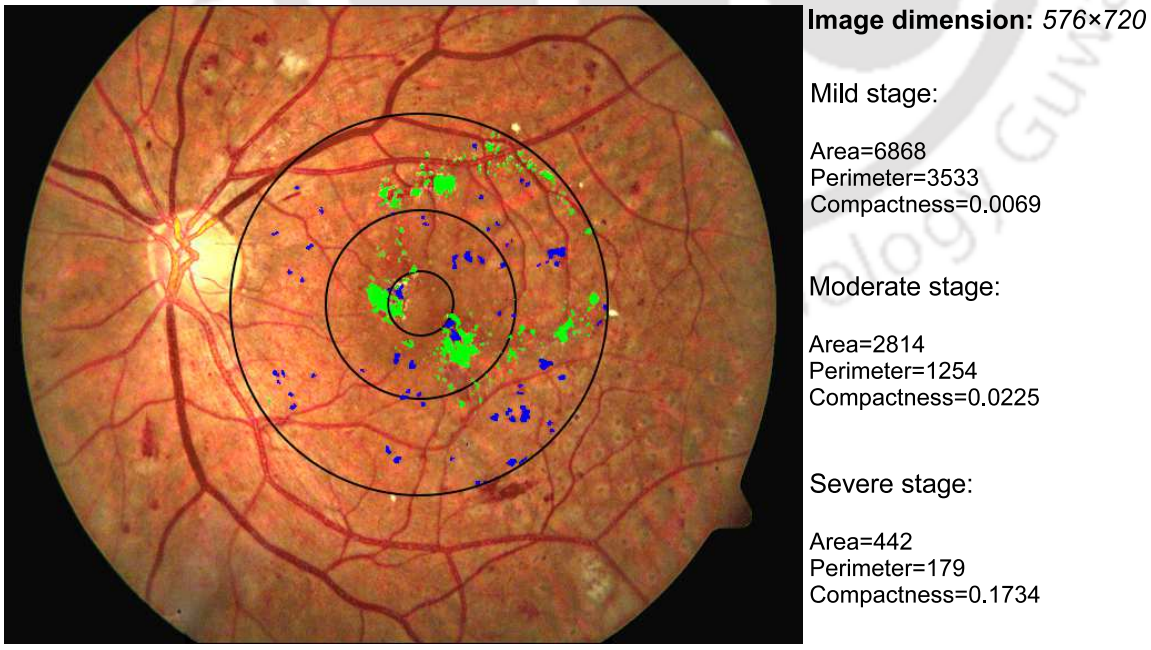

Figure 4.19: Example showing features extracted; area, perimeter and compactness of various DM stages represented by lesion availability within the concentric circles. Green coloured pixel here represent the HEs and Blue coloured pixels represent MAs and HMs.

we train and test the databases individually. The Gray Level Co-occurrence Matrix (GLCM) method extracts second-order statistical texture features [255]. In GLCM the texture feature is obtained by the occurrence of pairs of pixels in spatial functions. This spatial relationship exists in between neighboring pixels. The size of the GLCM is proportional to gray levels of the image. The combinations of gray levels variation in an image is tabulated with the help of GLCM in a matrix form. The relative and their orientations are the parameters of the co-occurrence matrix. The orientations are given in 0, 45, 90, and 135 degrees to represent horizontal, diagonal, vertical, and anti-diagonal respectively [255]. The GLCM algorithm is described in Algorithm 5. Along with texture; shape and position features are also included to classify the severity.

Algorithm 5: *GLCM feature extraction*

1 function GLCM;
Input : Lesion candidates, I_L
Output: GLCM features
2 Consider a operator Q that defines the position of two pixels relative to each other.
3 Consider an image f with L possible intensity levels.
4 Consider a matrix G, whose element $g(i,j)$ is the number of times that pixel pairs with intensities z_i and z_j occurs in image f in position specified by operator Q.
5 Consider, N is the number of rows and columns of image co-occurrence matrix G, $P(i,j)$ is the probability that a pair of points satisfying operator Q, have values (z_i, z_j). m_r and m_c are the mean of rows and columns respectively.
6 Consider, K is the row or column dimension of co-occurrence matrix G. The probability always in range $[0,1]$ and sum is always 1.

$$\sum_{i=1}^{K}\sum_{j=1}^{K} P_{i,j} = 1$$

7 Compute GLCM features:

- Energy (f_4): A measure of uniformity.

$$E = \sum_{i=1}^{K}\sum_{j=1}^{K} P_{i,j}^2 \tag{4.20}$$

- Contrast (f_5): Intensity contrast between a pixel and its neighbour.

$$C = \sum_{i=1}^{K}\sum_{j=1}^{K} (i-j)^2 P_{i,j} \tag{4.21}$$

- Correlation (f_6) & Dissimilarity (f_7): How a pixel is correlated and differ to its neighbour.

$$Corr = \sum_{i=1}^{K}\sum_{j=1}^{K} \frac{(i-m_r)(j-m_c)P_{i,j}}{\sigma_r \sigma_c} \quad , \quad D = \sum_{i,j=1}^{K} P_{i,j}\,|i-j| \tag{4.22}$$

- Homogeneity (f_8): Closeness of distribution of elements in the GLCM to the diagonal.

$$C = \sum_{i=1}^{K}\sum_{j=1}^{K} \frac{P_{i,j}}{1+(i-j)} \tag{4.23}$$

- Entropy (f_9): Measure of randomness.

$$H = \sum_{i,j=1}^{K} P_{i,j}\,(-\ln P_{i,j}) \tag{4.24}$$

4.3.2.2 Classification Using Support Vector Machine

Support Vector Machine is a popular supervised machine learning algorithm [256], which uses a structural risk minimization principle to construct hyperplanes and support vectors for better discrimination of lesion depositions in positive DM cases [45, 47, 48, 248]. Support vectors are the points lying close to the separating hyperplane. The maximum width, which is parallel to the separating hyperplane with no data points between them, is known as the margin. More is the margin between the two-class, more compelling is the hyperplane. The advantage of the SVM classifier is that it works for both separable and non-separable data. Non-separable data can be converted into a separable form using kernel functions such as linear, polynomial, quadratic, and radial basis function (RBF).

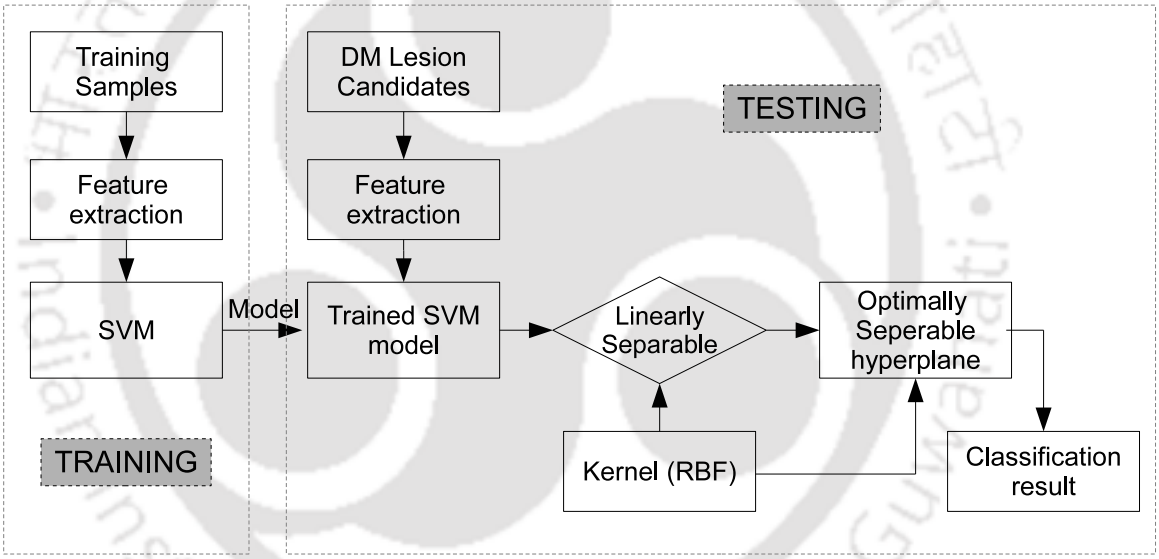

Figure 4.20: Block diagram of SVM classification scheme.

Figure 4.20 shows the block diagram of the SVM classification algorithm. As per the classification scheme, the features obtained from the lesion candidates of test set are given to the trained SVM classifier, which results in a binary matrix showing classification output. The RBF kernel function is applied to the SVM classifier with two widely used spread parameters (β and C), which are achieved using grid search method.

The e-ophtha EX dataset contains a total of 47 bright and 148 dark lesions containing images with few overlapping. Out of these, 33 bright and 69 dark lesion images represent positive DM cases. The identification scheme excludes the images which are OD centric, as the fovea information to classify DM is incomplete. One such example is represented in Figure 4.21. To train and cross-

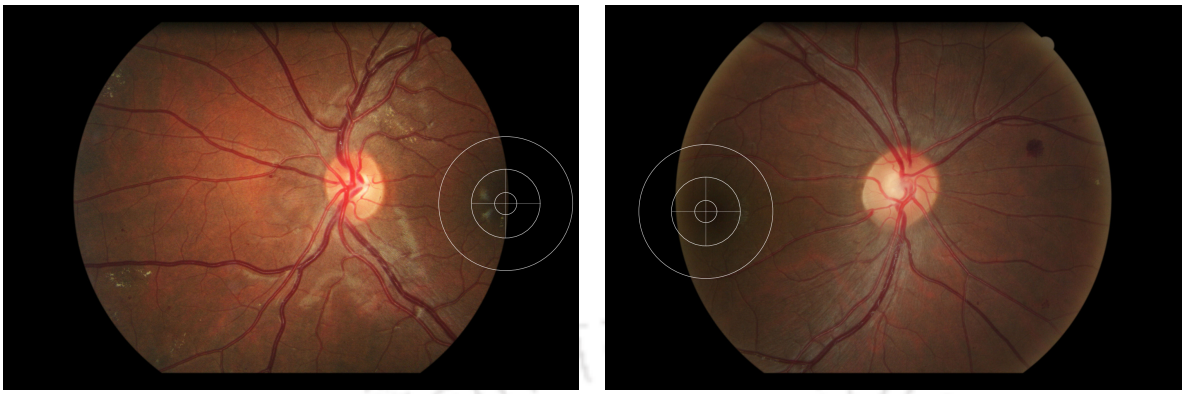

(a) (b)

Figure 4.21: Examples of OD centred fundus image from e-ophtha EX database where DM classification is not possible. Hence such cases are omitted.

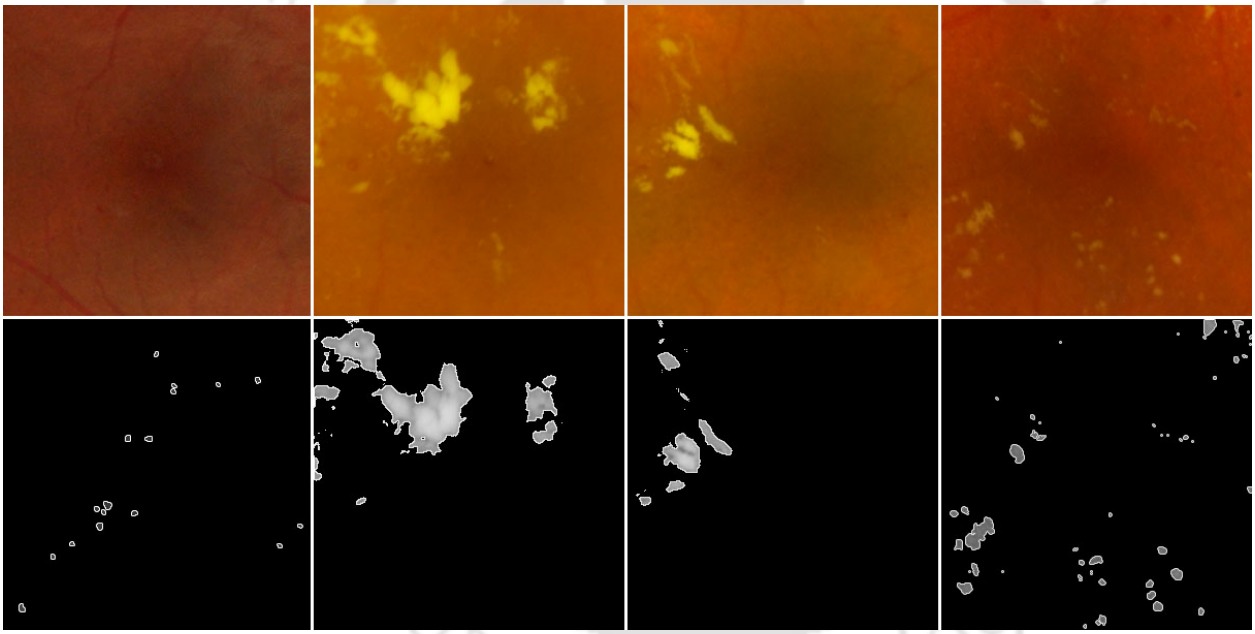

Figure 4.22: Detected lesions used for feature generations. Row 1 represents original image CSME regions and Row 2 represents corresponding detected lesions in green plane image.

validate the algorithm, the connected lesion segments are taken into consideration. Out of a total of 102 images, 80% (82 images) are considered for training the classifier. The rest 20% (20 images) are used for validation. The training sample, therefore, constitute total 1-50 connected regions [as shown in Figure 4.22], of size 20 to 500 pixel from every image of 81 manually selected ground truth data. These regions are divided into average and intense lesions. The division is based on the amount of lesion deposition. The SVM classifier is operated over e-ophtha EX dataset on pixel level with a 10-fold cross-validation. The database used for cross-validation is randomly split into 10

exclusive subsets of approximately equal size (D1, D2, D3,....., D10). The segments from a total of 81 images train the SVM classifier, and the remaining 21 images result in the binary matrix output. This procedure is repeated 10 times to obtain the required classification result.

To make a training vector set, the lesion candidates are manually selected from every trained images. From every pixel of lesion candidate the feature vector is generated based on 9 key features, $f_i, i = 1, 2, ...9$ The acquired training sample set (f_j, g_j) is utilized to train the SVM. Here g_j represents the category flag expressed as,

$$g_j = \begin{cases} -1 & , \quad f_j \in A \\ +1 & , \quad f_j \in B \end{cases} \tag{4.25}$$

where, $j \in \{1, 2, 3, ...W\}$, W is the dimension of sample vector set. In the training sample of the e-ophtha EX database, approximately $W = 13,700$ training samples are manually selected from 81 images. A and B represent the average and intense regions. The 10-fold cross-validation is repeated three times by considering three different manual segmentation of the data by three experts. This step is carried out to validate the accuracy of the algorithm. Similarly, the classification algorithm is tested on DRIVE (7images), HRF (14images), and DIARETDB1 (35images) databases using the annotations made by three experts.

4.3.2.3 Evaluation: Supervised DM classification

The images from the databases e-ophtha EX, DRIVE, HRF, and DIARETDB1 are processed with the second algorithm of lesion detection explained in subsections 4.1.2 and 4.2.2; and are subjected to DM classification and grading. The efficiency of the automated algorithm has been reported in Table 4.15. The algorithms detect DM classes with an overall efficiency of 98.73%. Once positive DM cases are classified into the respective stages of DM, the severity is graded with the application of SVM classifier, applying shape and GLCM based features.

Evaluation of the 10-fold cross-validation of the classifier is performed over the four databases. The performance measures such as sensitivity, PPV, and F1-Score are calculated for each image, with respect to it's mean and standard deviation within all images under consideration. For reliability testing of the classifier, the standard deviation of the three repeat evaluation is carried out. The three repeat evaluation mentioned here represents the testing of classifier over ground truth data generated by three experts. For repeatability examination, the analysis of variance (ANOVA) test [62] is

Table 4.15: Classification of DM classes on four databases

Databases	DM cases		Mild		Moderate		Severe	
	Positive DM cases	Detected DM cases	Input image	Detected image	Input image	Detected image	Input image	Detected image
e-ophtha EX	102	100	48	47	23	22	31	31
HRF	14	14	3	3	6	6	5	5
DIARETDB1	35	35	4	4	17	17	13	13
DRIVE	7	7	1	1	3	3	3	3
Total	158	156	56	55	49	48	52	52

carried out between the three repeats. The statistical analysis of the algorithm shows minimum and

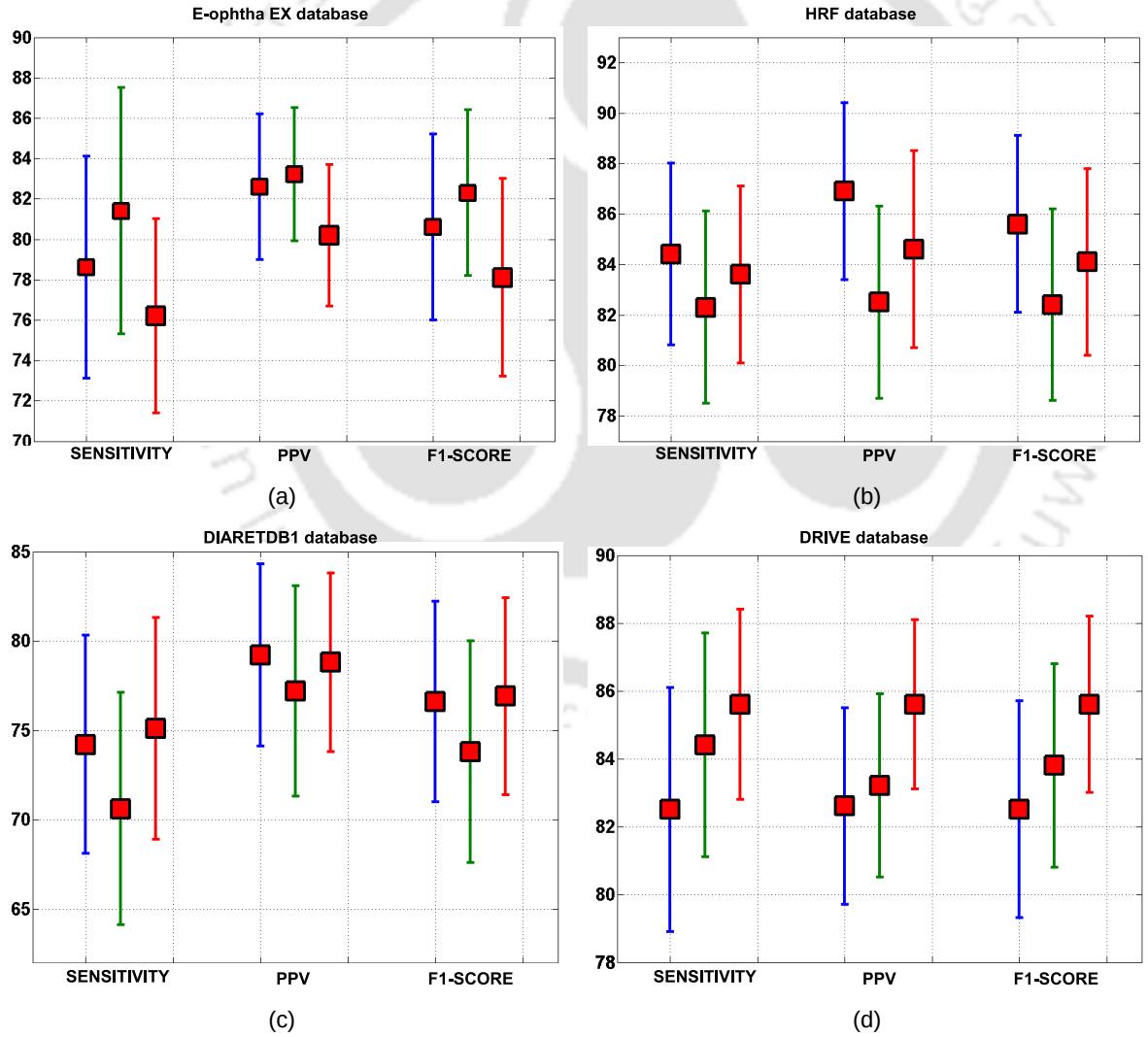

Figure 4.23: Statistical data analysis of classifier. Mean and standard deviation of sensitivity, PPV and F1-score. Three repeat measurements are shown by three different operators in blue, green and red colour: (a) e-ophtha EX database data (b) HRF database data (c) DIARETDB1 database data (d) DRIVE database data.

negligible differences between the three repeat measurements. The performance analysis on different databases with respect to three repeat tests is represented in Figure 4.23. The average mean and standard deviation of sensitivity, PPV, and F1-score for the four databases for three repeat evaluation tests are tabulated in Table 4.16. The repeatability of the algorithm is measured by calculating the standard deviation of the three sets concerning sensitivity, PPV, and F1-score for every image.

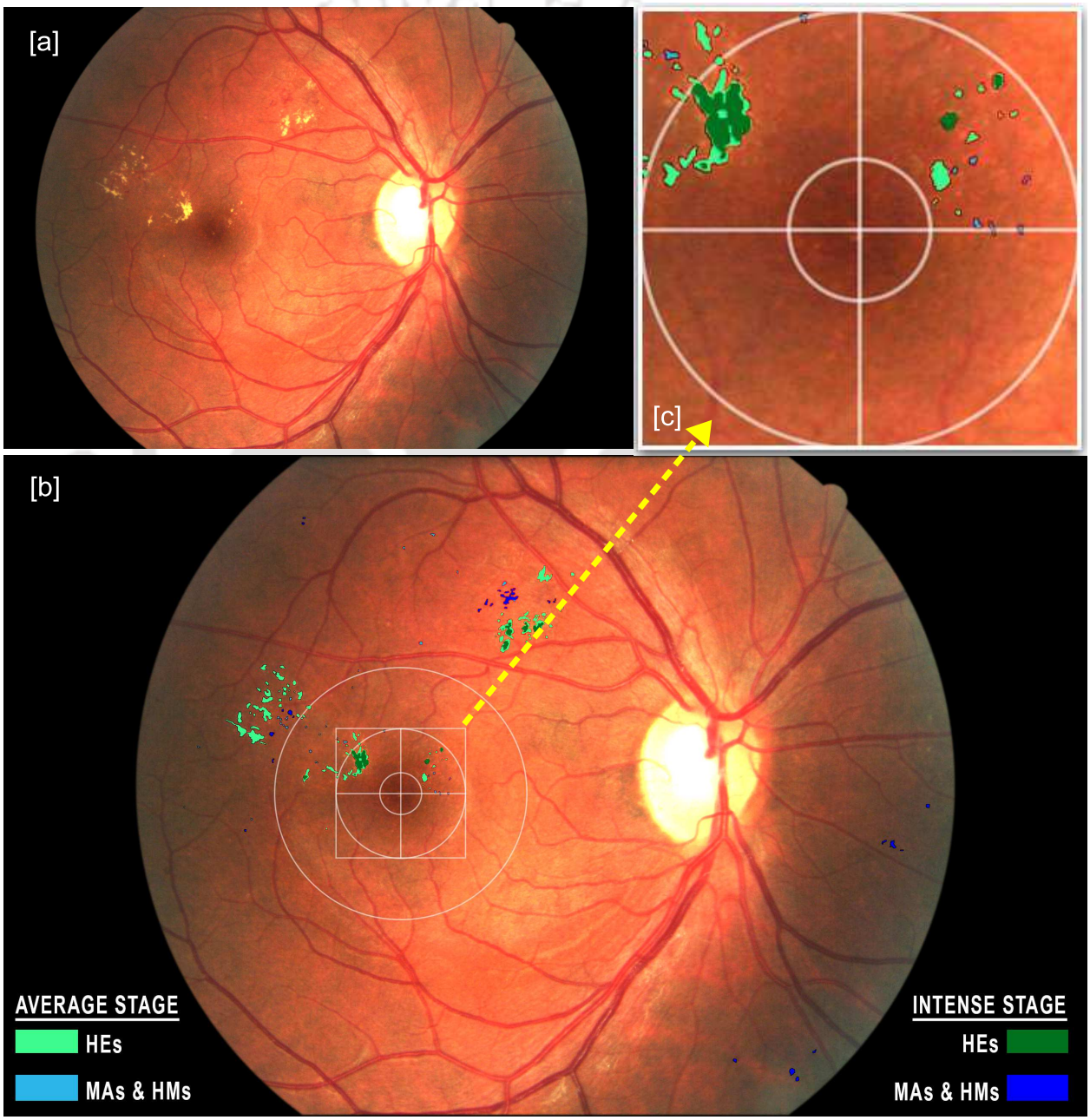

Figure 4.24: Classification and grading of DM: (a) Enhanced input image, (b) DM classification based on lesion position and deposition strength (green color lesion describes the HEs and blue color lesions are MAs and HMs), (c) Zoomed CSME region showing lesions presence and representation of average and intense lesions.

The value of standard deviation ranges from $0.2 \sim 5.2$ for the databases, which shows that the DM grading is sufficiently stable.

Table 4.16: Statistical data analysis with average mean and standard deviation of sensitivity, PPV and F1-score of four databases.

DATABASE	average Sensitivity	average PPV	average F1-score
e-ophtha EX	78.7±5.5	82.0±3.5	80.3±4.5
HRF	83.4±3.6	84.7±3.7	84.0±3.7
DIARETDB1	73.3±6.3	78.4±5.3	75.8±5.8
DRIVE	84.2±3.2	83.8±2.7	84.0±2.9

An example of DM grading from the e-ophtha EX database is shown in Figure 4.24. Here the stages of DM are classified, and the grading of DM based on lesion deposition intensity is presented for the whole image. As seen from the fundus image, the DM stage suffered by the patient is moderate. The intense classes are represented by dark intensity for both types of lesions. Here green color represents HEs and blue color for MAs and HMs.

4.4 Summary:

This chapter deals with the detection of diabetic lesions and the classification of diabetic maculopathy based on the deposition of these lesions in the macula neighborhood. The detection of both dark and bright lesions, comprising of MAs, HMs, and HEs, is a challenging task. Considering all the challenges, we have proposed detection algorithms that perform efficiently. Publicly available databases, namely DIARETDB0, DIARETDB1, MESSIDOR, HRF, e-OPHTHA, are analyzed for testing of the proposed algorithms.

The novelty of detection of HE is that it considers all the challenges of causing FPs during identification. The hindrance removed is, elimination of OD, lesions other than HE, reflections occurred during healthy retinal imaging such as BV and macular reflections. Detection and masking of OD using the property based on the presence of maximum BV helps in finding the exact location of OD. BV reflection is taken care of using the BV template obtained from the detection of major BVs. The macular reflection is eliminated considering the color property of the reflections. The reflection component consists of pixel values in blue color plane, where-as HE pixel values, in blue plane is zero. Utilization of the edge strength performs the isolation of HE from other bright lesions. The proposed method detects exudates containing both hard and soft with an average sensitivity of 77.73%, specificity

98.72%, and misclassified proportion of 1.003%. The detection of HE is tested using image-level evaluation and scored an average sensitivity of 96.87% and a positive predictive value of 93.10%. The pixel-level testing scored an average of 87% sensitivity, 90.5% PPV, and 88.7% F1-score.

The detection of MAs and HMs includes novelty of eliminating similar intensity BV pixels, which usually create FPs in the segmented output. These FPs are eliminated utilizing connectivity property, and the algorithm scores an average sensitivity of 87.58%, specificity 95.66%, and a misclassified proportion of 1.18% for both the lesions. This method eliminates maximum BVs except the non-connected ones. Hence, an enhanced algorithm is proposed considering the BV width property. The algorithm generates a response of 79.37% sensitivity and 73.76% PPV for MA and 91.56% sensitivity and 85.96% PPV for HM detection.

The detected lesion's locations are checked in fovea neighborhood for the classification of DM stages. The images scanned for the lesion localization are analyzed further. Stages of DM are marked at a distance of 2ODD, 1ODD, and 1/3ODD from the fovea center to mark mild, moderate, and severe stages. The proposed method detects DM with an average sensitivity of 98.05% and specificity of 98.86%. The average detection accuracy of the DM stages is 100%, 98.99%, and 100% for mild, moderate, and severe cases. The grading of these lesions is performed by investigating the features they possess. Shape features are explored to identify the compactness and area coverage by the lesions, and later Gray Level Co-occurrence Matrix method is used for determining texture features for identification of amount of deposition. These features are then introduced to a SVM classifier with a kernel of RBF to classify the depositions into two classes, namely average and intense. The algorithm detects DM classes with an overall efficiency of 98.73%. The statistical analysis of the classifier shows an overall average of 79.9$\pm$4.7% sensitivity, 82.2$\pm$3.8% PPV, and 81.0$\pm$4.2% F1 score. The standard deviation ranges from $0.2 \sim 5.2$ that represents a sufficiently stable DM grading.

The comparison of the proposed algorithms with standard methods shows that it performs better with more accuracy of detection along-with eliminating the hindrances faced during analysis.

The investigation of the retina using a fundus image is sufficient for the detection and evaluation of DM cases. But there are few complexities like swelling of the retina, retinal detachment, formation of cystoid fluids in cellular layers of the retina, are difficult to understand in fundus images. Therefore to diagnose DM with changes occurring in retinal layers we must investigate OCT images.

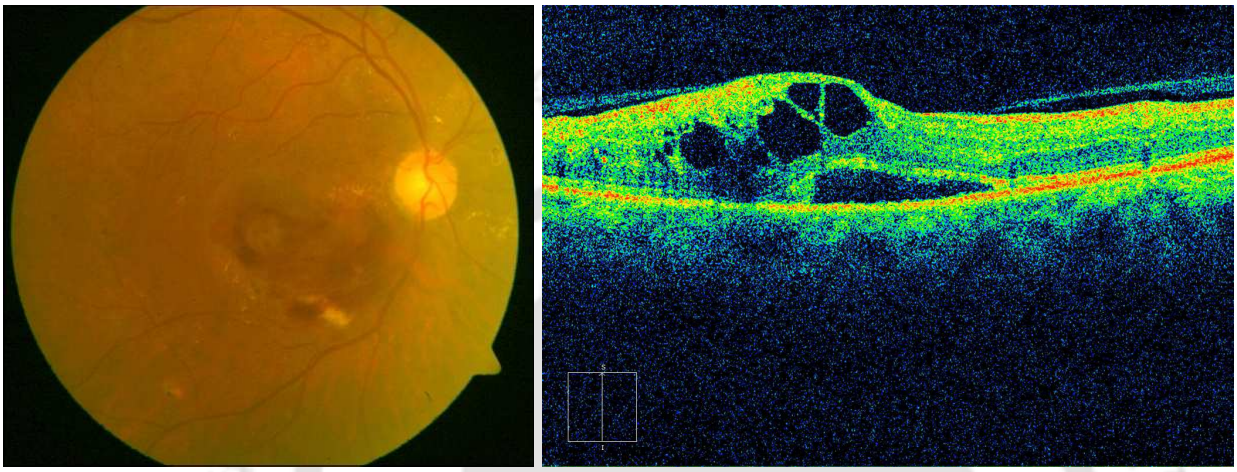

Figure 4.25: Patient retinal images: [a] Fundus image, [b] OCT image.

For example as seen in the Figure 4.25(a) one can presume that the patient has DM but when we investigate the corresponding OCT image of the same person as shown in Figure 4.25(b) it is very much clear that the severity is very high including macular swelling and cyst formations. Due to such reasons, the ophthalmologists suggests OCT image verification along with fundus image. Therefore, the analysis of OCT images for DM evaluation is taken into consideration, and an automatic detection method has been formulated and discussed in the next chapter.

5

Diabetic Maculopathy analysis using OCT Image

Contents

Diabetic maculopathy results from the leakage of extracellular fluids within the retinal layers. These depositions eventually form cystoid fluids or cysts, which increases the retinal thickness. Ophthalmologists observe the spread of the cysts and thickness of the retinal layers to determine the severity of the DM. As described in the previous chapter, the fundus image may not be sufficient for a reliable diagnosis of DM, as it does not provide the information of changes occurring within retinal layers. Therefore, in this chapter, we have exploited the OCT images for the detection and analysis of DM. Here in the proposed algorithm, we have measured the thickness of the Inner Limiting Membrane and Retinal Pigment Epithelium layer for the identification of DM and, afterward, detection of cyst and its spread within the retinal layers. As alluded in Chapter 1, Figure 1.13 the automated detection algorithm for analysis of DM using OCT image consists of three main steps; 1. speckle-noise elimination for better segmentation, 2. retinal layer localization for DM detection and 3. cystoid fluid detection for positive DM subjects. Processing of these individual steps is very much challenging due to various issues intervened. The details on handling these issues and the novelty of the algorithm are detailed in the subsequent subsections.

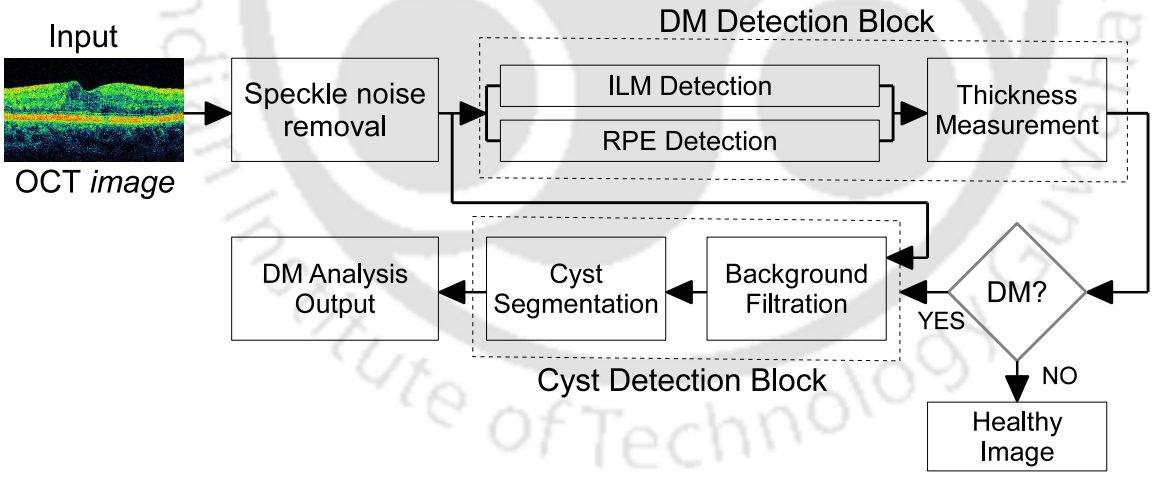

Figure 5.1: Block Diagram of the proposed method.

The block diagram, given in Figure 5.1, details the proposed algorithm. As per the block diagram, the algorithm first filters the speckle noise and is used for the detection of DM subjects. The DM identification constitute segmentation of the ILM and RPE layers and to investigate the thickness between them. If the calculated thickness is below critical thickness, the image is marked as a healthy image, otherwise considered as a DM subject. The DM subject is then analyzed for cyst identification. The cyst identification performs background filtration followed by cyst area segmentation. The final

output contains the DM analysis result with the detection of DM and area spread of the cysts present. **Chapter content:** The chapter proposes automated detection of DM using OCT images. The discussion starts with speckle noise removal in Section 5.1 continuing to DM detection in Section 5.2 and finally, cyst analysis in Section 5.3, with the algorithm evaluation in Section 5.4.

5.1 Speckle noise elimination

Speckle noise basically exists and degrades the quality of OCT images. As alluded in Chapter 2, Section 2.3, the elimination of speckle-noise is mandatory from the OCT image. The speckle-noise in the OCT image predominates the retinal layers and cyst boundary detection, which results in FP output that may lead to wrong thickness measurement or cyst area calculations. For removal of speckle noise and to improve the layer segmentation, bilateral and anisotropic filters are considered to be the best among conventional filtering techniques. But the limitation of both the method lies in bringing gradient reversal artifacts, where the gradient of the image tends to change direction after processing, causing cartooning effect to the output image [33, 208, 209]. Therefore, considering the limitation of the filtering methods, the guided image-based filtering [257] method is proposed for speckle noise removal from the OCT images. In Guided Image Filtering, the output image is the linear transformation of the input guided image. The novelty of the said method is that it is advantageous for speckle removal along with eliminating gradient reversal artifact and edge preservation to a maximum extent [257]. The output after GIF has a less smoothing effect [257]. This filtering method generates excellent performance in many applications, which includes image enhancement or smoothing, compression, matting, and de-hazing. [258–260]. It is one of the latest and fastest filters that preserve edges of the image.

Continuing further, the most explored speckle noise removal filters in OCT images, the bilateral and anisotropic filters are discussed in the following subsection, with the introduction of the guided image filter and explanation of its superiority by comparison of various properties to be observed over OCT images.

5.1.1 Bilateral Filter

Bilateral filtering is a non-linear, edge preserving smoothing filter used for speckle noise removal from OCT images [33, 208, 209]. In this method, the intensity of every pixel is substituted by the weighted

average of neighborhood pixels. It is mathematically represented as:

$$I^{filtered}(x) = \frac{1}{W_p} \sum_{x_i \in \Omega} I(x_i) f_r(||I(x_i) - I(x)||) g_s(||x_i - x||) \tag{5.1}$$

where, W_p be the normalization term is given by,

$$W_p = \sum_{x_i \in \Omega} f_r(||I(x_i) - I(x)||) g_s(||x_i - x||) \tag{5.2}$$

where, Output image is $I^{filtered}(x)$ filtering input image I, x is the current pixel coordinates, Ω is the window centered in x, f_r is the range kernel, and g_s is the spatial kernel.

This filtering method has been used in CAD findings of OCT images for removal speckle with edge-preserving, as referred in [34, 261–263]. The primary drawback that occurred during the process is the presence of gradient reversal over the output.

5.1.2 Anisotropic diffusion Filter

Anisotropic diffusion filter is also used for speckle noise reduction in OCT images [264]. It reduces noise with preserving the significant edges, and lines. The Anisotropic diffusion filter is defined as:

$$\frac{\partial I}{\partial t} = div(c(x,y,t)\nabla I) = \nabla c.\nabla I + c(x,y,t)\triangle I \tag{5.3}$$

where, $\triangle$ denotes Laplacian operator, ∇ is the gradient, $div(...)$ denotes the divergence operator and c(x,y,t) is the diffusion coefficient.

$$c(||\nabla I||) = e^{-(||\nabla I/K||)^2} \tag{5.4}$$

$$c(||\nabla I||) = \frac{1}{1 + (\frac{||\nabla I||}{K})^2} \tag{5.5}$$

The constant K handles the edge sensitivity.

The NCD filter is defined as:

$$\frac{dI}{dt} = \nabla.(c(Im(I)\nabla I) \tag{5.6}$$

where $Im(.)$ is the imaginary value and the diffusivity is defined as:

$$c(Im(I)) = \frac{exp(i\theta)}{1 + (\frac{Im(I)}{k\theta})^2} \tag{5.7}$$

where, k is a threshold parameter and $\theta \in (\pi/2; pi/2)$ is the phase angle.

This filter also suffers gradient reversal artifact like bilateral filter.

5.1.3 Guided Image Filter

The Guided Image Filter (GIF) [257] is a guidance based filter, which filters an image p by using a guidance image I. The output filtered image q is considered as linear transform of I which comprises of a window w_k centered at k^{th} pixel, given by,

$$q_i = x_k I_i + y_k, \forall i \in w_k \tag{5.8}$$

where, x_k and y_k are linear coefficients and w_k is the square window of size r. It also acts as an edge preserving filter, which means that q has an edge if I has an edge, because $\nabla q = x \nabla I$

Equation (5.8) is evaluated to find out the coefficients x_k and y_k which reduces the difference between the filtered output and the guided image. This can be done by organizing q as input p with subtracting unwanted texture or noise, given by equation (5.9).

$$q_i = p_i - n_i \tag{5.9}$$

So, to determine the coefficents x_k and y_k , the cost function $E(x_k, y_k)$ is minimized, given by equation (5.10), where ε is regularization parameter which prevents x_k from becoming larger.

$$E(x_k, y_k) = \sum_{i \in w_k} \left((x_k I_i + y_k - p_i)^2 + \varepsilon {x_k}^2 \right) \tag{5.10}$$

Equation (5.10) is solved by linear regression model and is given by equation (5.11) and (5.12), where μ_k and ${\sigma_k}^2$ are the mean and variance of I in window w_k, $|w|$ is the number of pixels in w_k and $\overline{\mathrm{p_k}} = \frac{1}{|w|} \sum_{i \in w_k} p_i$ which is the mean of p in w_k.

$$x_k = \frac{\frac{1}{|w|} \sum_{i \in w_k} I_i p_i - \mu_k \overline{\mathrm{p_k}}}{{\sigma_k}^2 + \varepsilon} = \frac{cov(I, p)}{var(I) + \varepsilon} \tag{5.11}$$

$$y_k = \overline{\mathrm{p_k}} - x_k \mu_k \tag{5.12}$$

Substituting equation (5.11) and (5.12) in (5.8), the final definition of GIF is given by,

$$q_i = \frac{1}{|w|} \sum_{k/i \in w_k} (x_k I_i + y_k) = \overline{\mathrm{x_i}} I_i + \overline{\mathrm{y_i}} \tag{5.13}$$

Here, $\overline{\mathrm{x_i}}$ and $\overline{\mathrm{y_i}}$ are the means of x_k and y_k in window w_k and $i \in w_k, k \in w_i$ are equal due to the symmetry of box window.

Algorithm 6: *Guided Image Filtering*

1 function GIF;
Input : Input image 'p', guided image 'I', 'ε' is the regularization parameter.
Output: Filtered output 'q'.
2 $mean_I = f_{mean}(I)$; $mean_p = f_{mean}(p)$;
$corr_I = f_{mean}(I \times I)$; $corr_{Ip} = f_{mean}(I \times p)$;
3 $var_I = corr_I - mean_I \times mean_I$;
$cov_{Ip} = corr_{Ip} - mean_I \times mean_p$;
4 $x = cov_{Ip}/(var_I + \varepsilon)$; $y = mean_p - x \times mean_I$;
5 $mean_x = f_{mean}(x)$; $mean_y = f_{mean}(y)$;
6 $q = mean_x \times I + mean_y$

Various steps of GIF is shown in Algorithm 6

Edge Preserving property: GIF is one of the effective edge preserving filter. This property can be explained as, say for GIF, guidance image is same as input image, that is, $I \equiv p$ which results equation (5.11) and (5.12) into $x_k = \sigma_k^2/\left(\sigma_k^2 + \varepsilon\right)$ and $y_k = \left(1 - \sigma_k^2\right)\mu_k$. Now, if $\varepsilon = 0$; $x_k = 1, y_k = 0$. Whereas, for $\varepsilon > 0$, there would be two conditions,

Condition 1: 'High Variance', that is if image I vary too much at w_k, results in $\sigma_k^2 \gg \varepsilon$ and $x_k \approx 1$ and $y_k \approx 0$. Which means if a pixel in the image lies in the boundary its value remains unchanged $(x \approx 1, y \approx 0, q \approx p)$.

Condition 2: 'Nil Variance', that is if image I is constant throughout at w_k, results in $\sigma_k^2 \ll \varepsilon$ and $x_k \approx 0; y_k \approx \mu_k$. Which means if a pixel lies in the flat of non varying region its value gets averaged of the neighborhood pixels $(x \approx 0, y \approx \mu, q \approx \overline{\mu})$.

Gradient preserving property: Along with edge-preserving property, GIF is independent of gradient reversal artifacts, unlike bilateral or anisotropic diffusion filter. To explain this property, let us refer to Figure 5.2 (*image courtesy* [257]). Here, a 1D input signal X (black color) and its edge-preserving output considered as base layer Y (red color) is shown. The third signal (blue color) shown is the detail layer Z obtained from $Z = X - Y$. As seen in the figure, the upper region signals correspond to the bilateral filter, and the lower region represents guided filter responses.

In case of bilateral filter the base layer is not compatible with input signal across the edge pixels

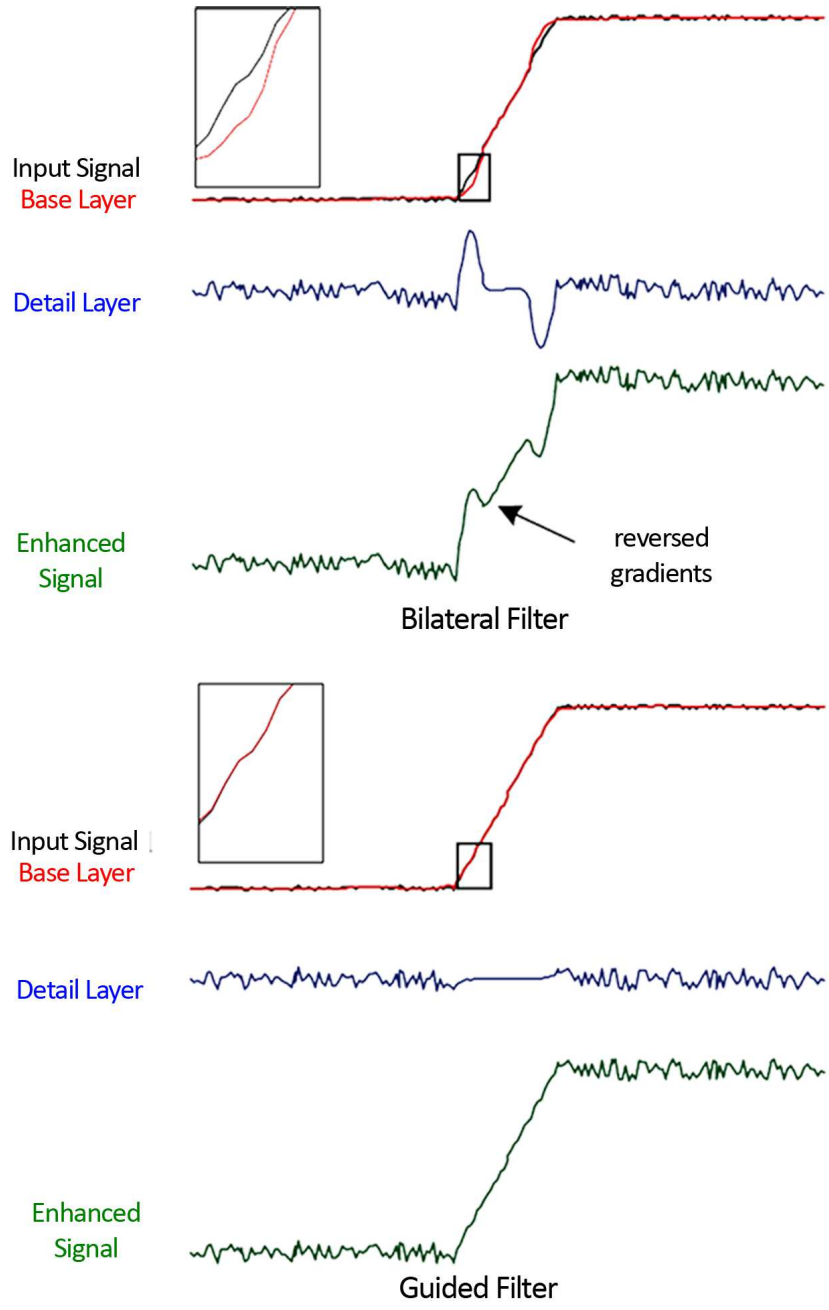

Figure 5.2: Comparison of Bilateral filter vs. GIF showing gradient reversal effect.

[referring the zoomed region of Figure 5.2]. As shown in Figure 5.3 (*image courtesy* [257]), the kernel of edge pixel for bilateral filter is biased as a result of abrupt change in the edges. For instance the filtered value is smaller than the original value resulting the filtered output Y sharper than input X. Now, if we consider the gradient of original image to be positive [$\delta_x X > 0$] it results in base signal as $\delta_x Y > \delta_x X$. Therefore computing the detail layer gradient it is found to be negative [$\delta_x Z = \delta_x X -$

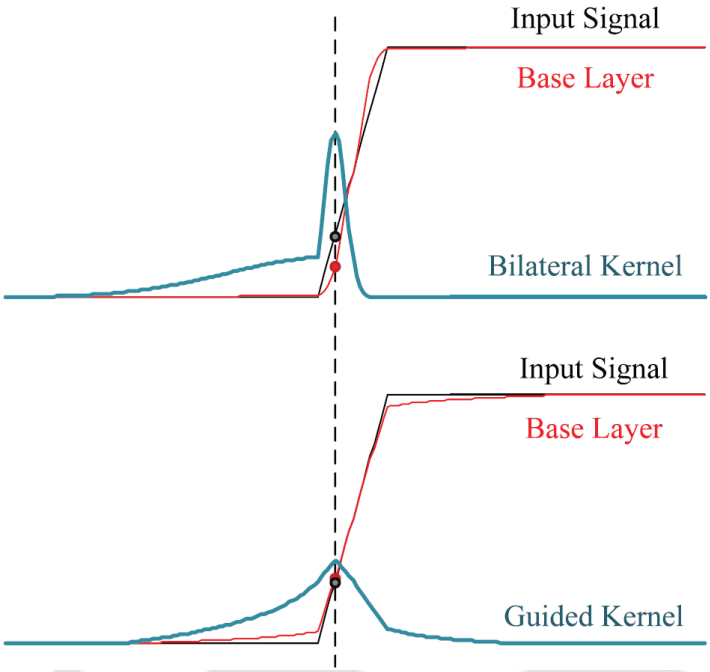

Figure 5.3: Results with filter kernels at a pixel on clean edge. Parameters of bilateral filter ($\sigma_s = 30, \sigma_r = 0.15$) and guided filte ($r = 30, \varepsilon = 0.15^2$), The edge height =1 and edge slope = 20 pixels.

$\delta_x Y < 0$], which represents reverse gradient direction [Figure 5.2 first waveform]. On recombination of detail layer with input signal the reverse gradient effect gets highlighted on the signal, as shown in Figure 5.2 enhanced signal in green color of the first waveform. Whereas, in case of gradient filter as discussed in edge preserving property, $x_k = \sigma_k^2 / \left(\sigma_k^2 + \varepsilon\right) < 1$ and y_k is constant. Hence, $\delta_x Y = x_k \delta_x X$ and detail layer gradient be $\delta_x Z = \delta_x X - \delta_x Y = (1 - x_k)\delta_x X$, implies that $\delta_x X$ and $\delta_x Z$ are in same direction. As we may see in Figure 5.3 the guided filter kernel assigned is small in value but it weights to the weaker side of the kernel resulting less biased avoiding reverse gradient as shown in second signal of Figure 5.2.

GIF in color image filtering: GIF can be easily shifted to color image filter by applying filtering operation individually to all the color planes. Let us consider guidance image I is multichannel, thus equation (5.8) can be rewritten as,

$$q_i = x_k^T I_i + y_k, \forall i \in w_k \tag{5.14}$$

where, I_i is a 3×1 color vector, x_k is a 3×1 coefficient vector, q_i and y_k are scalars. The corresponding

values of x_k and y_k are computed as,

$$x_k = \left(\sum\nolimits_k + \in U\right)^{-1} \left(\frac{1}{|w|}\sum_{i \in w_k} I_i p_i - \mu_k \overline{p}_k\right) \tag{5.15}$$

$$y_k = \overline{p}_k - x_k^T \mu_k \tag{5.16}$$

and thus the color guidance image is,

$$q_i = \overline{x}_i^T I_i + \overline{y}_i \tag{5.17}$$

where, $\sum_k$ is 3×3 covariance matrix of I in w_k and U is a 3×3 identity matrix. The edge-preserving property of color GIF is better than the grayscale GIF. Therefore color GIF is applied for the multiplicative speckle removal of OCT images, with preserving edge information for further processing. For more details about GIF, He et al. [257] may be referred. The performance comparison of GIF with conventional filters is described in the Experiments and Results, in Section 5.4.

5.2 Diabetic Maculopathy detection

The classification of an OCT image into normal and positive DM case requires the thickness measurement between the ILM and RPE layer of retina. An increase in the thickness between the layers as compared to normal healthy retina, indicate positive DM. As discussed in Chapter 1, Subsection 1.3.2 the thickness of ILM-RPE is measured in five different locations (referring Figure 1.17) of the OCT image. Therefore the correct segmentation of ILM and RPE layer, is mandatory for proper classification of DM. As alluded earlier, the detection of layers is affected by the presence of variational layer boundaries. The thickness of these layers at different points vary significantly for healthy and DM subjects. Hence, we apply the automated modified level set spatial fuzzy clustering algorithm (LSFCM) [265] for the identification of ILM and RPE layers from OCT images. The novelty of this experiment lies in the detection of all boundary pixels with the help of a level set algorithm whose initialization is provided by an automated fuzzy clustering algorithm. This process makes the level set algorithm automated apart from its nature of being manual. Figure 5.4 below shows the block diagram of DM detection using thickness evaluation of ILM and RPE layer.

The output of the GIF filter eliminating speckle noise is fed to automated modified LSFCM for the detection of the ILM and RPE layers. In this process the green plane of the GIF output is used for

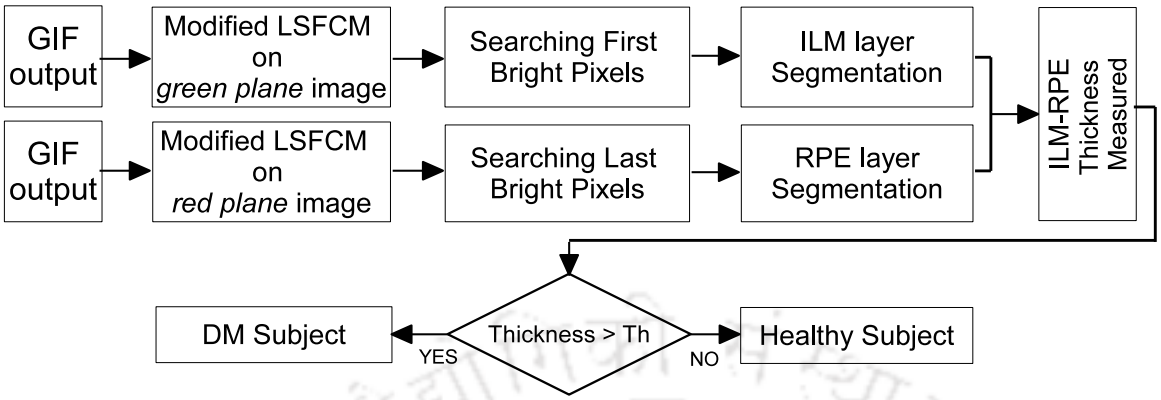

Figure 5.4: Block Diagram for Diabetic Maculopathy detection.

detection of the ILM layer (say case-I), and red plane GIF output for is used for RPE layer detection (say case-II). The output of the LSFCM from the case-I is searched for first positive pixel value in every column to identify the ILM layer, and the last pixel value is scanned column-wise from case-II LSFCM output for RPE layer identification. Once identified, the thickness between ILM and RPE is obtained by calculating the perpendicular column distance between them. The thickness measured is compared with a pre-set threshold. If the thickness is less than the threshold value the image is classified as healthy otherwise as positive DM subject. Below subsections detail the DM detection algorithm.

5.2.1 ILM layer detection

ILM layer is the first retinal layer. The detection of the ILM layer is possible with the fact that the filtered OCT image doesn't contain any information above the ILM layer. Modified LSFCM applied on the green channel of filtered OCT image, results in the detection of all the variational edges present in the image. After that, the scanning of the output image for the first positive intensity pixel in every consecutive column results in the detection of the ILM layer.

5.2.2 RPE layer detection

The RPE layer is the last layer of retina. It is visible on the color OCT images as the brightest pixel for each column of the matrix possessing a red color. Hence, the red channel of the filtered OCT image is taken into consideration, as it contains the maximum pixel value representing the RPE layer. The modified LSFCM algorithm is applied to this red plane image, which emphasizes on detecting the bright pixels corresponding to the RPE layer. The columns of the output image is searched for

the last bright pixel present in it. This process often leads to misclassification of the RPE layer if any other edge pixels exist below RPE. To avoid this misclassification, a post-processing is necessary. It is taken care of by considering a minimum distance between two successive last column pixels. If the distance is below 10 pixels, the pixel location is stored as RPE pixel. Otherwise, the row value of the comparing pixel location is given to the pixel under consideration, keeping the column position intact.

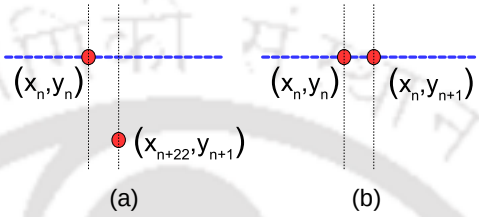

Figure 5.5: Correction in RPE segmentation: (a) Misclassified RPE pixel in position (x_{n+22}, y_{n+1}), (b) Corrected RPE pixel (x_n, y_{n+1}).

For example, refer to Figure 5.5, where the blue thick dotted line represents the RPE layer, and the red circles represent two consecutive segmented pixels. As seen in the figure, the second pixel located at (x_{n+22}, y_{n+1}) is misclassified as its distance from the previous pixel is 22. Therefore, the correction is made in the second pixel by shifting to previous row location (x_n, y_{n+1}) as shown in Figure 5.5 (b). The resultant image thus obtained contains a segmented RPE layer.

ILM-RPE detection in grayscale image: The GIF output of the grayscale image is applied to Modified LSFCM to determine the edges. The ILM layer is then obtained by searching for the first positive intensity pixel in every column, as specified in the case of green channel image of color OCT images. The RPE layer is obtained by searching the last brightest pixels in the corresponding column of the detected ILM layer. Similar to color image processing, the post-processing is also done for grayscale images for the RPE layer detection.

5.2.3 Thickness measurement

The changes occurring at the retinal layer with the progression of DM is evident with thickness alteration between the ILM and RPE layer. Retinal swelling causes increase of thickness above reasonable value, marking the presence of DM. The straight line distance between the tip of the ILM layer to the corresponding bottom point of the RPE layer represents the thickness. For the thickness evaluation process , we consider five-point measurement, as shown in Figure 5.6. From the clinical perspective, the ophthalmologists evaluate the thickness in microns. But as per the algorithm

requirement, we calculate the thickness in number of pixels present.

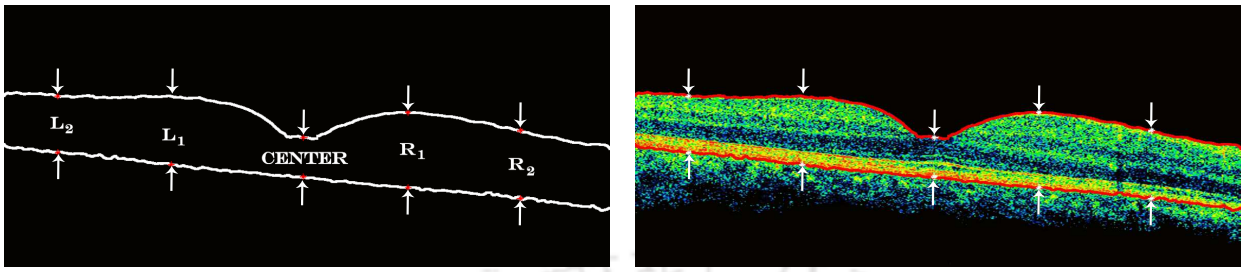

(a) (b)

Figure 5.6: Thickness measurement between ILM and RPE layer for OCT image: (a) Locations - Center, L_1, L_2, R_1 and R_2 (b) Labeling locations over color OCT image under evaluation.

As shown in Figure 5.6, the five different positions are referred to as follows; the foveal thickness is in the middle position of the image, named as 'center'. R_1 and L_1 are located at 230 pixels towards right and left from the center location, respectively. Similarly, R_2 and L_2 are at a distance of 450 pixels from the center. To generalize the thickness measurement for the evaluation of DM, we determine a reasonable value from a broad range of healthy OCT images. This threshold is set experimentally for the classification of healthy and DM cases. The threshold value calculated is discussed in Experiments and Results, Section 5.4.

5.3 Cyst analysis

The third step of analysis holds the detection of cyst formed. The challenge during the detection lies in the variation of texture in between retinal layers. The cystoid fluid or cysts are dark in intensity, but the presence of the variational background makes it difficult for identification. Therefore, in the proposed method, we have established a smoothing background filter. The Gaussian bandpass filter performs attenuation of components with frequencies other than the cysts present. The modified Nick's algorithm, derived from Niblack's algorithm [266] is then operated to locate cyst segments, and after that, the modified LSFCM is used to identify the exact boundary information of the cysts. The block diagram representation of the Cyst analysis is given in Figure 5.7.

5.3.1 Filter for background variation elimination

During identification of the cyst the background variation may interfere the segmentation process. Hence, in order to decrease the effect, Gaussian band pass filter (GBPF) defined by equation 5.18

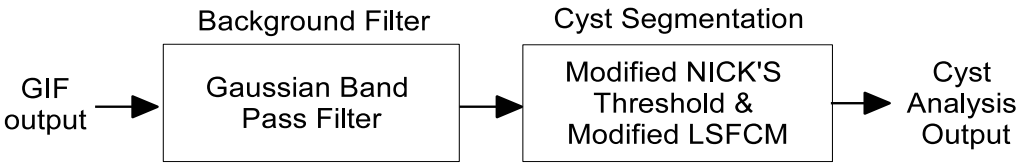

Figure 5.7: Block Diagram of Cyst analysis.

and 5.19 is used,

$$M_{LPF}(u,v) = e^{\frac{-L^2(u,v)}{2{L_1}^2}} \tag{5.18}$$

$$M_{HPF}(u,v) = 1 - e^{\frac{-L^2(u,v)}{2{L_2}^2}} \tag{5.19}$$

where, $M_{LPF}(u,v)$ and $M_{HPF}(u,v)$ are low pass filter (LPF) and high pass filter (HPF) component respectively. $L(u,v)$ is the distance between a point (u,v) in the frequency domain and the center of the frequency rectangle. The cut off frequency of the LPF and HPF is represented by L_1 and L_2 respectively. The relation between the cut off frequencies [267] is,

$$L_1 = 10 \times L_2 \tag{5.20}$$

The L_2 value must be selected appropriately. A low-value of L_2 results in blurring of regions eliminating edge information. On the other hand, very high value eliminates the moderate high-frequency edge information such as edges of smaller cysts. Here, in the proposed algorithm, the value $L_2 = 20$ is experimentally found to be best suited for the background smoothing operation.

5.3.2 Cyst segmentation

In order to locate cyst regions the background image is to be smoothed effectively. GBPF is performed over the green channel in the previous section removes the background variability. The image is binarized using modified Nick's threshold designed for HM detection, from our previous work [266] given by,

$$T_{DarkNick} = \frac{T_{Nick}}{\sqrt{NP}} \tag{5.21}$$

where, $T_{Nick} = m + k \times \sqrt{B + m^2}$ and $B = \sqrt{\frac{1}{NP}\sum_i (p_i - m)^2}$ having k is the Niblack factor, NP is number of pixels, m is mean pixel value and p_i is pixel value. To locate the variational boundaries

of the cysts modified LSFCM is applied later. The results so obtained shows detected cystoid fluid regions along with some FPs. It is observed that generally cystoid area will have a filled region of atleast 20 pixels in the present database resolution. In order to eliminate the FPs the morphological opening operation is performed to remove the regions having less than 20 pixels. Once identified the area of the cyst is calculated to determine the spread of the cyst within the retinal layers.

5.4 Experiments and Results

For evaluating the proposed algorithm, three databases are used. The first database is locally generated by collecting images from Guwahati Eye Institute (GEI), Guwahati. The GEI dataset contains a total of 260 OCT B-scan images with 187 healthy, 73 DM and 40 CME B-scans. The validation of the proposed algorithm is carried over this database. The dataset is annotated by two retinal experts independently and the labels are provided to each B-scan OCT images based on the observed changes in the anatomical features of the retina. For comparison of the algorithm with state-of-art methods, the second and third databases are used. The second database is a publicly available DME dataset from Duke University [218] comprising of 45 subjects (with 15 each of healthy, DME and AMD). Out of 45 images, the dataset of healthy and DME group (dataset D1) is considered for performance evaluation. The third database is MICCAI 2015's OPTIMA Cyst Segmentation (OCSC) dataset [268]. The dataset contains 15 training and 15 testing SD-OCT volumes with cysts resulting from retinal diseases like the retinal vein occlusion and the AMD. These volumes are acquired from different OCT imaging systems namely Spectralis, Cirrus, Topcon and Nidek. The dataset has manual annotation of cysts by two graders. This database is used for comparison of the cyst detection section of the proposed algorithm.

The experiments are performed on the color OCT image database of GEI for assessing the proposed method. The experiments include filtering of the OCT images using GIF to eliminate speckle noises to identify ILM and RPE layers for DM assessment, and localization of cysts present in the positive DM cases. Then, the results are compared with the existing algorithms of DM analysis. The following section presents the discussion of the experimental results in detail.

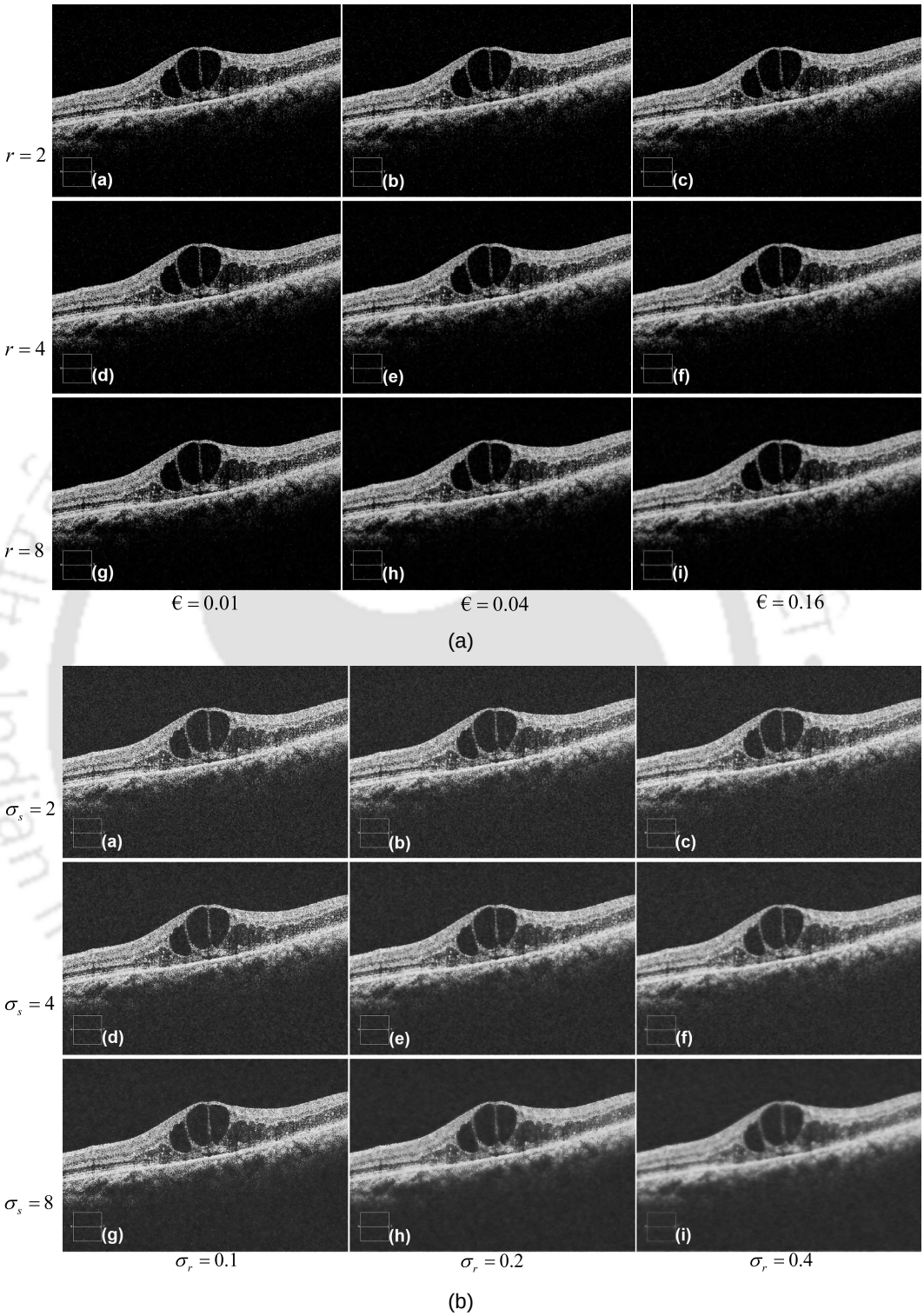

Figure 5.8: Speckle elimination and edge preserving results on Gray scale OCT image with various parameters where $(\sigma_r{}^2 \Leftrightarrow \in = 0.01, 0.04, 0.16)$ and $(\sigma_s \Leftrightarrow r = 2, 4, 8)$: (a) Guided Image Filter and (b) Bilateral Filter.

5.4.1 Performance evaluation of speckle noise removal

The experiment with the OCT image database starts with the removal of speckle noise, using GIF filter. The GIF method was not explored in OCT imaging applications earlier for enhancing edge information. To compare the performance of GIF over other methods, we have evaluated with conventionally used bilateral filter as it contains similar parameters as GIF. As we know, ε in GIF filter is similar to that of ${\sigma_r}^2$ of bilateral filter, and both parameters define "edge", which needs to be preserved $({\sigma_r}^2 \Leftrightarrow \in)$. Similarly, the size '$r$' of the window w_k of the guided filter and the σ_s parameter of bilateral filter resembles each other $(\sigma_s \Leftrightarrow r)$. Keeping these considerations in mind the GIF and bilateral filters are compared using the similar parameters $({\sigma_r}^2 \Leftrightarrow \in = 0.01, 0.04, 0.16)$ and $(\sigma_s \Leftrightarrow r = 2, 4, 8)$.

The comparison output thus obtained is shown in Figure 5.8. To quantitatively evaluate the result, the Peak Signal to Noise Ratio (PSNR) values are obtained for various parameters of $({\sigma_r}^2)$ and (σ_s) under consideration and tabulated in Table 5.1. The results show that the GIF has better PSNR values than conventional bilateral filter when applied on OCT images.

Table 5.1: Comparision of Bilateral Filter with GIF considering PSNR (in db) values

Bilateral filter				**Guided image filter**			
Parameters	$\sigma_s = 2$	$\sigma_s = 4$	$\sigma_s = 8$	Parameters	r=2	r=4	r=8
$\sigma_r = 0.1$	18.5160	18.6889	18.7359	$\in = 0.01$	37.7303	36.3688	35.8414
$\sigma_r = 0.2$	18.7813	18.6139	18.4912	$\in = 0.04$	33.2670	31.5545	30.9499
$\sigma_r = 0.4$	18.2862	17.7751	17.4236	$\in = 0.16$	30.6527	28.4809	27.6587

GIF evaluation on color OCT image: For evaluating the response of the GIF in color OCT images, each R, G, B image planes are independently filtered. The color GIF output preserves more edge details than a grayscale GIF output. For evaluating the response generated, the bilateral and anisotropic diffusion filter [261, 264], are applied to the color OCT image, and the output obtained is compared with GIF. Figure 5.9 shows the filtered output responses in order of Original noisy image, Bilateral, Anisotropic, and GIF output, respectively. Here a small region is zoomed to show the filter response and edge-preserving details. By observing the images, it can be mentioned that GIFs can filter the speckle noise along with preserving edge information. The bilateral filter responded to a blurring effect, and anisotropic diffusion filter to a motion blurring response in the filtered output, losing edge information. The PSNR values of the individual planes for the three filters are calculated and presented in Table 5.2. The PSNR values are found to be better for GIF in all the planes of color OCT image.

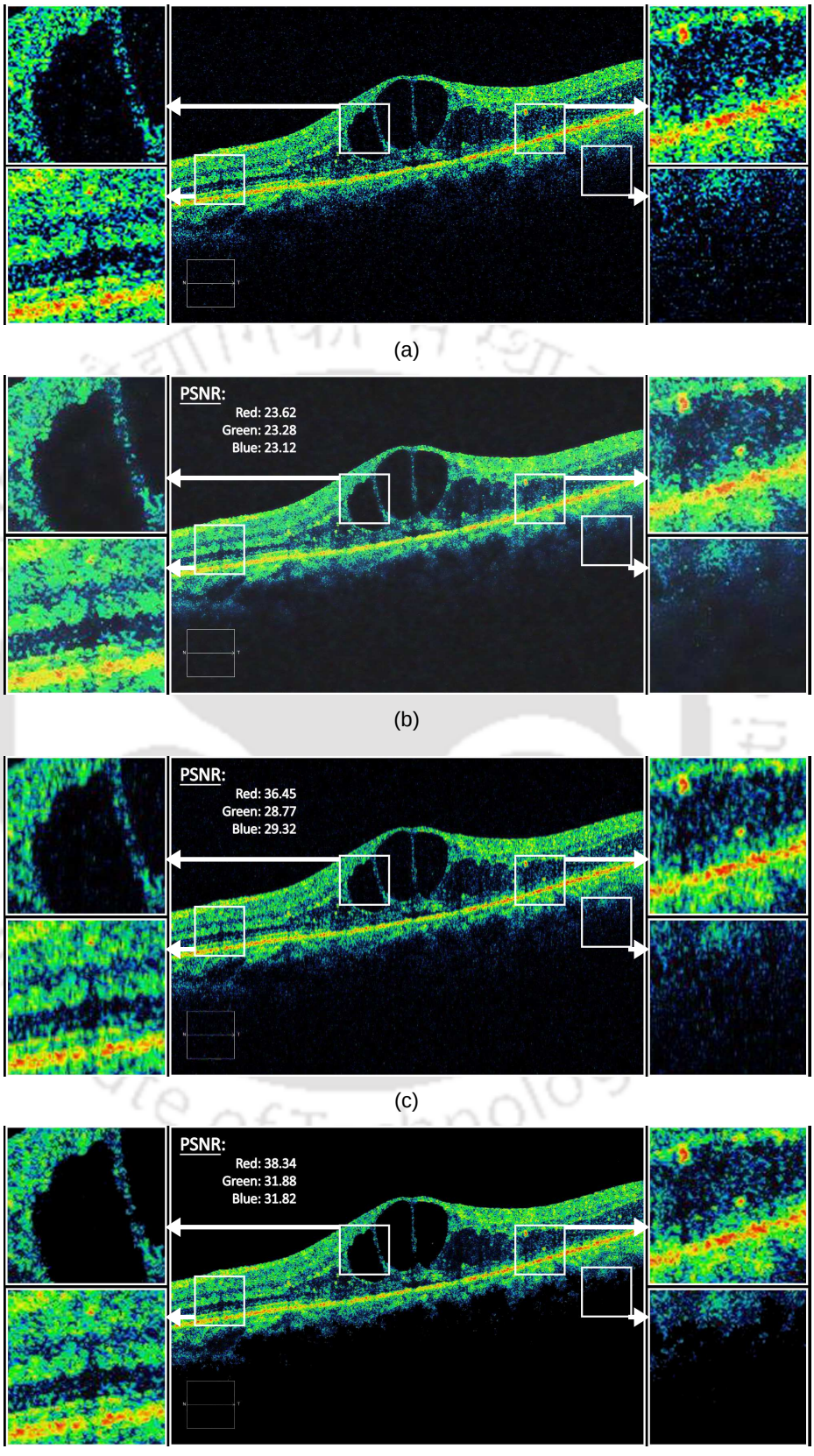

Figure 5.9: Comparison of filtering operations in Color OCT images considering similar radius σ_s = r = 2: (a) Original OCT image, (b) Bilateral filter, (c) Anisotropic Filter and (d) GIF.

Table 5.2: Table of Comparison for color image: (PSNR in db)

Input (OCT)	Anisotropic filter	Bilateral filter	GIF
R plane	36.45	23.62	38.34
G plane	28.77	23.28	31.88
B plane	29.32	23.12	31.82

5.4.2 Performance evaluation of DM detection

The filtered output image obtained is treated with the modified LSFCM to detect the variational retinal boundaries. Figure 5.10(a) represents the segmented regions, shown in green edge boundaries. The ILM layer segmented from the edge pixels using search of first positive intensity column pixel is shown in Figure 5.10(b). Later, Figure 5.10(c) shows the output edges marked over the red channel image. RPE layer is then segmented using the search of last positive intensity column pixel, and the result obtained is shown in Figure 5.10(d).

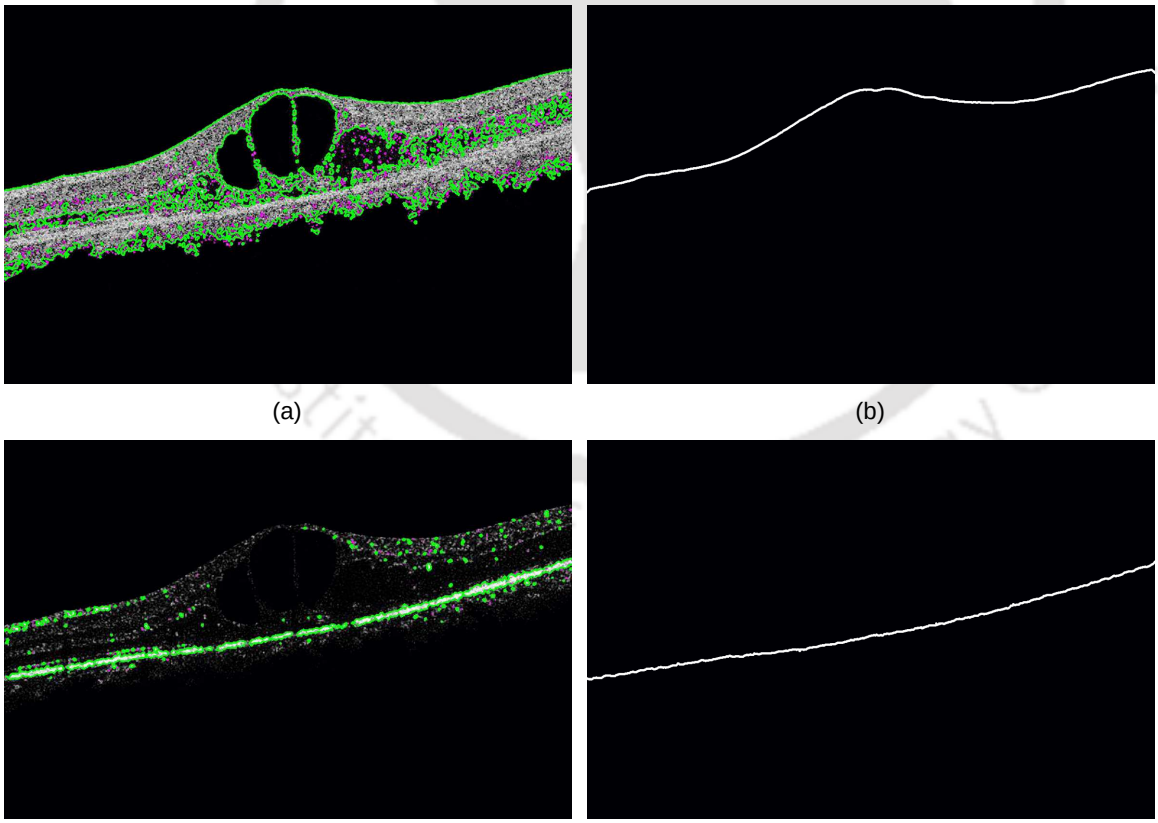

Figure 5.10: Steps showing proposed method for layer detection using LSFCM algorithm : (a) edges obtained on filtered green channel image for ILM layer detection, (b) detected ILM layer, (c) edges obtained on filtered red channel image for RPE layer detection, (d) detected RPE layer.

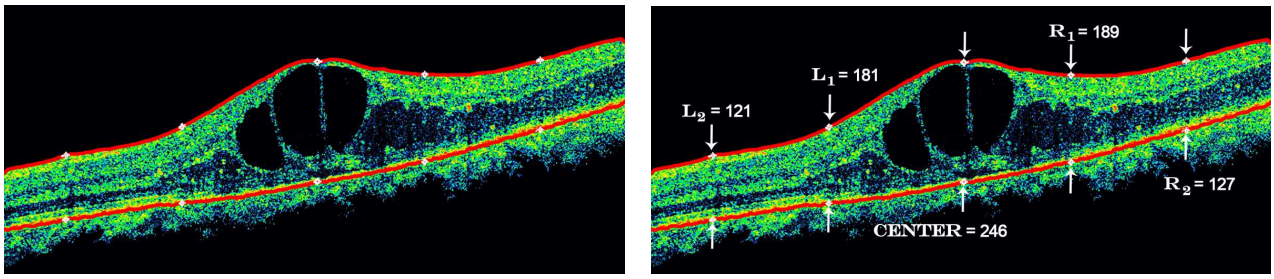

(a) (b)

Figure 5.11: Measurement of thickness between ILM and RPE layer for OCT image under evaluation; $L_2 = 121$, $L_1 = 181$, $CENTER = 246$, $R_1 = 189$ and $R_2 = 127$.

Table 5.3: Thickness difference of ILM and RPE layers of 50 patients to verify presence of ME

Observations	Center	R_1	R_2	L_1	L_2	Observations	Center	R_1	R_2	L_1	L_2
Image01	87	130	107	127	105	Image26	177	155	111	168	142
Image02	75	146	123	132	110	Image27	148	136	123	166	119
Image03	86	123	105	135	119	Image28	114	140	111	157	109
Image04	75	136	113	119	99	Image29	112	137	109	125	114
Image05	82	150	136	140	123	Image30	124	137	119	115	85
Image06	99	133	112	126	115	Image31	140	131	111	118	88
Image07	76	140	116	133	109	Image32	117	220	241	176	138
Image08	69	128	123	120	109	Image33	197	123	133	161	153
Image09	85	129	125	129	112	Image34	175	157	129	135	121
Image10	76	140	119	130	103	Image35	178	147	122	137	125
Image11	79	135	116	146	132	Image36	159	131	113	138	114
Image12	79	139	119	126	105	Image37	147	186	146	138	133
Image13	70	132	100	142	121	Image38	298	220	133	183	143
Image14	80	132	114	143	130	Image39	233	159	135	146	116
Image15	76	130	116	126	106	Image40	323	230	162	201	131
Image16	86	128	128	120	112	Image41	293	213	180	241	179
Image17	78	123	116	123	110	Image42	155	134	121	209	201
Image18	77	128	114	126	100	Image43	156	148	123	126	112
Image19	76	133	129	124	113	Image44	106	129	111	177	137
Image20	82	139	120	127	98	Image45	124	137	129	159	105
Image21	227	164	132	144	122	Image46	151	120	206	132	123
Image22	101	145	132	208	174	Image47	92	147	127	167	143
Image23	202	137	121	171	134	Image48	140	147	123	153	114
Image24	165	96	87	219	116	Image49	301	226	140	248	152
Image25	101	145	132	208	174	Image50	82	152	121	146	135

After obtaining the ILM and RPE layers, the thickness (pixel difference) between them is calculated for the classification of healthy and DM cases. After analyzing the thickness in 187 healthy OCT images, it is observed that the foveal region thickness ranges from 80 to 100 pixels, whereas, the neighborhood regions vary from 120 to 150 pixels. Hence thickness of 100 pixels in fovea and 150

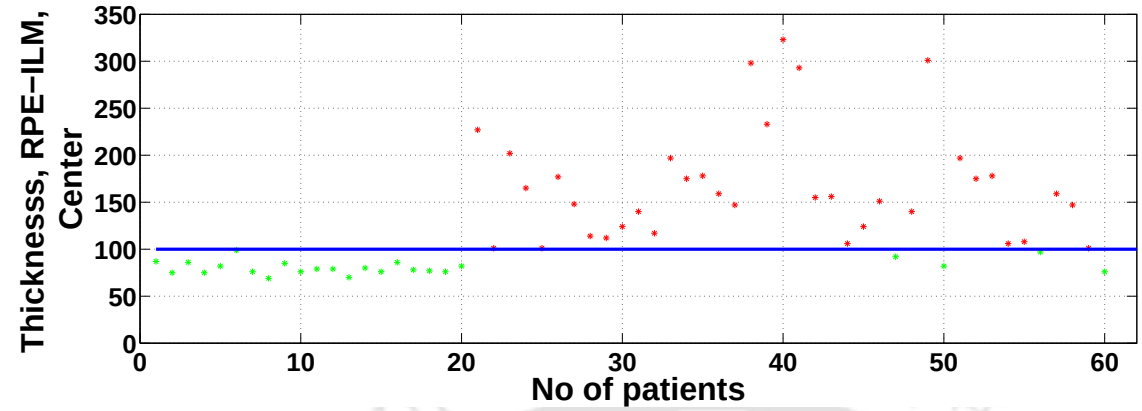

(a)

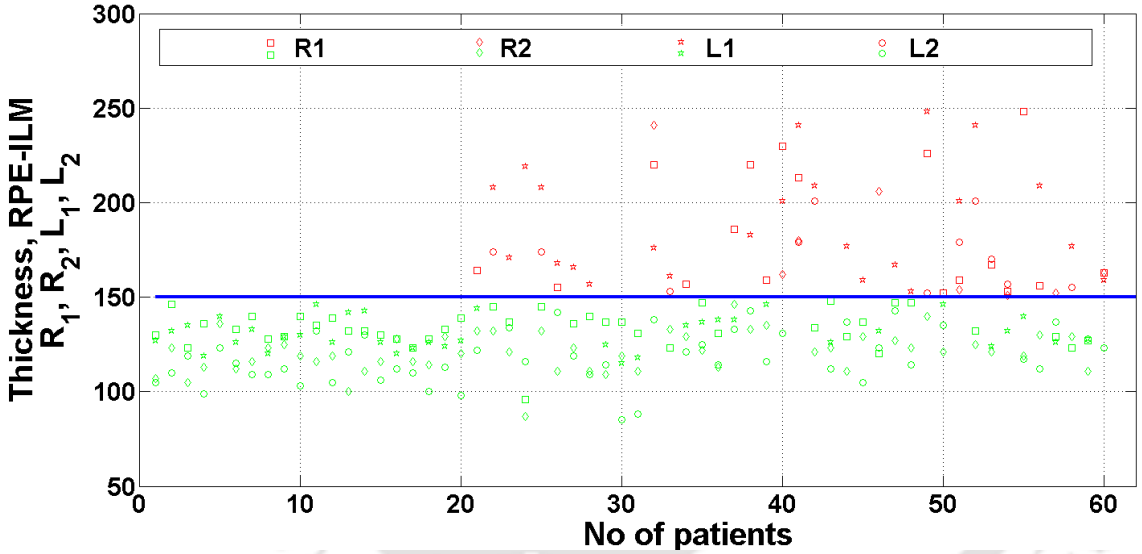

(b)

Figure 5.12: Thickness measurement between ILM and RPE layer of 60 patients: (a) Center foveal point, (b) R_1, R_2, L_1 and L_2 point.

pixels for neighborhood region is being used as a gold standard (Th) for classification of healthy and DM cases. These values may vary for different databases. The thickness measured for a given image is shown in Figure 5.11 for illustration. Table 5.3 shows the thickness of 20 healthy and 30 DM OCT images measured between ILM and RPE at five consecutive locations.

Quantitative Measures of Performance: To evaluate DM detection, the ILM - RPE layer thickness for all 260 images are obtained. Few values thus calculated (60 cases) are plotted in Figure 5.12 (a) and (b). Here, the blue line represents the threshold for DM identification. If the thickness in any of the five points exceeds the threshold, then it is considered to be a positive DM case. The result thus

obtained after applying the algorithm on all 260 images show 98.46% accuracy for identification of positive DM cases.

5.4.3 Performance evaluation of Cyst analysis

The positive DM images are later searched for the presence of cystoid fluid using GBPF and modified Nick's threshold with modified LSFCM. The segmented cyst region is obtained by processing the filtered green channel image, as shown in Figure 5.13(b). The segmented region are later marked over original image [Figure 5.13(c)] for better perception.

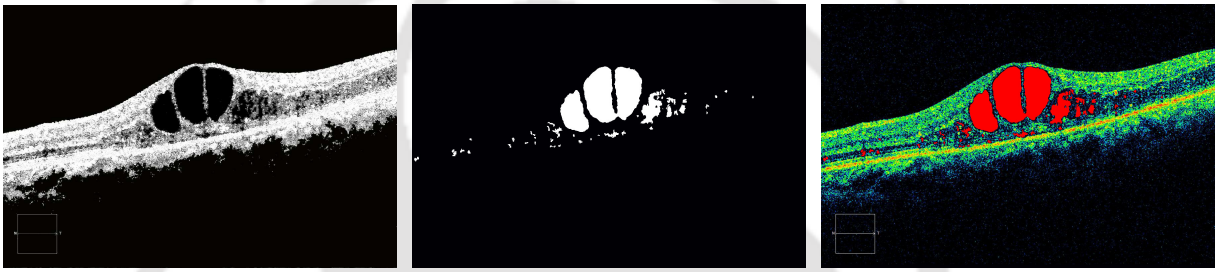

(a) (b) (c)

Figure 5.13: Steps showing proposed method for cystoid fluid detection: (a) GBPF output obtained processing green plane GIF image, (b) Segmented cystoid fluid using Nick's thresholding, (c) Detected cystoid marked in red over original OCT image.

Table 5.4: Evaluation of Cystoid detection percentage parameter values for 15 CME cases

Images	Sensitivity	Specificity	Accuracy	Measured cystoid area	True cystoid area	Absolute difference
Image 01	100	99	99	30.16	30	0.16
Image 02	100	95	96	30.30	30	0.30
Image 03	100	99	99	19.60	20	0.40
Image 04	100	99	99	29.00	30	1.00
Image 05	100	98	99	29.17	30	0.83
Image 06	100	99	99	29.40	30	0.60
Image 07	99	94	95	30.30	30	0.30
Image 08	99	99	99	30.00	30	0.00
Image 09	99	98	98	29.80	31	1.20
Image 10	99	99	99	31.40	32	0.60
Image 11	99	98	98	30.00	31	1.00
Image 12	99	98	98	34.80	36	1.20
Image 13	99	99	99	31.00	30	1.00
Image 14	99	99	99	30.90	31	0.10
Image 15	99	99	99	29.60	29	0.60

The performance of the cyst analysis system is evaluated by computing specificity, sensitivity, and accuracy using the manually annotated ground truth images. These are the parameters used

for verifying the efficiency of cyst segmentation algorithm. The average sensitivity, specificity, and accuracy obtained from cystoid detection are 98.3%, 97.9%, and 98.6%, respectively. The 40 CME cases, once evaluated, are subjected to estimation of percentage of area occupied by cystoid regions. This cystoid region of interest (ROI) area [42] is given by,

$$Cystoid\ ROI\ area = \frac{TP + FN}{\text{Total Retinal area}} \tag{5.22}$$

Where total Retinal Area is calculated from, TP+FP+TN+FN. Table 5.4 shows the calculation of cystoid area for 15 positive CME cases, along with sensitivity, specificity, and Accuracy. The average area calculated automatically for all 40 cases is found to be 29.7%. In order to evaluate the area calculated, it is compared with the manual cystoid area, and the average absolute difference is found to be 0.04%.

Figure 5.14 shows qualitative results on DM analysis on different subjects from GEI database. Here, stages shown includes GIF output, detected ILM and RPE layer, localized cysts and the detections overlapped over original input image. The OCT images selected from GEI database includes one healthy (row 1) and remaining DM subjects.

To prove the effectiveness of GIF, on the later stages of the proposed algorithm, the bilateral filter is applied in place of GIF, and the result obtained from various segmentation process is represented in Figure 5.15. Here, we may quickly notice the effect of improper speckle removal affecting the entire segmentation process. It can also be noted that the processing speed of GIF is found very less compared to anisotropic diffusion and bilateral filter.

5.4.4 Performance comparison of DM and Cystoid segmentation

There are various state-of-art methodologies in the literature for DM analysis [22,35–41,209,213,225, 226]. But the comparison with these methods is not possible due to non availability of the dataset used by them. In this connection one way out may be possible by implementing their algorithms. But it is not always convenient due to improper choice of parameters for our dataset. Therefore, following three set of evaluation have been carried out for the performance comparison of the proposed method. It included DM identification comparison over publicly available DME dataset [218]. Analysis of cyst detection by comparing over OCSC database [268] and error calculation on GEI database with respect to manual annotation.

The D1 from publicly available dataset by Srinivassan et al. [218] containing normal and DME

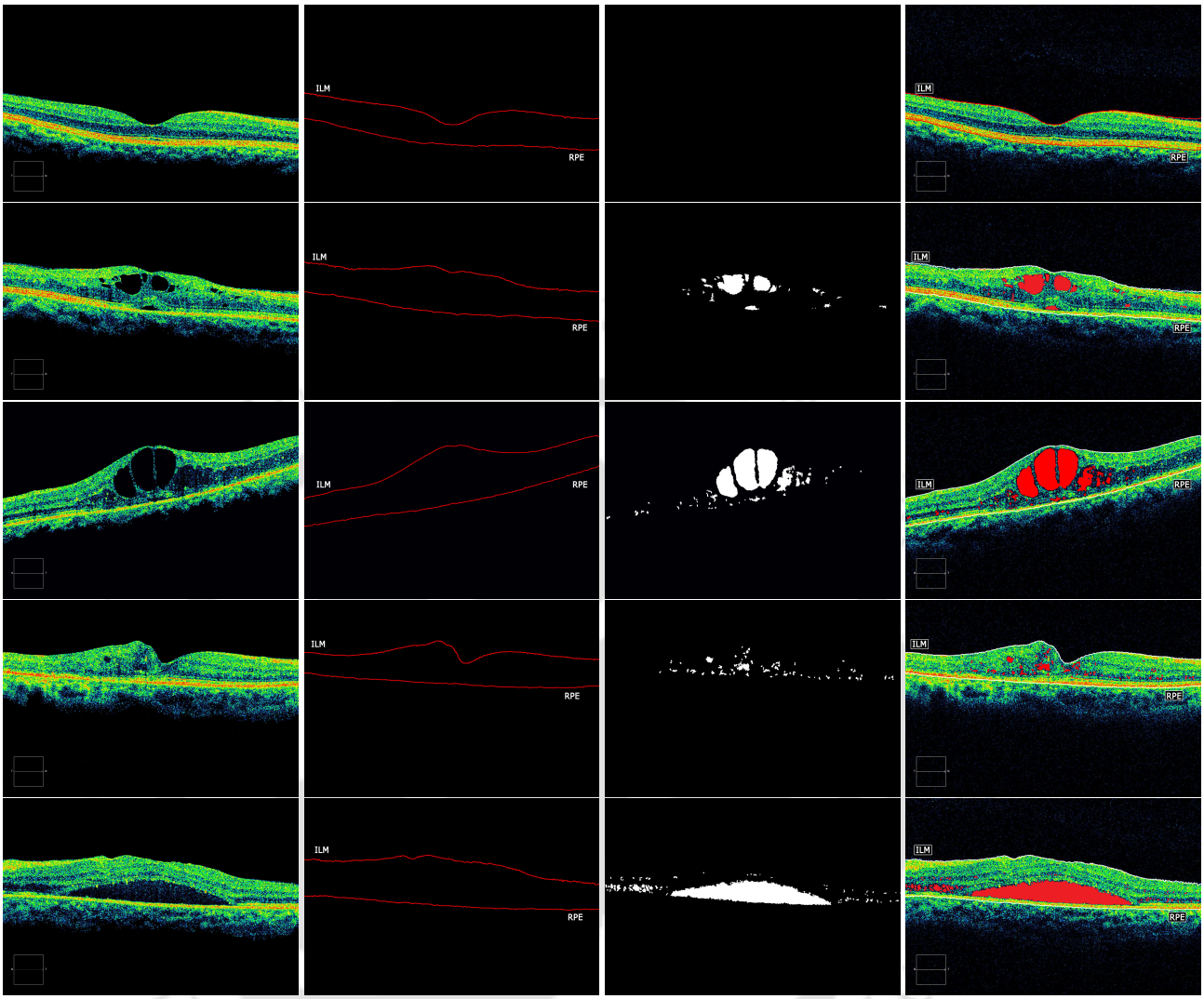

(a) (b) (c) (d)

Figure 5.14: Qualitative measure of DM detection stages on five different subjects from GEI database, top to bottom rows: [a] GIF filter output, [b] detected ILM and RPE layers, [c] Cyst detection, [d] Detection of ILM and RPE layers with cysts overlapped over input image for validation.

subjects is used by various researcher for evaluation of DM detection. Therefore, considering the same parameters for evaluation, it is best and efficient way to compare the performance of proposed algorithm. Following the state-of-art methods by Srinivassan et al. [218], Venhuizen et al. [269], Lemaitre et al. [270], Sidibe et al. [271] and Hussain et al. [272], we have computed the sensitivity, specificity, f1-score and accuracy and presented in Table 5.5.

As evident from the table our method outperforms the remaining state-of-art methodologies, except the sensitivity of Srinivissan et al. [218].

The performance measure of the cyst detection is carried out by computing the Dice coefficient (DC)

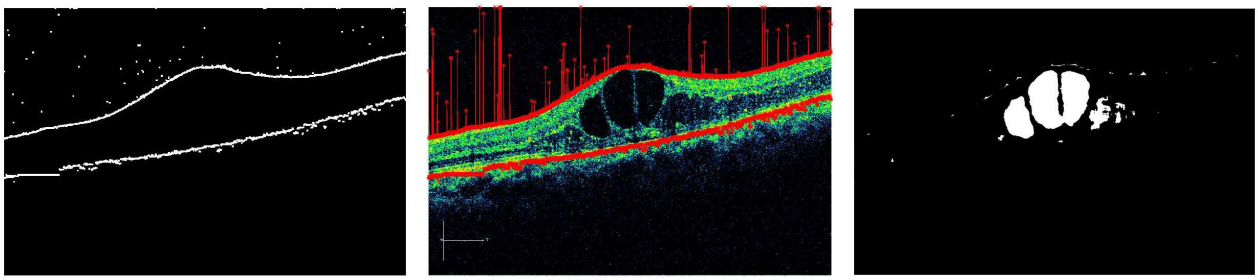

(a) (b) (c)

Figure 5.15: Result obtained by applying algorithm with bilateral filtering replacing GIF and showing the misclassified ILM and RPE edges due to incomplete removal of speckles: (a) Segmented ILM and RPE layer, (b) Marked layers on color OCT image, (c) Detected cystoid with increased number of false positives.

Table 5.5: Performance evaluation of the proposed algorithm for detection of DM and normal cases from D1 (partial Duke University) database

Methods	Sensitivity	Specificity	f1-score	Accuracy (%)
Srinivassan et al. [218]	**100**	86.67	93.75	93.33
Venhuizen et al. [269]	71.42	68.75	70.47	70.00
Lemaitre et al. [270]	86.67	100	92.86	93.33
Sidibe et al. [271]	80.00	100	88.89	90.00
Hussain et al. [272]	94.67	100	97.22	97.33
Proposed method	96.66	**100**	**98.30**	**98.33**

over OCSC [268] dataset following Gopinath et al. [273]. DC measures the variants of proposed algorithm along with the effect of modified nick's threshold used to segment the cysts. The DC is given by,

$$\text{Dice coefficient} = 2\frac{|\text{Detected} \cap \text{GT}|}{|\text{Detected}| + |\text{GT}|} \tag{5.23}$$

where, 'Detected' and 'GT' are detected cysts and ground truths respectively. The $|.|$ is the set size, and DC value varies from 0 to 1. For DC=1, specifies exact match of GT and automatically detected cysts. The computed overall mean and standard deviation of DC values for OCSC database is reported in Table 5.6 along with other state-of-art algorithms. G1 and G2 in the table present GT from two graders as provided in OCSC database. Here Unmasked (U) indicate the entire volume and Masked (M) denotes a 3mm central volume across macula as per [273].

The proposed method surpass the remaining algorithms for OCSC database. From the comparison it is evident that the DC value for U and M volumes are nearby, making the detection independent of location.

Table 5.6: Comparison of Dice Coefficient computed against Grader 1 (G1), Grader 2 (G2) and G1∩G2 for OCSC database with respect to unmask (U) and masked (M) volumes

Methods	U (mean/std)			M (mean/std)		
	G1	G2	G1∩G2	G1	G2	G1∩G2
de Sisternes et al. [274]	0.64/0.14	0.63/0.14	0.65/0.15	0.68/0.15	0.67/0.17	0.69/0.15
Venhuizen et al. [269]	0.56/0.20	0.55/0.22	0.54/0.20	0.61/0.19	0.60/0.19	0.59/0.19
Oguz et al. [275]	0.48/0.25	0.48/0.22	0.48/0.22	0.60/0.15	0.59/0.15	0.60/0.14
Esmaeili et al. [227]	0.46/0.25	0.45/0.24	0.45/0.25	0.55/0.27	0.55/0.27	0.55/0.28
Gopinath et al. [273]	0.67/0.17	0.68/0.17	0.69/0.18	0.70/0.17	0.70/0.15	0.71/0.16
Proposed method	**0.82/0.16**	**0.81/0.18**	**0.81/0.17**	**0.83/0.15**	**0.81/0.14**	**0.82/0.14**

The third set of evaluation shows a comparison of layer detection in the proposed method with manual annotation. The error between detected layers and ground truth is calculated. The average error is found to be 2.126 pixels. Observing all three evaluation criteria for performance measure, it has been proved beyond doubt that the proposed algorithm is not only effective and efficient in segmenting the layers of OCT image but also efficient enough in the detection of cystoid fluid.

5.5 Summary

It is important to detect and analyze DM in the early stage. Due to prolonged diabetes, abnormal blood vessels grow in the inner retinal layer. These vessels cause leakage within retinal layer which is not visible in fundus image. Hence, ophthalmologist use OCT image analysis for efficient diagnosis of DM, when it involves retinal layers. A computer-assisted layer detection and segmentation method for OCT images have been developed in this chapter for classification and analysis of such diseases. The proposed method is advantageous with respect to the removal of speckle noise and preserving edges to a large extent. It enables improved layer segmentation and detection of DM cases. The algorithm has been tested using 260 OCT B-scan images that are manually labeled by ophthalmologists of the Guwahati Eye Institute. The efficiency of DM detection is obtained to be 98.46%. The performance comparison of the same over D1 dataset of Duke University, surpass the other reported results. The proposed method has been further extended to determine the presence of cystoid fluid for CME cases. The cyst identification shows a sensitivity of 98.3%, a specificity of 97.9%, and an accuracy of 98.6%. The comparison of the proposed method over OCSC database reported better efficiency. The above results clearly show that the proposed method may be used as an effective solution in the detection of DM and CME.

6

Conclusions

Contents

In this concluding chapter, the summary of research work carried out is presented. The major contributions of the current work are briefly discussed. Lastly, the directions for future work are listed.

6.1 Overall Summary

The existing clinical practices in ophthalmology appear not to depend fully on the technological advancements. Starting from disease screening to treatment, management and monitoring leave space for improvement. In this direction, we contribute an engineering perspective in ophthalmology in the direction of image-based decision systems. Realizing the vast area of ophthalmology, this thesis targeted the challenges in automated diagnosis of Diabetic Maculopathy using fundus and optical coherence tomography images and proposed a set of algorithms to realize the same. The retinal images provide the clinical information of DM and investigating the same, ophthalmologists suggest the required diagnosis. But to cope up with the increasing number of diabetic patients, manual screening of DM is not sufficient and requires image-based decision systems.

In this research work, the automated algorithms for the analysis of DM based on the fundus images seek detection of the fovea, lesions present, and their positions in the fovea neighborhood. On the other hand, the investigation using the OCT images include detection of ILM and RPE layer thickness to estimate DM presence and to determine the cyst volume present in every DM subjects. The summary of the work done is presented below.

Chapter 1 starts with the introduction of eye physiology with an emphasis on the retina and proceeds to the changes taking place with the inception of DM. We forward the discussion with the techniques available for imaging the retina, including the clinical perspective of fundus and OCT images. Various changes observed during DM in the retina is then elaborated with the need for the computerized automated analysis. We pointed out the challenges and opportunities formulated during the detection process with a literature review of the automated methods on DM analysis. The chapter concludes with the scope of the present work.

In **Chapter 2**, we emphasize on the review of available methods for the requirement of automated analysis of DM using both fundus and OCT image. Here we identify the pros and cons of the algorithms to bridge the gap for obtaining efficient analysis. The review includes detection of the blood vessel, optic disc, macula, fovea, exudates, microaneurysms, and hemorrhages for examining fundus image to analyze DM. For OCT images, the review was focused on speckle noise

filtering, retinal layer segmentation, and cyst detection. From the detailed and deep literature review, we figure out the advantages of the automated methods using image processing framework. After identifying the research gaps, the problem to be addressed in this thesis work is formulated. The discussion then proceeds with the indication of the objectives to be achieved. The chapter describes the materials/database used for the investigations towards the end.

Chapter 3 is the first working chapter of the thesis. Here, we proposed an algorithm for automated fovea detection, which is mandatory for the DM analysis using fundus images. The utilization of BV property for the detection of fovea makes the algorithm robust and independent of the OD-fovea relation. The sliding window to search for minimum horizontal BV edges enables efficient detection of the region of interest containing fovea. The systematic detection and masking of OD and exudates from the retinal image add advantage to the process. The OD ROI location information helps us to find the accurate position of the fovea utilizing the appropriate threshold. We evaluated the algorithm using a threshold of a maximum of 50 pixels of Euclidean distance between the location of the automatically and manually detected fovea. The detection algorithm was efficient but remained with a limitation on pathological images where abnormalities involve fovea. To overcome this, we proposed an ellipse template using major BV arteries and manual fovea position. The matching of the template positioned at the OD center detects the fovea location. The advantage of the ellipse template was that it could process both right and left eye images. The updated method detects fovea in challenging cases where the previous method failed to perform.

Chapter 4 deals with the identification of retinal changes that occur during DM and later classify its stages based on the position of these changes over fundus image. Here, we segmented out the deposition of blood, and its constituents called HM, MA, exudate (mainly HE), and observed their position with respect to fovea. The fovea localization was investigated in the previous chapter. After proper elimination of OD, searching for yellowish pixels with the help of the hue plane image identified all exudate components. But the challenge of retinal reflection removal and HE identification became possible only with the introduction of shade correction with RGB color plane property and standard deviation filter to remove weak edge segments. The detection of MA and HM was also efficient with the help of isolation of BVs using region growing technique. But including the BV thickness information helped the algorithm to obtain higher efficiency by eliminating the smaller blood vessels as FPs during detection. The presence of lesions in the fovea neighborhood determines the presence

of DM. Apart from detecting the DM, an additional feature for classifying the severity level of DM is also included. This is done by estimating the amount of deposition of lesions in the fovea region. We realized this investigation with the help of SVM classifier using texture features and the area covered by the lesions. Using the proposed algorithm, we could generate a report not only on DM presence but also on its severity with the help of its position and deposition amount, over fundus images.

Chapter 5 presented the analysis of retinal layers to identify and evaluate DM using OCT images. The requirement of this analysis is essential with the fact that the retinal layer study can not be investigated with the help of the fundus image. In this chapter, we proposed an algorithm for the efficient identification of DM. The important task of speckle noise removal from OCT images is done with the help of guided image filter. The elimination of speckle noise and retaining edges of the layer, served the later process to perform better. The modified level set fuzzy C means algorithm were used for the ILM and RPE layer detection despite variational edge strengths. The database generated from local hospitals helped in the evaluation process, as there are very few publicly available databases. The images from publicly available Duke University database is used for performance comparison of DM detection with state-of-the art methods. The application of a Gaussian bandpass filter successfully eliminated the background variation to help the identification of cyst. The application of Modified Nick's threhold with modified LSFCM detects the cyst efficiently and outperforms the other available algorithm on comparison over OCSC database. The algorithm discussed so far detects the DM presence by obtaining the ILM-RPE thickness measurement and provides a cyst analysis report for the DM patients.

The proposed algorithms provided better identification of DM in both fundus and OCT images and performed an efficient analysis of the same. The summary presents that the proposed image-based decision system-generated may help the ophthalmologists with an additional tool to enhance the early diagnosis. The significant contributions in this connection are achieved and discussed in the following section.

6.2 Contributions

There are various other tools available in the literature for the automated diagnosis for DM. In comparison to those, the work done in this thesis upgrades the analysis process with a higher efficiency and faster detection. The major contributions of this dissertation are as follows,

(i) Accurate field of view of fundus image for analysis enhances the segmentations.

(ii) Avascular property of fovea increases the efficiency of fovea detection, and ellipse template fitting makes it robust.

(iii) HE detection is improved with the removal of retinal reflections.

(iv) Inclusion of cross-sectional width information of BVs, enhances dark lesion detection.

(v) Classification based on deposition level adds additional information on DM severity assessment.

(vi) Guided image filtering for speckle noise removal enhances the DM detection using OCT images.

6.3 Scope for the Future work

In addition to the research work of this dissertation, it generates the foundation for other major challenges. A few of them are discussed below.

(i) The automated algorithm proposed for DM analysis using fundus image performs classification for the severity. As a future direction, we may update and train the system for grading of DM with addition of the evaluation criteria used by ophthalmologists during diagnosis. Also the algorithm can further be modified for AMD analysis.

(ii) The proposed algorithm investigates the presence of pathological signs only in the macula and fovea regions. But they may exist in the peripheral region of fundus image also which affects the peripheral vision. This gives the scope for further investigations in this directions.

(iii) In OCT analysis, we have discussed the detection of ILM and RPE layers for identification of DM. The scope for using the present algorithm with new modules to analyze remaining retinal layers could be explored for a more comprehensive analysis. The detection of the exudate can also be added for better diagnosis.

Another span of future direction can be investigation of the algorithm over various severity level of DM. It requires more data set containing severity level annotations for automated predictions. Hence acquiring such data sets is also essential future work.

(iv) In this dissertation, we have generated algorithms for both fundus and OCT image analysis. With the use of proper database containing both fundus and OCT images of the same patients, algorithms may be updated to obtain correlation in the study with addition of case history. Generating such a better image-based decision system assist ophthalmologists and remote eye care to serve mankind better.

References

[1] O. Troy Bedinghaus, *Macular Edema Causes and Treatments*, Very well health Std., May 2019. [Online]. Available: https://www.verywellhealth.com/macular-edema-3421779

[2] G. Coscas, J. Cunha-Vaz, and A. Loewenstein, *Macular Edema: A Practical Approach*, C. Gabriel, J. Vaz, A. Loewenstein, and G. Soubrane, Eds. Karger Medical and Scientific Publishers, 2010, vol. 47.

[3] K. Boyd, *Eye Health A-Z*, American Academy of Ophthalmology Std., November 2019. [Online]. Available: https://www.aao.org/eye-health/diseases/macular-edema-symptoms

[4] MedicineNet, *Eye anatomy*, MedicineNet, Icahn School of Medicine at Mount Sinai Std., July 2019. [Online]. Available: https://www.medicinenet.com/image-collection/eye_anatomy_detail_picture/picture.htm

[5] R. S. Eshaq, A. M. Aldalati, J. S. Alexander, and N. R. Harris, "Diabetic retinopathy: Breaking the barrier," *Pathophysiology: The Official Journal of The International Society for Pathophysiology*, vol. 24, no. 4, pp. 229 – 241, December 2017.

[6] M. Mookiah, U. Acharya, H. Fujita, J. Tan, C. Chua, S. Bhandary, A. Laude, and L. Tong, "Application of different imaging modalities for diagnosis of diabetic macular edema: A review," *Computers in Biology and Medicine*, vol. 66, pp. 295–315, November 2015.

[7] O. Faust, R. Acharya U, E. Ng, K.-H. Ng, and J. S. Suri, "Algorithms for the automated detection of diabetic retinopathy using digital fundus images: A review," *Journal of Medical Systems*, vol. 36, no. 1, pp. 145–157, February 2012.

[8] J. P. Medhi and S. Dandapat, "An effective fovea detection and automatic assessment of diabetic maculopathy in color fundus images," *Computers in Biology and Medicine*, vol. 74, pp. 30–44, July 2016.

[9] F. CE, *Diabetic retinopathy*, Mayo Foundation for Medical Education and Research (MFMER) Std., January 2019. [Online]. Available: https://www.mayoclinic.org/diseases-conditions/diabetic-retinopathy/symptoms-causes/syc-20371611

[10] S. M. Daniele Veritti, *Microaneurysms key in detecting diabetic retinopathy*, Ocular Surgery News Europe Edition Std., January 2019. [Online]. Available: https://www.healio.com/news/ophthalmology/20120225/microaneurysms-key-in-detecting-diabetic-retinopathy

[11] J. P. Medhi, "An approach for automatic detection and grading of macular edema," in *Medical Imaging: Concepts, Methodologies, Tools, and Applications*. IGI Global, 2017, pp. 1677–1702.

[12] F. Harney, "Diabetic retinopathy," *Medicine*, vol. 34, no. 3, pp. 95–98, March 2006.

[13] M. M. Marcet, *Eyewiki*, American academy of Ophthalmology Std., October 2017. [Online]. Available: http://eyewiki.aao.org

[14] J. D. Du, W.-K. Fong, S. Caliph, and B. J. Boyd, "Lipid-based drug delivery systems in the treatment of wet age-related macular degeneration," *Drug Delivery and Translational Research*, vol. 6, no. 6, pp. 781–792, December 2016.

[15] M. R. K. Mookiah, U. R. Acharya, C. K. Chua, C. M. Lim, E. Ng, and A. Laude, "Computer-aided diagnosis of diabetic retinopathy: A review," *Computers in Biology and Medicine*, vol. 43, no. 12, pp. 2136 – 2155, December 2013.

[16] P. H. Scanlon, “Diabetic retinopathy,” *Medicine*, vol. 47, no. 2, pp. 77–85, December 2019.

[17] M. D. Abràmoff, M. K. Garvin, and M. Sonka, “Retinal imaging and image analysis,” *IEEE Reviews in Biomedical Engineering*, vol. 3, pp. 169–208, December 2010.

[18] M. U. Saeed and J. D. Oleszczuk, “Advances in retinal imaging modalities: Challenges and opportunities,” *World Journal of Ophthalmology*, vol. 6, no. 2, pp. 10–19, May 2016.

[19] Walsh, *New York Eye and Ear Infirmary of Mount Sinai*, Mount Sinai Health System Hospital Campuses Std., September 2017. [Online]. Available: http://www.nyee.edu/patient-care/ophthalmology/retina/history

[20] N. Salamat, M. M. S. Missen, and A. Rashid, “Diabetic retinopathy techniques in retinal images: A review,” *Artificial Intelligence in Medicine*, vol. 97, pp. 168–188, June 2019.

[21] P. H. Scanlon, “Diabetic retinopathy,” *Medicine*, vol. 38, no. 12, pp. 656–660, December 2010.

[22] A. Chan, J. S. Duker, H. Ishikawa, T. H. Ko, J. S. Schuman, and J. G. Fujimoto, “Quantification of photoreceptor layer thickness in normal eyes using optical coherence tomography,” *Retina (Philadelphia, Pa.)*, vol. 26, no. 6, pp. 655–660, July 2006.

[23] P. F. Sharp, J. Olson, F. Strachan, J. Hipwell, A. Ludbrook, and et al, *The value of digital imaging in diabetic retinopathy*, S. Bailey and S. L. Lloyd, Eds. Gray Publishing, Tunbridge Wells, Kent, 2003, vol. 7, no. 30.

[24] H. Li and O. Chutatape, “Automated feature extraction in color retinal images by a model based approach,” *IEEE Transactions on Biomedical Engineering*, vol. 51, pp. 246–254, January 2004.

[25] H. Narasimha-Iyer, A. Can, B. Roysam, C. Stewart, H. Tanenbaum, A. Majerovics, and H. Singh, “Robust detection and classification of longitudinal changes in color retinal fundus images for monitoring diabetic retinopathy,” *IEEE Transactions on Biomedical Engineering*, vol. 53, no. 6, pp. 1084–1098, June 2006.

[26] J. M. Provis, P. L. Penfold, E. E. Cornish, T. M. Sandercoe, and M. C. Madigan, “Anatomy and development of the macula: specialisation and the vulnerability to macular degeneration,” *Clinical and Experimental Optometry*, vol. 88, no. 5, pp. 269 – 281, September 2005.

[27] R. Biyani and B. Patre, “Algorithms for red lesion detection in diabetic retinopathy: A review,” *Biomedicine & Pharmacotherapy*, vol. 107, pp. 681–688, November 2018.

[28] P. F. Sharp, J. Olson, F. Strachan, J. Hipwell, A. Ludbrook, M. O’Donnell, S. Wallace, K. Goatman, A. Grant, and Waugh, “The value of digital imaging in diabetic retinopathy,” *Health technology assessment (Winchester, England)*, vol. 7, no. 30, pp. 1–119, January 2003.

[29] W. Drexler and J. G. Fujimoto, “State-of-the-art retinal optical coherence tomography,” *Progress in retinal and eye research*, vol. 27, no. 1, pp. 45–88, January 2008.

[30] M. Bashkansky and J. Reintjes, “Statistics and reduction of speckle in optical coherence tomography,” *Optics Letters*, vol. 25, no. 8, pp. 545–547, April 2000.

[31] A. M. Abhishek, T. T. Berendschot, S. V. Rao, and S. Dabir, “Segmentation and analysis of retinal layers (ILM & RPE) in optical coherence tomography images with edema,” *2014 IEEE Conference on Biomedical Engineering and Sciences,*, pp. 204–209, December 2014.

[32] Z. Amini and H. Rabbani, “Statistical modeling of retinal optical coherence tomography,” *IEEE Transactions on Medical Imaging*, vol. 35, no. 6, pp. 1544–1554, January 2016.

[33] N. M. Grzywacz, J. de Juan, C. Ferrone, D. Giannini, D. Huang, G. Koch, V. Russo, O. Tan, and C. Bruni, “Statistics of optical coherence tomography data from human retina,” *IEEE Transactions on Medical Imaging*, vol. 29, no. 6, pp. 1224–1237, June 2010.

[34] S. Lu, C.-l. Cheung, J. Liu, J. H. Lim, C. K.-S. Leung, and T. Y. Wong, “Automated layer segmentation of optical coherence tomography images,” *IEEE Transactions on Biomedical Engineering*, vol. 57, no. 10, pp. 2605–2608, June 2010.

[35] D. Koozekanani, K. Boyer, and C. Roberts, "Retinal thickness measurements from optical coherence tomography using a markov boundary model," *IEEE Transactions on Medical imaging*, vol. 20, no. 9, pp. 900–916, September 2001.

[36] D. C. Fernández, H. M. Salinas, and C. A. Puliafito, "Automated detection of retinal layer structures on optical coherence tomography images," *Optics Express*, vol. 13, no. 25, pp. 10 200–10 216, December 2005.

[37] M. Shahidi, Z. Wang, and R. Zelkha, "Quantitative thickness measurement of retinal layers imaged by optical coherence tomography," *American Journal of Ophthalmology*, vol. 139, no. 6, pp. 1056–1061, June 2005.

[38] M. Baroni, P. Fortunato, and A. La Torre, "Towards quantitative analysis of retinal features in optical coherence tomography," *Medical Engineering & Physics*, vol. 29, no. 4, pp. 432–441, May 2007.

[39] D. C. Fernandez, "Delineating fluid-filled region boundaries in optical coherence tomography images of the retina," *IEEE Transactions on Medical Imaging*, vol. 24, no. 8, pp. 929–945, August 2005.

[40] A. M. Bagci, M. Shahidi, R. Ansari, M. Blair, N. P. Blair, and R. Zelkha, "Thickness profiles of retinal layers by optical coherence tomography image segmentation," *American Journal of Ophthalmology*, vol. 146, no. 5, pp. 679–687, November 2008.

[41] A. Yazdanpanah, G. Hamarneh, B. Smith, and M. Sarunic, "Intra-retinal layer segmentation in optical coherence tomography using an active contour approach," *International Conference on Medical Image Computing and Computer-Assisted Intervention,*, pp. 649–656, September 2009.

[42] G. R. Wilkins, O. M. Houghton, and A. L. Oldenburg, "Automated segmentation of intraretinal cystoid fluid in optical coherence tomography," *IEEE Transactions on Biomedical Engineering*, vol. 59, no. 4, pp. 1109–1114, January 2012.

[43] M. B. Lundquist, N. Sharma, and K. Kewalramani, "Patient perceptions of eye disease and treatment in bihar india," *Methods*, vol. 34, no. 10, p. 29, August 2012.

[44] E. H. Sankara Nethralaya, *Sankara Nethralaya*, Std., May 2019. [Online]. Available: http://www.sankaranethralaya.org/teleophthalmology.html

[45] A. Tariq, M. Akram, A. Shaukat, and S. Khan, "A computer aided system for grading of maculopathy," *Cairo International Biomedical Engineering Conference,*, pp. 31–34, December 2012.

[46] A. Tariq, M. U. Akram, A. Shaukat, and S. A. Khan, "Automated detection and grading of diabetic maculopathy in digital retinal images," *Journal of Digital Imaging*, vol. 26, no. 4, pp. 803–812, August 2013.

[47] A. Punnolil, "A novel approach for diagnosis and severity grading of diabetic maculopathy," *International Conference on Advances in Computing Communications and Informatics,*, pp. 1230–1235, August 2013.

[48] M. U. Akram, M. Akhtar, and M. Y. Javed, "An automated system for the grading of diabetic maculopathy in fundus images," *International Conference on Neural Information Processing,*, pp. 36–43, November 2012.

[49] S. H. M. Alipour, H. Rabbani, M. Akhlaghi, A. M. Dehnavi, and S. H. Javanmard, "Analysis of foveal avascular zone for grading of diabetic retinopathy severity based on curvelet transform," *Graefe's Archive for Clinical and Experimental Ophthalmology*, vol. 250, no. 11, pp. 1607–1614, November 2012.

[50] P. C. Siddalingaswamy and K. Prabhu, "Automatic grading of diabetic maculopathy severity levels," *International Conference on Systems in Medicine and Biology,*, pp. 331–334, December 2010.

[51] M. H. Ang, R. Acharya, S. V. Sree, T.-C. Lim, and J. S. Suri, "Computer-based identification of diabetic maculopathy stages using fundus images," *Multi Modality State-of-the-Art Medical Image Segmentation and Registration Methodologies*, vol. 1, no. 1, pp. 377–399, May 2011.

[52] J. Nayak, P. S. Bhat, and U. Acharya, "Automatic identification of diabetic maculopathy stages using fundus images," *Journal of Medical Engineering & Technology*, vol. 33, no. 2, pp. 119–129, January 2009.

[53] A. D. Fleming, K. A. Goatman, S. Philip, G. J. Prescott, P. F. Sharp, and J. A. Olson, "Automated grading for diabetic retinopathy: a large-scale audit using arbitration by clinical experts," *British Journal of Ophthalmology*, vol. 94, no. 12, pp. 1606–1610, December 2010.

[54] L. Giancardo, F. Meriaudeau, T. P. Karnowski, Y. Li, S. Garg, K. W. T. Jr., and E. Chaum, "Exudate-based diabetic macular edema detection in fundus images using publicly available datasets," *Medical Image Analysis*, vol. 16, no. 1, pp. 216 – 226, January 2012.

[55] S. Lim, W. M. D. W. Zaki, A. Hussain, S. Lim, and S. Kusalavan, "Automatic classification of diabetic macular edema in digital fundus images," *IEEE Colloquium on Humanities, Science and Engineering,*, pp. 265–269, December 2011.

[56] K. Sreejini and V. Govindan, "Automatic grading of severity of diabetic macular edema using color fundus images," *3rd International Conference on Advances in Computing and Communications,*, pp. 177–180, August 2013.

[57] Z. Y. Zaidi, M. U. Akram, and A. Tariq, "Retinal image analysis for diagnosis of macular edema using digital fundus images," *IEEE Jordan Conference on Applied Electrical Engineering and Computing Technologies,*, pp. 1–5, December 2013.

[58] A. Hunter, J. A. Lowell, B. Ryder, A. Basu, and D. Steel, "Automated diagnosis of referable maculopathy in diabetic retinopathy screening," *Annual International Conference of the IEEE Engineering in Medicine and Biology Society,*, pp. 3375–3378, September 2011.

[59] K. Deepak and J. Sivaswamy, "Automatic assessment of macular edema from color retinal images," *IEEE Transactions on Medical Imaging*, vol. 31, no. 3, pp. 766–776, December 2012.

[60] C. G. Baby and D. A. Chandy, "Content-based retinal image retrieval using dual-tree complex wavelet transform," *International Conference on Signal Processing, Image Processing & Pattern Recognition,*, pp. 195–199, February 2013.

[61] A. M. Naguib, A. M. Ghanem, and A. S. Fahmy, "Content based image retrieval of diabetic macular edema images," *IEEE 26th International Symposium on Computer-Based Medical Systems,*, pp. 560–562, June 2013.

[62] S. Ibrahim, P. Chowriappa, S. Dua, U. R. Acharya, K. Noronha, S. Bhandary, and H. Mugasa, "Classification of diabetes maculopathy images using data-adaptive neuro-fuzzy inference classifier," *Medical & Biological Engineering & Computing*, vol. 53, no. 12, pp. 1345–1360, December 2015.

[63] A. Tariq and M. Akram, "An automated system for colored retinal image background and noise segmentation," *IEEE Symposium on Industrial Electronics Applications,*, pp. 423–427, October 2010.

[64] S. A. Salem, N. M. Salem, and A. K. Nandi, "Segmentation of retinal blood vessels using a novel clustering algorithm (RACAL) with a partial supervision strategy," *Medical & Biological Engineering & Computing*, vol. 45, no. 3, pp. 261–273, March 2007.

[65] G. B. Kande, P. V. Subbaiah, and T. S. Savithri, "Unsupervised fuzzy based vessel segmentation in pathological digital fundus images," *Journal of Medical Systems*, vol. 34, no. 5, pp. 849–858, October 2010.

[66] J. Ng, S. Clay, S. A. Barman, A. Fielder, M. Moseley, K. Parker, and C. Paterson, "Maximum likelihood estimation of vessel parameters from scale space analysis," *Image and Vision Computing*, vol. 28, no. 1, pp. 55–63, January 2010.

[67] V. M. Saffarzadeh, A. Osareh, and B. Shadgar, "Vessel segmentation in retinal images using multi-scale line operator and k-means clustering," *Journal of Medical Signals and Sensors*, vol. 4, no. 2, pp. 122–129, June 2014.

[68] R. Panda, N. B. Puhan, and G. Panda, "Hausdorff symmetry operator towards retinal blood vessel segmentation," *19th International Conference on Digital Signal Processing,*, pp. 611–616, August 2014.

[69] Y. Q. Zhao, X. H. Wang, X. F. Wang, and F. Y. Shih, "Retinal vessels segmentation based on level set and region growing," *Pattern Recognition*, vol. 47, no. 7, pp. 2437–2446, July 2014.

[70] S. Roychowdhury, D. D. Koozekanani, and K. K. Parhi, “Dream: Diabetic retinopathy analysis using machine learning,” *IEEE Journal of Biomedical and Health Informatics*, vol. 18, no. 5, pp. 1717–1728, December 2014.

[71] C. Zhu, B. Zou, R. Zhao, J. Cui, X. Duan, Z. Chen, and Y. Liang, “Retinal vessel segmentation in colour fundus images using extreme learning machine,” *Computerized Medical Imaging and Graphics*, vol. 100, no. 55, pp. 68–77, January 2017.

[72] N. Memari, A. R. Ramli, M. I. B. Saripan, S. Mashohor, and M. Moghbel, “Supervised retinal vessel segmentation from color fundus images based on matched filtering and adaboost classifier,” *PLoS ONE*, vol. 12, no. 12, pp. 335–370, December 2017.

[73] S. Akbar, M. Sharif, M. U. Akram, T. Saba, T. Mahmood, and M. Kolivand, “Automated techniques for blood vessels segmentation through fundus retinal images: A review,” *Microscopy Research and Technique*, vol. 82, no. 2, pp. 153–170, February 2019.

[74] E. Emary, H. M. Zawbaa, A. E. Hassanien, G. Schaefer, and A. T. Azar, “Retinal blood vessel segmentation using bee colony optimisation and pattern search,” *International Joint Conference on Neural Networks,*, pp. 1001–1006, July 2014.

[75] A. E. Hassanien, E. Emary, and H. M. Zawbaa, “Retinal blood vessel localization approach based on bee colony swarm optimization, fuzzy c-means and pattern search,” *Journal of Visual Communication and Image Representation*, vol. 31, no. 1, pp. 186–196, August 2015.

[76] W. Wang, J. Zhang, W. Wu, and S. Zhou, “An automatic approach for retinal vessel segmentation by multi-scale morphology and seed point tracking,” *Journal of Medical Imaging and Health Informatics*, vol. 8, no. 2, pp. 262–274, February 2018.

[77] A. P. Condurache and A. Mertins, “Segmentation of retinal vessels with a hysteresis binary-classification paradigm,” *Computerized Medical Imaging and Graphics*, vol. 36, no. 4, pp. 325–335, June 2012.

[78] Z. Xiao, M. Adel, and S. Bourennane, “Bayesian method with spatial constraint for retinal vessel segmentation,” *Computational and Mathematical Methods in Medicine*, vol. 2013, no. 1, pp. 326–335, January 2013.

[79] R. Vega, G. Sanchez-Ante, L. E. Falcon-Morales, H. Sossa, and E. Guevara, “Retinal vessel extraction using lattice neural networks with dendritic processing,” *Computers in Biology and Medicine*, vol. 58, pp. 20–30, March 2015.

[80] S. W. Franklin and S. E. Rajan, “Computerized screening of diabetic retinopathy employing blood vessel segmentation in retinal images,” *Biocybernetics and Biomedical Engineering*, vol. 34, no. 2, pp. 117–124, January 2014.

[81] G. Azzopardi, N. Strisciuglio, M. Vento, and N. Petkov, “Trainable cosfire filters for vessel delineation with application to retinal images,” *Medical Image Analysis*, vol. 19, no. 1, pp. 46–57, January 2015.

[82] Q. Li, B. Feng, L. Xie, P. Liang, H. Zhang, and T. Wang, “A cross-modality learning approach for vessel segmentation in retinal images,” *IEEE Transactions on Medical Imaging*, vol. 35, no. 1, pp. 109–118, July 2015.

[83] M. Bertalmio, G. Sapiro, V. Caselles, and C. Ballester, “Image inpainting,” *27th Annual Conference on Computer Graphics and Interactive Techniques,*, pp. 417–424, July 2000.

[84] J. P. Medhi and S. Dandapat, “Analysis of maculopathy in color fundus images,” *Annual IEEE India Conference,*, pp. 1–4, August 2014.

[85] W. A.-N. S. Sekhar and A. Nandi, “Automated localisation of optic disk and fovea in retinal fundus images,” *European Signal Processing Conference,*, pp. 1–5, August 2008.

[86] D. Welfer, J. Scharcanski, and D. R. Marinho, “A coarse-to-fine strategy for automatically detecting exudates in color eye fundus images,” *Computerized Medical Imaging and Graphics*, vol. 34, no. 3, pp. 228 – 235, April 2010.

[87] C. Köse, U. Sevik, and O. Gençalioğlu, “Automatic segmentation of age-related macular degeneration in retinal fundus images,” *Computers in Biology and Medicine*, vol. 38, no. 5, pp. 611 – 619, April 2008.

[88] A. Allam, A. Youssif, and A. Ghalwash, “Automatic segmentation of optic disc in eye fundus images: a survey,” *ELCVIA: Electronic Letters on Computer Vision and Image Analysis*, vol. 14, no. 1, pp. 1–20, April 2015.

[89] C. Sinthanayothin, J. F. Boyce, H. L. Cook, and T. H. Williamson, “Automated localisation of the optic disc, fovea, and retinal blood vessels from digital colour fundus images,” *British Journal of Ophthalmology*, vol. 83, no. 8, pp. 902–910, August 1999.

[90] R. Chrástek, M. Wolf, K. Donath, G. Michelson, and H. Niemann, “Optic disc segmentation in retinal images,” *Bildverarbeitung für die Medizin 2002,*, pp. 263–266, January 2002.

[91] T. Walter and J.-C. Klein, “Segmentation of color fundus images of the human retina: Detection of the optic disc and the vascular tree using morphological techniques,” *International Symposium on Medical Data Analysis,*, pp. 282–287, October 2001.

[92] E. J. Carmona, M. Rincón, J. García-Feijoó, and J. M. Martínez-de-la Casa, “Identification of the optic nerve head with genetic algorithms,” *Artificial Intelligence in Medicine*, vol. 43, no. 3, pp. 243–259, July 2008.

[93] S. Lu, “Accurate and efficient optic disc detection and segmentation by a circular transformation,” *IEEE Transactions on Medical Imaging*, vol. 30, no. 12, pp. 2126–2133, April 2011.

[94] R. Abdel-Ghafar and T. Morris, “Progress towards automated detection and characterization of the optic disc in glaucoma and diabetic retinopathy,” *Medical Informatics and the Internet in Medicine*, vol. 32, no. 1, pp. 19–25, January 2007.

[95] X. Zhu, R. M. Rangayyan, and A. L. Ells, “Detection of the optic nerve head in fundus images of the retina using the hough transform for circles,” *Journal of Digital Imaging*, vol. 23, no. 3, pp. 332–341, June 2010.

[96] A. V. Sagar, S. Balasubramanian, and V. Chandrasekaran, “Automatic detection of anatomical structures in digital fundus retinal images,” *Conference on Machine Vision Applications,*, pp. 483–486, May 2007.

[97] A. Aquino, M. E. Gegúndez-Arias, and D. Marín, “Detecting the optic disc boundary in digital fundus images using morphological, edge detection, and feature extraction techniques,” *IEEE Transactions on Medical Imaging*, vol. 29, no. 11, pp. 1860–1869, May 2010.

[98] A. Dehghani, H. A. Moghaddam, and M.-S. Moin, “Optic disc localization in retinal images using histogram matching,” *EURASIP Journal on Image and Video Processing*, vol. 2012, no. 1, pp. 1–11, December 2012.

[99] X. Zhu and R. M. Rangayyan, “Detection of the optic disc in images of the retina using the hough transform,” *30th Annual International Conference of the IEEE Engineering in Medicine and Biology Society,*, pp. 3546–3549, August 2008.

[100] H. Tjandrasa, A. Wijayanti, and N. Suciati, “Optic nerve head segmentation using hough transform and active contours,” *Telkomnika*, vol. 10, no. 3, pp. 531–536, September 2012.

[101] M. Lalonde, M. Beaulieu, and L. Gagnon, “Fast and robust optic disc detection using pyramidal decomposition and hausdorff-based template matching,” *IEEE Transactions on Medical Imaging*, vol. 20, no. 11, pp. 1193–1200, November 2001.

[102] A. Osareh, M. Mirmehdi, B. Thomas, and R. Markham, “Comparison of colour spaces for optic disc localisation in retinal images,” *Object recognition supported by user interaction for service robots,*, vol. 1, pp. 743–746, August 2002.

[103] A. Hoover and M. Goldbaum, “Locating the optic nerve in a retinal image using the fuzzy convergence of the blood vessels,” *IEEE Transactions on Medical Imaging*, vol. 22, no. 8, pp. 951–958, July 2003.

[104] M. Foracchia, E. Grisan, and A. Ruggeri, “Detection of optic disc in retinal images by means of a geometrical model of vessel structure,” *IEEE Transactions on Medical Imaging*, vol. 23, no. 10, pp. 1189–1195, October 2004.

[105] J. Lowell, A. Hunter, D. Steel, A. Basu, R. Ryder, E. Fletcher, and L. Kennedy, “Optic nerve head segmentation,” *IEEE Transactions on Medical Imaging*, vol. 23, no. 2, pp. 256–264, February 2004.

[106] F. Ter Haar, “Automatic localization of the optic disc in digital colour images of the human retina,” *Utrecht University*, 2005. [Online]. Available: http://citeseerx.ist.psu.edu/viewdoc/download?doi=10.1.1.102.8187&rep=rep1&type=pdf

[107] M. Park, J. S. Jin, and S. Luo, “Locating the optic disc in retinal images,” *International Conference on Computer Graphics, Imaging and Visualisation,*, pp. 141–145, April 2006.

[108] A. D. Fleming, K. A. Goatman, S. Philip, J. A. Olson, and P. F. Sharp, “Automatic detection of retinal anatomy to assist diabetic retinopathy screening,” *Physics in Medicine & Biology*, vol. 52, no. 2, pp. 331–345, December 2006.

[109] J. Park, N. T. Kien, and G. Lee, “Optic disc detection in retinal images using tensor voting and adaptive mean-shift,” *IEEE International Conference on Intelligent Computer Communication and Processing,*, pp. 237–241, April 2007.

[110] H. Ying, M. Zhang, and J.-C. Liu, “Fractal-based automatic localization and segmentation of optic disc in retinal images,” *29th Annual International Conference of the IEEE Engineering in Medicine and Biology Society,*, pp. 4139–4141, May 2007.

[111] A. A.-H. A.-R. Youssif, A. Z. Ghalwash, and A. A. S. A.-R. Ghoneim, “Optic disc detection from normalized digital fundus images by means of a vessels’ direction matched filter,” *IEEE Transactions on Medical Imaging*, vol. 27, no. 1, pp. 11–18, December 2008.

[112] M. Niemeijer, M. D. Abràmoff, and B. Van Ginneken, “Fast detection of the optic disc and fovea in color fundus photographs,” *Medical image analysis*, vol. 13, no. 6, pp. 859–870, June 2009.

[113] R. M. Rangayyan, X. Zhu, F. J. Ayres, and A. L. Ells, “Detection of the optic nerve head in fundus images of the retina with gabor filters and phase portrait analysis,” *Journal of Digital Imaging*, vol. 23, no. 4, pp. 438–453, January 2010.

[114] M. Zubair, A. Yamin, and S. A. Khan, “Automated detection of optic disc for the analysis of retina using color fundus image,” *IEEE International Conference on Imaging Systems and Techniques,*, pp. 239–242, August 2013.

[115] C. Y. Yu and S. S. Yu, “Automatic localization of the optic disc based on iterative brightest pixels extraction,” *International Symposium on Computer, Consumer and Control,*, pp. 613–616, July 2014.

[116] A. Singh, M. K. Dutta, M. ParthaSarathi, V. Uher, and R. Burget, “Image processing based automatic diagnosis of glaucoma using wavelet features of segmented optic disc from fundus image,” *Computer Methods and Programs in Biomedicine*, vol. 124, no. 100, pp. 108–120, February 2016.

[117] S. Maheshwari, R. B. Pachori, V. Kanhangad, S. V. Bhandary, and U. R. Acharya, “Iterative variational mode decomposition based automated detection of glaucoma using fundus images,” *Computers in Biology and Medicine*, vol. 88, no. 15, pp. 142–149, June 2017.

[118] J. E. Koh, E. Y. Ng, S. V. Bhandary, A. Laude, and U. R. Acharya, “Automated detection of retinal health using phog and surf features extracted from fundus images,” *Applied Intelligence*, vol. 48, no. 5, pp. 1–15, May 2018.

[119] Q. Abbas, “Glaucoma-deep: detection of glaucoma eye disease on retinal fundus images using deep learning,” *International Journal of Advanced Computer Science and Applications*, vol. 8, no. 6, pp. 41–5, June 2017.

[120] J. Staal, M. D. Abràmoff, M. Niemeijer, M. A. Viergever, and B. Van Ginneken, “Ridge-based vessel segmentation in color images of the retina,” *IEEE Transactions on Medical Imaging*, vol. 23, no. 4, pp. 501–509, July 2004.

[121] A. Sopharak, B. Uyyanonvara, S. Barman, and T. H. Williamson, “Automatic detection of diabetic retinopathy exudates from non-dilated retinal images using mathematical morphology methods,” *Computerized Medical Imaging and Graphics*, vol. 32, no. 8, pp. 720 – 727, 2008.

[122] D. Welfer, J. Scharcanski, and D. R. Marinho, “Fovea center detection based on the retina anatomy and mathematical morphology,” *Computer Methods and Programs in Biomedicine*, vol. 104, no. 3, pp. 397 – 409, March 2011.

[123] S. Zheng, L. Pan, J. Chen, and L. Yu, “Automatic and efficient detection of the fovea center in retinal images,” *7th International Conference on Biomedical Engineering and Informatics,*, pp. 145–150, October 2014.

[124] J. P. Medhi, M. K. Nath, and S. Dandapat, “Automatic grading of macular degeneration from color fundus images,” *World Congress on Information and Communication Technologies,*, pp. 511–514, October 2012.

[125] J. Singh, G. Joshi, and J. Sivaswamy, “Appearance-based object detection in colour retinal images,” *15th IEEE International Conference on Image Processing,*, pp. 1432–1435, October 2008.

[126] M. Niemeijer, M. Abramoff, and B. van Ginneken, “Segmentation of the optic disc, macula and vascular arch in fundus photographs,” *IEEE Transactions on Medical Imaging*, vol. 26, no. 1, pp. 116–127, January 2007.

[127] R. J. Chalakkal, W. H. Abdulla, and S. S. Thulaseedharan, “Automatic detection and segmentation of optic disc and fovea in retinal images,” *IET Image Processing*, vol. 12, no. 11, pp. 2100–2110, February 2018.

[128] M. Niemeijer, B. van Ginneken, S. R. Russell, M. S. Suttorp-Schulten, and M. D. Abramoff, “Automated detection and differentiation of drusen, exudates, and cotton-wool spots in digital color fundus photographs for diabetic retinopathy diagnosis,” *Investigative Ophthalmology & Visual Science*, vol. 48, no. 5, pp. 2260–2267, November 2007.

[129] K. W. Tobin, E. Chaum, V. P. Govindasamy, and T. P. Karnowski, “Detection of anatomic structures in human retinal imagery,” *IEEE Transactions on Medical Imaging*, vol. 26, no. 12, pp. 1729–1739, November 2007.

[130] M. E. Gegundez-Arias, D. Marin, J. M. Bravo, and A. Suero, “Locating the fovea center position in digital fundus images using thresholding and feature extraction techniques,” *Computerized Medical Imaging and Graphics*, vol. 37, no. 5-6, pp. 386–393, January 2013.

[131] K. S. Chin, E. Trucco, L. Tan, and P. J. Wilson, “Automatic fovea location in retinal images using anatomical priors and vessel density,” *Pattern Recognition Letters*, vol. 34, no. 10, pp. 1152–1158, July 2013.

[132] A. Giachetti, L. Ballerini, E. Trucco, and P. J. Wilson, “The use of radial symmetry to localize retinal landmarks,” *Computerized Medical Imaging and Graphics*, vol. 37, no. 5-6, pp. 369–376, June 2013.

[133] M. U. Akram, A. Tariq, S. A. Khan, and M. Y. Javed, “Automated detection of exudates and macula for grading of diabetic macular edema,” *Computer Methods and Programs in Biomedicine*, vol. 114, no. 2, pp. 141–152, May 2014.

[134] S. Zheng, L. Pan, J. Chen, and L. Yu, “Automatic and efficient detection of the fovea center in retinal images,” *7th International Conference on Biomedical Engineering and Informatics,*, pp. 145–150, October 2014.

[135] E.-F. Kao, P.-C. Lin, M.-C. Chou, T.-S. Jaw, and G.-C. Liu, “Automated detection of fovea in fundus images based on vessel-free zone and adaptive gaussian template,” *Computer Methods and Programs in Biomedicine*, vol. 117, no. 2, pp. 92–103, September 2014.

[136] R. Kamble, M. Kokare, G. Deshmukh, F. A. Hussin, and F. Mériaudeau, “Localization of optic disc and fovea in retinal images using intensity based line scanning analysis,” *Computers in Biology and Medicine*, vol. 87, no. 6, pp. 382–396, August 2017.

[137] X. Cao, J. Lin, L. Xue, and L. Yu, “A novel method of detecting and locating the macula based on morphological features fitting,” *5th International Conference on Information Science and Control Engineering,*, pp. 75–78, July 2018.

[138] B. Al-Bander, W. Al-Nuaimy, B. M. Williams, and Y. Zheng, “Multiscale sequential convolutional neural networks for simultaneous detection of fovea and optic disc,” *Biomedical Signal Processing and Control*, vol. 40, pp. 91–101, February 2018.

[139] T. Walter, J. C. Klein, P. Massin, and A. Erginay, “A contribution of image processing to the diagnosis of diabetic retinopathy-detection of exudates in color fundus images of the human retina,” *IEEE Transactions on Medical Imaging*, vol. 21, no. 10, pp. 1236–1243, October 2002.

[140] M. García, C. I. Sánchez, M. I. López, D. Abásolo, and R. Hornero, “Neural network based detection of hard exudates in retinal images,” *Computer Methods and Programs in Biomedicine*, vol. 93, no. 1, pp. 9–19, May 2009.

[141] A. Sopharak, M. N. Dailey, B. Uyyanonvara, S. Barman, T. Williamson, K. T. Nwe, and Y. A. Moe, “Machine learning approach to automatic exudate detection in retinal images from diabetic patients,” *Journal of Modern optics*, vol. 57, no. 2, pp. 124–135, June 2010.

[142] B. Harangi and A. Hajdu, “Automatic exudate detection by fusing multiple active contours and regionwise classification,” *Computers in Biology and Medicine*, vol. 54, pp. 156–171, November 2014.

[143] P. Khojasteh, B. Aliahmad, and D. K. Kumar, “A novel color space of fundus images for automatic exudates detection,” *Biomedical Signal Processing and Control*, vol. 49, pp. 240–249, March 2019.

[144] R. Besenczi, J. Tóth, and A. Hajdu, “A review on automatic analysis techniques for color fundus photographs,” *Computational and Structural Biotechnology Journal*, vol. 14, no. 100, pp. 371–384, January 2016.

[145] S. Joshi and P. Karule, “A review on exudates detection methods for diabetic retinopathy,” *Biomedicine & Pharmacotherapy*, vol. 97, pp. 1454–1460, January 2018.

[146] S. Ravishankar, A. Jain, and A. Mittal, “Automated feature extraction for early detection of diabetic retinopathy in fundus images,” *IEEE Conference on Computer Vision and Pattern Recognition,*, pp. 210–217, November 2009.

[147] C. Jayakumari and T. Santhanam, “An intelligent approach to detect hard and soft exudates using echo state neural network,” *Information Technology Journal*, vol. 7, no. 2, pp. 386–395, July 2008.

[148] A. Sopharak, B. Uyyanonvara, and S. Barman, “Automatic exudate detection from non-dilated diabetic retinopathy retinal images using fuzzy c-means clustering,” *Sensors*, vol. 9, no. 3, pp. 2148–2161, August 2009.

[149] A. G. Karegowda, S. Bhattacharyya, M. Jayaram, and A. Manjunath, “Exudates detection in retinal images using knnfp and wknnfp classifiers,” *Artificial Intelligent Systems and Machine Learning*, vol. 3, no. 7, pp. 419–425, May 2011.

[150] F. Amel, M. Mohammed, and B. Abdelhafid, “Improvement of the hard exudates detection method used for computer-aided diagnosis of diabetic retinopathy,” *International Journal of Image, Graphics & Signal Processing*, vol. 4, no. 4, pp. 19–27, May 2012.

[151] A. S. A. Alharthi and V. Emamian, “An automated mechanism for early screening and diagnosis of diabetic retinopathy in human retinal images,” *Current Journal of Applied Science and Technology*, vol. 12, no. 1, pp. 1–15, March 2016.

[152] C. I. Sánchez, R. Hornero, M. I. López, M. Aboy, J. Poza, and D. Abásolo, “A novel automatic image processing algorithm for detection of hard exudates based on retinal image analysis,” *Medical Engineering & Physics*, vol. 30, no. 3, pp. 350–357, April 2008.

[153] B. Nagy, B. Harangi, B. Antal, and A. Hajdu, “Ensemble-based exudate detection in color fundus images,” *7th International Symposium on Image and Signal Processing and Analysis,*, pp. 700–703, March 2011.

[154] I. Soares, M. Castelo-Branco, and A. M. Pinheiro, “Exudates dynamic detection in retinal fundus images based on the noise map distribution,” *19th European Signal Processing Conference,*, pp. 46–50, June 2011.

[155] A. Z. Rozlan, H. Hashim, S. F. S. Adnan, C. A. Hong, and M. Mahyudin, “A proposed diabetic retinopathy classification algorithm with statistical inference of exudates detection,” *International Conference on Electrical, Electronics and System Engineering,*, pp. 90–95, May 2013.

[156] K. Soman and D. Ravi, “Detection of exudates in human fundus image with a comparative study on methods for the optic disk detection,” *International Conference on Information Communication and Embedded Systems,*, pp. 1–5, August 2014.

[157] D. Kayal and S. Banerjee, “A new dynamic thresholding based technique for detection of hard exudates in digital retinal fundus image,” *International Conference on Signal Processing and Integrated Networks,*, pp. 141–144, January 2014.

[158] J. Kaur and D. Mittal, “Segmentation and measurement of exudates in fundus images of the retina for detection of retinal disease,” *Journal of Biomedical Engineering and Medical Imaging*, vol. 2, no. 1, p. 27, September 2015.

[159] M. Haloi, S. Dandapat, and R. Sinha, “A gaussian scale space approach for exudates detection, classification and severity prediction,” *arXiv preprint arXiv:1505.00737*, May 2015.

[160] P. M. Rokade and R. R. Manza, “Automatic detection of hard exudates in retinal images using haar wavelet transform,” *Eye*, vol. 4, no. 5, pp. 402–410, November 2015.

[161] T. Jaya, J. Dheeba, and N. A. Singh, “Detection of hard exudates in colour fundus images using fuzzy support vector machine-based expert system,” *Journal of Digital Imaging*, vol. 28, no. 6, pp. 761–768, May 2015.

[162] K. Wisaeng, N. Hiransakolwong, and E. Pothiruk, “Automatic detection of exudates in retinal images based on threshold moving average models,” *Biophysics*, vol. 60, no. 2, pp. 288–297, February 2015.

[163] S. S. RAJA and S. Vasuki, “Screening diabetic retinopathy in developing countries using retinal images,” *Applied Medical Informatics*, vol. 36, no. 1, pp. 13–22, May 2015.

[164] R. Annunziata, A. Garzelli, L. Ballerini, A. Mecocci, and E. Trucco, “Leveraging multiscale hessian-based enhancement with a novel exudate inpainting technique for retinal vessel segmentation,” *IEEE Journal of Biomedical and Health Informatics*, vol. 20, no. 4, pp. 1129–1138, June 2015.

[165] P. Asha and S. Karpagavalli, “Diabetic retinal exudates detection using machine learning techniques,” *International Conference on Advanced Computing and Communication Systems,*, pp. 1–5, April 2015.

[166] J. Lachure, A. Deorankar, S. Lachure, S. Gupta, and R. Jadhav, “Diabetic retinopathy using morphological operations and machine learning,” *IEEE International Advance Computing Conference,*, pp. 617–622, May 2015.

[167] M. Partovi, S. H. Rasta, and A. Javadzadeh, “Automatic detection of retinal exudates in fundus images of diabetic retinopathy patients,” *Journal of Research in Clinical Medicine*, vol. 4, no. 2, pp. 104–109, May 2016.

[168] R. K. Senapati *et al.*, “Bright lesion detection in color fundus images based on texture features,” *Bulletin of Electrical Engineering and Informatics*, vol. 5, no. 1, pp. 92–100, March 2016.

[169] P. Khojasteh, L. A. P. Júnior, T. Carvalho, E. Rezende, B. Aliahmad, J. P. Papa, and D. K. Kumar, “Exudate detection in fundus images using deeply-learnable features,” *Computers in Biology and Medicine*, vol. 104, pp. 62–69, November 2019.

[170] B. Lay, C. Baudoin, and J.-C. Klein, “Automatic detection of microaneurysms in retinopathy fluoroangiogram,” *Applications of Digital Image Processing VI,*, vol. 432, pp. 165–174, January 1984.

[171] T. Spencer, R. P. Phillips, P. F. Sharp, and J. V. Forrester, “Automated detection and quantification of microaneurysms in fluorescein angiograms,” *Graefe's Archive for Clinical and Experimental Ophthalmology*, vol. 230, no. 1, pp. 36–41, June 1992.

[172] T. Spencer, J. A. Olson, K. C. McHardy, P. F. Sharp, and J. V. Forrester, “An image-processing strategy for the segmentation and quantification of microaneurysms in fluorescein angiograms of the ocular fundus,” *Computers and Biomedical Research*, vol. 29, no. 4, pp. 284–302, August 1996.

[173] M. J. Cree, J. A. Olson, K. C. McHardy, P. F. Sharp, and J. V. Forrester, “A fully automated comparative microaneurysm digital detection system,” *Eye 11*, vol. 11, no. 5, pp. 622–628, September 1997.

[174] A. D. Fleming, S. Philip, K. A. Goatman, J. A. Olson, and P. F. Sharp, “Automated microaneurysm detection using local contrast normalization and local vessel detection,” *IEEE Transactions on Medical Imaging*, vol. 25, no. 9, pp. 1223–1232, December 2006.

[175] L. Streeter and M. J. Cree, “Microaneurysm detection in colour fundus images,” *Image Vision Computing New Zealand*, vol. 1, pp. 280–285, November 2003.

[176] D. Usher, M. Dumskyj, M. Himaga, T. H. Williamson, S. Nussey, and J. Boyce, “Automated detection of diabetic retinopathy in digital retinal images: a tool for diabetic retinopathy screening,” *Diabetic Medicine*, vol. 21, no. 1, pp. 84–90, July 2004.

[177] T. Walter, P. Massin, A. Erginay, R. Ordonez, C. Jeulin, and J.-C. Klein, “Automatic detection of microaneurysms in color fundus images,” *Medical Image Analysis*, vol. 11, no. 6, pp. 555–566, November 2007.

[178] M. Niemeijer, B. Van Ginneken, J. Staal, M. S. Suttorp-Schulten, and M. D. Abràmoff, “Automatic detection of red lesions in digital color fundus photographs,” *IEEE Transactions on Medical Imaging*, vol. 24, no. 5, pp. 584–592, September 2005.

[179] A. J. Frame, P. E. Undrill, M. J. Cree, J. A. Olson, K. C. McHardy, P. F. Sharp, and J. V. Forrester, “A comparison of computer based classification methods applied to the detection of microaneurysms in ophthalmic fluorescein angiograms,” *Computers in Biology and Medicine*, vol. 28, no. 3, pp. 225–238, June 1998.

[180] J. Hipwell, F. Strachan, J. Olson, K. McHardy, P. Sharp, and J. Forrester, “Automated detection of microaneurysms in digital red-free photographs: a diabetic retinopathy screening tool,” *Diabetic Medicine*, vol. 17, no. 8, pp. 588–594, October 2000.

[181] G. Gardner, D. Keating, T. H. Williamson, and A. T. Elliott, “Automatic detection of diabetic retinopathy using an artificial neural network: a screening tool,” *British Journal of Ophthalmology*, vol. 80, no. 11, pp. 940–944, August 1996.

[182] X. Zhang and O. Chutatape, “A SVM approach for detection of hemorrhages in background diabetic retinopathy,” *Proceedings IEEE International Joint Conference on Neural Networks,*, vol. 4, pp. 2435–2440, July 2005.

[183] M. J. Cree, “The waikato microaneurysm detector,” *the University of Waikato*, July 2008.

[184] L. Giancardo, F. Meriaudeau, T. P. Karnowski, Y. Li, K. W. Tobin, and E. Chaum, “Microaneurysm detection with radon transform-based classification on retina images,” *Annual International Conference of the IEEE Engineering in Medicine and Biology Society,*, pp. 5939–5942, August 2011.

[185] A. Mizutani, C. Muramatsu, Y. Hatanaka, S. Suemori, T. Hara, and H. Fujita, “Automated microaneurysm detection method based on double ring filter in retinal fundus images,” *SPIE Medical Imaging 2009: Computer-Aided Diagnosis,*, vol. 7260, pp. 72 601N–1, February 2009.

[186] M. U. Akram, S. Khalid, and S. A. Khan, “Identification and classification of microaneurysms for early detection of diabetic retinopathy,” *Pattern Recognition*, vol. 46, no. 1, pp. 107–116, April 2013.

[187] M. U. Akram, S. Khalid, A. Tariq, and S. A. Khan, “Detection and classification of retinal lesions for grading of diabetic retinopathy,” *Computers in Biology and Medicine*, vol. 45, pp. 161–171, March 2014.

[188] Y. Hatanaka, T. Nakagawa, Y. Hayashi, M. Kakogawa, A. Sawada, K. Kawase, T. Hara, and H. Fujita, “Improvement of automatic hemorrhage detection methods using brightness correction on fundus images,” *SPIE Medical Imaging 2008: Computer-Aided Diagnosis,*, vol. 6915, pp. 69 153E–1, April 2008.

[189] G. Quellec, M. Lamard, P. M. Josselin, G. Cazuguel, B. Cochener, and C. Roux, “Detection of lesions in retina photographs based on the wavelet transform,” *International Conference of the IEEE Engineering in Medicine and Biology Society,*, pp. 2618–2621, May 2006.

[190] G. Quellec, M. Lamard, P. Josselin, G. Cazuguel, B. Cochener, and C. Roux, “Optimal wavelet transform for the detection of microaneurysms in retina photographs,” *IEEE Transactions on Medical Imaging*, vol. 27, no. 9, pp. 1230–1241, June 2008.

[191] B. Zhang, X. Wu, J. You, Q. Li, and F. Karray, “Hierarchical detection of red lesions in retinal images by multiscale correlation filtering,” *SPIE Medical Imaging 2009: Computer-Aided Diagnosis,*, vol. 7260, pp. 72 601L–1, April 2009.

[192] J. Zhang, Wu and Karray, "Detection of microaneurysms using multi-scale correlation coefficients," *Pattern Recognition*, vol. 43, no. 6, pp. 2237–2248, June 2010.

[193] S. Ding and W. Ma, "An accurate approach for microaneurysm detection in digital fundus images," *22nd IEEE International Conference on Pattern Recognition,*, pp. 1846–1851, October 2014.

[194] A. Rocha, T. Carvalho, H. F. Jelinek, S. Goldenstein, and J. Wainer, "Points of interest and visual dictionaries for automatic retinal lesion detection," *IEEE Transactions on Biomedical Engineering*, vol. 59, no. 8, pp. 2244–2253, October 2012.

[195] B. Zhang, F. Karray, Q. Li, and L. Zhang, "Sparse representation classifier for microaneurysm detection and retinal blood vessel extraction," *Information Sciences*, vol. 200, pp. 78–90, October 2012.

[196] M. Javidi, H.-R. Pourreza, and A. Harati, "Vessel segmentation and microaneurysm detection using discriminative dictionary learning and sparse representation," *Computer Methods and Programs in Biomedicine*, vol. 139, pp. 93–108, March 2017.

[197] J. I. Orlando, E. Prokofyeva, M. del Fresno, and M. B. Blaschko, "An ensemble deep learning based approach for red lesion detection in fundus images," *Computer Methods and Programs in Biomedicine*, vol. 153, pp. 115–127, August 2018.

[198] M. J. van Grinsven, B. van Ginneken, C. B. Hoyng, T. Theelen, and C. I. Sánchez, "Fast convolutional neural network training using selective data sampling: application to hemorrhage detection in color fundus images," *IEEE Transactions on Medical Imaging*, vol. 35, no. 5, pp. 1273–1284, December 2016.

[199] L. Dai, R. Fang, H. Li, X. Hou, B. Sheng, Q. Wu, and W. Jia, "Clinical report guided retinal microaneurysm detection with multi-sieving deep learning," *IEEE Transactions on Medical Imaging*, vol. 37, no. 5, pp. 1149–1161, December 2018.

[200] C. I. Sánchez, R. Hornero, A. Mayo, and M. García, "Mixture model-based clustering and logistic regression for automatic detection of microaneurysms in retinal images," *SPIE Medical Imaging 2009: Computer-Aided Diagnosis,*, vol. 7260, pp. 72 601M–1, April 2009.

[201] C. Agurto, V. Murray, E. Barriga, S. Murillo, M. Pattichis, H. Davis, S. Russell, M. Abràmoff, and P. Soliz, "Multiscale AM-FM methods for diabetic retinopathy lesion detection," *IEEE Transactions on Medical Imaging*, vol. 29, no. 2, pp. 502–512, May 2010.

[202] M. D. Saleh and C. Eswaran, "An automated decision-support system for non-proliferative diabetic retinopathy disease based on mas and has detection," *Computer Methods and Programs in Biomedicine*, vol. 108, no. 1, pp. 186–196, May 2012.

[203] I. N. Figueiredo, S. Kumar, C. M. Oliveira, J. D. Ramos, and B. Engquist, "Automated lesion detectors in retinal fundus images," *Computers in Biology and Medicine*, vol. 66, pp. 47–65, August 2015.

[204] F. Ren, P. Cao, W. Li, D. Zhao, and O. Zaiane, "Ensemble based adaptive over-sampling method for imbalanced data learning in computer aided detection of microaneurysm," *Computerized Medical Imaging and Graphics*, vol. 55, pp. 54–67, January 2017.

[205] R. Srivastava, L. Duan, D. W. Wong, J. Liu, and T. Y. Wong, "Detecting retinal microaneurysms and hemorrhages with robustness to the presence of blood vessels," *Computer Methods and Programs in Biomedicine*, vol. 138, pp. 83–91, December 2017.

[206] S. S. Kar and S. P. Maity, "Automatic detection of retinal lesions for screening of diabetic retinopathy," *IEEE Transactions on Biomedical Engineering*, vol. 65, no. 3, pp. 608–618, January 2017.

[207] L. Tang, M. Niemeijer, J. M. Reinhardt, M. K. Garvin, and M. D. Abramoff, "Splat feature classification with application to retinal hemorrhage detection in fundus images," *IEEE Transactions on Medical Imaging*, vol. 32, no. 2, pp. 364–375, May 2012.

[208] P. Duraisamy, A. Ei-Saba, X. Yuan, and B. Giri, "Visual contrast enhancement of optical coherence tomography images by combined and image fusion methods," *International Conference on Computing Communication and Networking Technologies,*, pp. 1–1, June 2010.

[209] Y. Liu, Y. Liang, Z. Tong, X. Zhu, and G. Mu, “Contrast enhancement of optical coherence tomography images using least squares fitting and histogram matching,” *Optics Communications*, vol. 279, no. 1, pp. 23–26, November 2007.

[210] M. Haeker, M. Abramoff, R. Kardon, and M. Sonka, “Segmentation of the surfaces of the retinal layer from OCT images,” *International Conference on Medical Image Computing and Computer-Assisted Intervention,*, pp. 800–807, May 2006.

[211] M. K. Garvin, M. D. Abràmoff, R. Kardon, S. R. Russell, X. Wu, and M. Sonka, “Intraretinal layer segmentation of macular optical coherence tomography images using optimal 3-D graph search,” *IEEE Transactions on Medical Imaging*, vol. 27, no. 10, pp. 1495–1505, June 2008.

[212] R. Kafieh, H. Rabbani, and S. Kermani, “A review of algorithms for segmentation of optical coherence tomography from retina,” *Journal of Medical Signals and Sensors*, vol. 3, no. 1, p. 45, January 2013.

[213] S. J. Chiu, M. J. Allingham, P. S. Mettu, S. W. Cousins, J. A. Izatt, and S. Farsiu, “Kernel regression based segmentation of optical coherence tomography images with diabetic macular edema,” *Biomedical Optics Express*, vol. 6, no. 4, pp. 1172–1194, November 2015.

[214] I. Ghorbel, F. Rossant, I. Bloch, S. Tick, and M. Paques, “Automated segmentation of macular layers in OCT images and quantitative evaluation of performances,” *Pattern Recognition*, vol. 44, no. 8, pp. 1590–1603, February 2011.

[215] K. Vermeer, J. Van der Schoot, H. Lemij, and J. De Boer, “Automated segmentation by pixel classification of retinal layers in ophthalmic OCT images,” *Biomedical Optics Express*, vol. 2, no. 6, pp. 1743–1756, December 2011.

[216] J. Y. Lee, S. J. Chiu, P. P. Srinivasan, J. A. Izatt, C. A. Toth, S. Farsiu, and G. J. Jaffe, “Fully automatic software for retinal thickness in eyes with diabetic macular edema from images acquired by cirrus and spectralis systems,” *Investigative Ophthalmology & Visual Science*, vol. 54, no. 12, pp. 7595–7602, August 2013.

[217] A. Lang, A. Carass, M. Hauser, E. S. Sotirchos, P. A. Calabresi, H. S. Ying, and J. L. Prince, “Retinal layer segmentation of macular OCT images using boundary classification,” *Biomedical Optics Express*, vol. 4, no. 7, pp. 1133–1152, December 2013.

[218] P. P. Srinivasan, L. A. Kim, P. S. Mettu, S. W. Cousins, G. M. Comer, and Izatt, “Fully automated detection of diabetic macular edema and dry age-related macular degeneration from OCT images,” *Biomedical Optics Express*, vol. 5, no. 10, pp. 3568–3577, December 2014.

[219] J. Duan, C. Tench, I. Gottlob, F. Proudlock, and L. Bai, “New variational image decomposition model for simultaneously denoising and segmenting optical coherence tomography images,” *Physics in Medicine & Biology*, vol. 60, no. 22, pp. 8901–8911, June 2015.

[220] M. A. Hussain, A. Bhuiyan, A. Turpin, C. D. Luu, R. T. Smith, R. H. Guymer, and R. Kotagiri, “Automatic identification of pathology-distorted retinal layer boundaries using SD-OCT imaging,” *IEEE Transactions on Biomedical Engineering*, vol. 64, no. 7, pp. 1638–1649, July 2016.

[221] Z. Gao, W. Bu, X. Wu, and Y. Zheng, “Intra-retinal layers segmentation of macular OCT images based on the graph optimal approach,” *9th International Congress on Image and Signal Processing, BioMedical Engineering and Informatics,*, pp. 1359–1364, November 2016.

[222] A. ElTanboly, A. Palacio, A. M. Shalaby, A. E. Switala, O. Helmy, S. Schaal, and A. El-Baz, “An automated approach for early detection of diabetic retinopathy using SD-OCT images,” *Frontiers in Bioscience (Elite edition)*, vol. 10, no. 2, pp. 197–207, May 2018.

[223] A. González, B. Remeseiro, M. Ortega, M. G. Penedo, and P. Charlón, “Automatic cyst detection in OCT retinal images combining region flooding and texture analysis,” *26th IEEE International Symposium on Computer-Based Medical Systems,*, pp. 397–400, March 2013.

[224] X. Chen, M. Niemeijer, L. Zhang, K. Lee, M. D. Abràmoff, and M. Sonka, “Three-dimensional segmentation of fluid-associated abnormalities in retinal OCT: probability constrained graph-search-graph-cut,” *IEEE Transactions on Medical Imaging*, vol. 31, no. 8, pp. 1521–1531, March 2012.

[225] X. Xu, K. Lee, L. Zhang, M. Sonka, and M. D. Abràmoff, “Stratified sampling voxel classification for segmentation of intraretinal and subretinal fluid in longitudinal clinical OCT data,” *IEEE Transactions on Medical Imaging*, vol. 34, no. 7, pp. 1616–1623, September 2015.

[226] H. Bogunović, M. D. Abràmoff, and M. Sonka, “Geodesic graph cut based retinal fluid segmentation in optical coherence tomography,” *International Joint Conference on Neural Networks,*, pp. 49–56, October 2015.

[227] M. Esmaeili, A. M. Dehnavi, H. Rabbani, and F. Hajizadeh, “Three-dimensional segmentation of retinal cysts from spectral-domain optical coherence tomography images by the use of three-dimensional curvelet based K-SVD,” *Journal of Medical Signals and Sensors*, vol. 6, no. 3, pp. 166–173, November 2016.

[228] G. N. Girish, B. Thakur, S. R. Chowdhury, A. R. Kothari, and J. Rajan, “Segmentation of intra-retinal cysts from optical coherence tomography images using a fully convolutional neural network model,” *IEEE Journal of Biomedical and Health Informatics*, vol. 23, no. 1, pp. 296–304, January 2019.

[229] DRIVE Database:, *Research Section, Digital Retinal Image for Vessel Extraction (DRIVE) Database*, Utrecht, The Netherlands, University Medical Center Utrecht, Image Science Institute Std., May 2019. [Online]. Available: http://www.isi.uu.nl/Research/Databases/DRIVE

[230] DIARETDB0 Database:, *diabetic retinopathy database and evaluation protocol 0 (DIARETDB0)*, Medical image understanding and analysis Std., May 2019. [Online]. Available: http://www.it.lut.fi/project/imageret/diaretdb0/

[231] DIARETDB1 Database:, *diabetic retinopathy database and evaluation protocol 1 (DIARETDB1)*, Medical image understanding and analysis Std., May 2019. [Online]. Available: http://www2.it.lut.fi/project/imageret/diaretdb1/

[232] MESSIDOR Database:, *Methods to evaluate segmentation and indexing techniques in the field of retinal ophthalmology (MESSIDOR)*, Std., May 2019. [Online]. Available: http://messidor.crihan.fr/download-en.php

[233] HRF Database:, *High-Resolution Fundus Image Database (HRF)*, University of Erlangen Nuremberg Lehrstuhl fuer Mustererkennung, Erlangen Germany Std., May 2019. [Online]. Available: http://www5.cs.fau.de/research/data/fundus-images/

[234] E. Decencière, G. Cazuguel, X. Zhang, G. Thibault, J.-C. Klein, F. Meyer, B. Marcotegui, G. Quellec, M. Lamard, R. Danno *et al.*, “Teleophta: Machine learning and image processing methods for teleophthalmology,” *Innovation and Research in BioMedical Engineering*, vol. 34, no. 2, pp. 196–203, April 2013.

[235] C. I. Sánchez, R. Hornero, M. I. López, M. Aboy, J. Poza, and D. Abásolo, “A novel automatic image processing algorithm for detection of hard exudates based on retinal image analysis,” *Medical Engineering & Physics*, vol. 30, no. 3, pp. 350 – 357, April 2008.

[236] S. P., *Morphological Image Analysis: Principles and Applications.*, 2nd ed. Heidelberg: Springer, 2003.

[237] N. Otsu, “A threshold selection method from gray-level histograms,” *IEEE Transactions on Systems, Man and Cybernetics*, vol. 9, no. 1, pp. 62–66, January 1979.

[238] C. Sinthanayothin, J. F. Boyce, T. H. Williamson, H. L. Cook, E. Mensah, S. Lal, and D. Usher, “Automated detection of diabetic retinopathy on digital fundus images.” *Diabetic medicine : A Journal of the British Diabetic Association*, vol. 19, no. 2, pp. 105–112, February 2002.

[239] X. Zhang, G. Thibault, E. Decencière, B. Marcotegui, and Bruno, “Exudate detection in color retinal images for mass screening of diabetic retinopathy,” *Medical Image Analysis*, vol. 18, no. 7, pp. 1026 – 1043, October 2014.

[240] J. D, *Parametric Equation of a Circle*, Math Open Reference Std., June 2019. [Online]. Available: https://www.mathopenref.com/ellipse.html

[241] D. R. Cox and D. V. Hinkley, *Theoretical statistics*. CRC Press, 1979.

[242] A. Stuart, M. G. Kendall *et al.*, *The advanced theory of statistics*. Griffin, 1963.

[243] Neyman and Jerzy, “X — outline of a theory of statistical estimation based on the classical theory of probability,” *Philosophical Transactions of the Royal Society of London. Series A, Mathematical and Physical Sciences*, vol. 236, no. 767, pp. 333–380, January 1937.

[244] R. Halir and J. Flusser, “Numerically stable direct least squares fitting of ellipses,” *6th International Conference in Central Europe on Computer Graphics and Visualization,*, vol. 98, pp. 125–132, March 1998.

[245] B. Harangi and A. Hajdu, “Improving automatic exudate detection based on the fusion of the results of multiple active contours,” *IEEE 10th International Symposium on Biomedical Imaging,*, pp. 45–48, April 2013.

[246] B. Harangi, I. Lazar, and A. Hajdu, “Automatic exudate detection using active contour model and region-wise classification,” *Annual International Conference of the IEEE Engineering in Medicine and Biology Society,*, pp. 5951–5954, August 2012.

[247] D. Godse and D. Bormane, “Automated localization of optic disc in retinal images,” *International Journal of Advanced Computer Science and Applications*, vol. 4, no. 2, pp. 65–71, December 2013.

[248] L. Giancardo, F. Meriaudeau, T. P. Karnowski, Y. Li, S. Garg, K. W. Tobin Jr, and E. Chaum, “Exudate-based diabetic macular edema detection in fundus images using publicly available datasets,” *Medical Image Analysis*, vol. 16, no. 1, pp. 216–226, November 2012.

[249] E. Imani and H.-R. Pourreza, “A novel method for retinal exudate segmentation using signal separation algorithm,” *Computer Methods and Programs in Biomedicine*, vol. 133, pp. 195–205, June 2016.

[250] Q. Liu, B. Zou, J. Chen, W. Ke, K. Yue, Z. Chen, and G. Zhao, “A location-to-segmentation strategy for automatic exudate segmentation in colour retinal fundus images,” *Computerized Medical Imaging and Graphics*, vol. 55, no. 1, pp. 78–86, May 2017.

[251] W. Kusakunniran, Q. Wu, P. Ritthipravat, and J. Zhang, “Hard exudates segmentation based on learned initial seeds and iterative graph cut,” *Computer Methods and Programs in Biomedicine*, vol. 158, pp. 173–183, July 2018.

[252] S. Long, X. Huang, Z. Chen, S. Pardhan, and D. Zheng, “Automatic detection of hard exudates in color retinal images using dynamic threshold and SVM classification: algorithm development and evaluation,” *Bio-Medical research international*, vol. 29, no. 1, pp. 101–109, January 2019.

[253] D. Michael, M. Niemeijer, A. Osareh, and D. Simmons, *Automated Image Detection of Retinal Pathology*, F. Herbert, Jelinek, and M. J. Cree, Eds. CRC Press. Taylor & Francis Group, 2010.

[254] A. Augustin, F. Bandello, G. Coscas, and C. C. Garcher, *Macular Edema, A Practical Approach*, C. Gabriel, J. Vaz, A. Loewenstein, and G. Soubrane, Eds. Karger, 2010, vol. 47.

[255] Albregtsen and Fritz, “Statistical texture measures computed from gray level coocurrence matrices,” *Image processing laboratory, Department of Informatics, University of OSLO*, vol. 5, no. 01, pp. 01–14, April 2008.

[256] C. Cortes and V. Vapnik, “Support-vector networks,” *Machine Learning*, vol. 20, no. 3, pp. 273–297, June 1995.

[257] K. He, J. Sun, and X. Tang, “Guided image filtering,” *IEEE Transactions on Pattern Analysis and Machine Intelligence*, vol. 35, no. 6, pp. 1397–1409, September 2013.

[258] W. Ni and X. Gao, “Despeckling of SAR image using generalized guided filter with bayesian nonlocal means,” *IEEE Transactions on Geoscience and Remote Sensing*, vol. 54, no. 1, pp. 567–579, August 2016.

[259] C. Ttofis, C. Kyrkou, and T. Theocharides, “A low-cost real-time embedded stereo vision system for accurate disparity estimation based on guided image filtering,” *IEEE Transactions on Computers*, vol. 65, no. 9, pp. 2678–2693, December 2016.

[260] C. C. Pham and J. W. Jeon, “Efficient image sharpening and denoising using adaptive guided image filtering,” *IET Image Processing*, vol. 9, no. 1, pp. 71–79, August 2014.

[261] H. M. Salinas and D. C. Fernandez, “Comparison of PDE-based nonlinear diffusion approaches for image enhancement and denoising in optical coherence tomography,” *IEEE Transactions on Medical Imaging*, vol. 26, no. 6, pp. 761–771, May 2007.

[262] L. Zhang, W. Zhu, F. Shi, H. Chen, and X. Chen, “Automated segmentation of intraretinal cystoid macular edema for retinal 3D OCT images with macular hole,” *IEEE 12th International Symposium on Biomedical Imaging,*, pp. 1494–1497, April 2015.

[263] Y. Huang, R. P. Danis, J. W. Pak, S. Luo, J. White, X. Zhang, A. Narkar, and A. Domalpally, “Development of a semi-automatic segmentation method for retinal OCT images tested in patients with diabetic macular edema,” *PloS ONE*, vol. 8, no. 12, pp. e82 922–1, March 2013.

[264] N. Padmasini, K. S. Abbirame, S. M. Yacin, and R. Umamaheswari, “Speckle noise reduction in spectral domain optical coherence tomography retinal images using anisotropic diffusion filtering,” *International Conference on Science Engineering and Management Research,*, pp. 1–5, Nov 2014.

[265] B. N. Li, C. K. Chui, S. Chang, and S. H. Ong, “Integrating spatial fuzzy clustering with level set methods for automated medical image segmentation,” *Computers in Biology and Medicine*, vol. 41, no. 1, pp. 1–10, January 2011.

[266] P. Bharali, J. P. Medhi, and S. Nirmala, “Detection of hemorrhages in diabetic retinopathy analysis using color fundus images,” in *IEEE 2nd International Conference on Recent Trends in Information Systems (ReTIS)*. IEEE, March 2015, pp. 237–242.

[267] J. P. Medhi and S. Dandapat, “Improved analysis of diabetic maculopathy using level set spatial fuzzy clustering,” *22nd National Conference on Communication,*, pp. 1–6, March 2016.

[268] J. Wu, A.-M. Philip, D. Podkowinski, B. S. Gerendas, G. Langs, C. Simader, S. M. Waldstein, and U. M. Schmidt-Erfurth, “Multivendor spectral-domain optical coherence tomography dataset, observer annotation performance evaluation, and standardized evaluation framework for intraretinal cystoid fluid segmentation,” *Journal of Ophthalmology*, vol. 206, pp. 949–955, January 2016.

[269] F. G. Venhuizen, B. van Ginneken, B. Bloemen, M. J. van Grinsven, R. Philipsen, C. Hoyng, T. Theelen, and C. I. Sánchez, “Automated age-related macular degeneration classification in oct using unsupervised feature learning,” *SPIE Medical Imaging 2015: Computer-Aided Diagnosis,*, vol. 9414, pp. 94 141I–1, April 2015.

[270] G. Lemaître, M. Rastgoo, J. Massich, C. Y. Cheung, T. Y. Wong, E. Lamoureux, D. Milea, F. Mériaudeau, and D. Sidibé, “Classification of SD-OCT volumes using local binary patterns: experimental validation for DME detection,” *Journal of Ophthalmology*, vol. 2016, pp. 568–578, June 2016.

[271] D. Sidibe, S. Sankar, G. Lemaitre, M. Rastgoo, J. Massich, C. Y. Cheung, G. S. Tan, D. Milea, E. Lamoureux, and T. Y. Wong, “An anomaly detection approach for the identification of DME patients using spectral domain optical coherence tomography images,” *Computer Methods and Programs in Biomedicine*, vol. 139, pp. 109–117, April 2017.

[272] M. A. Hussain, A. Bhuiyan, C. D. Luu, R. T. Smith, R. H. Guymer, H. Ishikawa, J. S. Schuman, and K. Ramamohanarao, “Classification of healthy and diseased retina using SD-OCT imaging and random forest algorithm,” *PloS ONE*, vol. 13, no. 6, pp. 9–19, September 2018.

[273] K. Gopinath and J. Sivaswamy, “Segmentation of retinal cysts from optical coherence tomography volumes via selective enhancement,” *IEEE Journal of Biomedical and Health Informatics*, vol. 23, no. 1, pp. 273–282, February 2018.

[274] L. de Sisternes, J. Hong, T. Leng, and D. L. Rubin, “A machine learning approach for device-independent automated segmentation of retinal cysts in spectral domain optical coherence tomography images,” *Proceeding Optima Challenge-MICCAI*, 2015.

[275] I. Oguz, L. Zhang, M. D. Abràmoff, and M. Sonka, “Optimal retinal cyst segmentation from OCT images,” *SPIE Medical Imaging 2016: Image Processing,*, vol. 9784, pp. 97 841E–1, April 2016.

LIST OF PUBLICATIONS

Journal Publication: Refereed Journals:

(1) J. P. Medhi and S. Dandapat, “An effective fovea detection and automatic assessment of diabetic maculopathy in color fundus images”. *Computers in Biology and Medicine*, Elsevier, Vol. 74, pp. 30-44, April, 2016.

Manuscripts Submitted

(1) J. P. Medhi, S. Choudhury, S. R. Nirmala and S. Dandapat, “Improved Detection and Analysis of Macular Edema using Guided Image Filtering with Modified Level set Spatial Fuzzy Clustering on OCT images”, *Biomedical Signal Processing and Control*, Elsevier.

(2) J. P. Medhi and S. Dandapat, “Enhanced segmentation of retinopathy lesions for diagnosis of Diabetic Maculopathy using color fundus images”, *Image and Vision Computing*, Elsevier.

(3) J. P. Medhi, K. Bora and S. Dandapat, “Automated detection of fovea using ellipse fitting on fundus image.” *Image and Vision Computing*, Elsevier.

Article in Book:

(1) J. P. Medhi, *Intelligent Applications for Heterogeneous System Modeling and Design. IGI Global*, vol. 1, no. 1, ch. “An Approach for Automatic Detection and Grading of Macular Edema”, pp. 204-231, August 2015.

Refereed Conferences:

(1) J. P. Medhi and S. Dandapat, “Improved analysis of Diabetic Maculopathy using level set spatial fuzzy clustering,” *Twenty Second National Conference on Communication (NCC)*, Guwahati, pp. 1-6, March 2016.

(2) P. Bharali, J. P. Medhi and S. R. Nirmala, “Detection of hemorrhages in diabetic retinopathy analysis using color fundus images,” in *IEEE Second International Conference on Recent Trends in Information Systems (ReTIS)*, pp. 237-242, July 2015.

(3) J. P. Medhi and S. Dandapat,“Automatic detection of fovea using property of vessel free region,” *Twenty First National Conference on Communications (NCC)*, pp. 1-6 , March 2015.

(4) J. P. Medhi and S. Dandapat, “Analysis of Maculopathy in Color Fundus Images,” *Annual IEEE India Conference (INDICON)*, pp. 1-4, December 2014.

(5) J. P. Medhi, M. K. Nath and S. Dandapat, “Automatic grading of macular degeneration from color fundus images.” *IEEE World Congress on Information and Communication Technologies (WICT)* pp. 511-514, October 2012.